EPFL

Thèse n° 8588

Leveraging meteorological radars to investigate the influence of atmospheric dynamics on snowfall microphysics

Présentée le 6 septembre 2021

Faculté de l'environnement naturel, architectural et construit
Laboratoire de télédétection environnementale
Programme doctoral en génie civil et environnement

pour l'obtention du grade de Docteur ès Sciences

par

Josué Etienne GEHRING

Acceptée sur proposition du jury

Prof. M. Lehning, président du jury
Prof. A. Berne, directeur de thèse
Prof. D. Moisseev, rapporteur
Prof. M. R. Kumjian, rapporteur
Prof. H. Wernli, rapporteur

École polytechnique fédérale de Lausanne

2021

“Mais ce qui m’étonna le plus de tout, fut qu’entre ceux de ces grains qui tombèrent les derniers, j’en remarquai quelques-uns qui avaient autour de soi six petites dents [...], elles paraissaient manifestement être faites d’une neige fort subtile qui s’était attachée autour d’eux depuis qu’ils étaient formés, ainsi que s’attache la gelée blanche autour des plantes. [...] Seulement avais-je de la peine à imaginer qui pouvait avoir formé et compassé si justement ces six dents autour de chaque grain. [...] la chaleur [...] y avait aussi ému quelques vapeurs que ce même vent avait chassées contre ces grains, où elles s’étaient gelées en forme de petits poils fort déliés, [...] et ils avaient ainsi composé ces six dents.”

René Descartes, *Les Météores* in *Discours de la méthode*, 1637

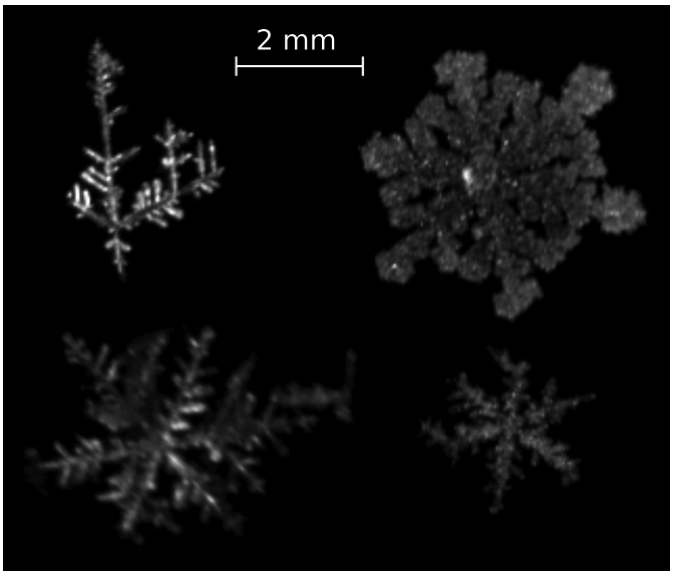

Photographs of ice crystals taken in February and March 2018 in the county of Pyeongchang, South Korea.

Acknowledgements

First, I would like to thank my supervisor, Alexis Berne, for the opportunity to conduct such an exciting PhD project involving field campaigns in regions I would have probably never gone to, opening both my scientific and cultural horizons. Thank you for your time and flexibility, you were always available for meetings and to provide feedback, which guided me through this PhD adventure.

I would also like to thank the jury members for their useful comments on the manuscript and the interesting discussion during the private defence.

International field campaigns require local support: a special thanks goes to the Korea Meteorological Administration and the Australian Antarctic Division. In particular, I want to thank Kwonil Kim for helping to operate the instruments during the ICE-POP 2018 campaign and KwangDeuk Ahn for explaining to us the different facets of Korean culture. I also want to thank Simon Alexander for organising and supporting the PLATO campaign at Davis, Antarctica. A special thanks also goes to Andrew Klekociuk, Derryn Harvie, Fränzi, and Tom for your help in deploying and debugging the instruments at Davis.

A successful PhD would not be possible without amazing lab mates: thanks to all LTE members for the interesting scientific discussions, laughter, and good times spent together. I feel like naming a few: Jacopo for teaching me everything on the MXPol radar and inspiring my PhD work. Étienne for the long scientific discussions and valuable contributions to my case studies. Monika, Anne-Claire, Gionata, Alfonso for your help in data processing or reviewing the manuscript.

Fulfilling the objectives of this PhD would not have been possible without external collaborations: thank you Annika Oertel for your expertise on warm conveyor belts and to the IAC-ETH Dynamo group for welcoming me during the online ECMWF workshop.

I am grateful to everyone who spent a bit of their time proofreading my manuscript.

Finally, I express all my gratitude to my friends and family, in particular my parents, for their support throughout my studies and for always believing in me. Last but not least, with love, to you Kristina for your permanent support and for sharing many beautiful moments together over the last few years.

Morges, July 20, 2021 J. G.

Abstract

Precipitation is the result of a chain of meteorological processes ranging from the large- (>1000 km) to the micro-scale (<1 m). While the transport of moisture and lifting mechanisms leading to cloud formation are mostly governed by dynamical processes, the formation and growth of hydrometeors are ultimately determined by microphysical processes. A proper understanding of the complex interactions between atmospheric dynamics and microphysics is of paramount importance to accurately forecast precipitation. In particular, snowfall microphysics is greatly influenced by dynamical processes, such as turbulence and updraughts. Yet, the impact of atmospheric dynamics on snowfall microphysics remains poorly understood.

In this thesis, meteorological radar observations and atmospheric model simulations are combined to investigate how dynamical processes occurring at different scales can influence snowfall microphysics. We exploit the synergies between measurements collected with an X-band dual-polarisation Doppler radar (named MXPol), a W-band vertically pointing Doppler radar, and a multi-angle snowflake camera (MASC). Hydrometeor classifications (retrieved from MXPol and MASC data) are used to identify the key microphysical processes at play. The objectives of this thesis are twofold: (i) collect data on clouds and precipitation during two field campaigns in South Korea and Antarctica, and (ii) leverage this data to investigate how dynamical processes influenced the microphysics of two snowfall events.

First, a four-month dataset of ground-based radar and in situ measurements collected during the International Collaborative Experiments for PyeongChang 2018 Olympic and Paralympic winter games (ICE-POP 2018) is presented. The dataset includes nine precipitation events with a total accumulation of 195 mm of equivalent liquid precipitation. The hydrometeor classifications reveal that aggregate snowflakes were dominant and that some events featured significant riming. Second, measurements of clouds and precipitation during a three-month intensive campaign at Davis station, East Antarctica are introduced. The MASC classification shows that aggregates and graupel particles were the dominant hydrometeor types that could be identified at ground level. The hydrometeor classification based on MXPol data suggests that crystals were dominant higher up in the clouds, while aggregates and rimed particles were mainly observed below 1000 m a.s.l. Supercooled liquid water was a transient feature of the events we analysed, consistent with observations of rimed particles. Altogether, both datasets collected during this thesis represent an opportunity to study snowfall microphysics thanks to the complementarity of Doppler radar data and snowflake photographs in two regions where such measurements were not available before.

The second part of this thesis is devoted to the analysis of two snowfall events. First, a case

study of the most intense precipitation event of the ICE-POP 2018 dataset reveals that a warm conveyor belt associated with a low pressure system provided ideal conditions for riming and aggregation through the generation of turbulence and supercooled liquid water in the large-scale ascent. These processes led to enhanced precipitation rates of up to 12 mm h^{-1} and a total accumulation of 57 mm of equivalent liquid precipitation in 21 h.
The second case study shows that orographic gravity waves determined the evolution and distribution of snowfall during an atmospheric river event over Davis in the Vestfold Hills, East Antarctica. Despite the intense moisture advection by the atmospheric river, little precipitation was observed at Davis due to intense snowfall sublimation by foehn winds associated with the orographic gravity waves. We propose that this mechanism could contribute to the extremely dry climate of the Vestfold Hills, one of the rare ice-free regions of Antarctica.
Altogether, this thesis offers two unique datasets which are available to the scientific community and can be used for future studies on snowfall microphysics. It also contributes to a better understanding of how atmospheric dynamics can influence snowfall microphysics. In particular, it illustrates how processes occurring at different spatial scales can determine the dominating snowfall microphysical processes.

Résumé

Les précipitations sont le résultat d'une chaîne de processus météorologiques allant de l'échelle synoptique (> 1000 km) à la micro-échelle (< 1 m). Tandis que le transport d'humidité et les mécanismes de soulèvement conduisant à la formation des nuages sont principalement gouvernés par des processus dynamiques, la formation et la croissance des hydrométéores sont en fin de compte déterminées par des processus microphysiques. Une bonne compréhension des interactions complexes entre la dynamique de l'atmosphère et la microphysique est primordiale pour une prévision précise des précipitations. En particulier, la microphysique de la neige est fortement influencée par des processus dynamiques, tels que la turbulence et les courants ascendants. Cependant, l'impact de la dynamique atmosphérique sur la microphysique de la neige est encore mal compris.

Dans cette thèse, des observations de radars météorologiques et des simulations de modèles atmosphériques sont combinées pour examiner comment des processus dynamiques se produisant à des échelles différentes peuvent influencer la microphysique de la neige. Nous tirons profit de la synergie des mesures collectées par un radar Doppler bande X à double polarisation (nommé MXPol), un profileur Doppler bande W (nommé WProf) et une caméra à flocons de neige (nommée MASC). Des classifications d'hydrométéores (extraites des données de MXPol et du MASC) sont utilisées pour identifier les processus microphysiques principaux. Les objectifs de cette thèse sont doubles : (i) collecter des mesures de nuages et de précipitations durant deux campagnes de mesures en Corée du Sud et en Antarctique et (ii) exploiter ces données pour étudier comment des processus dynamiques influencent la microphysique de deux événements neigeux.

Premièrement, un jeu de données de quatre mois de mesures radars et in situ depuis le sol durant une campagne de mesure internationale pour les jeux Jeux olympiques et paralympiques d'hiver de 2018 (ICE-POP 2018) est présenté. Ce jeu de données comprend neuf événements de précipitations avec une accumulation totale de 195 mm d'équivalent en eau liquide. Les classifications d'hydrométéores révèlent que les agrégats étaient dominants et que certains événements comprenaient du givrage significatif. Deuxièmement, des mesures de nuages et précipitations durant une campagne de mesures de trois mois à la station Davis en Antarctique orientale sont présentées. La classification du MASC montre que les agrégats et la neige roulée représentaient les types d'hydrométéores dominants identifiés au sol. La classification d'hydrométéore extraite des données de MXPol suggère que les cristaux de glace dominaient la partie supérieure des nuages, tandis que les agrégats et les particules givrées ont été observées principalement en dessous de 1000 m d'altitude. De l'eau surfondue était présente de manière

transitoire durant les événements analysés, en accord avec des observations de particules givrées. En somme, les deux jeux de données collectés durant cette thèse représentent une opportunité pour étudier la microphysique de la neige grâce à la complémentarité des mesures radars Doppler et des photographies de flocons de neige dans deux régions où de telles mesures n'étaient pas disponibles par le passé.
La deuxième partie de cette thèse est consacrée à l'analyse de deux événements neigeux. Premièrement, une étude de cas de l'événement de précipitations le plus intense de la campagne ICE-POP 2018 montre qu'une ceinture d'écoulement chaude (*warm conveyor belt*) associée à un système dépressionnaire a fourni les conditions de givrage et d'aggrégation idéales par la génération d'eau surfondue dans le courant synoptique ascendant et de turbulence. Ces processus ont conduit à une intensification du taux de précipitation jusqu'à 12 mm h^{-1} et une accumulation totale de 57 mm d'équivalent en eau liquide en 21 h.
La deuxième étude de cas montre que des ondes orographiques ont été déterminantes dans l'évolution et la distribution des chutes de neige durant un événement de rivière atmosphérique à Davis dans les Collines de Vestfold, en Antarctique orientale. Malgré l'advection intense d'humidité par la rivière atmosphérique, peu de précipitations ont été observées à Davis, à cause de la forte sublimation des chutes de neige par un vent de foehn associé aux ondes orographiques. Nous proposons que ce mécanisme pourrait contribuer au climat extrêmement sec des Collines de Vestfold, une des rares régions libres de neige et de glace en Antarctique.
En conclusion, cette thèse offre deux jeux de données uniques qui sont disponibles pour la communauté scientifique et peuvent être utilisés pour des études futures sur la microphysique de la neige. Elle contribue aussi à une meilleure compréhension de la manière dont la dynamique atmosphérique peut influencer la microphysique de la neige. En particulier, elle illustre comment des processus se produisant à différentes échelles spatiales peuvent déterminer les processus microphysiques dominants.

“Perfect crystals are frequently covered over and lines of beauty obliterated by such granular coatings. Granulation often proceeds to such a degree, and the true crystals are so deeply coated over and imbedded within it, that the character of the nucleus does not reveal itself, except under the closest examination.”

Wilson A. Bentley, in *Bentley* (1902)

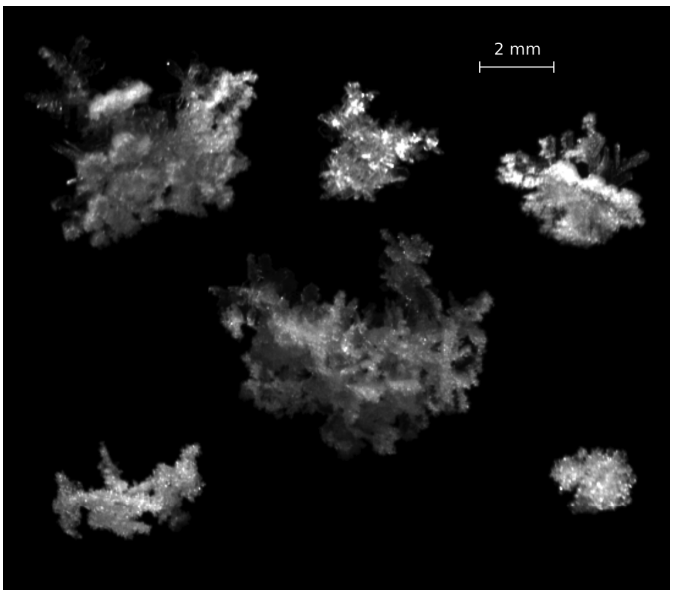

Photographs of rimed snowflakes taken in February and March 2018 in the county of Pyeongchang, South Korea.

Contents

Most important symbols

Symbol	Units	Description
D	[mm]	Particle diameter (or reference size)
$f_{hh(vv)}$	[m] or [cm]	Complex forward scattering amplitude, horizontal (vertical) polarisation
K	[–]	Dielectric factor of an hydrometeor type
K_{dp}	[° km^{-1}]	Specific differential phase shift upon propagation
K_i	[–]	Dielectric factor of ice
K_w	[–]	Dielectric factor of liquid water
$N(D)$	[mm^{-1} m^{-3}]	Drop size distribution or particle size distribution
P	[W] or [dBm]	Power
P_t	[W] or [mW]	Power transmitted by a radar
P_r	[W] or [mW]	Power received by a radar
r or R	[m] or [km]	Range distance
V_D	[m s^{-1}]	Doppler velocity velocity
Z	[dBZ] or [mm^6 m^{-3}]	Radar reflectivity factor
Z_{DR}	[dB]	Differential reflectivity
Z_e	[dBZ] or [mm^6 m^{-3}]	Equivalent radar reflectivity factor
$Z_{H(V)}$	[dBZ]	Radar horizontal (vertical) equivalent reflectivity factor
η	[m^{-1}]	Radar reflectivity
λ	[m] or [mm] or [cm]	Radar wavelength
ρ_{hv}	[–]	Co-polar correlation coefficient
σ_v	[m s^{-1}]	Doppler spectral width
σ_b	[m^2] or [cm^2]	Backscattering cross-section

Most important acronyms

Acronym	Description
2DVD	2-Dimensional Video Disdrometer
AG	Aggregates
AR	Atmospheric river
AWS	Automatic weather station
BASTA	Name of the W-band Doppler cloud profiler used during PLATO
BKC	Bokwang 1-ri community centre, a place in South Korea
CC	Column crystals
CPC	Combination of column and plate crystals
DFR	Dual-frequency ratio
DGW	Daegwallyeong, a place in South Korea
DJF	December–January–February
DPP	Dual-pulse pair
ECMWF	European Centre for Medium-Range Weather Forecasts
EPE	Extreme precipitation event
EPFL	Ecole Polytechnique Fédérale de Lausanne
ERA5	A reanalysis dataset from ECMWF
FFT	Fast-Fourier transform
FMCW	Frequency modulated continuous wave
GR	Graupel
GWU	Gangneung Wonju national university
ICE-POP 2018	International Collaborative Experiments for PyeongChang 2018 Olympic and Paralympic winter games
IFS	Integrated forecast system
IVT	Integrated vapour transport
IWV	Integrated water vapour
LWC	Liquid water content
LWP	Liquid water path
MASC	Multi-angle snowflake camera
MHS	Mayhills, a place in South Korea
MRR	Micro rain radar
MXPol	Mobile X-band Polarimetric

OGWs	Orographic gravity waves
PAMTRA	Passive and Active Microwave-TRansfer Model
PC	Plate crystals
PLATO	Precipitation over Land And The Southern Ocean
PPI	Plan position indicator
PV	Potential vorticity
RHi(l)	Relative humidity with respect to ice (liquid water)
RHI	Range height indicator
RMAN	name of the Raman lidar used during the PLATO campaign
SLW	Supercooled liquid water
VHF	Very high frequency
WBF	Wegener-Bergeron Findeisen process
WCB	Warm conveyor belt
WRF	Weather Research and Forecasting

1 Introduction and background

Precipitation is a fundamental component of the water cycle. It is the main source of freshwater and therefore plays a crucial role in ensuring the long term sustainability of communities and ecosystems. Half of the precipitation events on Earth originate from snow (*Field and Heymsfield*, 2015), either directly when snowfall reaches the ground, or indirectly when rainfall is the result of snowfall melting aloft in the atmosphere. The greatest accumulation of Earth's freshwater reservoirs is in the form of ice stored in glaciers. Therefore understanding how precipitation, and in particular snow, forms in the atmosphere is of primary importance.

From a meteorological perspective, precipitation is the result of a chain of processes ranging from the large- (>1000 km) to the micro-scale (<1 m). Precipitation formation depends on at least two conditions: the presence of moisture and a nucleation and growth mechanism. Nucleation of cloud particles is favoured by the presence of aerosols onto which water vapour may condense and/or deposit. Condensation and/or deposition are generally provided by the lifting and subsequent cooling of air masses. The moisture source and the lifting mechanism can be of either large- or local-scale origin. For instance, low pressure systems transport moisture over several thousands of kilometres from their genesis region to their impact zone. Horizontal shearing and stretching within low pressure systems then create zones of enhanced horizontal temperature gradients, commonly referred to as fronts. In turn, fronts induce vertical air motion because of the different air densities associated with sharp temperature gradients. Clouds form as a result of adiabatic cooling in the ascending air masses and eventually produce precipitation. In the mid-latitudes, fronts are responsible for most of the precipitation (*Baumgartner and Reichel*, 1975). On the other end of the spectrum, precipitation can be produced locally by convection or orographic lifting. With the former, the ascending motion is induced by convective instability, which can occur for instance when the ground absorbs solar radiation and creates a layer of warm (lighter) air below colder (denser) air. In the latter case, a moist airflow can be simply forced to ascend by the presence of an obstacle, such as a mountain. The transport of moisture and the lifting mechanisms are part of the field of *atmospheric dynamics*. The formation and growth of precipitating particles, called *hydrometeors*, occur through a variety of micro-scale physical processes, which in the

atmospheric science community constitute the field of *microphysics*. Precipitation is hence governed by processes ranging from the large- to the micro-scale. Moreover, precipitation intensity is determined by the interplay between atmospheric dynamics and microphysics. Dynamical processes play a particularly important role for snowfall, since snowflakes are more easily affected by wind and turbulence than faster-falling raindrops. Accurate precipitation forecasting requires a good understanding of these interactions across scales, which is made possible by the combination of modelling and observational studies (*Morrison et al.*, 2020).

This thesis is devoted to investigating the influence of atmospheric dynamics on snowfall microphysics by means of atmospheric models and meteorological radars. In particular, data collected during field campaigns in South Korea and Antarctica will be used. The next section provides a brief historical overview of research into snowfall microphysics and introduces the main processes by which small ice crystals grow into larger snowflakes. Then, the fundamentals of radar measurements relevant to retrieving and interpreting snowfall microphysics are presented. Next, the peculiarity of Antarctic meteorology will be presented. Finally, this introductory chapter ends with the research's objectives and an outline of this thesis.

1.1 Snowfall microphysics

1.1.1 An historical overview of research in snowfall microphysics

The fascination with snowflake geometry has a long history. One of the oldest accounts dates back to 135–150 BCE when Chinese scholar Han Ying compared the hexagonal symmetry of snowflakes to the pentagonal symmetry of certain flowers. It was only in the early modern period that European scientists investigated the structure of snowflakes. In 1611, Johannes Kepler suggested a scientific explanation for the symmetry of snow crystals (see *Kepler and Hardie*, 2014). In his famous meteorological treatise *Les Météores* (see *Frank*, 1982), René Descartes recorded observations made with the naked eye of snow crystals in 1637. The first documented photographs of snowflakes (Fig. 1.1a) are attributed to *Bentley* (1902), who recorded the weather conditions associated with various types of snowflakes. He noted the dependence of the crystals' shapes on temperature and wind, mentioning for instance that wind may prevent the perfect growth of crystals or lead to aggregation. He also mentioned that aggregates and 'heavy granular covered crystals' (probably referring to rimed crystals) are a product of the lower or intermediate parts of clouds. His pioneering work identified weather conditions that influence snowflakes' morphology before the field of snowfall microphysics really existed. Another scientific breakthrough were the first laboratory experiments by Ukichiro Nakaya in the 1930s (*Nakaya*, 1954). He was able to synthetically reproduce snow crystals of different shapes (defining their *habit*) by varying temperature and water vapour saturation. By doing so, he defined what is known as the snow crystal morphology diagram (Fig. 1.1b), which was confirmed by later observations (e.g., *Kobayashi*, 1961). This discovery linked a crystal's habit to the temperature and humidity conditions in which it grew. Therefore if the vertical profiles of temperature and humidity are known (for example with radiosounding

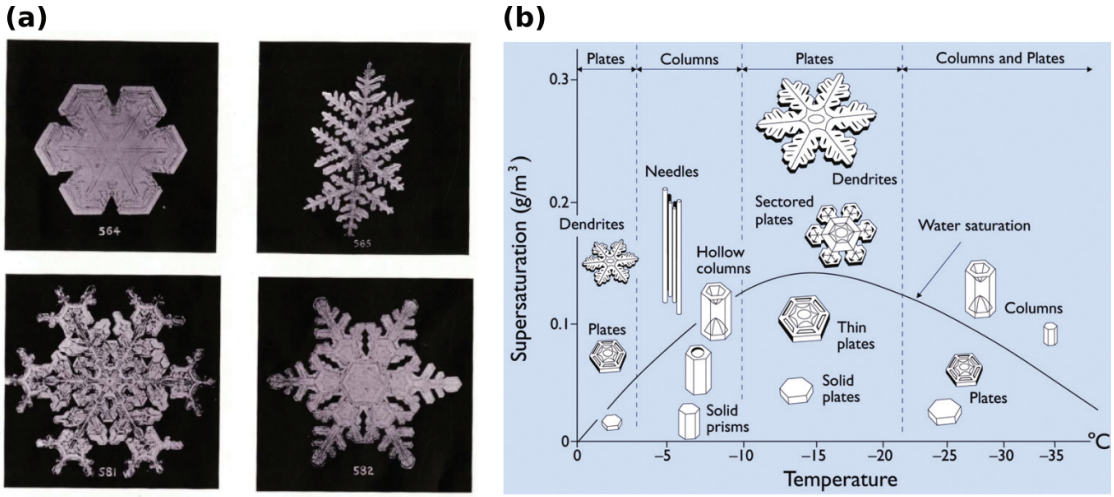

Figure 1.1 – **(a)** Photomicrographs of snow crystals from *Bentley* (1902). **(b)** The snow crystal morphology diagram resulting from the work of *Nakaya* (1954), republished from *Libbrecht* (2005); permission conveyed through Copyright Clearance Center, Inc.

measurements), one can determine the altitude range of the ice crystals' growth based on their characteristics at ground level.

1.1.2 Snowfall microphysical processes

In this section, the main snowfall microphysical processes investigated in this thesis are presented. Their effect on shape, bulk density (hereafter simply density), fall speed, and orientation, as well as the conditions favouring them, are discussed.

Vapour deposition

Ice crystals initially form by homogeneous freezing of cloud droplets or heterogeneous ice nucleation, when a cloud extend at temperatures below 0 °C. Heterogeneous ice nucleation occurs with the help of aerosols, which reduce the energy barrier required for the formation of an ice embryo by offering a solid surface onto which the ice embryo can form (*Lohmann et al.*, 2016). The first mechanism taking place after the formation of an ice embryo is usually growth by vapour deposition. The habit of the growing ice crystal depends on the temperature and the excess humidity with respect to ice saturation (called *supersaturation*). The higher the supersaturation, the more complex the habit. For instance ice crystals tend to grow into dendrites for supersaturations higher than 0.15 g m^{-3} (Fig. 1.1b). Certain habits are generated only at very specific temperatures and supersaturation regimes (e.g. needles), while others can grow under less strict conditions (e.g. plates). Hence the presence of needles can be used as a proxy for specific conditions found in clouds.

Depositional growth is ultimately limited by the availability of water vapour: if supersaturation

with respect to ice goes down to zero, depositional growth will stop. The presence of supercooled liquid water (SLW) can however provide a crucial source of water vapour. Since the saturation vapour pressure over liquid water is higher than over ice, once the vapour pressure goes below saturation with respect to liquid, liquid droplets will evaporate and hence maintain supersaturation with respect to ice. This favours the depositional growth of ice crystals at the expense of liquid droplets until they have all evaporated, or the supersaturation with respect to ice goes down to zero. This process is known as the Wegener-Bergeron-Findeisen (WBF, *Wegener*, 1911) process. It is most efficient when the difference between the saturation vapour pressure over ice and liquid is the largest (i.e. between −8 °C and −16 °C). As a consequence, the WBF process promotes the growth of plates compared to other habits (Fig. 1.1b). The most intense growth of ice crystals occurs on their edges, where the local field of vapour pressure is the highest. Therefore, ice crystals tend to grow along their major dimension (*Ryzhkov and Zrnic*, 2019a), if vapour deposition occurs in the same temperature range where they have formed. This implies that depositional growth decreases crystals' minor-to-major axis ratio (hereafter *aspect ratio*). A notable exception is capped columns, which form when columnar crystals fall in a region where planar growth dominates, resulting in plates growing on the edges of the columns. The fact that the most intense growth of ice crystals occurs on their edges also means that the most efficient habit growth is seen in dendritic crystal since dendrites have greater surface areas available along their edges. The net result of this and the WBF process is that depositional growth is the most efficient between about −10 °C and −20 °C (*Takahashi et al.*, 1991), with dendrites forming above (liquid) water saturation, and plates' growth enhanced by the WBF process in the presence of droplets below (liquid) water saturation.

The density of pristine ice crystals depends primarily on their habit, with plates having greater densities than dendrites and needles (*Andrić et al.*, 2013; *Hogan et al.*, 2002).

Riming

Riming is the collision and subsequent freezing of SLW droplets onto solid hydrometeors. While SLW may exist at temperatures as low as −40 °C, riming is mostly observed between −12 °C and 0 °C (*Kneifel and Moisseev*, 2020). Riming increases the total precipitating mass by converting cloud water into precipitation. *Moisseev et al.* (2017) showed that riming was responsible for 5% to 40% of snowfall mass during 22 winter storms in Finland. Other studies in the Sierra Nevada (USA) and on the island of Hokkaido (Japan) showed that 30% to 60% of the snowfall mass consisted of frozen SLW droplets. It follows that riming has a significant impact on snowfall accumulation.

Riming also increases a hydrometeor's density, such that a rimed particle has a density between that of a raindrop and an aggregate or ice crystal (*Lohmann et al.*, 2016). Riming makes the particles more spherical, so that a fully rimed particles (i.e. *graupel*, Fig. 1.2c) has an aspect ratio close to one (*Garrett et al.*, 2015). The increase in both density and aspect ratio causes the fall speed of snowflakes to increase with increasing riming. The orientation of falling rimed

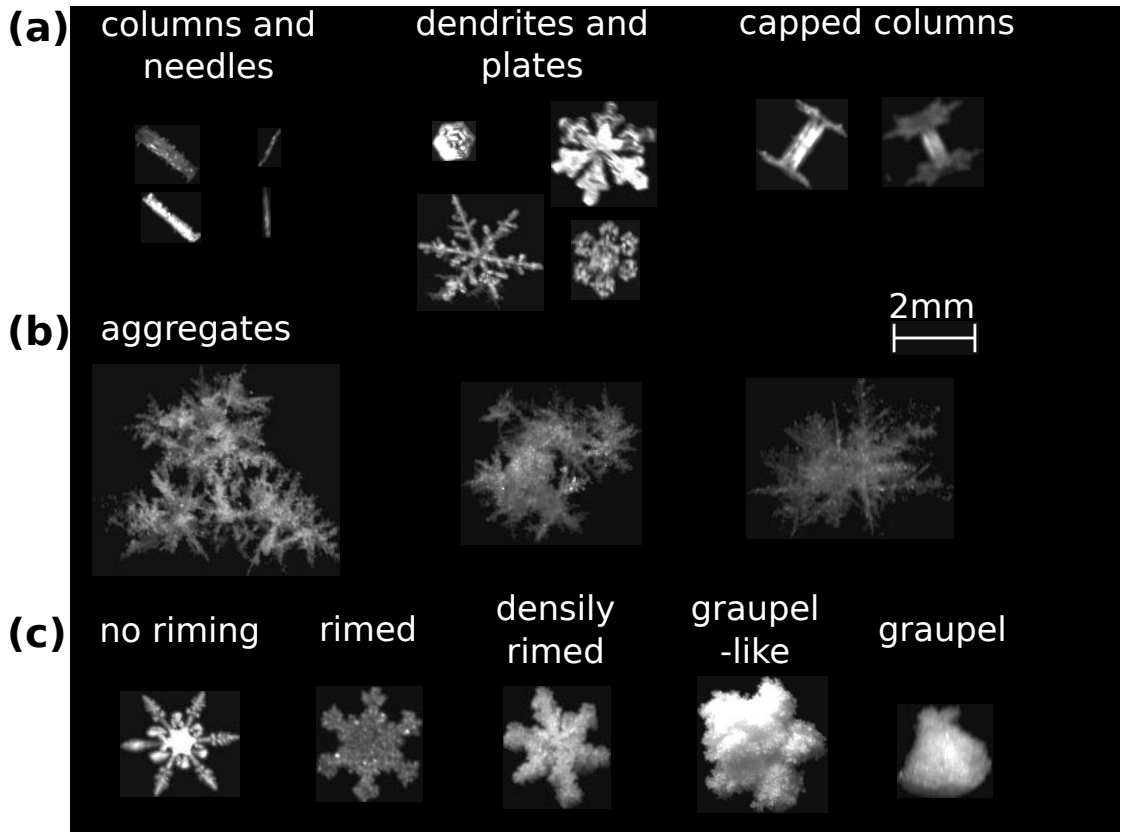

Figure 1.2 – Snowflake photographs illustrating the result of the processes of **(a)** vapour deposition, **(b)** aggregation, and **(c)** riming. Adapted from *Praz et al.* (2017)

particles is similar to crystals, with their major axis oriented close to horizontal.

A prerequisite for riming to occur is the presence of SLW. If there is no external process to maintain saturation over water, the SLW droplets will be depleted by the WBF process at the benefit of depositional growth. The SLW droplets might also freeze before they all evaporate during the WBF process. To maintain SLW droplets, their depletion by the WBF process has to be compensated by dynamical mechanisms, such as condensation or nucleation in ascending motions, or advection of water droplets. *Heymsfield* (1977) proposed that a critical vertical velocity is required to maintain SLW and *Korolev and Mazin* (2003) introduced a theoretical framework to compute this critical velocity as a function of pressure, temperature, and size distributions of liquid and ice particles. In summary, either updraughts or advection of water droplets are needed to maintain SLW and allow sustained riming to take place.

A possible additional effect of riming is the generation of secondary ice particles. The most common mechanism referred to is the splintering of freezing droplets during riming (so-called Hallett-Mossop process, *Hallett and Mossop*, 1974). However, other secondary ice generation processes can occur in the presence of SLW, such as ice fragmentation and droplet shattering (*Korolev and Leisner*, 2020).

Aggregation

When ice crystals collide with each other, they may clump together forming an *aggregate*. Two main mechanisms exist that influence the *sticking efficiency* upon collision. One is the ability of the crystals to interlock their branches, already referred to as mechanical interlocking by *Nakaya* (1954). The habit of the ice crystal is the main factor influencing this interlocking ability (hereafter referred to as 'mechanical aggregation'). For instance, the branches of dendrites make them more likely to interlock than the flatter surfaces of plates. *Connolly et al.* (2012) showed a maximum of sticking efficiency at a temperature around −15 °C. Other studies showed a peak ranging between −12.5 °C and −17 °C (*Hosler and Hallgren*, 1960; *Mitchell*, 1988). These temperatures correspond to the conditions of dendritic growth above water saturation (Fig. 1.1b), confirming that dendritic crystals are more likely to aggregate by interlocking branches. *Connolly et al.* (2012) hypothesised that interlocking enhances *sintering* by allowing enough time for vapour to deposit on the contact points of the ice crystals.

The second mechanism is determined by the presence of a quasi-liquid layer forming on ice crystal surfaces at temperatures higher than −25 °C (*Li and Somorjai*, 2007). The thickness of this quasi-liquid layer increases with increasing temperature and so does the sticking efficiency (*Lohmann et al.*, 2016). This phenomenon has been experienced by anyone trying to make a snowball from dry snow compared to wetter snow at higher temperatures and will be hereafter referred to as 'wet aggregation'.

Temperature and humidity are the main variables influencing mechanical and wet aggregation. While aggregation has been observed at temperatures as low as −60 °C (*Connolly et al.*, 2005; *Field and Heymsfield*, 2003), it is most efficient at temperatures above about −20 °C (*Hobbs et al.*, 1974; *Phillips et al.*, 2015). The most recent laboratory and modelling studies (*Connolly et al.*, 2012; *Phillips et al.*, 2015) agree that the peak in efficiency is found around −15 °C and is attributed to mechanical aggregation, which then enhances sintering. However, *Connolly et al.* (2012) mention that it is valid for the early stage of aggregation (particles smaller than 500 µm). The interplay between these two aggregation mechanisms may depend on the stage of aggregation. *Phillips et al.* (2015) found that the higher the degree of aggregation of the colliding snowflakes, the higher their sticking efficiency by mechanical aggregation. They propose that snow grows in positive feedback, with aggregates collecting more crystals as they become stickier. The observations of *Hobbs et al.* (1974) in the Cascade mountains showed that the maximum probability of aggregation is found at a temperature around 0 °C. Therefore, these studies suggest that for small particles, mechanical aggregation seems dominant with maximum efficiency at −15 °C, while for larger ones both wet and mechanical aggregation are significant and the maximum efficiency is close to 0 °C. More experimental studies are needed to investigate the role of particle size in sticking efficiencies (*Phillips et al.*, 2015).

The aspect ratio of aggregates is lower than that of rimed particles and tends to have a broader distribution (*Garrett et al.*, 2015). *Moisseev et al.* (2015) suggested that early aggregates can be relatively oblate. As aggregation continues, the aspect ratio will increase and thus the shape of

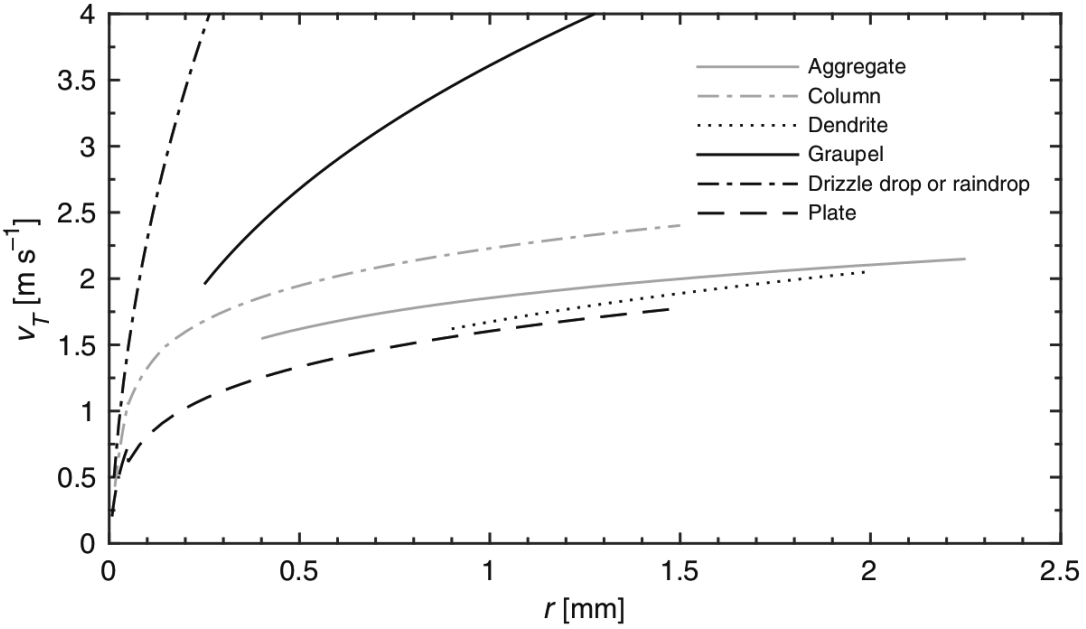

Figure 1.3 – Terminal velocities (V_T) of different hydrometeors as a function of their maximum dimension (r) from the parameterisation of *Mitchell and Heymsfield* (2005). Figure from *Lohmann et al.* (2016) with permission from Cambridge University Press.

aggregates strongly depends on the stage of aggregation. Aggregates tend to be more randomly oriented than ice crystals, owing to their size and irregular shapes (*Ryzhkov and Zrnic*, 2019b; *Wang*, 2013). *Garrett et al.* (2015) showed that the orientation of aggregates depends more on turbulence than on their riming degree and dimension, with turbulent conditions favouring more random orientations. Unrimed aggregates have a lower density than ice crystals and rimed particles. The fall speed of aggregates depends both on their riming degree and crystal type composition. *Barthazy and Schefold* (2006) showed that the fall speed of aggregates composed of needles or plates depends strongly on the riming degree, while those consisting of dendrites or mixed habits do not show a dependence on riming. This shows that identifying aggregation purely from changes in hydrometeors fall speed is not possible as it depends on riming and crystals' habits. However, Fig. 1.3 provides a relation between the terminal velocity of different hydrometeors and their size. Aggregates tend to have slightly higher fall speeds than planar crystals (i.e. dendrites and plates), but smaller than columns and much smaller than graupel.

Turbulence not only affects the orientation of aggregates, but it also increases the probability of collision between falling particles and hence enhances the process of aggregation (*Houze and Medina*, 2005; *Medina et al.*, 2005). Updraughts increase the time particles are suspended in the air, which also promotes aggregation (*Garrett*, 2019). This shows that dynamical conditions, such as updraughts and turbulence, can favour aggregation. As opposed to riming, aggregation does not directly increase the precipitating mass. However, it does produce larger targets for the accretion of SLW droplets and hence indirectly increases the precipitating mass through

the process of riming (*Houze and Medina*, 2005).

1.2 Meteorological radars for snowfall microphysical studies

1.2.1 Reflectivity and the radar equation

The use of radars in meteorology dates back to the 1940s, as World War II reached its climax. Radars were first designed to detect aircraft by using radiowaves (frequency < 1 GHz). At these low frequencies, precipitation was not visible. The development of the magnetron, working at microwave frequencies (1–100 GHz), allowed smaller radars to be built. Echoes from unrecognised targets were detected on the first microwave radar images and were initially considered as clutter. It was soon acknowledged that precipitation was causing these echoes and that radars represented a serious potential for meteorology (*Fabry*, 2015). This led to the birth of radar meteorology and enabled the collection of the first meteorological measurements at the mesoscale, filling an observational gap between the synoptic- and the micro-scale. While surface weather charts were already being created based on local observations in the mid 19th century, the spatial resolution of these measurements only allowed for the observation of synoptic-scale weather systems.

The principle of meteorological radars is based on the backscattering properties of hydrometeors. Let us consider a radar emitting electromagnetic waves in pulses of duration τ and with a beamwidth θ in the atmosphere. The volume sampled by this radar at a range r can be defined by [1]:

$$V = \frac{1}{8}\pi r^2 \theta^2 c\tau \tag{1.1}$$

where θ is typically (for the radars used in this thesis) of the order of 1° and the range resolution $c\tau/2$ around 75 m ($\tau \sim 0.5\,\mu$s; c is the speed of light). We hereafter consider that the sampling volume V is populated by hydrometeors and therefore refrain from using the general term of 'targets'. When a wave pulse encounters hydrometeors, part of the energy will be absorbed by the water molecules (hence attenuating the signal) while most of it will be scattered. The fraction of energy, per unit pulse duration, scattered back towards the radar is given by the *radar equation*, which can be written in a simplified form as:

$$\frac{P(r)}{P_t} = \frac{C \cdot \eta}{r^2} \tag{1.2}$$

where $P(r)$ is the backscattered power from a population of hydrometeors at a distance r received by a radar emitting a total power P_t. C is a constant that depends only on the specifications of the radar. r is given by $r = c\Delta t/2$, where Δt is the time it takes for a pulse to cover twice (from the radar to the target and vice-versa) the distance to the target. From

[1] Equation 1.1 is a simplification assuming that the radar beam is cylindrical and the power density is the same within the beam. Typical radar antenna beams are more Gaussian and the Probert-Jones approximation (*Probert-Jones*, 1962) should be used to describe the sampling volume more accurately.

Eq. (1.2) we see that the fraction of power received is inversely proportional to the squared distance to the hydrometeors' population and proportional to the *reflectivity* η [m^{-1}], defined as:

$$\eta \equiv \int_{D_{min}}^{D_{max}} \sigma_b(D) N(D) dD \tag{1.3}$$

where $\sigma_b(D)$ [m^2] is the backscattering cross-section and $N(D)$ [$mm^{-1}\,m^{-3}$] is the number concentration of hydrometeors with an equivolume spherical diameter between D and $D+dD$ [mm]. $\sigma_b(D)$ does not correspond to the hydrometeor's geometrical cross-section, but can be interpreted as the area that the radar 'sees', which is proportional to the amount of energy backscattered towards it, hence the name backscattering cross-section. σ_b depends on D, the radar wavelength λ, and the *dielectric constant* or *relative permittivity* ϵ_r, which is a complex number quantifying the scattering (its real part) and absorption (its complex part) properties of a material to electromagnetic radiation (*Kumjian*, 2018). Figure 1.4 shows the relation between the normalised σ_b and D for three common radar wavelengths. One can see that σ_b exhibits a power law relation for $D << \lambda$ with an exponent of 6 (the slope of the lines in log-space). This is the Rayleigh scattering regime, for which σ_b can be approximated as:

$$\sigma_b(D) \approx \frac{\pi^5}{\lambda^4} D^6 |K|^2 \tag{1.4}$$

where K is the dielectric factor and depends only on ϵ_r as:

$$|K|^2 \equiv \left| \frac{\epsilon_r - 1}{\epsilon_r + 2} \right|^2 \tag{1.5}$$

For materials with similar dielectric properties (i.e. the same K), a shorter radar wavelength λ will increase the backscatter cross-section (it modifies the intercept in log-space, Fig. 1.4). This is why radars with shorter wavelengths are more sensitive to smaller hydrometeors.

Combining Eq. (1.3) with Eq. (1.4) we can redefine the reflectivity in the Rayleigh regime as:

$$\eta \approx \frac{\pi^5}{\lambda^4} |K|^2 \int_{D_{min}}^{D_{max}} D^6 N(D) dD \tag{1.6}$$

This expression of η shows an interesting feature: the integral part contains only meteorological information. We can hence define it as a new variable purely related to the microstructure of precipitation, the *radar reflectivity factor* [$mm^6\,m^{-3}$]:

$$Z \equiv \int_{D_{min}}^{D_{max}} D^6 N(D) dD \tag{1.7}$$

Z is the 6th moment of the drop size distribution $N(D)$, which means that in the Rayleigh regime a radar 'sees' mainly large particles (Fig. 1.5). If one applies Eq. (1.7) to the discrete

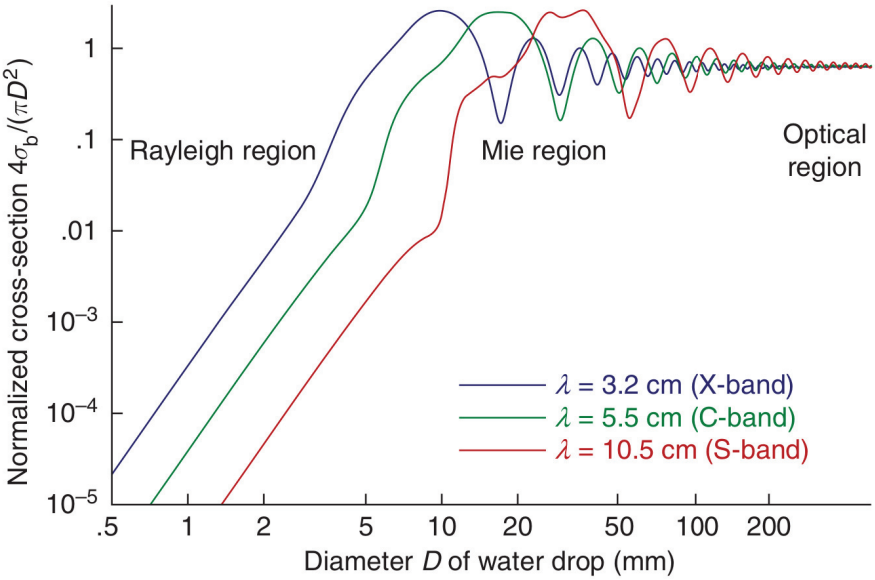

Figure 1.4 – Normalised backscatter cross-section for spherical raindrops as a function of their diameter for three common radar wavelengths. Figure from *Fabry* (2015) with permission from Cambridge University Press.

case illustrated in Fig. 1.5, it becomes evident that Z is dominated by the largest drop. The computation of Z from the radar equation requires knowledge on the dielectric nature of the targets, since Z is linked to η through K (Eq. 1.6 and 1.7). However, the nature of the targets and their scattering regime is not known in advance. We therefore define a variable called the *equivalent reflectivity factor* (Z_e), which assumes that the targets consist of spherical liquid drops behaving as Rayleigh scatterers (i.e. $D << \lambda$), as:

$$\eta \approx \frac{\pi^5}{\lambda^4} |K_w|^2 Z_e \tag{1.8}$$

We hereafter simply use the term reflectivity to refer to the equivalent reflectivity factor. $|K_w|^2$ in Eq. (1.8) is the squared modulus of the dielectric factor of liquid water, which for typical radar wavelengths (~ 1 cm) is 0.93. For solid ice, $|K_i|^2$ is 0.42 and for snow, it decreases with decreasing density (*Ryzhkov and Zrnic*, 2019b), which shows that snowflakes have a smaller backscatter cross-section than raindrops of similar sizes. Moreover, the reflectivity of snowflakes is proportional to D^4, instead of D^6 for raindrops (Eq. 5.14 in *Ryzhkov and Zrnic*, 2019c), because the density of snowflakes is inversely proportional to their dimension. This and the fact that $|K_i|^2$ is smaller than $|K_w|^2$, explains why the reflectivity of snow is usually smaller than rain, even if snowflakes can be larger and can be found in higher concentrations than raindrops.

By measuring the transmitted and received power, and the distance to the hydrometeor population, we can now compute a meteorologically relevant variable (Z_e) using only the

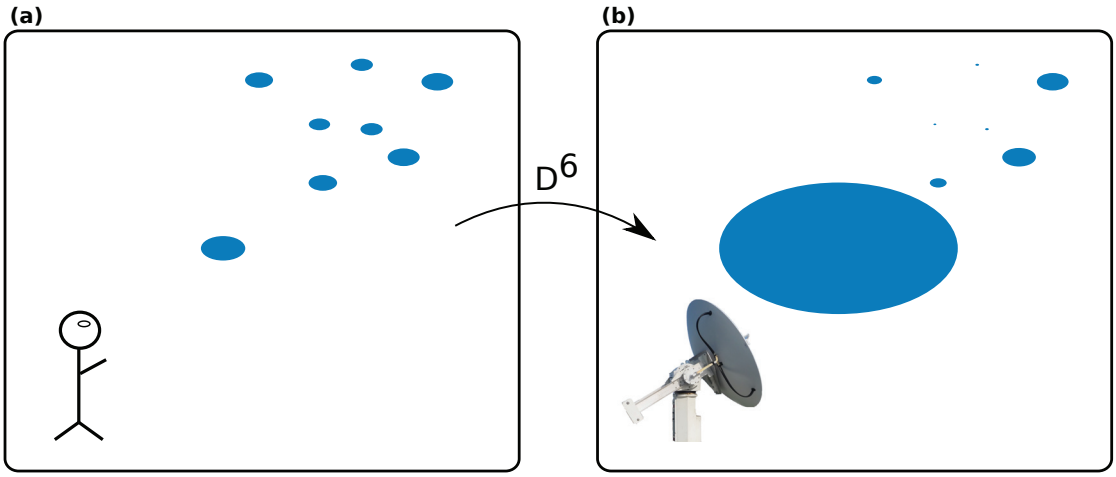

Figure 1.5 – Conceptual scheme of how a human observer **(a)** and a radar **(b)** would 'see' the same size distribution of raindrops. Note how the differences in sizes are enhanced by the D^6 operator. For simplifications, the aspect ratio is constant for all raindrops and D has been defined as the major axis.

radar equation (Eq. 1.2). From Fig. 1.5 and Eq. (1.7), it is evident that Z_e will span many orders of magnitude. For this reason, we usually convert Z_e in decibels with:

$$Z_e[dBZ] = 10\log_{10}\left(\frac{Z_e[\mathrm{mm^6\,m^{-3}}]}{1\,[\mathrm{mm^6\,m^{-3}}]}\right) \tag{1.9}$$

where dBZ stands for 'decibels relative to linear Z units'.

1.2.2 The Doppler velocity spectrum

In the previous section, we introduced the most common radar variable Z_e, which gives information on the intensity of precipitation at a given range. The second most common variable is the Doppler velocity, which is measured from the time rate of change of the backscattered signal phase due to the Doppler effect (see *Kumjian*, 2018). This gives us information on the hydrometeors' radial velocity. For a radar measuring at horizontal incidence, the Doppler velocity is related to the radial wind velocity, under the assumption that the hydrometeors are advected by the wind and behave as passive tracers. For a radar measuring at vertical incidence, the Doppler velocity is the reflectivity-weighted sum of the vertical wind velocity and the hydrometeors' fall speeds. Hence Doppler velocity provides information on the dynamics of the flow. With the advent of Doppler weather radars storing the full Doppler spectrum in the 1970s, it became possible to retrieve microphysical information from Doppler radar measurements. The Doppler spectrum shows the power contribution from hydrometeors as a function of their Doppler velocity. The main variables retrieved from the Doppler spectrum are the mean Doppler velocity V_D [$\mathrm{m\,s^{-1}}$] and the Doppler spectral width σ_v [$\mathrm{m\,s^{-1}}$], which

are defined as:

$$V_D = \frac{1}{P}\int_{v_{min}}^{v_{max}} v \cdot S(v)\,dv \tag{1.10}$$

$$\sigma_v^2 = \frac{1}{P}\int_{v_{min}}^{v_{max}} (v - V_D)^2 \cdot S(v)\,dv \tag{1.11}$$

where P is the total power, which is related to Z_e and defined as:

$$P = \int_{v_{min}}^{v_{max}} S(v)\,dv \tag{1.12}$$

and $S(v)$ [dBm m^{-1} s^{-1}] is the Doppler power spectrum. From Eq. (1.10), we see that the mean Doppler velocity is the power-weighted (or reflectivity-weighted) mean of the spectrum. Knowing that the power scattered by the hydrometeors is proportional to D^6 in the Rayleigh regime (Eq. 1.4), it means that V_D is mainly influenced by the largest hydrometeors. The spectral width is the square root of the variance of the Doppler spectrum (Eq. 1.11). It is a measure of changes of wind velocity (e.g. turbulence, wind shear) and/or a large range of particles' fall speeds within the sampling volume. The Doppler spectrum is probably the only way to access 'subgrid' information within the sampling volume and hence provide valuable information on the microstructure of precipitation. Figure 1.6a shows an example of a range spectrogram (i.e. the Doppler spectrum as a function of range). One can see a population of hydrometeor falling below 4000 m. The spectrum at 4000 m (Fig. 1.6b upper panel) shows that the mode of Doppler velocity is of about -1 m s^{-1}. The variation of the mode of Doppler velocity is due either to microphysical processes affecting the fall speed or variations in vertical wind velocity. For instance, at 2200 m it is very likely that an updraught increased the Doppler velocity. Below 1800 m a second population of particles is visible with a mode of Doppler velocity of around 0 m s^{-1}. This bimodality is visible in the spectrum at 1500 m (Fig. 1.6b lower panel). This could indicate, for instance, the presence of SLW droplets. The example of Fig. 1.6 shows that both microphysical and dynamical processes can be inferred from the interpretation of the Doppler spectrum. It is however often difficult to disentangle both of them and ideally cases with negligible vertical wind velocities are required for microphysical retrievals (*Kalesse et al.*, 2016).

The availability of the Doppler spectrum opened new research possibilities in the field of microphysical studies with Doppler radars. *Atlas et al.* (1973) showed how to compute the drop size distribution from the Doppler spectrum at vertical incidence. *Mosimann et al.* (1993) and *Mosimann* (1995) developed a method to determine the degree of riming of snow crystals from mean Doppler velocity measurements of vertically pointing (profiler) Doppler radars. This method is based on the increasing fall speeds of hydrometeors due to increasing degree of riming. *Kneifel and Moisseev* (2020) revisited this method to derive a long-term statistics of riming. *Zawadzki et al.* (2001) used the full Doppler spectrum to study the microphysical evolution of falling snowflakes. They found a bimodality in the spectra (similar to Fig. 1.6), and they attributed one mode to the fall velocity of rimed particles and the other to SLW droplets.

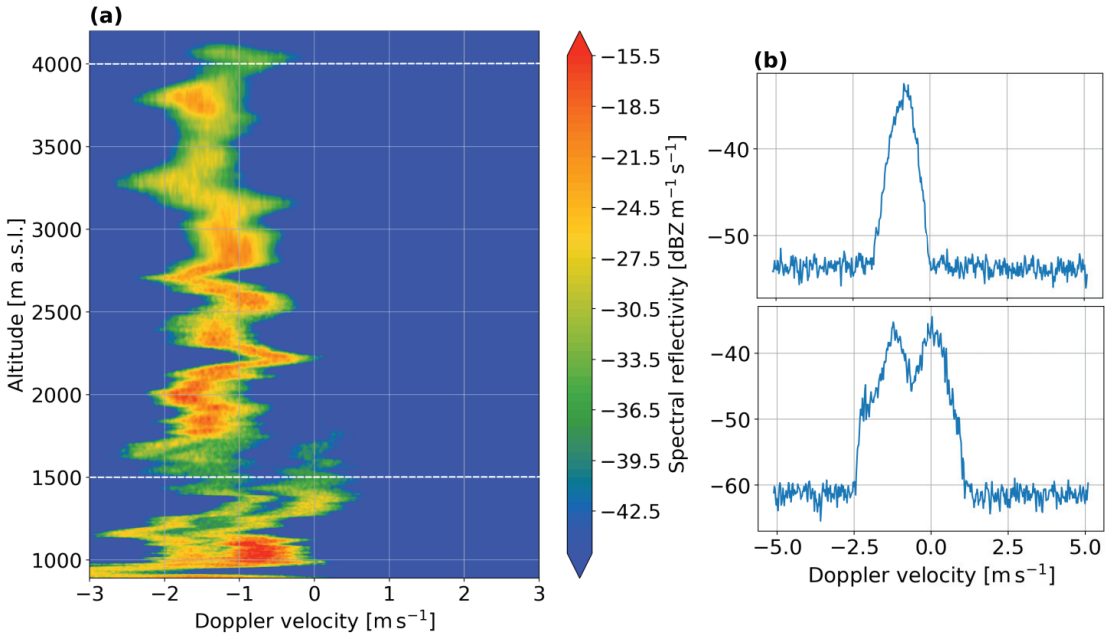

Figure 1.6 – Example of Doppler spectra from a 94 GHz vertically pointing radar in Pyeongchang, South Korea at 789 m a.s.l. at 21:10 UTC 28 February 2018. Negative (positive) Doppler velocity are downwards (upwards). **(a)** Range spectrogram and **(b)** individual spectra, the upper (lower) panel corresponds to the height of the upper (lower) white dashed lines in **(a)**.

However, the detection of SLW droplets in Doppler spectra is limited by the sensitivity of the radar. The innovative work of *Lhermitte* (1987) allowed the development of millimetre wavelength (cloud) radars, which have a higher sensitivity than lower frequency radars (see Eq. 1.4 and Fig. 1.4) and can also detect sub-millimetre cloud particles. This motivated the development of specific cloud radar components so that now cloud radars are widely used for long-term monitoring and deployed on mobile platforms including aircraft, ships and even satellites (*Kollias et al.*, 2007). *Luke et al.* (2010) leveraged cloud radar Doppler spectra to automatically detect SLW in mixed-phase clouds. More recently *Kalesse et al.* (2016) studied the fingerprints of riming on the Doppler spectra of a case where a seeder cloud was precipitating ice crystals in a SLW layer. They were able to identify clear signatures of riming in the Doppler spectra as strong bimodalities associated with rimed snow and ice. These studies show that the Doppler spectrum provides a wealth of information to retrieve snowfall microphysical processes.

1.2.3 Polarimetric variables

Shortly after Doppler spectral information was used for microphysical characterisations, Doppler dual-polarisation (polarimetric) radars were developed for a wide range of applications (*Berne and Krajewski*, 2013), among which microphysical retrievals. In the previous

sections, we assumed no particular polarisation of the electromagnetic signal. When an electromagnetic wave travels through atmospheric scatterers, such as hydrometeors, part of it is scattered towards the source (i.e. the radar) in the same polarisation plan (co-polar signal) and another part is scattered in the opposite polarisation plan (cross-polar signal). If electromagnetic waves are transmitted in both horizontal and vertical polarisations, the total power (i.e. the sum of the co-polar and cross-polar signals) received at horizontal polarisation is more related to the horizontal dimension of the hydrometeors, while the total power received at vertical polarisation is more related to its vertical dimension. A more detailed introduction to the physics of polarisation in radar meteorology can be found in *Kumjian* (2018). We assume hereafter a radar operating in simultaneous transmission and reception mode (*Ryzhkov et al.*, 2005). Polarimetric variables are defined by contrasting both the amplitude and the phase of the total signal received at horizontal and vertical polarisations. The main polarimetric variables used in this thesis are presented below.

Differential reflectivity Z_{DR}

The non-sphericity of hydrometeors motivated, since the early development of polarimetric radars (*Seliga and Bringi*, 1976), the definition of a new variable comparing the reflectivity at horizontal (Z_H) and vertical (Z_V) polarisation. This led to the definition of differential reflectivity (Z_{DR} [dB]), which is defined as the difference $Z_H - Z_V$ when expressed in dB [2]. Z_{DR} is linked to the reflectivity-weighted mean aspect ratio and the dielectric constant of hydrometeors. For dielectrically similar hydrometeors, oblate (prolate) particles will exhibit positive (negative) Z_{DR} in dB. For a given aspect ratio, Z_{DR} increases with an increasing dielectric constant. As explained in *Kumjian* (2013a), this is particularly relevant to identify the habit in regions dominated by depositional growth. Since for dry snow crystals, the dielectric constant is related to the particle density (*Ryzhkov and Zrnic*, 2019b), higher-density crystals have a higher Z_{DR} than lower-density ones. This allows distinguishing crystals with similar aspect ratios, but with different densities, such as plates and dendrites. Z_{DR} is a priori independent of particle number concentration.

Specific differential phase shift upon propagation K_{dp}

The idea behind differential phase shift is that the phase speed of an electromagnetic wave propagating through a population of hydrometeors will decrease, hence acquiring a phase shift with respect to the same wave in vacuum. This phase shift depends on the size, number concentration, and dielectric constant of the hydrometeors. Non-spherical hydrometeors will decrease the waves' phase speed of the polarisation oriented along their major axis much more than along their minor axis. Therefore, taking the difference in phase shift between the horizontal and vertical polarisations provides information on the hydrometeors' shape. The differential phase shift generally increases with increasing range, since it reveals the difference

[2] We use hereafter the convention of capitalised subscripts for Z_H (Z_{DR}) when expressed in dBZ (dB)

in phase shifts along the entire path. A useful quantity is the one-way rate of change of differential phase shift with range, called the specific differential phase shift upon propagation K_{dp} [° km^{-1}]. It is defined as:

$$K_{dp} = \frac{180}{\pi} 10^3 \lambda \int_{D_{min}}^{D_{max}} Re[f_{hh}(D) - f_{vv}(D)] N(D) dD \tag{1.13}$$

where f_{hh} and f_{vv} are the forward complex scattering amplitudes at horizontal and vertical polarisation, respectively. The scattering amplitude is related to the scattering cross-section by: $\sigma_{hh(vv)} = 4\pi |f_{hh(vv)}|^2$, where $\sigma_{hh(vv)}$ is the scattering cross-section at horizontal (vertical) polarisation. Re is the real part operator. K_{dp} has the advantage not to be affected by attenuation or miscalibration of the radar, unlike Z_H and Z_{DR}. However it is not a direct radar measurement and needs to be estimated from the total differential phase shift, which also depends on the backscattering phase delay and the phase difference between the two transmit waves at range zero. In this thesis, we will use the method from *Schneebeli et al.* (2014) to estimate K_{dp}.

The main difference between K_{dp} and Z_{DR} is that K_{dp} is less sensitive to the hydrometeor's size. For snow, it has been shown that K_{dp} is proportional to the mean diameter of the size distribution, while Z_H (and hence Z_{DR}) is a fourth-moment of the size distribution for snow (*Ryzhkov and Zrnic*, 2019c). This makes K_{dp} useful to detect a high concentration of relatively small anisotropic particles, even in the presence of large aggregates. Therefore relatively high K_{dp} values observed together with low Z_{DR} can indicate a mixture of aggregates or rimed particles with oblate ice crystals. This can be the case for instance when secondary ice production occurs (*Grazioli et al.*, 2015a).

Co-polar correlation coefficient ρ_{hv}

Radar variables are usually computed as average values over several pulses to collect more samples and reduce the noise of the measurements. The correlation coefficient between the co-polar signals at horizontal and vertical polarisations carries relevant meteorological information and defines the co-polar correlation coefficient ρ_{hv} (e.g. *Bringi and Chandrasekar*, 2001). ρ_{hv} can be interpreted as the variability of the particles' intrinsic Z_{DR} (*Kumjian*, 2018): a value close to 1.0 indicates a low variability and ρ_{hv} will decrease with increasing variability of particles shapes in the sampling volume. The most common applications of ρ_{hv} are the discrimination of non-meteorological echoes (e.g. *Rico-Ramirez and Cluckie*, 2008) and the detection of the melting layer (e.g. *Wolfensberger et al.*, 2016). ρ_{hv} will only be indirectly used in this thesis as an input for a hydrometeor classification method based on polarimetric variables (*Besic et al.*, 2016) and for ground echoes filtering.

1.2.4 Microphysical signatures in polarimetric variables

In this section, the qualitative evolution of polarimetric variables during the microphysical processes presented in Sect. 1.1.2 are presented. For a quantitative approach, the reader is referred to *Ryzhkov and Zrnic* (2019a).

Vapour depositional growth

Recalling the fact that pristine ice crystals become increasingly anisotropic (decrease in aspect ratio) as they grow, vapour deposition tends to increase Z_H, Z_{DR}, and K_{dp}. In particular, since the most efficient growth of ice occurs at temperatures around −15 °C, the strongest enhancement of Z_H, Z_{DR}, and K_{dp} are usually measured at this temperature range and are associated with either planar or dendritic growth. Since aggregation is also efficient at this temperature range, the dendritic growth signature can be restricted to a layer of a few hundred metres before aggregation starts to dominate.

Aggregation

Aggregates usually have a lower density than the crystals they are made of, which leads to a decrease in both Z_{DR} and K_{dp} for regions dominated by aggregation. Aggregates also tend to be less anisotropic than crystals and fall with more chaotic orientations, due to their increase in Reynolds number (*Ryzhkov and Zrnic*, 2019b). This also contributes to the overall decrease in Z_{DR} and K_{dp}, but the polarimetric signature is dominated by the decrease in density (*Kumjian*, 2013a). As proposed by *Moisseev et al.* (2015) this signature may however depend on the stage of aggregation. They argue that, at the early stage, aggregates are oblate particles and lead to a maximum in K_{dp}, which they observe at a temperature of −15 °C, which corresponds both to maximum efficiency of depositional growth and aggregation for small particles. This shows that at the early stage of aggregation both oblate early aggregates and ice crystals can be found and that the decrease in Z_{DR} and K_{dp} is likely observed once aggregates get bigger. The sharp increase in Z_H during aggregation, due to the faster increase in size compared to depositional growth, is often a clear indicator of where aggregation starts.

Riming

The effect of riming on dual-polarisation variables is ambiguous (*Moisseev et al.*, 2017). On the one hand, it enhances the particles' density, which would increase its dielectric response and hence Z_{DR} and K_{dp}. On the other hand, it tends to make them more spherical and hence decreases both Z_{DR} and K_{dp}. Furthermore, if the temperature is between −8 °C and −3 °C, the Hallett-Mossop mechanism may be active and lead to a high concentration of splinters, which in this temperature range will grow as needles or columns (Fig. 1.1b). This increases mainly K_{dp}, since Z_{DR} is much less sensitive to a high concentration of small particles than K_{dp}. *Moisseev et al.* (2017) investigated this ambiguity by verifying the following conceptual model:

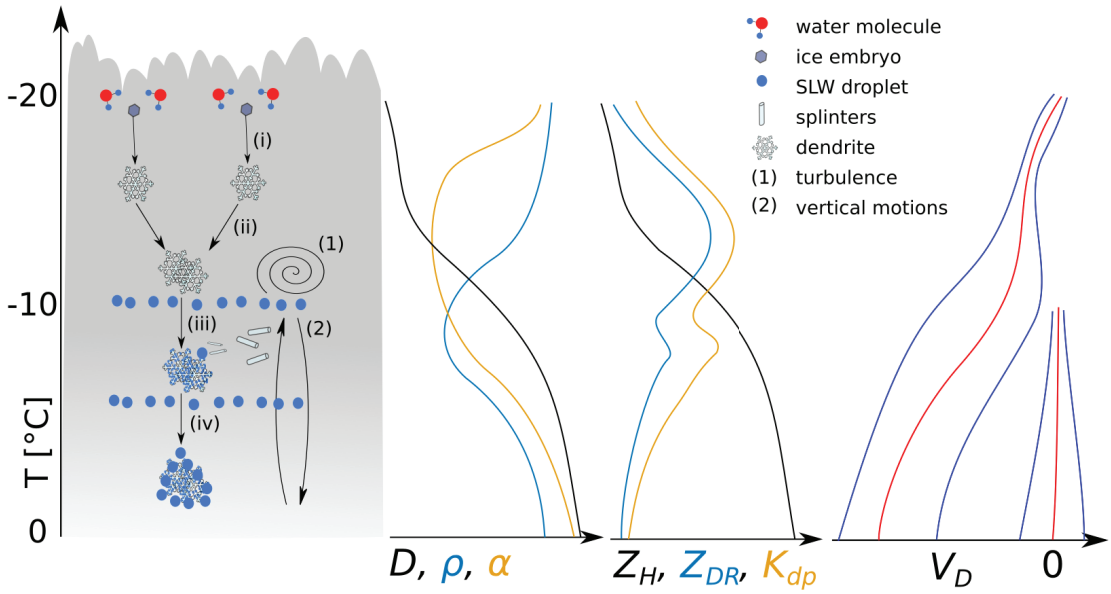

Figure 1.7 – Conceptual schematic of (i) vapour deposition, (ii) aggregation, (iii) early stage of riming, and (iv) later stage of riming (graupel). D is the hydrometeors' maximum dimension, ρ their density, and α their aspect ratio. The red line represents the mode of Doppler velocity (V_D), the blue lines the spread. The second set of red and blue lines represent a secondary mode. Vertical wind velocity is not taken into account in the evolution of Doppler velocity.

during the initial riming stage of aggregates, the rimed mass fills the voids of the particle without changing its shape. This should lead to an increase of both Z_{DR} and K_{dp}, because of the increase in density (*Bringi and Chandrasekar*, 2001). For ice crystals, the initial stage of riming increases their minor axis and hence decreases Z_{DR}. In the later stage of riming, the rime mass will accumulate on the snowflake and make it more spherical. This second stage does not change the density significantly but makes the particle more spherical, which would act to decrease both Z_{DR} and K_{dp}. They could verify this model with two case studies. *Li et al.* (2018) confirmed this result on 49 snowstorms and showed that the distinction between the two stages of riming was possible for reflectivity values higher than 15 dBZ, while the polarimetric signatures remained ambiguous below. This shows that the effect of riming on dual-polarisation variables depends on the initial particles' sizes and, as for aggregation, on the stage of riming (*Moisseev et al.*, 2017).

Summary of microphysical signatures

Figure 1.7 shows a schematic of the microphysical processes presented in this chapter and their effect on density, aspect ratio, the polarimetric variables, and the Doppler spectrum. It is meant to summarise the concepts presented and serve as a reference for the next chapters of this thesis. It is by no mean representative of the full complexity of snowfall microphysics. Figure 1.7 can be read as follows: (i) as the ice embryos grow by vapour deposition into den-

drites (assuming water saturation), the aspect ratio drastically decreases, the density slightly decreases and the size increases. This leads to a slight increase of Z_H, a large positive gradient (downward relative) of Z_{DR} and K_{dp}, and a slight increase in the magnitude of Doppler velocity (assumed to be unaffected by vertical wind velocity for the sake of conceptualisation). (ii) As the dendrites grow large enough to fall and turbulence enhances the probability of collision, they will likely aggregate, which leads to a sharp decrease of density, an increase in aspect ratio, a sharp increase in size and hence Z_H, and a decrease in Z_{DR} and K_{dp}. The magnitude of Doppler velocity will increase more slowly and the spectrum broadens due to the variety of particles' fall speeds. (iii) Due to the presence of SLW generated and sustained by an updraught, riming will fill the voids in the aggregates, hence increasing their density and not affecting significantly their aspect ratio. This leads to an increase in Z_H, Z_{DR}, K_{dp}, and a steeper increase in mean Doppler velocity, due to the increase in density. The SLW droplets manifest as a secondary mode of Doppler velocity with a much smaller magnitude than the precipitating particles. As the SLW droplets freeze on the aggregate, they may eject splinters through the Hallett-Mossopp process, which then grow as needles or columns. Other secondary ice production processes could also occur at this temperature range. These secondary ice particles contribute to the enhancement in K_{dp} due to their high concentration, but not in Z_{DR} since they are small. They may also contribute to the secondary mode in the Doppler spectrum. (iv) As rime accumulates on the surface of the particles, it increases its aspect ratio, while its density is less affected. This leads to an increase in Z_H and a decrease in Z_{DR} and K_{dp}. The fall speed continues to increase and the newly formed graupel particle will eventually reach the ground.

1.3 The peculiarity of Antarctic meteorology

In this section, some of the important aspects of Antarctic meteorology relevant to this thesis are introduced. Antarctica is known as the most remote continent on Earth and endures probably the harshest environmental conditions. It holds the lowest temperature record (−89.2 °C at Vostok station, *Turner et al.*, 2009). It is one of the driest places on Earth: the McMurdo dry valleys are a polar desert (*Doran et al.*, 2002) with annual precipitation not exceeding 50 mm (*Fountain et al.*, 2010), mainly because of strong foehn winds (*Speirs et al.*, 2013). Finally, it is probably the windiest place on Earth with mean annual wind speeds between 9 and 19 m s^{-1} at coastal stations, including Dumont d'Urville (*King and Turner*, 1997). These meteorological records are mainly because Antarctica is a mountainous continent located at a pole: the high interior plateau makes it possible to reach extremely low temperatures in winter, which would not be possible in the Arctic because the ocean keeps the temperature warmer. These cold air masses together with the topography are responsible for dry katabatic winds. The presence of a continent at the South pole is also responsible for a strong meridional temperature gradient at the shorelines. This baroclinic zone at low levels is responsible for mesoscale disturbances which propagate eastward along the coast (*King and Turner*, 1997). Another reason for cyclogenesis around the periphery of Antarctica is related to terrain-induced instability (*Davies and*

Schär, 1991).

The difference in the landmass distribution between the southern and northern hemispheres leads to a greater meridional temperature gradient in the South and hence to stronger baroclinic developments over the Southern Ocean. Additionally, because no continent can slow down the development of these cyclones, the Antarctic coast usually experiences the dissipation of mature depressions (*King and Turner*, 1997). Finally, an interesting peculiarity of Antarctic meteorology is the presence of katabatic wind systems. The low-level divergence over the Antarctic interior must be compensated by upper-level convergence. This constitutes a thermally direct circulation where cold air diverges at low levels, while warmer air from the mid-latitudes is advected at higher levels (*King and Turner*, 1997). This is a key difference with the mid-latitudes, where katabatic winds are either the result of diurnal heating in absence of synoptic forcing or are the consequence of a specific synoptic configuration (e.g. the Bora flow). These ingredients make the Antarctic coast the scene of diverse meteorological phenomena, including cyclolysis, mesoscale cyclogenesis, frontal precipitation, and strong katabatic winds.

1.4 Research objectives and outline of the thesis

The previous sections showed that snowfall microphysics is controlled by physical quantities such as temperature, moisture content, vertical wind velocity, and turbulence. These variables in turn influence snowfall intensity, as well as the habit and density of snowflakes, which then determine the snow accumulation, and the height and stability of the snowpack. Finally, these quantities are governed by dynamical processes ranging from the synoptic- to the local-scale. For instance, SLW can be formed in the large-scale ascent associated with a warm front (e.g. *Keppas et al.*, 2018) or be produced by localised updraughts forced by the orography (*Houze and Medina*, 2005; *Medina et al.*, 2005). The nature of the problem lies in the difficulty of disentangling the role of local versus large-scale processes on snowfall microphysics. In this thesis, a combination of ground-based in situ and radar measurements with atmospheric model simulations is used to link microphysical observations to particular dynamical processes. In particular, we will use an X-band polarimetric radar, a W-band Doppler cloud profiler, and a multi-angle snowflake camera. This combination benefits from the polarimetric information of the X-band radar, the higher sensitivity of the cloud profiler, and the in situ information from the snowflake camera. The objectives are twofold: (i) to collect ground-based radar and in situ measurements during two field campaigns in South Korea and Antarctica, and (ii) to leverage these data to investigate the dynamics and microphysics of two snowfall events that took place in these contrasting geographical and climatological regions. In particular, the following questions are addressed:

1. How do the datasets collected during these two field campaigns compare in terms of snowfall microphysics?

2. How representative are these two datasets with respect to the regional climatology?
3. What is the contribution of these datasets to the scientific community and what could they be used for?
4. What were the most significant dynamical processes influencing the evolution, distribution, and microphysics of precipitation during the two snowfall events?
5. At which spatial scales did these processes take place?
6. How were they influenced by geographical features?
7. What were the common characteristics and the main differences between the two snowfall events?

This thesis is structured as follows: In the first part, the data collected in Pyeongchang, South Korea (Chap. 2) and Davis, Antarctica (Chap. 3) are presented and the questions 1 to 3 are addressed. In the second part, we address questions 4 to 7 with two case studies. First, an intense snowfall event in South Korea associated with a warm front and featuring significant aggregation and riming is analysed (Chap. 4). Chapter 5 follows on a second case study during which a foehn wind led to the total sublimation of snowfall over Davis, on the coast of East Antarctica. Finally, a concluding summary and open research questions are presented in Chap. 6.

2 Ground-based radar and in situ measurements of clouds and precipitation in Gangwon, South Korea

This chapter is adapted from the postprint version of the article:

- Gehring, J., A. Ferrone, A.-C. Billault-Roux, N. Besic, K. D. Ahn, G. Lee, and A. Berne (2021a), Radar and ground-level measurements of precipitation collected by the École Polytechnique Fédérale de Lausanne during the International Collaborative Experiments for PyeongChang 2018 Olympic and Paralympic winter games, *Earth System Science Data, 13*(2), 417–433, doi: 10.5194/essd-13-417-2021

It presents the dataset we collected during the ICE-POP 2018 campaign in South Korea. The processing of the data from each instrument is explained and three major precipitation events are illustrated with the measurements.

2.1 Summary

This chapter describes a four-month dataset of precipitation and cloud measurements collected during the International Collaborative Experiments for PyeongChang 2018 Olympic and Paralympic winter games (ICE-POP 2018). This chapter aims to describe the data collected by the Environmental Remote Sensing Laboratory of EPFL. The dataset includes observations from an X-band dual-polarisation Doppler radar, a W-band Doppler cloud profiler, a multi-angle snowflake camera and a two-dimensional video disdrometer (*Gehring et al.*, 2020a). Classifications of hydrometeor types derived from dual-polarisation measurements and snowflake photographs are presented. The dataset covers the period from 15 November 2017 to 18 March 2018 and features nine precipitation events with a total accumulation of 195 mm of equivalent liquid precipitation. This represents 85% of the climatological accumulation over this period. To illustrate the available data, measurements corresponding to three major precipitation events are presented. The synoptic situations of these events were contrasted and influenced the precipitation type and accumulation. The hydrometeor classifications

reveal that aggregate snowflakes were dominant and that some events featured significant riming. The combination of dual-polarisation variables and high-resolution Doppler spectra with ground level snowflake images makes this dataset particularly suited to study snowfall microphysics in a region where such measurements were not available before.

2.2 Introduction

Precipitation measurements in mountainous regions are paramount to characterise the spatial distribution of precipitation and understand the effect of orography on microphysics. South Korea's geographical environment provides a unique setting for precipitation studies: its location on a mountainous peninsula in the mid-latitudes is prone to large moisture advection by baroclinic systems and orographic lifting driving cloud and precipitation formation. Unlike other mountain ranges such as the Alps, the Rockies, the Olympic Mountains, the Cascade Mountains and the Coast Mountains (*Bougeault et al.*, 2001; *Saleeby et al.*, 2009; *Houze et al.*, 2017; *Stoelinga et al.*, 2003; *Joe et al.*, 2010), the study of precipitation in the Taebaek Mountains across the Korean Peninsula has not been as extensive. *Kim et al.* (2018) investigated the microphysics of two snowfall events in the Taebaek Mountains during the Experiment on Snow Storms At Yeongdong (ESSAY) campaign using radiosoundings, snowflake images and numerical simulations. They suggested that future field campaigns should include dual-polarisation radars and a multi-angle snowflake camera (MASC) to better understand the microphysics of precipitation in this region. There was hence a need for a precipitation measurement campaign in the Taebaek Mountains with remote sensing and in situ measurements.

Several past field campaigns demonstrated the usefulness of combined remote sensing and in situ measurements for snowfall studies. The TOSCA (Technology Options and Strategies towards Climate friendly transport) project in the Bavarian Alps in Germany (*Löhnert et al.*, 2011) combined vertically pointing radars, radiometers and optical disdrometers among others to better characterise the vertical distribution of snowfall for satellite retrievals and numerical model validations. During the 2015/16 fall–winter season, the OLYMPEX (Olympic Mountain Experiment) campaign (*Houze et al.*, 2017) took place in the vicinity of the mountainous Olympic Peninsula, USA, to study how Pacific precipitation systems are influenced by the orography. The BAECC (Biogenic Aerosols–Effects on Clouds and Climate) field campaign (*Petäjä et al.*, 2016) provided 8 months of measurements in Hyytiälä, Finland, to study biogenic aerosols, clouds and precipitation and their interactions. In situ and remote sensing instruments have also proven very useful to study atmospheric radiation, cloud and precipitation properties in polar regions. The North Slope of Alaska atmospheric observatory (*Verlinde et al.*, 2016) in Utqiaġvik (formerly Barrow) and Oliktok provides a long series of measurements including radiometers, lidars, cloud radars and a MASC among many other instruments. Another major Arctic measurement site is located at Summit Camp, Greenland, where the ICECAPS (Integrated Characterization of Energy, Clouds, Atmospheric State, and Precipitation at Summit; *Shupe et al.*, 2013) field campaign was conducted to collect measurements of radiation, clouds and precipitation to study the energy and hydrological budgets of the Greenland Ice Sheet.

In Antarctica, the APRES3 (Antarctic Precipitation, Remote Sensing from Surface and Space) field campaign (*Genthon et al.*, 2018) provided the first dual-polarisation radar measurements from November 2015 to February 2016. Along with snowflake photographs, measurements of micro rain radar and lidar, the dataset led to unprecedented insights into Antarctic snowfall microphysics (*Grazioli et al.*, 2017a). Finally, the AWARE (U.S. Department of Energy Atmospheric Radiation Measurement (ARM) West Antarctic Radiation Experiment) campaign (*Lubin et al.*, 2020) gathered cloud radars, lidars, radiometers, aerosols and microphysical measurements from December 2015 to December 2016 at McMurdo Station, Antarctica. This unique dataset offers numerous cases for mixed-phase cloud parameterisation in weather and climate models. The measurements of these field campaigns allowed for innovative studies and new insights into cloud and precipitation processes in these various regions (*Kalesse et al.*, 2016; *von Lerber et al.*, 2017; *Grazioli et al.*, 2017b; *Cole et al.*, 2017; *Zagrodnik et al.*, 2019). For a better understanding of cloud and precipitation processes in the Taebaek Mountains, a field campaign combining remote sensing and in situ measurements is needed. The PyeongChang 2018 Olympic and Paralympic winter games were the opportunity to initiate interest and collaboration for such a campaign. Indeed, accurate weather forecasts during Winter Olympic Games are an organisational need and a real scientific challenge. It is also a great opportunity to foster international collaboration and gather the atmospheric science community. One successful example of such a joint effort was the Science of Nowcasting Olympic Weather for Vancouver 2010 campaign, which led to novel findings on precipitation (*Thériault et al.*, 2012; *Schuur et al.*, 2014; *Berg et al.*, 2017) and nowcasting (*Haiden et al.*, 2014), as well as to new instrumental developments (*Boudala et al.*, 2014). Along the same line, the Korea Meteorological Administration organised the International Collaborative Experiments for PyeongChang 2018 Olympic and Paralympic winter games (ICE-POP 2018). The main goals of ICE-POP 2018 were to support forecasters with high-resolution model simulations and radar data, as well as to gain more insight into orographic precipitation in the Taebaek Mountains. For this purpose, remote sensing and in situ measurements of clouds and precipitation were conducted in the province of Gangwon-do between November 2017 and May 2018.

This chapter presents the data collected by the Environmental Remote Sensing Laboratory of EPFL during ICE-POP 2018. It includes measurements from an X-band dual-polarisation Doppler radar, a W-band Doppler cloud profiler, a multi-angle snowflake camera and a two-dimensional video disdrometer. Such a dataset is unique, as it includes multi-frequency radar and ground-based measurements in a region where similar measurements were scarce before ICE-POP 2018. Section 2.3 presents the campaign and the instrumental setup and Sect. 2.4 describes the data processing. Section 2.5 illustrates the dataset with measurements and hydrometeor classifications corresponding to three major events. Section 2.6 closes this chapter with concluding remarks.

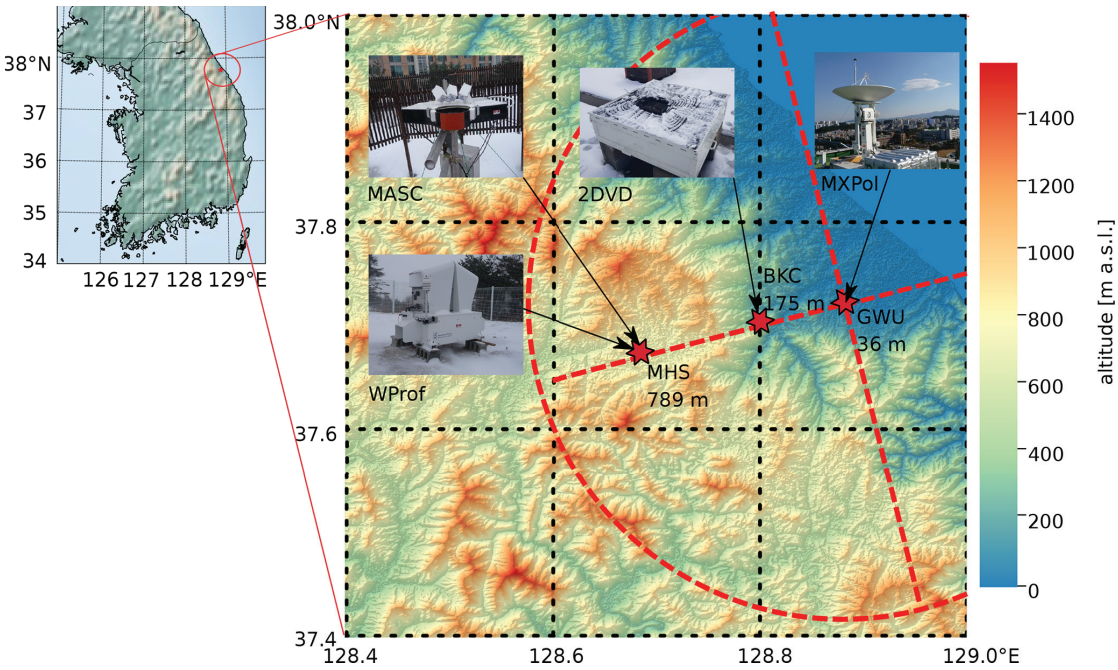

Figure 2.1 – Location of the instruments used for this dataset. A digital elevation model shows the topography of the region and its location within South Korea. The red dotted lines and circle show the extent of the main RHIs (27.2 km) and PPI (28.4 km radius), respectively. Note that the MASC was located at BKC from 15 November 2017 to 20 February 2018 and at MHS afterwards.

2.3 Geographical location, measurement sites and instruments

In this chapter, we will focus on the data collected by a mobile X-band dual-polarisation Doppler (polarimetric) radar (MXPol), a W-band Doppler cloud profiler (WProf), a multi-angle snowflake camera (MASC) and a two-dimensional video disdrometer (2DVD). Figure 2.1 shows the location of the instruments. The Taebaek Mountains are extending over the eastern coast of the Korean Peninsula. Two measurement sites were located on the eastern foot of the Taebaek Mountains, in the city of Gangneung. The first one was in the Gangneung Wonju national university (GWU) at 66 m a.s.l. The second one was in Bokwang 1-ri community centre (BKC) 6 km inland from Gangneung at 175 m a.s.l. The third measurement site Mayhills (MHS) was located in the Taebaek Mountains in the county of Pyeongchang at 789 m a.s.l. 19 km inland of GWU. Radiosoundings were launched by the Korea Meteorological Administration (KMA) in Daegwallyeong (DGW), 2 km from MHS. Solar noon is between 03:00 UTC (in November) and 03:30 UTC (in March).

2.3.1 X-band polarimetric radar: MXPol

The scanning X-band polarimetric radar, named MXPol, was installed in GWU on the coast of the East Sea (Sea of Japan). The main variables retrieved from MXPol measurements in

Table 2.1 – Description of WProf chirps

	Range	Range resolution	Doppler interval	Doppler resolution	Integration time
chirp2	[2016, 9984] m	32.5 m	$[-5.1, 5.1]\,\mathrm{m\,s^{-1}}$	$0.020\,\mathrm{m\,s^{-1}}$	0.82 s
chirp1	[603, 1990] m	11.2 m	$[-5.1, 5.1]\,\mathrm{m\,s^{-1}}$	$0.020\,\mathrm{m\,s^{-1}}$	0.37 s
chirp0	[100, 598] m	5.6 m	$[-7.16, 7.13]\,\mathrm{m\,s^{-1}}$	$0.028\,\mathrm{m\,s^{-1}}$	0.18 s

dual-pulse pair (DPP) mode are the equivalent reflectivity factor at horizontal polarisation Z_H [dBZ], the differential reflectivity Z_{DR} [dB], the specific differential phase shift on propagation K_{dp} [°km^{-1}], the co-polar correlation coefficient ρ_{hv} [-], the mean Doppler velocity V_D [m s^{-1}] and the Doppler spectral width σ_v [m s^{-1}]. Additionally, in fast-Fourier transform (FFT) mode, the full Doppler spectrum at 0.17 m s^{-1} resolution is retrieved at each range gate. MXPol operates at 9.41 GHz with a typical angular resolution of 1°, range resolution of 75 m, non-ambiguous range of 120 km and Nyquist velocity of 39 m s^{-1} in DPP or 11 m s^{-1} in FFT mode. Only the data up to 28 km range are saved, since the decrease in sensitivity and increase in sampling volume make the further gates less relevant for microphysical studies. A more technical description of MXPol can be found in *Schneebeli et al.* (2013). The main scan cycle was composed of two hemispherical range height indicators (RHIs) at 227° and 317° azimuth in FFT and DPP modes, respectively. The former is towards MHS, while the latter is perpendicular to this direction following the coast as shown by the red dotted line in Fig. 2.1. The two RHIs were followed by one plan position indicator (PPI) in DPP mode at 6° elevation. The cycle was either completed by two other RHIs or PPIs depending on the event. The scan cycle had a 5 min duration and was repeated indefinitely. At least once an hour, a PPI at 90° elevation in FFT mode was performed for Z_{DR} calibration.

2.3.2 W-band cloud profiler: WProf

A W-band Doppler cloud profiler (WProf) was deployed at the Mayhills site (MHS). WProf is a frequency modulated continuous wave (FMCW) radar operating at 94 GHz at a single polari-

Table 2.2 – Specifications of MXPol and WProf

Specifications	MXPol	WProf
Frequency	9.41 GHz	94 GHz
3 dB beamwidth	1.27°	0.53°
Sensitivity at 8 km	5 dBZ	−40 dBZ
Transmission type	pulsed	FMCW
Polarisation	dual-polarisation	single-polarisation
Range resolution	75 m	5.6, 11.2, 32.5 m

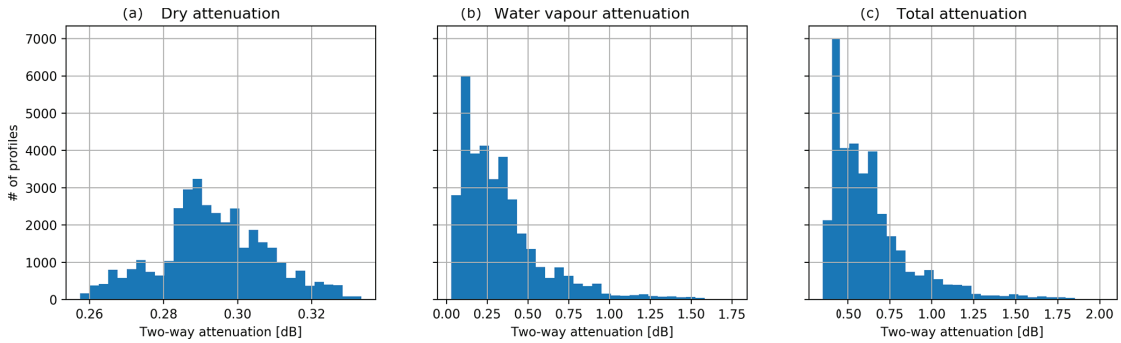

Figure 2.2 – Distribution of two-way attenuation (up to 10 km) at 94 GHz for **(a)** dry air, **(b)** water vapour, and **(c)** total attenuation computed with PAMTRA for all profiles of WProf interpolating at 5 min the radiosounding data.

sation. It allows for measuring with different ranges and Doppler resolutions, typically using three vertical chirps (Table 2.1). The main variables retrieved are the equivalent reflectivity factor Z, V_D, σ_v, skewness, and kurtosis. The full Doppler spectrum is also available. More details on WProf can be found in *Küchler et al.* (2017). WProf contains a 89 GHz radiometer, which can be used to retrieve the liquid water path (LWP) and the integrated water vapour (IWV). We computed LWP and IWV using the method described in *Billault-Roux and Berne* (2021). The brightness temperature measurements had a bias of 20 K, which we corrected. After correction the root mean squared error (RMSE) is 2.88 K. The RMSE of LWP and IWV are 86.5 g m^{-2} and 1.72 kg m^{-2}, respectively, taking radiosoundings as the reference. More information on the uncertainty of this algorithm can be found in *Billault-Roux and Berne* (2021). In particular, note that the accuracy deteriorates in case of intense precipitation. WProf was calibrated by the manufacturer Radiometer Physics GmbH just before the ICE-POP 2018 campaign. This included a calibration of the 89 GHz radiometer with liquid nitrogen and a calibration of the radar with disdrometers following the method of *Myagkov et al.* (2020). The uncertainty of WProf reflectivity calibration is ±1 dB. This calibration correction was applied to the data available on PANGAEA (*Gehring et al.*, 2020a). The radomes were in good shape and were not changed between the calibration and the field campaign. The blowers, which prevent liquid water from accumulating on the radomes, were switched on all the time. The radar pointing was evaluated by checking the levels at the beginning and the end of the campaign. The levels showed that the radar was pointing almost perfectly vertically. However, since the vertical alignment was not monitored constantly, the spectral and Doppler velocity data should be interpreted carefully, especially in case of strong horizontal winds.

2.3.3 Multi-angle snowflake camera: MASC

A multi-angle snowflake camera (MASC) was deployed in a double-fence windshield in MHS. The MASC is composed of three coplanar cameras separated by an angle of 36°. As hydrometeors fall in the triggering area, high-resolution stereographic pictures are taken, and their fall velocities are measured. A complete description of the MASC can be found in *Garrett et al.*

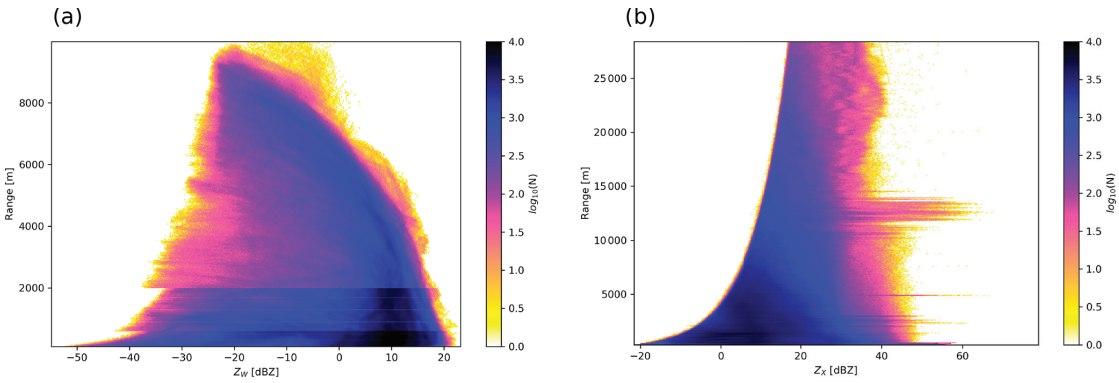

Figure 2.3 – Range distribution of reflectivity values for **(a)** WProf and **(b)** MXPol during all precipitation events (see Fig. 2.4). The colour bar shows the number of measurements per range gate. The total number of measurement points is 1.24×10^8 for WProf and 2.25×10^8 for MXPol.

(2012). The MASC images were used as input parameters to a solid hydrometeor classification algorithm. Individual particles are classified into six solid hydrometeor types, namely small particles (SPs), columnar crystals (CCs), planar crystals (PCs), a combination of column and plate crystals (CPCs), aggregates (AGs), and graupel (GR). In addition a riming index ranging from 0 to 1 is computed. A detailed explanation of the algorithm is provided in *Praz et al.* (2017). Note that the riming index of melting particles and raindrops computed by this method is usually quite high. One should not consider the riming index for particles with a melting probability higher than 50%.

2.3.4 Two-dimensional video disdrometer: 2DVD

A two-dimensional video disdrometer (2DVD) was deployed in BKC. A detailed description of the instrument can be found in *Kruger and Krajewski* (2002) and *Schönhuber et al.* (2007). Here we will describe the general measurement principle. Two orthogonal light sources are projected onto a line-scan camera. Particles falling through the light sheets project a one-dimensional section on the photodetectors. These one-dimensional profiles are then combined to form a two-dimensional view of the particle. Horizontal wind induces a horizontal displacement of the particles such that the superposition of the one-dimensional sections can lead to distorted particles. This issue is investigated with numerical simulations in *Nešpor et al.* (2000). The two orthogonal two-dimensional projections yield three-dimensional shape information, which can be used to compute the equivalent drop diameter and the aspect ratio. This makes it possible to compute the raindrop size distribution. Since the vertical distance between the two light sheets is known, the particles' fall velocities can also be computed. 2DVD data can also be used for snowfall microphysics studies. *Brandes et al.* (2007) derived the particle size distribution from 2DVD data in Colorado. *Huang et al.* (2010) and *Huang et al.* (2015) used a 2DVD to derive radar reflectivity–snowfall rate relations. Finally, *Grazioli et al.* (2014) used 2DVD data to develop a supervised hydrometeor classification method.

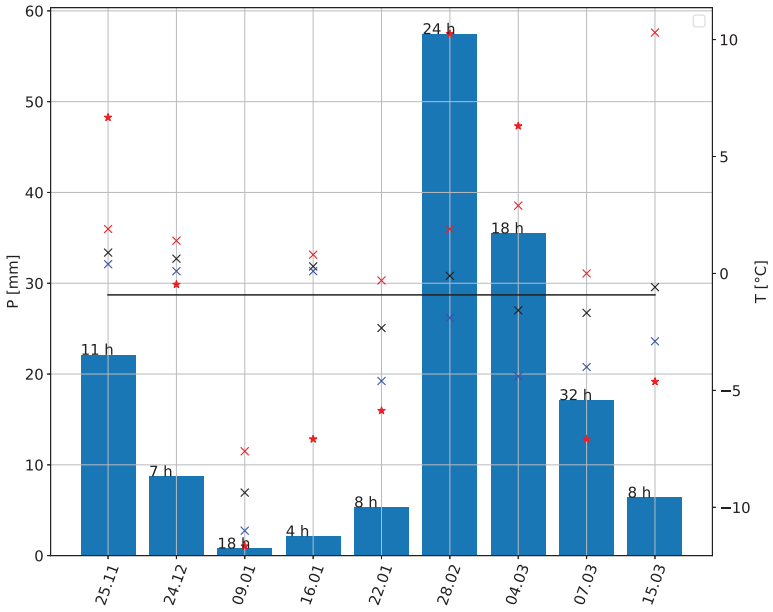

Figure 2.4 – Precipitation accumulation (blue bars), mean precipitation rates (red star) in mm h^{-1}, maximum temperature (red cross), mean temperature (black cross), and minimum temperature (blue cross). The black line shows the mean precipitation rate during precipitation events. The duration of the events is written on top of the bars. The precipitation and temperature data come for a Pluvio^2 weighing rain gauge and a Vaisala weather station located in MHS.

2.4 Data processing

2.4.1 MXPol

First, the noise floor is determined from the raw power following the method from *Hildebrand and Sekhon* (1974). Then, the polarimetric variables are computed based on the backscattering covariance matrix following *Doviak and Zrnic* (1993). The computation of K_{dp} is based on an ensemble of Kalman filters as detailed in *Schneebeli et al.* (2014).

Calibration

To monitor the stability of the radar signal, a radar target simulator (RTS, http://www.palindrome-rs.ch/products/radar-target-simulator/, last access: 04 September 2020) developed by Palindrome Remote Sensing GmbH was installed during the campaign. Unfortunately, due to technical issues during the campaign, the data could not be used for calibration of the radar. However, we conducted dedicated calibration measurements with the RTS in July 2018 just after the ICE-POP 2018 campaign. The results showed that the reflectivity measurements have errors smaller than 1 dBZ.

Table 2.3 – Date and time of the start and end of the precipitation events. The four major events presented here and in Chap. 4 are highlighted in bold.

ID	Start [UTC]	End [UTC]
1	**06:30 25 Nov 2017**	**17:30**
2	00:00 24 Dec 2017	07:00
3	00:00 09 Jan 2018	18:00
4	20:00 16 Jan 2018	23:59
5	06:30 22 Jan 2018	14:30
6	**00:00 28 Feb 2018**	**23:59**
7	**12:00 04 Mar 2018**	**06:00 05 Mar 2018**
8	**10:00 07 Mar 2018**	**18:00 08 Mar 2018**

Hydrometeor classification

The dual-polarisation observables were used to feed the hydrometeor classification from *Besic et al.* (2016). The centroids of all four polarimetric variables used for the classification have been trained on MXPol data from various field campaigns in the Swiss Alps, in Ardèche (France), in Antarctica and on the present dataset in South Korea. Recently, *Besic et al.* (2018) developed a de-mixing approach of this hydrometeor classification, in which the proportion of hydrometeors for each radar sampling volume is estimated, instead of one dominant class. The classes are crystals, aggregates, light rain, rain, rimed ice particles, vertically aligned ice, wet snow, ice hail, and high-density graupel and melting hail. This approach is essentially built upon the concept of entropy, as defined in *Besic et al.* (2016), which reflects the uncertainty with which a hydrometeor class is assigned to one sampling volume. This de-mixing method has the advantage of revealing the spectrum of hydrometeors present in the observed precipitation. The classification was applied to all RHIs of the precipitation events shown in Table 2.3. Only the RHIs towards MHS and the data above 2000 m a.s.l. have been selected for the hydrometeor classification shown in Sect. 2.5, because of ground echoes contamination and partial beam filling below this altitude. Also, the data have been averaged between 7 and 20 km horizontal distance from MXPol and only elevation angles between 5° and 45° are considered.

Table 2.4 – Data amount for all instruments

MXPol	62 h, 4166 RHIs, 2036 PPIs
WProf	121 h, 146 548 profiles
MASC	29 886 triplets
2DVD	2 304 730 drops

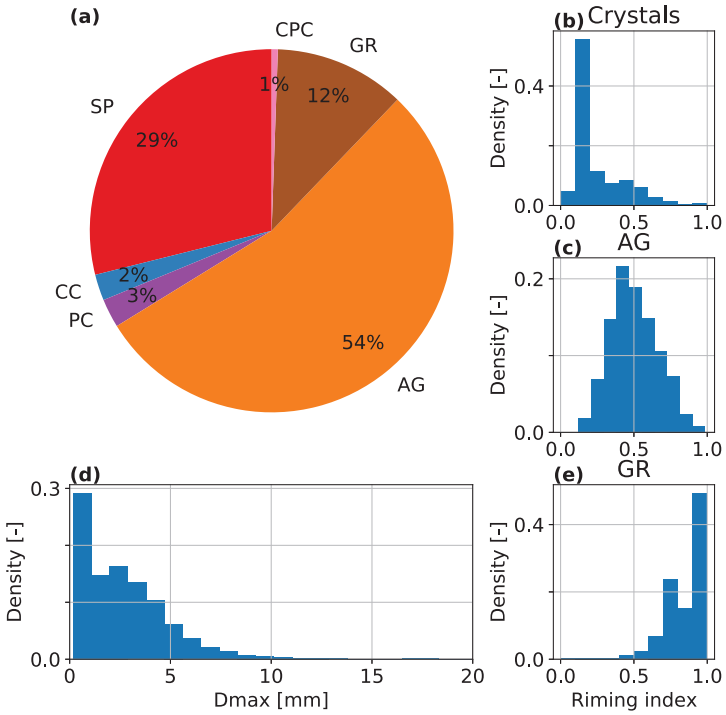

Figure 2.5 – MASC statistics from 22 November 2017 to 21 March 2018. **(a)** Pie chart of hydrometeor classes: small particles (SP), columnar crystals (CC), aggregates (AG), planar crystals (PC), graupel (GR), and combination of columnar and planar crystals (CPC). **(b)**,**(c)**, and **(e)** histograms of the riming index for individual classes. The classes CC, PC, and CPC have been merged to a parent class 'crystals' in **(b)**. **(d)** Histogram of the maximum diameter (Dmax). The sample size is 14006.

Differential reflectivity bias correction

For a correct interpretation of Z_{DR}, the offset introduced by the existence of differences in amplitude in the horizontal and vertical channels needs to be subtracted. This calibration can be achieved by analysing Z_{DR} values in a specific subset of the range gates of the vertical PPI, which were performed at least once an hour during the whole campaign. Unfortunately, MXPol is affected by extremely high Z_{DR} values in the low gates, probably caused by issues on the transmit-receive limiter. Therefore, a classical calibration procedure such as the one described in *Gorgucci et al.* (1999) cannot be applied. Instead, we decided to select the range interval used for the correction among the upper gates, which were unaffected by the issue. The first step of the calibration procedure was the removal of data with signal-to-noise ratios lower than 5 dB or $\rho_{hv} < 0.95$. For each PPI, we also removed the range gates in which we encountered at least one non-valid Z_{DR} measurement, to avoid introducing a bias caused by some angles being over-represented. Subsequently, we computed, for each range gate, the standard deviation of

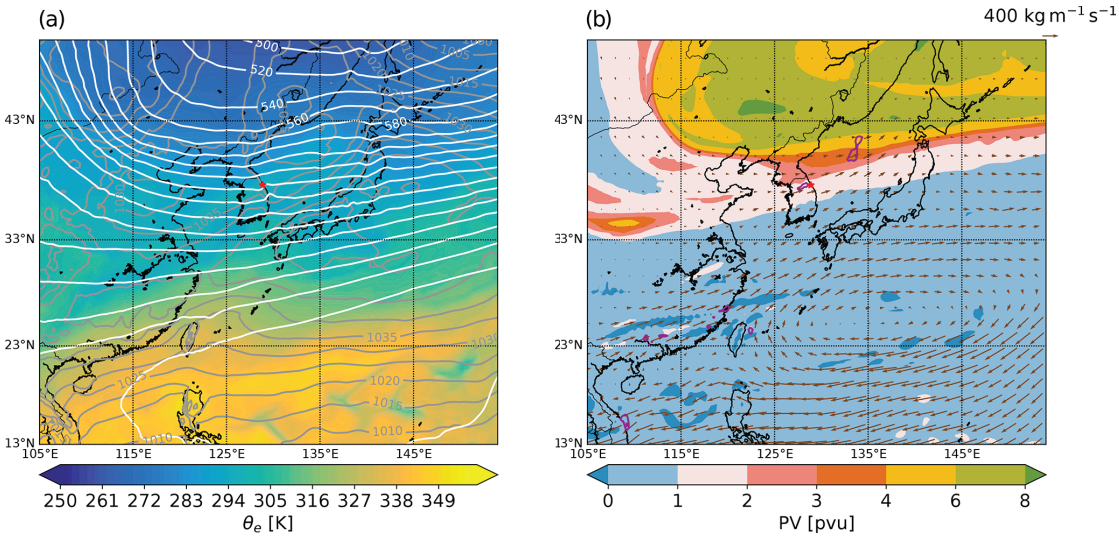

Figure 2.6 – Synoptic meteorological fields at 12:00 UTC on 25 November 2017 from ERA5 reanalysis. **(a)** Sea level pressure (grey contours, labels in hPa), 500 hPa geopotential height (white contours, labels in decameters) and 850 hPa equivalent potential temperature (θ_e, shading). **(b)** Potential vorticity at 315 K (shading; potential vorticity unit (PVU) = 1×10^{-6} K m^2 kg^{-1} s^{-1}), vertically integrated water vapour flux (brown arrows) and precipitation rate (purple contours every 2 mm h^{-1})

the Z_{DR} distribution over the whole campaign duration. This standard deviation is remarkably constant more than 1 km above the radar, while its magnitude increases rapidly in the closest gates, due to the issue mentioned before. After computing the median of these values in the top 25% of the range gates, we impose a maximum threshold of 0.1 dB on the absolute difference between the standard deviation at each range gate and the median value. The median of all Z_{DR} values from the range gates satisfying the condition is 2.66 dB with 50% of the values within 0.32 dB. This median value of 2.66 dB was subtracted from all Z_{DR} measurements to get the corrected Z_{DR} dataset.

2.4.2 MASC

The raw data from the MASC are stereographic photographs of hydrometeors and measurements of fall velocities. *Praz et al.* (2017) developed a hydrometeor classification and riming index estimation of MASC pictures based on a multinomial logistic regression model. More recently, *Hicks and Notaroš* (2019) used convolutional neural networks to classify MASC snowflake images. In this chapter, we will use the algorithm from *Praz et al.* (2017) to classify the MASC data collected during ICE-POP 2018. We will show the hydrometeor classification, as well as the riming index and melting probability results. Note that the riming index of small particles is not reliable, since it is computed over a few pixels only. Therefore we discard small particle in the time series of riming index (i.e. Figs. 2.7, 2.9, 2.11). In addition, raindrops appear as small bright spots in MASC images (reflection of flashes) and are hence classified as

small particles. Therefore, removing small particles from the riming index statistics avoids the bias related to raindrops.

Schaer et al. (2020) developed a method to classify MASC images as blowing snow, precipitation or a mixture of those. This makes it possible to filter the results and minimise the influence of possible blowing snow. Even though a double-fence windshield was present during the ICE-POP 2018 campaign, 31% of the particles were classified either as a mixture of precipitation and blowing snow or pure blowing snow. In the present dataset, all particles are retained, but the information needed to filter out blowing snow particles is added. As explained in *Schaer et al.* (2020) a threshold of 0.193 on the normalised angle ψ can be used with $\psi < 0.193$ corresponding to pure precipitation. The results of the MASC hydrometeor classification shown in this thesis correspond to pure precipitation only.

2.4.3 WProf

The raw data from WProf were saved without any filtering, in the form of raw Doppler spectra. The spectra are then de-aliased with an algorithm based on the minimisation of the spectral width at each range gate, similar to *Ray and Ziegler* (1977). This method assumes aliasing up to one folding, which is sufficient for the Nyquist intervals considered here (Table 2.1). From the de-aliased spectra, the noise floor was determined using the method from *Hildebrand and Sekhon* (1974). The moments (V_D, Z, σ_v, skewness and kurtosis) are then computed from the de-aliased spectra above the noise floor.

Atmospheric gas attenuation

To correct for attenuation due to atmospheric gases, we used the Passive and Active Microwave TRansfer Model (PAMTRA *Mech et al.*, 2020) available at https://github.com/igmk/pamtra (last access: 27 May 2020) and humidity, temperature and pressure profiles from radiosoundings launched at DGW. Radiosoundings were usually available every 3 h, but sometimes up to 12 h. To quantify the temporal variability, we computed the variogram of IWV from all radiosoundings and concluded that the decorrelation time is long enough, so we can expect relatively accurate interpolated values in between radiosoundings. We hence decided to compute a linear interpolation between the two nearest radiosoundings in time to get the profiles at a 5 min resolution, which was then used to compute the gas attenuation and applied to each WProf profile. Figure 2.2 shows the histograms of dry air, water vapour, and total two-way attenuation at W-band from 30 November 2017 to 31 March 2018, which corresponds to the period during which radiosoundings are available. Outside of this period, the WProf reflectivity measurements were not corrected for attenuation. For dry air the values range from about 0.26 dB to 0.33 dB. For water vapour, the values range from nearly 0 dB to 1.75 dB. The attenuation depends on the absolute humidity, and hence the range of values is larger, going from very dry air to a saturated environment. The total two-way attenuation (up to 10 km) varies between 0.3 dB to 2 dB.

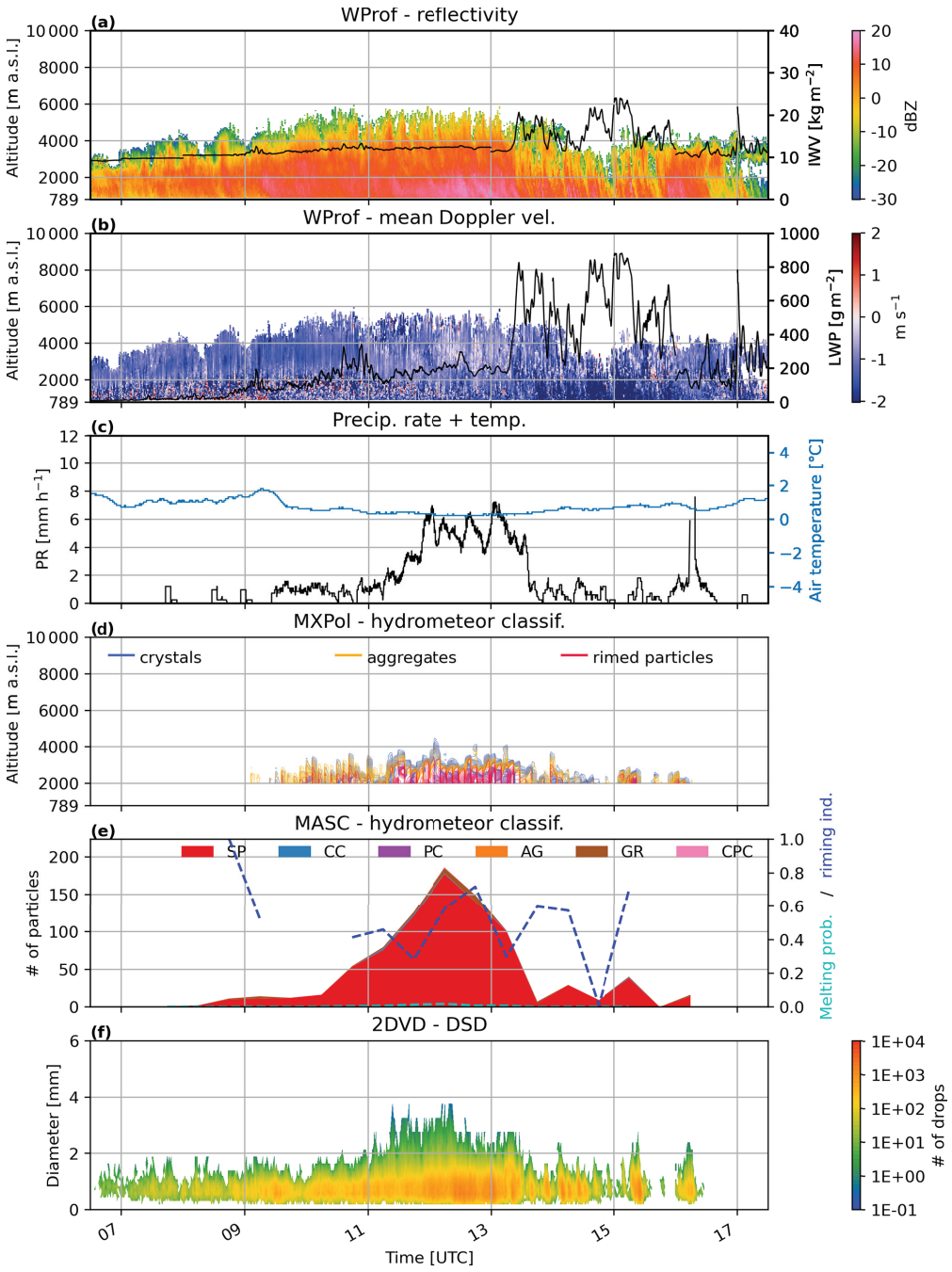

Figure 2.7 – Time series on 25 November 2017 of **(a)** reflectivity and IWV, **(b)** mean Doppler velocity (defined positive upwards) and LWP from WProf, **(c)** precipitation rate (PR) and air temperature at MHS, and **(d)** hydrometeor classification from MXPol (see Sect. 2.4.1). The isolines represent the proportion of each hydrometeor class normalised by the average number of pixels per time step (contour interval is 2%). **(e)** Hydrometor classification from the MASC, melting probability, and riming index (see Sects. 2.3.3 and 2.4.2), and **(f)** drop size distribution from the 2DVD. For this event, the MASC was located at BKC at 175 m.a.s.l. together with the 2DVD. The gap of PR around 16:00 UTC in **(c)** is due to a technical issue with the rain gauge.

2.4.4 Sensitivity

To visualise the sensitivity of WProf and MXPol, Fig. 2.3 shows the empirical joint distributions of range and reflectivity values during all precipitation events of the ICE-POP 2018 campaign. The minimum measured reflectivity values represent the sensitivity. A threshold on the signal-to-noise ratio of 0 dB was applied to MXPol and WProf data in all figures presented. For WProf (Fig. 2.3a) we can clearly see the effect of the three vertical chirps on the minimum detectable reflectivity. One can see that WProf has a higher sensitivity than MXPol at all range gates.

2.5 Overview of the campaign

Figure 2.4 shows precipitation and temperature information during the precipitation events. Table 2.3 shows the exact date and time of the different events. The atmospheric conditions during the ICE-POP 2018 campaign were climatologically cold and dry. The winter 2018 (December 2017 – February 2018) had a total precipitation accumulation of 93 mm in MHS, while the climatological value (*KMA*, 2011) is 153 mm in DGW, 2 km from MHS. The major precipitation event on 28 February 2018 contributed to 62% of the winter 2018 precipitation accumulation, which shows that the rest of the winter was extremely dry (36 mm excluding the 28 February event). March featured a few significant precipitation events leading to 83 mm of precipitation accumulation, while the climatological value is 76 mm. In this section we will present the following events: 25 November 2017, 04–05 and 07–08 March 2018. A case study of the 28 February event is presented in Chap. 4. These events stand out due to their significant precipitation accumulation.

Table 2.4 shows the amount of data collected by each instrument. The measurement time from MXPol does not take into account the repositioning of the antenna between each scan, which typically takes the same time as the scan averaged over the whole cycle. This is why the measurement duration from MXPol is about half that from WProf, which measured continuously. The number of triplets captured by the MASC indicates the number of sets of three pictures captured by the three cameras. For each picture, the classification selects one particle that is in focus. The maximum rate of images is 2 Hz; hence only two hydrometeors can be identified every second. The 2DVD measures continuously at a rate of 34.1 kHz and can identify multiple particles in its sampling area, unlike the MASC. This explains why the number of particles captured by the 2DVD is two orders of magnitude greater than the number of triplets of the MASC.

Figure 2.5 shows the MASC statistics over the whole campaign. From all the available triplets we selected the ones with a quality index greater than 9 (very sharp images, see *Praz et al.*, 2017) leading to a total of 14 006 snowflakes. In this thesis, we always show MASC classification data for triplets and with this filtering on the quality index. Aggregates are the dominating hydrometeor class, followed by small particles, which are likely ice crystals too small to be identified. Graupel is the third dominant class, while the proportion of all crystals sum up to only 6%. Aggregates have the broadest distribution of riming indexes with a mode slightly

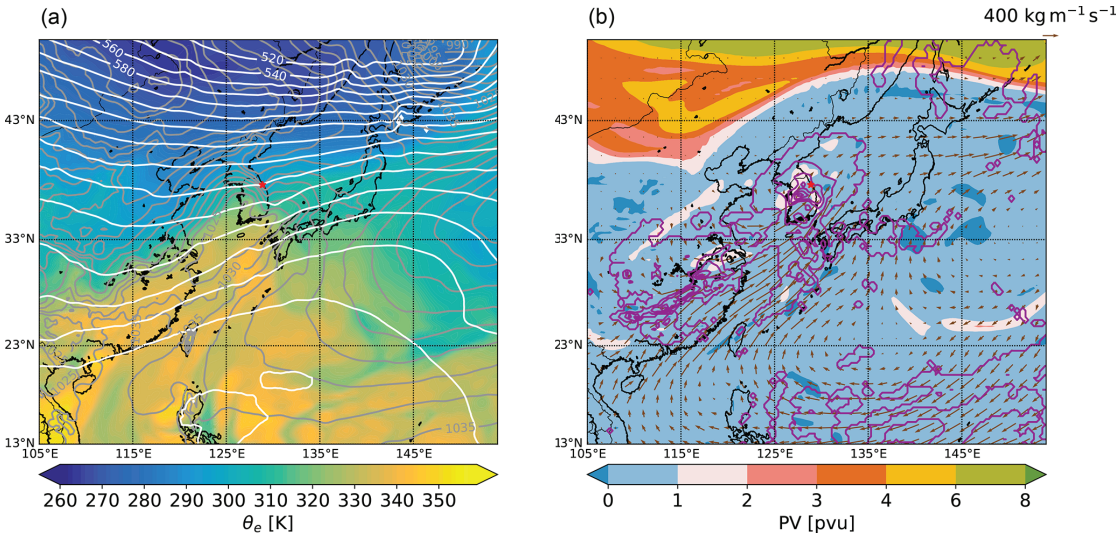

Figure 2.8 – As for Fig. 2.6 except at 15:00 UTC on 04 March 2018

below 0.5, while crystals are much less rimed and graupel have clearly a mode of riming index close to one. The distribution of maximum dimension shows that most particles are smaller than 5 mm, with a mode around 1 mm.

2.5.1 25 November 2017

The 25 November 2017 event has the third-largest precipitation accumulation but the second-largest mean precipitation rate (see Fig. 2.4). Figure 2.6 shows a strong westerly flow associated with a broad upper-level trough. Analysis of backward trajectories (not shown) revealed that the moisture was pumped from the Yellow Sea and lifted over the topography leading to a broad cloud and precipitation system.

Figure 2.7a shows the reflectivity measured by WProf. The precipitating cloud is shallow with a cloud top at 4800 m. Precipitation starts at 08:00 UTC and lasts until 16:00 UTC. Figure 2.7b shows the Doppler velocity measured by WProf. Except for some local turbulence below 2000 m, there are no significant updraughts in the cloud. One can observe that rimed particles dominate below 3000 m a.s.l. from 11:30 to 13:30 UTC (dominance of red shades in Fig. 2.7d).

Figure 2.7e shows a time series of the classification from the MASC. At this time, the MASC was in BKC at only 175 m a.s.l., and it observed almost exclusively raindrops, which are classified as small particles (*Praz et al.*, 2017). Figure 2.7f shows the drop size distribution computed from 2DVD data at BKC. The largest raindrops are observed during the most intense precipitation period (11:00–13:00 UTC) and correspond to the highest vertical extension of the cloud.

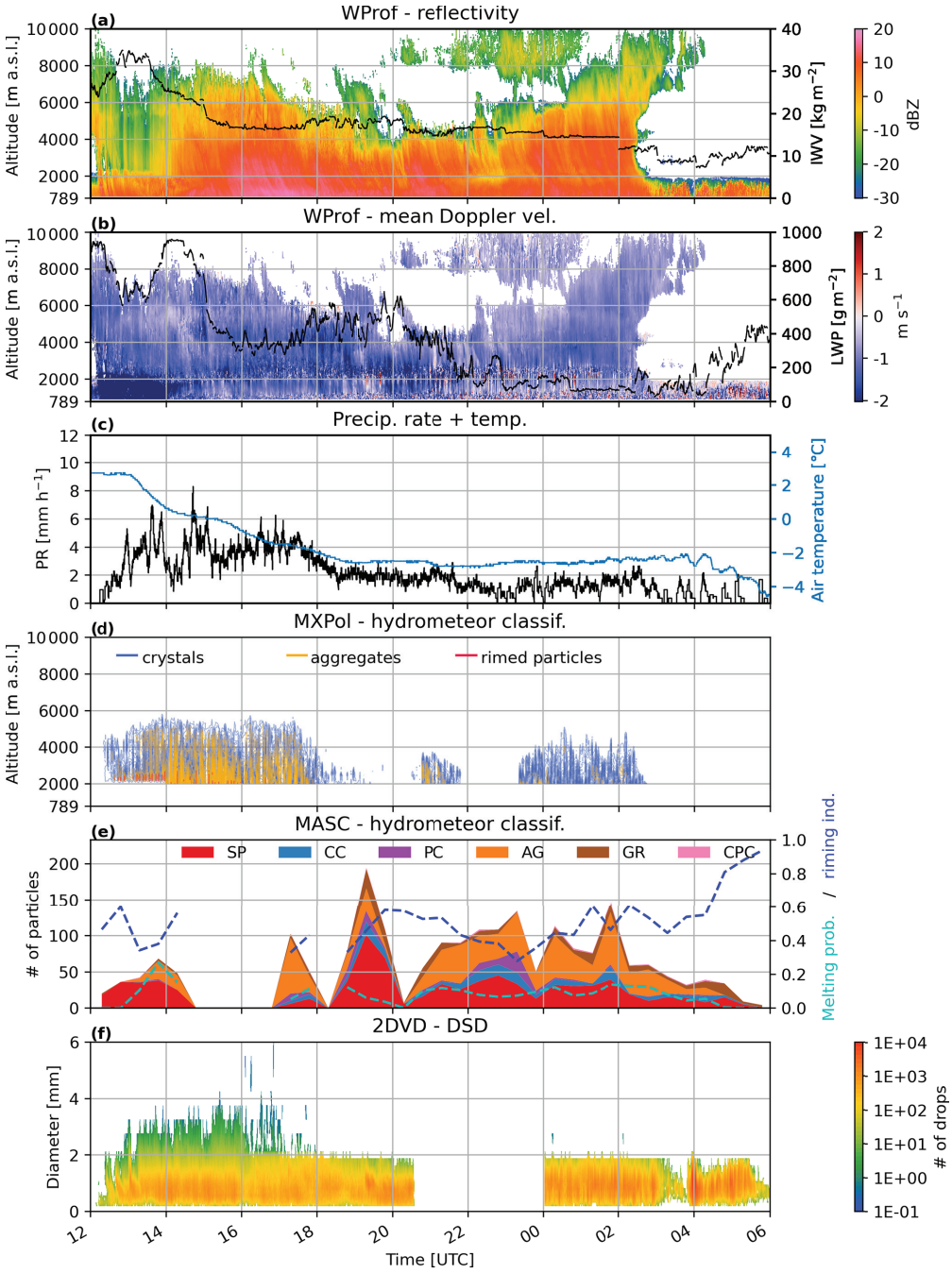

Figure 2.9 – As for Fig. 2.7 except from 04 to 05 March 2018. The MASC was located at MHS at 789 m a.s.l. as WProf, while the 2DVD was located at BKC at 175 m a.s.l. The gap between 20:30 and 00:00 UTC in **(f)** is due to a technical issue with the 2DVD.

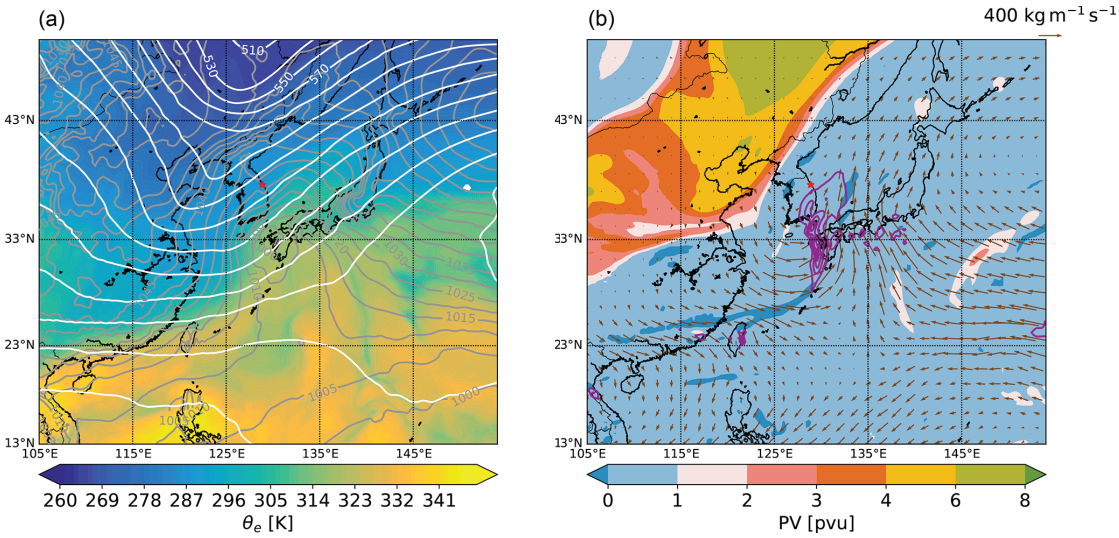

Figure 2.10 – As for Fig. 2.6 except at 00:00 UTC on 08 March 2018

2.5.2 04 March 2018

The 04 March 2018 event has the second-largest precipitation accumulation. Figure 2.8 shows the synoptic conditions. There is a strong south-westerly flow advecting significant moisture from the Yellow Sea, as can be seen by the integrated vapour fluxes (brown arrows) reaching 1000 kg m^{-1} s^{-1} and a low pressure system located south of the Korean Peninsula. This large moisture transport leads to widespread precipitation over the Korean Peninsula with a maximum over the centre of South Korea. The equivalent potential temperature shows the presence of warm and humid air reaching the cyclone's centre. The large sea level pressure gradient on the eastern Korean coast suggests the presence of strong easterly winds. This easterly flow impinging the Taebaek Mountains from the East Sea (Sea of Japan) might have been orographically lifted and participated in an enhancement of the observed precipitation.

Figure 2.9a, b shows the reflectivity and Doppler velocity from WProf. The beginning of the event is dominated by rain with a melting layer around 2500 m which appears clearly from the Doppler velocity (i.e. the sharp gradient in Doppler velocity showing the transition from snowflakes to more quickly falling raindrops). One can see the attenuation in the rain as a sharp decrease in Z_e above 2000 m around 12:00 to 14:00 UTC. The melting layer abruptly drops to the ground level (i.e 789 m a.s.l. at MHS) at 14:00 UTC as temperatures quickly dropped below 0 °C (Fig. 2.9c). The cloud contains mainly crystals and aggregates (Fig. 2.9d), but also some rimed particles above the rain between 12:00 and 14:00 UTC.

Figure 2.9e shows the time series from the MASC classification. One can see that small particles (i.e. raindrops in this case) are dominating until just before 14:00 UTC. Aggregates are then the dominant hydrometeor type, apart from small particles. Graupel particles are more numerous compared to the previous events.

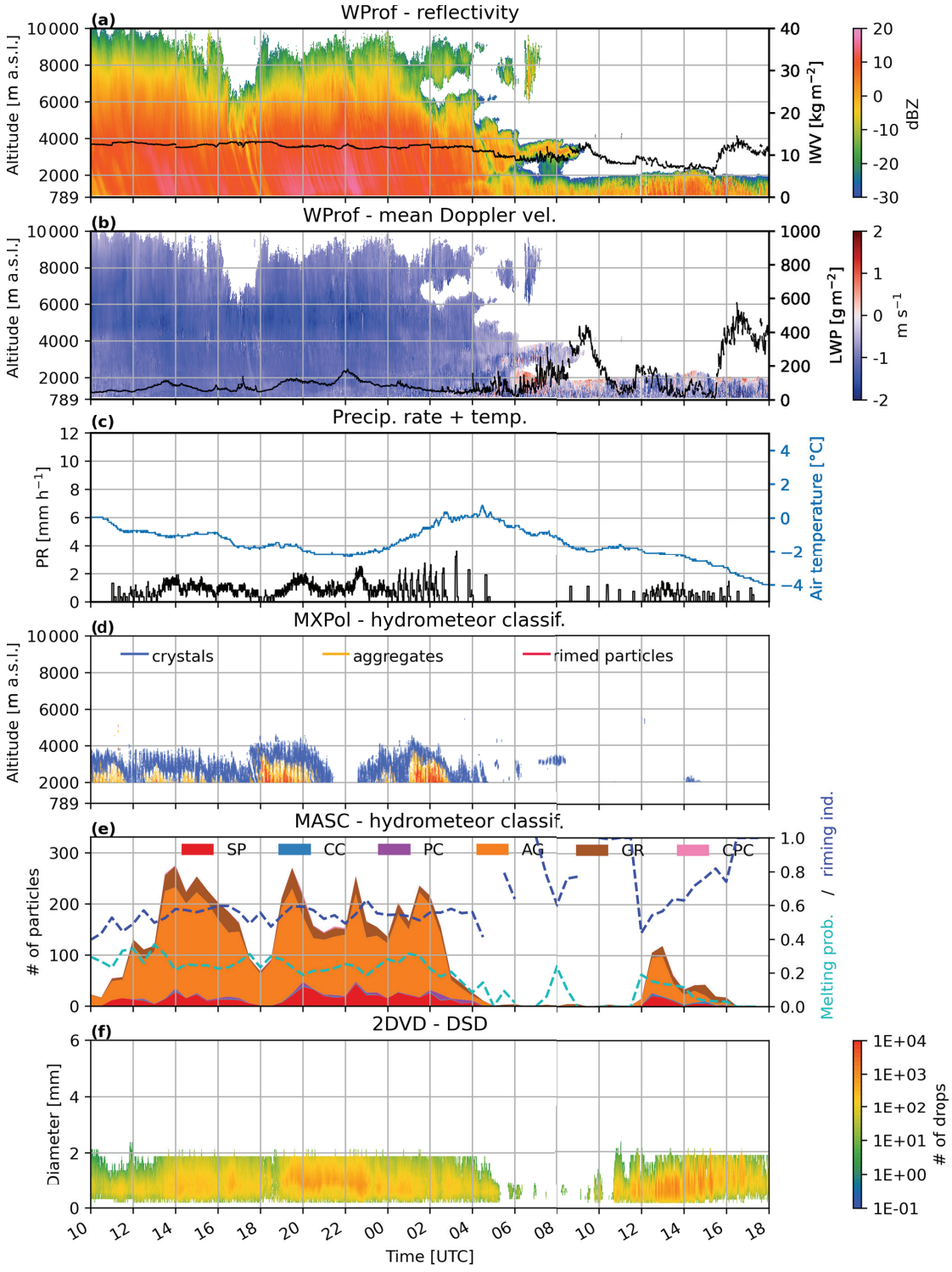

Figure 2.11 – As for Fig. 2.7 except from 07 to 08 March 2018. The MASC was located at MHS at 789 m a.s.l. as WProf, while the 2DVD was located at BKC at 175 m a.s.l.

2.5.3 07 March 2018

The 07 March 2018 event was the fourth-most important in terms of precipitation accumulation (see Fig. 2.4), but was the longest one because of a shallow precipitating system which lasted 12 hours after the main part of the event. On 07 March 00:00 UTC an upper-level trough is moving eastwards from China (Fig. 2.10). The Korean Peninsula is under the influence of a ridge and clear sky conditions dominate. As the trough moves, moist unstable air from the Yellow Sea is advected over the Korean Peninsula and precipitation sets in. Starting from 07 March 15:00 UTC a low pressure system develops south of the Korean peninsula and the trough becomes a broad PV streamer. The precipitation intensity increases until the PV streamer passes over the Korean Peninsula. At 18:00 UTC the precipitation weakens, while the low pressure system is further intensifying on the eastern flank of the PV streamer and reaches Japan with more intense precipitation than observed on the Korean Peninsula.

Figure 2.11a, b shows the reflectivity and Doppler velocity from WProf. The nimbostratus cloud associated with the surface cyclone generates precipitation, which starts around 10:00 UTC and lasts until 04:00 UTC. A shallower precipitating system brings again precipitation from around 08:30 UTC to 19:00 UTC. The radar-based classification (Fig. 2.11d) shows mainly crystals and some aggregates. Since only values above 2000 m are considered and the precipitating cloud after 06:00 UTC 08 March is below 2000 m, no hydrometeors are present in the classification of Fig. 2.11d after 06:00 UTC 08 March. However, the riming index shows a maximum during this period and correlates well with the LWP (Fig 2.11b,e), suggesting that heavily rimed particles are present in this shallow precipitating cloud.

2.6 Conclusions

In this chapter, we presented a four-month dataset of cloud and precipitation measurements by an X-band polarimetric radar, a W-band Doppler cloud profiler, a MASC, and a 2DVD in the county of Pyeongchang in South Korea during the ICE-POP 2018 campaign. The dataset is unique as it represents, together with other ICE-POP measurements, the first observations of clouds and precipitation with radars at different frequencies and ground-based in situ measurements in the Taebaek Mountains. It is complementary to similar datasets in other regions and allows for comparing snowfall microphysical studies in different geographic contexts. In particular, it is relevant to validate conceptual models of orographic precipitation drawn for other mountain chains such as the studies of *Houze and Medina* (2005), *Panziera et al.* (2015), and *Grazioli et al.* (2015b).

The campaign was characterised by mostly cold, dry and windy weather. However, four major precipitation events took place and contributed to 68% of the total precipitation accumulation over the campaign (25 November 2017 to 15 March 2018). We presented the meteorological conditions and data from three of these four events. The dominant hydrometeor types during the campaign were aggregates and rimed particles. The presence of SLW was confirmed for all events by the presence of graupel particles in MASC images and a hydrometeor classification

based on MXPol polarimetric variables. This dataset is particularly suited to study snowfall microphysics, thanks to the synergy between dual-polarisation and spectral information at different frequencies, as well as snowflake photographs.

Future studies could use the data presented in this chapter together with other measurements from ICE-POP 2018. This includes radar data at X, Ku and Ka bands and is particularly suited for microphysical studies with multi-frequency measurements.

3 Ground-based remote sensing and in situ measurements of clouds and precipitation at Davis, East Antarctica

Section 3.3 of this chapter is partly adapted from the preprint version of the article:

- Gehring, J., E. Vignon, A.-C. Billault-Roux, A. Ferrone, A. Protat, S. P. Alexander, and A. Berne (2021b), The influence of orographic gravity waves on precipitation during an atmospheric river event at Davis, Antarctica, *Journal of Geophysical Research: Atmospheres, submitted*

3.1 Summary

Observations of clouds and precipitation during an intensive measurement campaign at Davis, East Antarctica between November 2018 and February 2019 are presented. This includes data collected by an X-band dual-polarisation Doppler radar, a W-band Doppler cloud profiler, a Raman lidar, and a multi-angle snowflake camera. A classification of snowflake images shows that aggregate and graupel were the dominant hydrometeor types that could be identified at ground level. A hydrometeor classification based on dual-polarisation variables suggests that crystals were dominating higher up in the clouds, while aggregates and rimed particles were mainly observed below 1000 m a.s.l. Analyses of two precipitation events showed that supercooled liquid water was present both at cloud-top and above the well-mixed boundary layer, in agreement with recent lidar observations at Davis and Mawson stations, East Antarctica. The synergy between multi-frequency, spectral, and dual-polarisation Doppler radar data with lidar measurements and snowflake images in this dataset offers one of the rare opportunities to study snowfall microphysics and evaluate atmospheric models in Antarctica.

3.2 Introduction

Precipitation in Antarctica plays a key role in the global hydrological cycle, as it is the main positive contribution to the Antarctic ice sheet (*Krinner et al.*, 2007), the largest freshwater

reservoir on Earth (*Hirano et al.*, 2020). Understanding why the ice sheets lose mass is one of the six priorities for Antarctic science (*Kennicutt et al.*, 2014). It is hence crucial to monitor precipitation in Antarctica to understand its spatial and temporal variability (*Eisen et al.*, 2008), which are both significantly impacted by climate change (*Genthon et al.*, 2009/ed). However, the remoteness of the continent and the harsh environmental conditions make the use of instruments a challenging task. Until recently, observations of precipitation were either human-based observations (*König-Langlo et al.*, 1998) or satellite-based (*Palerme et al.*, 2014). The recent increase in spaceborne remote sensing (CloudSat, *Stephens et al.*, 2002; CALIPSO, *Winker et al.*, 2003) and derived products (DARDAR, *Delanoë and Hogan*, 2010; *Ceccaldi et al.*, 2013) has proven useful to monitor precipitation over high southern latitudes (*Listowski et al.*, 2019). However, limitations of spaceborne remote sensing, such as coarse spatial and temporal resolutions, ground clutter and the 'blind range' (inability to measure below a certain height, *Maahn et al.*, 2014), make it difficult to observe small-scale precipitation regimes. This is why dedicated field campaigns with a suite of ground-based in situ and remote sensing instruments are needed to study local patterns of precipitation in Antarctica. In the last decade, multiple efforts have been made in this direction. In 2010 a meteorological observatory was established in Princess Elizabeth, Dronning Maud Land, East Antarctica (*Gorodetskaya et al.*, 2015). The combination of in situ and radar snowfall rate measurements with ERA-Interim reanalyses allowed *Gorodetskaya et al.* (2014) to show that intense meridional moisture transports by atmospheric rivers (ARs) were responsible for extreme precipitation events over coastal Dronning Maud Land. They showed that five ARs contributed to 80% of the outstanding yearly precipitation accumulation in 2011. The APRES3 campaign (Antarctic Precipitation, Remote Sensing from Surface and Space; *Genthon et al.*, 2018), which started in November 2015 in Dumont D'Urville provided the first dual-polarisation radar measurements in Antarctica along with snowflake photographs and micro rain radar (MRR) observations among others. Such field programs can reveal the importance of processes as observed in one particular location for the entire Antarctic continent. For instance, the work of *Grazioli et al.* (2017b) showed that low-level sublimation by katabatic winds, as observed originally in Dumont D'Urville, takes place over most coastal regions of Antarctica and lead to a decrease of 17% of total snowfall on the continental scale and up to 35% on the margins of East Antarctica. These results were recently confirmed by *Agosta et al.* (2019). *Grazioli et al.* (2017b) also pointed out that low-level sublimation significantly affects satellite-based precipitation measurements close to the ground, since the blind range can be above the sublimation layer. This strengthens the need for more ground-based precipitation measurements. The AWARE (U.S. Department of Energy Atmospheric Radiation Measurement (ARM) West Antarctic Radiation Experiment) campaign provided the first triple-frequency radar observations in Antarctica from December 2015 to December 2016 in McMurdo Station (*Lubin et al.*, 2020). This dataset allowed them to identify key differences in cloud and aerosol properties compared to two Arctic sites and to perform model evaluations.

Davis station (69°S, 78°E) is located on the coast of the Vestfold Hills, just north-east of the Amery Ice Shelf. The Vestfold Hills are one of the few ice-free regions in Antarctica, which

makes it part of the Antarctic oasis (*Pickard*, 1986). This is due mostly to its precipitation climatology with only 70.9[1] mm mean annual precipitation and 7.5 mm in December–January–February (DJF). Davis station, with its 1.8 °C mean daily maximum temperature and 8.3 h mean daily sunshine in DJF, is known as the 'Antarctic Riviera' (*Summerson and Bishop*, 2011), because it is both relatively warm and dry. Recent studies (e.g. *Turner et al.*, 2019; *Wille et al.*, 2021) suggest that extreme precipitation events by large meridional moisture advection contribute significantly to the precipitation climatology over Prydz Bay. Yet the micro-climate of the Vestfold Hills questions the validity of these continental-scale studies for this particular location. It is hence necessary to collect dedicated measurements at Davis to better understand the mechanisms leading to precipitation in the Vestfold Hills.

In this chapter, we present the data of an intensive observation period of the Precipitation over Land And The Southern Ocean (PLATO) project at Davis, collected from November 2018 to February 2019. It combines measurements from an X-band dual-polarisation Doppler radar, a W-band Doppler cloud profiler, a Raman Lidar and a multi-angle snowflake camera. It is the first time that remote sensing instruments dedicated to cloud and precipitation observations were installed at Davis, following the success of recent field experiments conducted in other locations on the continent.

The chapter is structured as follows. We describe the geographical location and the instruments in Sect. 3.3. Section 3.4 presents technical challenges encountered during the campaign and recommendations for future field experiments. Section 3.5 introduces statistical results over the whole campaign, as well as two illustrative precipitation events. Finally, we conclude and propose suggestions for future work in Sect. 3.6.

3.3 Vestfold Hills geography and the PLATO campaign at Davis

PLATO is a project coordinated and logistically supported by the Australian Antarctic Division that aims to characterise precipitation over the Southern Ocean and Antarctica and evaluate the precipitation products obtained by satellites and atmospheric models. The central field campaign was organised at Davis with an intensive observation period from November 2018 to February 2019. Davis is located in the Vestfold Hills, one of the few ice-free regions of Antarctica, at the foot of a steep transition from the elevated ice sheet to the coast (Fig. 3.1). The ice ridge at 1000 m a.s.l. located about 80 km to the north-east of Davis (Fig. 3.1 and 3.5) can generate orographic gravity waves (OGWs) under north-easterly flow conditions (*Alexander and Murphy*, 2015; *Alexander et al.*, 2017). Chapter 5 shows how OGWs generated by this ice-ridge can impact the precipitation distribution. The Amery Ice Shelf starts at about 120 km to the south-west of Davis (Fig. 3.5). In November and December 2018 the sea around Davis was covered by ice, while in January and February 2019 only scattered patches of sea ice were present. Solar noon is between 06:30 UTC (November) and 07:00 UTC (February). In

[1] climatological values at Davis are computed over the period 1960–2021, http://www.bom.gov.au/climate/averages/tables/cw_300000_All.shtml, last accessed: 13 May 2021

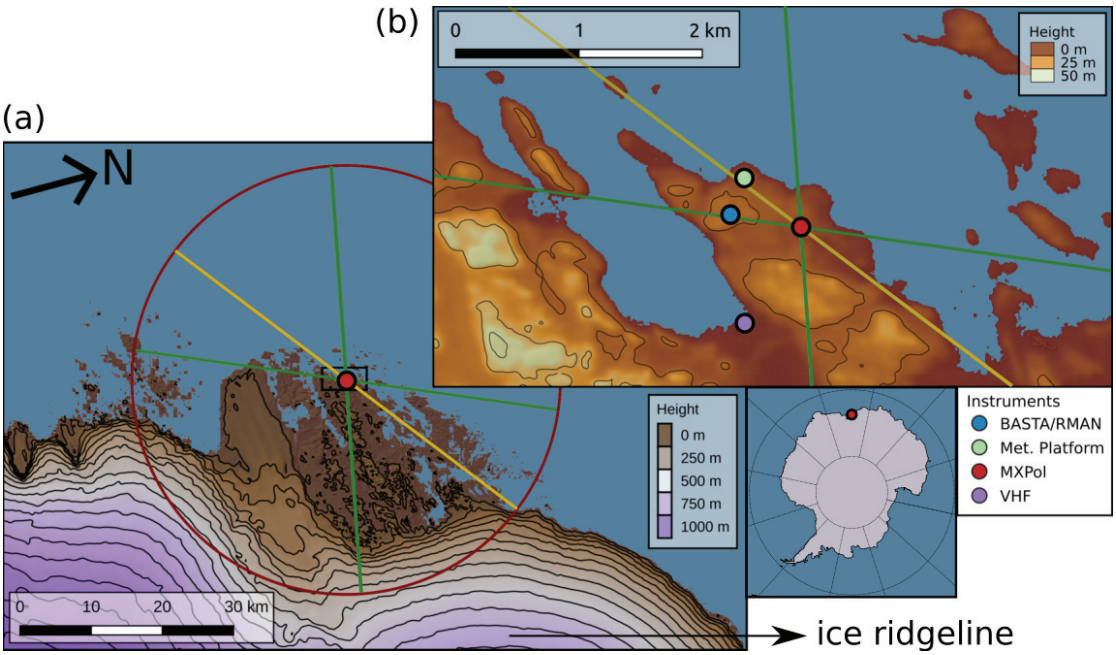

Figure 3.1 – Topography of **(a)** the Vestfold Hills and **(b)** Davis station. The coloured lines show the RHIs of MXPol, the yellow one correspond to the RHI at 52° azimuth. The red circle shows the extent of the PPI. The locations of the instruments are shown in **(b)**. The colours correspond to altitude in m a.s.l. The altitude contours of **(a)** are shown every 100 m and of **(b)** every 20 m. The main ice ridgeline responsible for the generation of OGWs is shown with an arrow. The blue corresponds to altitudes smaller or equal to 0 m a.s.l.

this study, we focus on the data collected by the X-band polarimetric radar MXPol, a W-band Doppler cloud profiler (hereafter BASTA), and a Raman lidar (hereafter RMAN). In addition, we use radiosounding data (12-hourly resolution) and wind, temperature, pressure, and humidity measurements from an automatic weather station (AWS) located at Davis and managed by the Australian Bureau of Meteorology.

X-band polarimetric radar: MXPol

MXPol was installed at Davis station about 600 m from the location of BASTA/RMAN and a meteorological platform (Met. Platform, Fig. 3.1). Apart from the scan cycle, all the technical descriptions of Sect. 2.3.1 apply to this campaign as well. The scan cycle was composed of three hemispherical range height indicators (RHIs) at 23° (in FFT), 52° (in DPP) and 101° (in DPP) azimuth. The first RHI is conducted towards the location of BASTA and RMAN, the second one towards a meteorological platform with other instruments not used in this study, and the third one towards the ice sheet (red dashed lines in Fig. 3.1). The cycle was completed by one plan position indicator (PPI) in DPP mode at 4° elevation (red dashed circle in Fig. 3.1) and one PPI in FFT mode at 90° elevation (for Z_{DR} monitoring). The scan cycle had a 5 min duration and was repeated indefinitely.

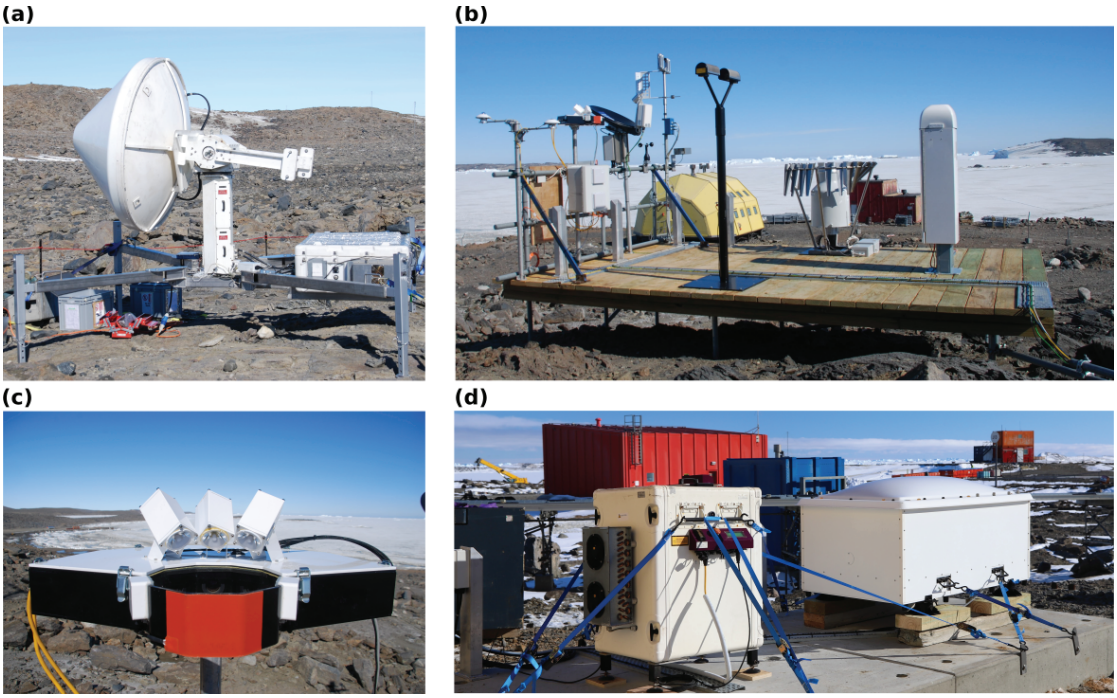

Figure 3.2 – Pictures of **(a)** MXPol, **(b)** the meteorological platform, **(c)** the MASC, and **(d)** RMAN (left) and BASTA (right) at Davis in November 2018. **(a)**-**(c)** Photos by J. Gehring, **(d)** photo by S.P. Alexander.

Z_{DR} has been calibrated by subtracting a time-dependent offset from the original Z_{DR} field, according to the algorithm described in *Ferrone and Berne* (2021). Following the criteria described in the article, only the region between 1067 m and 3681 m above the radar has been extracted from the 90° PPIs (2932 over the whole campaign) and considered suitable for calibration purposes. The median Z_{DR} values from this vertical profile have been used as input for an ordinary Kriging interpolation, which temporal variability was dictated by a spherical variogram fit, with a range of 527 minutes, a partial sill of 0.0034dB^2 and a nugget of 0.0003dB^2. The median Z_{DR} offset of the 6495 scans (restricted to the precipitation events of Table 3.1) is 0.53 dB and the interquartile range is 0.03 dB, showing that the Z_{DR} offset was stable in time.

During the 23° RHI and 90° PPI, the full Doppler spectrum at 0.17 m s^{-1} resolution was retrieved. The MXPol data processing described in Sect. 2.4.1 also applies to this campaign. We will show the hydrometeor de-mixing classification of all RHIs for horizontal distances greater than 6 km and excluding elevation angles between 45° and 135°.

W-band cloud profiler: BASTA

BASTA is a 95 GHz single-polarisation FMCW Doppler cloud profiler, with a beamwidth of 0.4° (*Delanoë et al.*, 2016). The radar operates on a 12 s cycle, based on four 3 s modes using

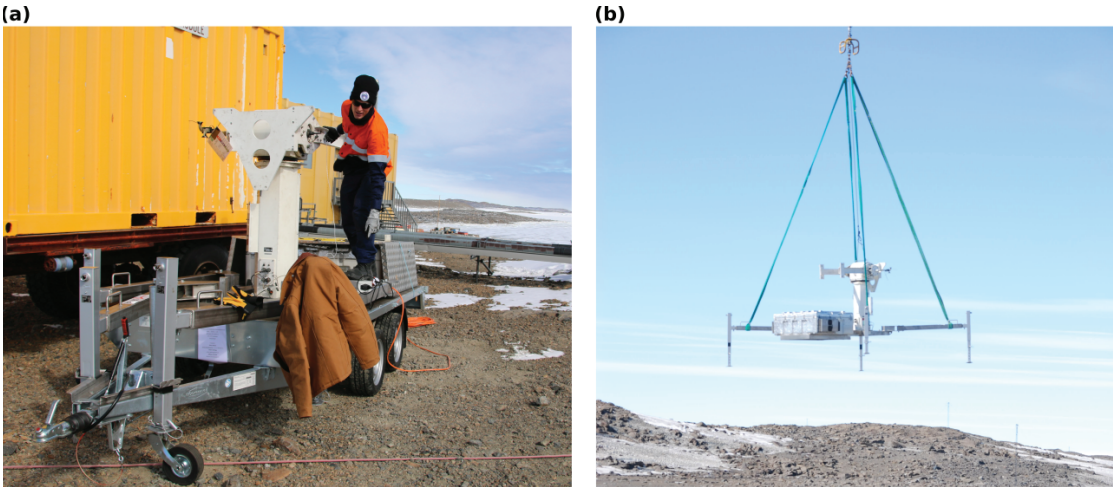

Figure 3.3 – Pictures of MXPol mounted on the trailer **(a)** and during helicopter transportation **(b)** at Davis in November 2018. Photos by J. Gehring **(a)** and F. Gerber **(b)**.

different range resolutions (ranging from 12.5 m to 100 m), corresponding to different Nyquist velocities and minimum detectable signal. The final product used in this study merges the four modes to provide 12 s resolution, 25 m vertical resolution profiles of reflectivity and Doppler velocity. BASTA has been calibrated following the procedure outlined in *Protat et al.* (2019), using statistical comparisons with T-matrix 95 GHz calculations from optical disdrometer observations (*Klepp et al.*, 2018) and with an MRR-PRO 24 GHz vertically-pointing radar observations (*Klugmann et al.*, 1996) collected during the second phase of the Clouds, Aerosols, Precipitation, Radiation, and atmospherIc Composition Over the southeRN ocean (CAPRICORN) experiment (*Mace and Protat*, 2018; *McFarquhar et al.*, 2020), which took place just before the PLATO campaign. The consistency of all radar measurements of PLATO has also been established to be better than 1 dB by statistically comparing MXPol, MRR-PRO, and BASTA observations collected during PLATO.

Raman lidar: RMAN

RMAN (Leosphere RMAN-511) is a vertically-pointing cloud-aerosol mini-Raman lidar measuring elastic backscatter and depolarisation ratio at 355 nm, with a typical range resolution of 15 m and temporal resolution of 35 s (*Royer et al.*, 2014). While the RMAN system also includes a Raman scattering channel, the sensitivity of the system is such that long integration times in cloud-free tropospheric air are used for calibration (*Alexander and Protat*, 2019). From these lidar observations, cloud thermodynamic phase (liquid, ice, supercooled liquid water, and mixed-phase) is estimated first from the lidar backscatter and depolarisation ratio using the algorithm described in *Alexander and Protat* (2018), then refined using cloud radar observations following *Noh et al.* (2019). In this study, we will only use the supercooled liquid water (SLW) category of this cloud classification.

3.3.1 Multi-angle snowflake camera: MASC

The MASC was installed on the Met. Platform (Fig. 3.1) with other in situ and remote sensing instruments not presented here. The technical characteristics and data processing are identical to Sect. 2.3.3 and 2.4.2. Note that the MASC was not protected by a double-fence windshield as was the case during the ICE-POP 2018 campaign. However, only 17% (compared to 31% during ICE-POP 2018) of the particles were classified either as a mixture of precipitation and blowing snow or pure blowing snow. A likely reason is that during ICE-POP 2018 the soil was covered with snow after the first precipitation event, while in the Vestfold Hills, snow never accumulated on the ground for more than a day, decreasing drastically the amount of blowing snow. Also, the ice sheet is located about 20 km from the station and no strong blowing snow events from the ice sheet were observed.

3.4 Technical challenges related to instruments' operation

The harsh environmental conditions prevailing in the southernmost continent and the complex logistics are often cited as some of the reasons for the scarcity of ground-based measurements in Antarctica (*Grazioli et al.*, 2017a; *King and Turner*, 1997). Despite the relatively clement weather conditions and the logistical support offered by the Australian Antarctic Division during the campaign, we faced technical challenges, which will be briefly described in this section, together with recommendations for future campaigns.

3.4.1 Faulty triggering of the MASC cameras

During the first snowfall event of 16 November 2018 (Table 3.1), which brought about 2 cm of snow at Davis, the MASC photographed only two triplets, while the infrared sensors detected

Table 3.1 – Date and time of the start and end of the precipitation events. The events presented here and in Chap. 5 are highlighted in bold.

ID	Start [UTC]	End [UTC]
1	21:30 14 Nov 2018	16:00 16 Nov 2018
2	**00:00 29 Nov 2018**	**10:00**
3	02:00 16 Dec 2018	20:00
4	00:00 03 Jan 2019	02:00 04 Jan 2019
5	10:00 04 Jan 2019	16:00
6	**19:00 05 Jan 2019**	**00:00 07 Jan 2019**
7	**02:00 08 Jan 2019**	**09:00 10 Jan 2019**
8	20:00 22 Jan 2019	06:00 24 Jan 2019
9	01:00 26 Jan 2019	10:00 27 Jan 2019
10	00:00 31 Jan 2019	16:00 02 Feb 2019
11	22:00 03 Feb 2019	03:00 05 Feb 2019

Table 3.2 – Measurement periods of the PLATO instruments

Instrument	Measurement period
MXPol	28 Nov 2018 – 22 Jan 2019
BASTA	11 Nov 2018 – 05 Feb 2019
RMAN	12 Nov 2018 – 04 Feb 2019
MASC	16 Nov 2018 – 06 Feb 2019

a few thousand falling particles. This suggests that the cameras were not triggered properly. We installed the MASC in a lab to perform oscilloscope measurements and realised that the triggering signal to the cameras was too weak. However, about 90% of the falling objects used for testing were photographed. After installing it outside again, no pictures of the same objects were recorded. We suspected that interference from other instruments could modify the triggering signal or that the colder temperature would deteriorate some of the electronic components. After carefully checking all the electronic components we realised that one resistor was too low and one transistor damaged. The behaviour of these components was likely impacted by the temperature, such that inside the triggering signal was just enough to start the cameras. Once we replaced these components on 30 December 2018, the MASC was working fine outside. This explains why few MASC snowflake images are available before this date (see Sect. 3.5.1). The temperature dependence of this issue explained why we did not identify this problem during the pre-campaign testing conducted at EPFL. For future field experiments, we suggest testing all the instruments in meteorological conditions as close to those expected during the campaign as possible. This is certainly not always possible and field experiments, in particular in Antarctica, will always come with unexpected issues.

3.4.2 MXPol upgrade to a modular system

Since the location of MXPol during PLATO was not decided beforehand, there remained the possibility that it needed to be transported by helicopter, in case the site would not be accessible with a pick-up. This required building a new modular structure for MXPol composed of a removable trailer and an independent frame. The advantage is that without the trailer MXPol weighs 900 kg and is transportable by most helicopters. In the previous configuration, MXPol could not be deployed without the trailer and the whole system weighed above 1000 kg. Figure 3.3 illustrates the modular system and Fig. 3.2a shows MXPol once deployed. This modular system proved to be adapted for both transportation and deployment during PLATO and the following campaign in Antarctica where it was mounted on a sledge, instead of a trailer. It represents a proof of concept for future campaigns in remote locations.

3.4.3 Late deployment and early removal of MXPol

The shorter measurement period of MXPol (see Table 3.2) was due to unforeseen logistical and administrative complications. We looked for a suitable site when we were already at Davis to have a better idea of the location with maximised visibility. The site we chose required MXPol to be transported by helicopter, instead of a pick-up as for other possible locations with reduced visibility. This delayed its installation and hastened its removal due to the availability of the helicopters on site. As a consequence, we missed four precipitation events (Table 3.1), which significantly decreased the volume of data compared to the other instruments. This impacted MXPol data collection more than a partly reduced visibility would have. For future campaigns, we highly recommend making a definitive choice of instrument locations beforehand and anticipating the constraints related to deployment and removal that could significantly reduce the amount of data collected.

3.4.4 Strong wind and antenna pointing accuracy

During the 08 to 10 January 2019 event a sustained wind of around 20 $\mathrm{m\,s^{-1}}$ lasted for about 24 hours (see Sect. 5.5). This caused the antenna to shake and hence decreased the pointing accuracy. It was also likely the cause of an elevation offset in the encoder of the antenna position during this event. The correction of this offset is presented in Appendix A. The strong wind events characterising the climate of most Antarctic locations remains a challenge not only for snow measurements at ground level but also for ground-based remote sensing. Considering the higher wind speeds encountered during winter, future campaigns aiming for year-long measurements in Antarctica should identify possible solutions for scanning radars. One possibility would be to protect the whole radar with a radome, not only the antenna as for MXPol.

3.5 Overview of the campaign

As stated in Sect. 3.2, Davis has a dry climate with only 7.5 mm of precipitation in DJF. The total precipitation during the campaign (i.e. 11 November 2018–06 February 2019) amounts to 2.6 mm, which represents 43% of the climatology over the same period. The PLATO campaign was hence particularly dry. The absolute amounts of precipitation must however be interpreted with care: the Australian Bureau of Meteorology reports precipitation measurements at Davis only if the wind speed is smaller than 10 $\mathrm{m\,s^{-1}}$, due to blowing and drifting snow contamination. Since the median wind speed conditioned to precipitation events at Davis is 10 $\mathrm{m\,s^{-1}}$ (*Vignon et al.*, 2019), half of the precipitation periods are not measured, which leads to a significant underestimation. Most instruments were operational from mid-November 2018 to the beginning of February 2019, except MXPol (Table 3.2). Figure 3.4 shows the MASC statistics for the period 29 November 2018 to 06 February 2019. A total of 1230 snowflakes were captured (after merging the images from the three cameras) from which 444 with a quality index greater than 9 (very sharp images, see *Praz et al.*, 2017) were selected.

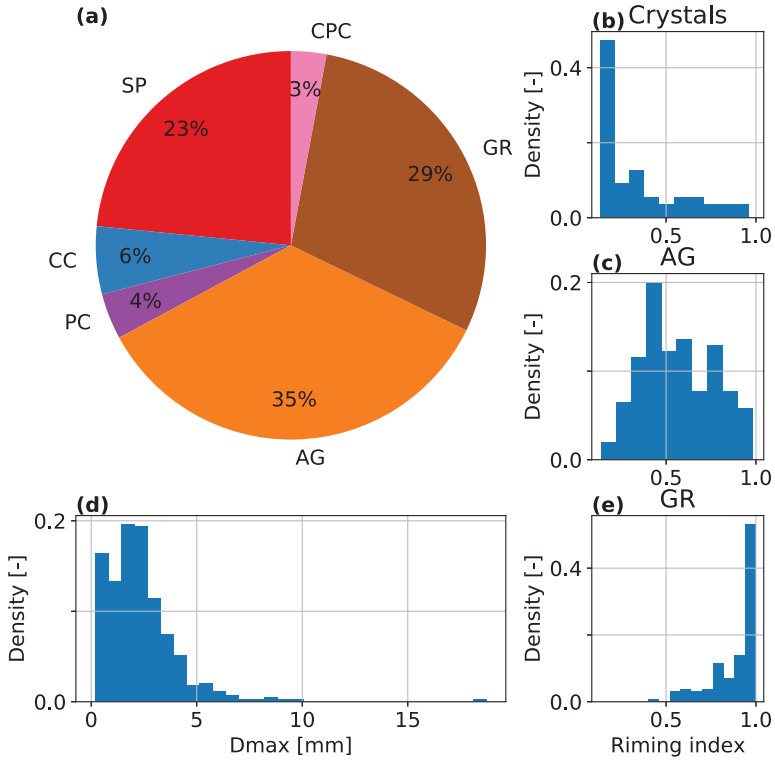

Figure 3.4 – MASC statistics from 29 November 2018 to 06 February 2019. **(a)** Pie chart of hydrometeor classes: small particles (SP), columnar crystals (CC), aggregates (AG), planar crystals (PC), graupel (GR), and combination of columnar and planar crystals (CPC). **(b)**,**(c)**, and **(e)** Histograms of the riming index for individual classes. The classes CC, PC, and CPC have been merged to a parent class 'crystals' in **(b)**. **(d)** Histogram of the maximum diameter (Dmax). The sample size is 444.

The dominant hydrometeor classes are aggregates and graupel. The proportion of all crystal classes sum up to only 13%. However, most small particles are likely to consist of crystals that are too small to be classified. *Grazioli et al.* (2017a) used the same MASC instrument in Dumont d'Urville, East Antarctica. Their statistics over a similar period (i.e. from November 2015 to January 2016) show significantly less graupel and aggregates and more small particles. The latter is probably due to blowing snow during katabatic wind events in Dumont d'Urville. Including blowing snow in our statistics only increases the sample size by 20% and does not change the proportions of classes significantly, except for a small increase in small particles. The relative proportions of the other classes remained almost unchanged. This suggests that the differences with *Grazioli et al.* (2017a) cannot be explained only by the presence of blowing snow in their dataset. We can therefore conclude that, over a similar period, we observed more aggregates and graupel, relative to the proportion of crystals, at Davis than *Grazioli et al.*

(2017a) in Dumont d'Urville. *Fitch et al.* (2021) showed that under strong wind conditions ($\geq 5\ \mathrm{m\,s^{-1}}$), high-density rimed particles are more likely to be observed by the MASC than large low-density aggregates. Since the wind speed during MASC measurements at Davis was mostly above $5\ \mathrm{m\,s^{-1}}$, we can expect that the classification is biased towards graupel particles compared to aggregates. The distributions of riming index (Fig. 3.4b, c, e) shows that crystals are the least rimed classes, while aggregates have a larger mode and dispersion of riming indexes. Graupel particles have clearly a mode of riming index of 1. These distributions are very similar to *Grazioli et al.* (2017a). The distribution of maximum dimensions (Fig. 3.4d) shows that most particles were smaller than 5 mm, with a mode of about 2 mm. In the ICE-POP 2018 dataset, the mode was 1 mm and a higher proportion of particles were bigger than 5 mm (Fig 2.5).

In the next sections, we illustrate the available data on two precipitation events (EV1 and EV2) for which all instruments were operational. A case study of the 08 to 10 January 2019 event is presented in Chap. 5 and illustrates how this dataset, together with atmospheric model simulations, can be used to investigate the detailed microphysics and dynamics of snowfall at Davis.

3.5.1 EV1: 29 November 2018

On 29 November 2018, a broad trough was located to the west of Davis and advects a north-northeasterly flow to the Ingrid Christensen Coast (Fig 3.5). A zone of integrated water vapour (IWV) reaching $2\ \mathrm{kg\,m^{-2}}$ is organised along a weak frontal zone marking the boundary between colder air in the western part of Prydz Bay and warmer air pushed by a low pressure located further east (at 110°E). This moderate moisture advection brought an increase in low clouds to Davis with light snowfall from about 05:00 to 08:00 UTC (Fig. 3.6). A SLW layer is detected by RMAN cloud classification around 1000 m, consistent with the radiosounding at 00:00 UTC (Fig. 3.7b). This SLW layer is capped by a temperature inversion at the top of a well-mixed region (Fig. 3.7a). Before about 05:00 UTC the cloud is extending only up to 1200 m and is topped by turbulent updraughts (Fig. 3.6b). After 05:00 UTC the cloud top is at about 2500 m and is less turbulent, however, updraughts are embedded lower in the cloud. MXPol classification shows almost only crystals, consistent with the MASC classification.

The lack of MXPol data above about 1000 m after 05:30 UTC is due to a sensitivity issue, where further gates were affected by significant noise. The 00:00 UTC radiosounding shows a strong vertical wind shear at around 700 m with a south-westerly flow below and a north-easterly flow above linked to the trough. This wind shear is colocated with a minimum in relative humidity and wind speed suggesting the presence of two distinct air masses. The 12:00 UTC radiosounding has similar behaviour, showing that the wind shear separating these two layers of air is not only a transient feature of this event.

In summary, this event was characterised by light snowfall tied to a cloud system extending up to 2500 m. Before the onset of precipitation, SLW is present below 1000 m and is associated

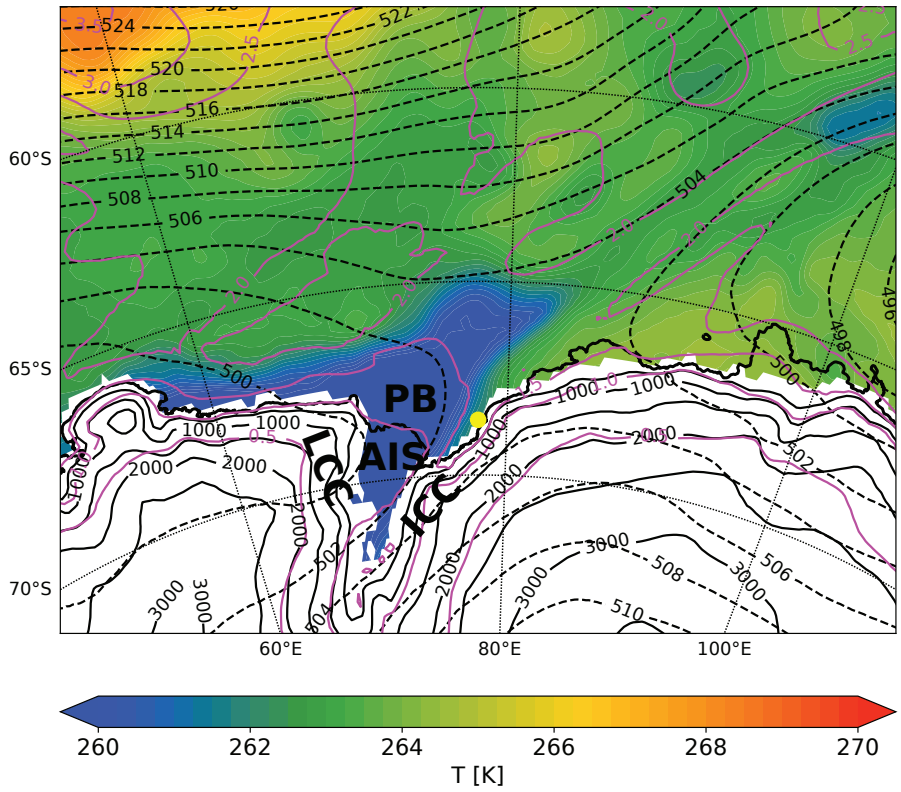

Figure 3.5 – Synoptic situation at 06:00 UTC on 29 November 2018 from ERA5 data. Temperature at 850 hPa (shading in K, masked for altitudes greater than 100 m a.s.l.), IWV (magenta contours in $kg\,m^{-2}$), geopotential height at 500 hPa (dashed contours in decametres), and topography (solid black contours in m a.s.l.). The thicker black contour highlights the coastlines. Davis is shown with the yellow dot, Prydz Bay (PB) is between the Ingrid Christen Coast (ICC) and the Lars Christensen Coast (LCC). The Amery Ice Shelf (AIS) is in the southern part of PB.

with a temperature inversion and a well-mixed boundary layer. Hydrometeor classifications showed the dominance of crystals, consistent with the rather low reflectivity values.

3.5.2 EV3: 06 January 2019

On 06 January 2019 a small scale circulation linked to a minimum of 500 hPa geopotential height (Fig. 3.8) colocated with a low pressure system (not shown) developed over Prydz Bay. This system brought an increase in humidity over the Ingrid Christensen Coast as illustrated by the enhanced IWV in the warm sector of this low pressure. No upper-level forcing could be identified at the dynamical tropopause, suggesting that this system is confined to the middle troposphere.

At 00:00 UTC a precipitating cloud associated with this low pressure system was extending up to 4000 m a.s.l. and brought snowfall to Davis (Fig. 3.9a). This precipitating system was dominated by ice crystals, except during the most intense snowfall periods where aggregates

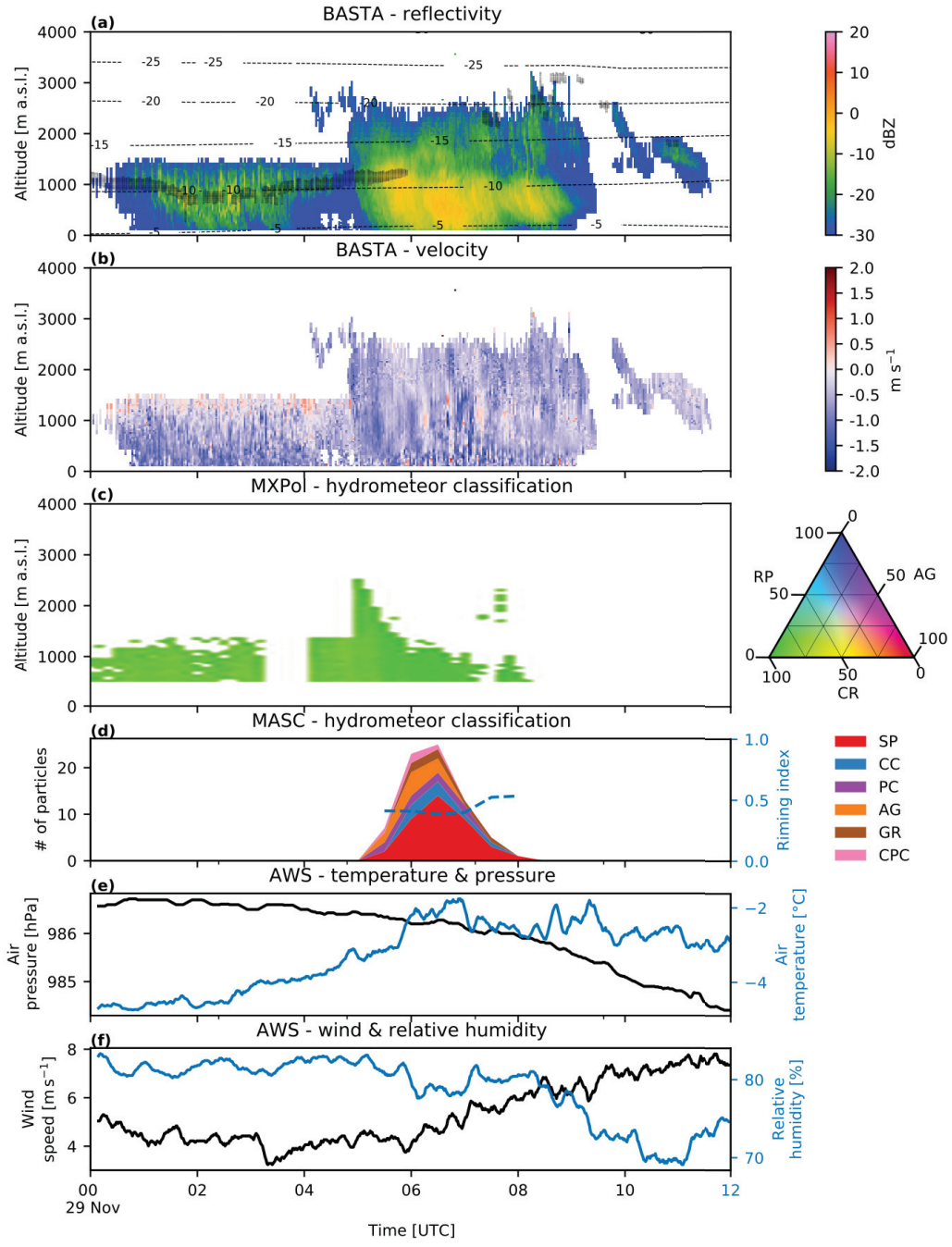

Figure 3.6 – Time series from 00:00 to 12:00 UTC on 29 November 2018 of **(a)** reflectivity of BASTA (coloured shading), isotherms from ERA5 (dashed contours in °C), and SLW from RMAN (black shading), **(b)** mean Doppler velocity from BASTA (defined positive upwards), **(c)** hydrometeor classification based on all MXPol RHIs (shading, see Sect. 3.3), and **(d)** hydrometeor classification from the MASC, and riming index (see Sects. 2.3.3 and 2.4.2). **(e)** Air pressure and temperature, and **(f)** wind speed and relative humidity from the AWS. The colours of the 00:00 and 12:00 UTC labels correspond to the radiosoundings shown in Fig. 3.7

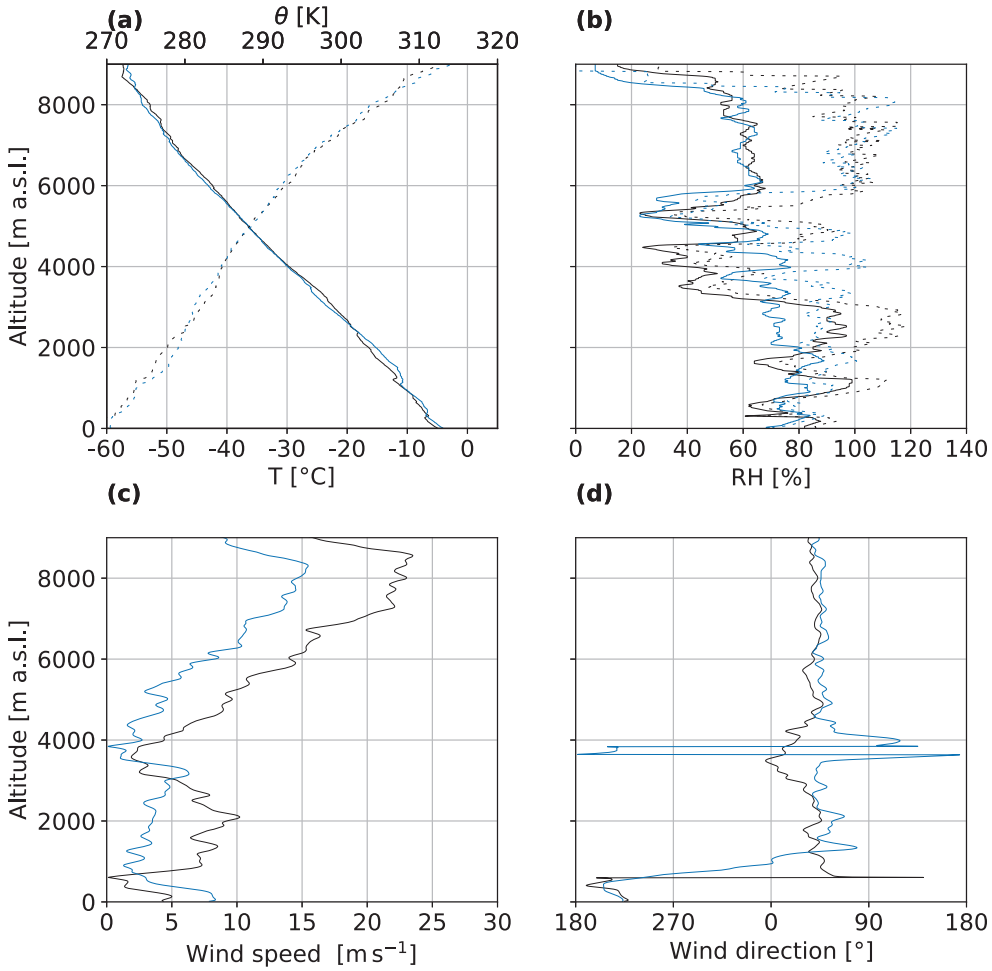

Figure 3.7 – Radiosoundings launched at Davis station at 00:00 UTC (black) and 12:00 UTC (blue) on 29 November 2018 of **(a)** temperature (T, solid lines) and potential temperature (θ, dashed lines), **(b)** relative humidity with respect to liquid (solid lines) and ice (dashed lines), **(c)** wind speed, and **(d)** wind direction

were equally present (Fig. 3.9c). Due to the relatively strong wind (Fig. 3.9f), few particles were captured by the MASC. The MASC classification shows the dominance of aggregates around 07:00 UTC on 06 January followed by small particles, which were likely ice crystals too small to be classified. This difference with respect to MXPol classification can be explained by the fact that the falling particles may aggregate below the minimum altitude used for MXPol classification. Also since the air was subsaturated below 1000 m (00:00 UTC sounding in Fig. 3.10b), sublimation occurs below 500 m and the ice crystals are more likely to sublimate completely than aggregates.

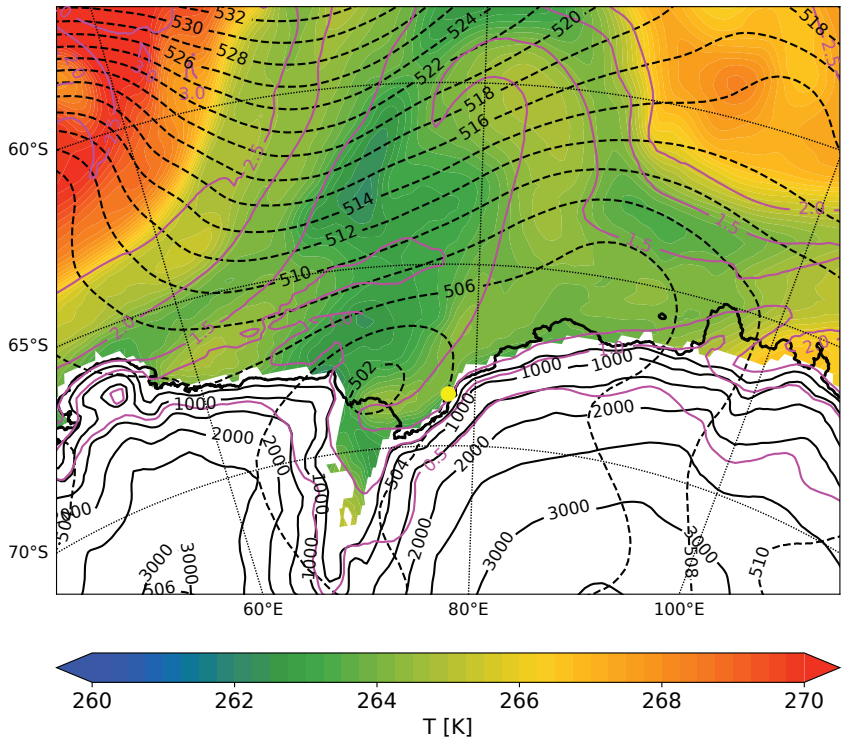

Figure 3.8 – As for Fig. 3.5 except at 00:00 UTC on 06 January 2019

This could explain the difference in the dominating hydrometeor classes between the ground and in the cloud, together with limitations inherent to the comparison of in situ versus remote sensing-based classifications (e.g. sampling technique, sensitivity to different sizes). At around 10:00 UTC the proportion of graupel particles was increasing. It is worth noting that the period with the largest number of MASC images (08:00 to 12:00 UTC) corresponds to the minimum wind speed (Fig. 3.9f), despite the lower reflectivity values than earlier in the event. This suggests that under calmer wind conditions, many more particles would be detected during the rest of the event. Figure 3.12 shows a selection of the highest quality images from the MASC, which turned out to be all during the minimum of wind speed. One can observe a variety of aggregates and one graupel particle, with riming indexes ranging from 0.30 to 0.87. The diversity of habits observed within the aggregates (e.g. sectored plates and dendrites at 09:20 UTC) suggests that vapour deposition took place at different temperatures and supersaturations. The well-preserved shapes of the crystals constituting some of the aggregates (e.g. at 09:20 and 09:40) suggest that the conditions were not too turbulent.

After the passage of the main precipitating cloud, snow showers can be observed between 14:00 and 22:00 UTC. These showers were associated with riming as indicated by MXPol classification (e.g. around 19:00 UTC in Fig. 3.9c), consistent with the presence of SLW in the RMAN cloud classification (Fig. 3.9a). Note that since the MXPol classification shows the proportion of hydrometeors within all RHIs up to 28 km range, showers that are not passing over Davis do appear in Fig. 3.9c, but are not visible over Davis. This is the case for the regions

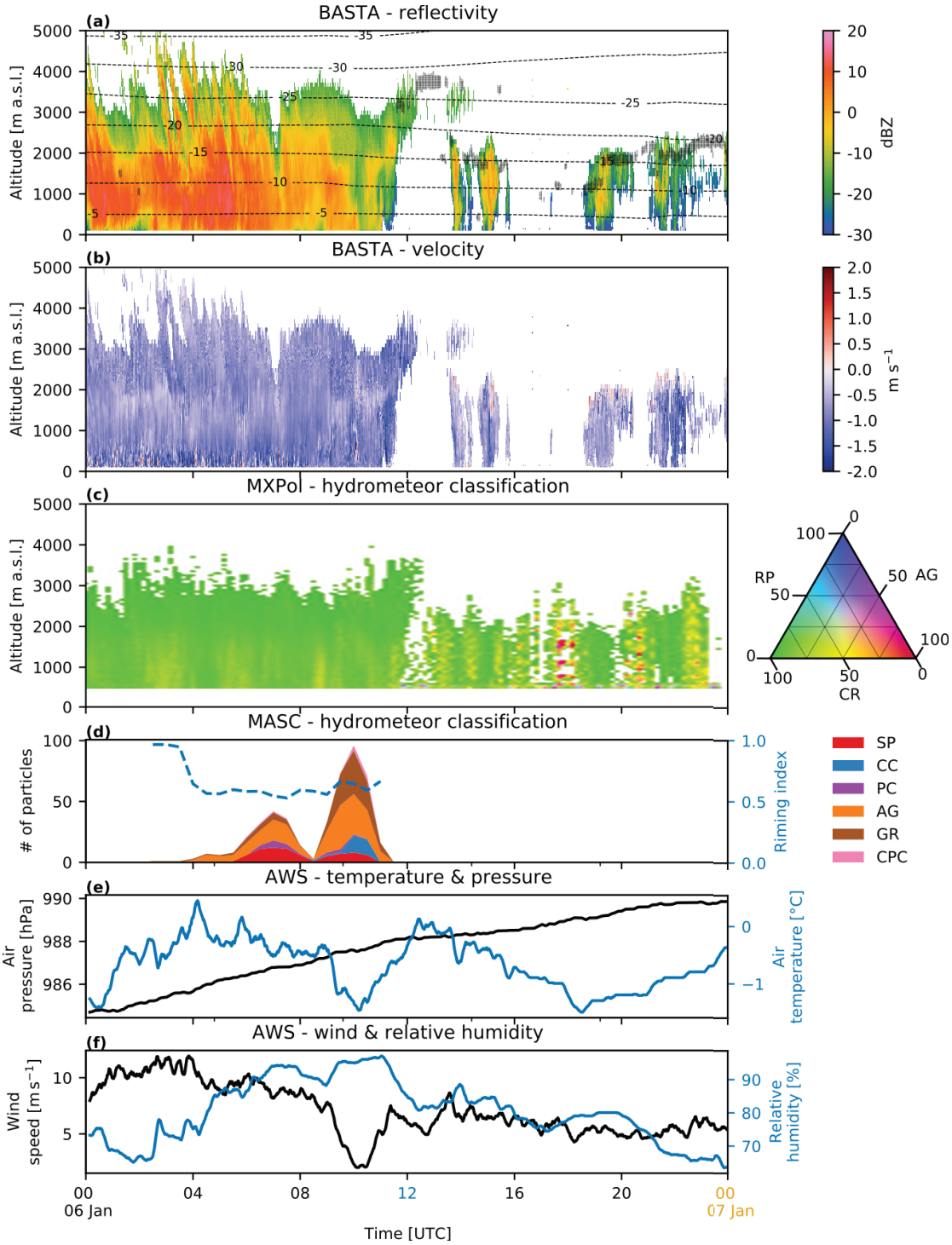

Figure 3.9 – As for Fig. 3.6, except showing the time series from 00:00 UTC on 06 January to 00:00 UTC on 07 January 2019. The colours of the 00:00 and 12:00 UTC labels correspond to the radiosoundings shown in Fig. 3.7

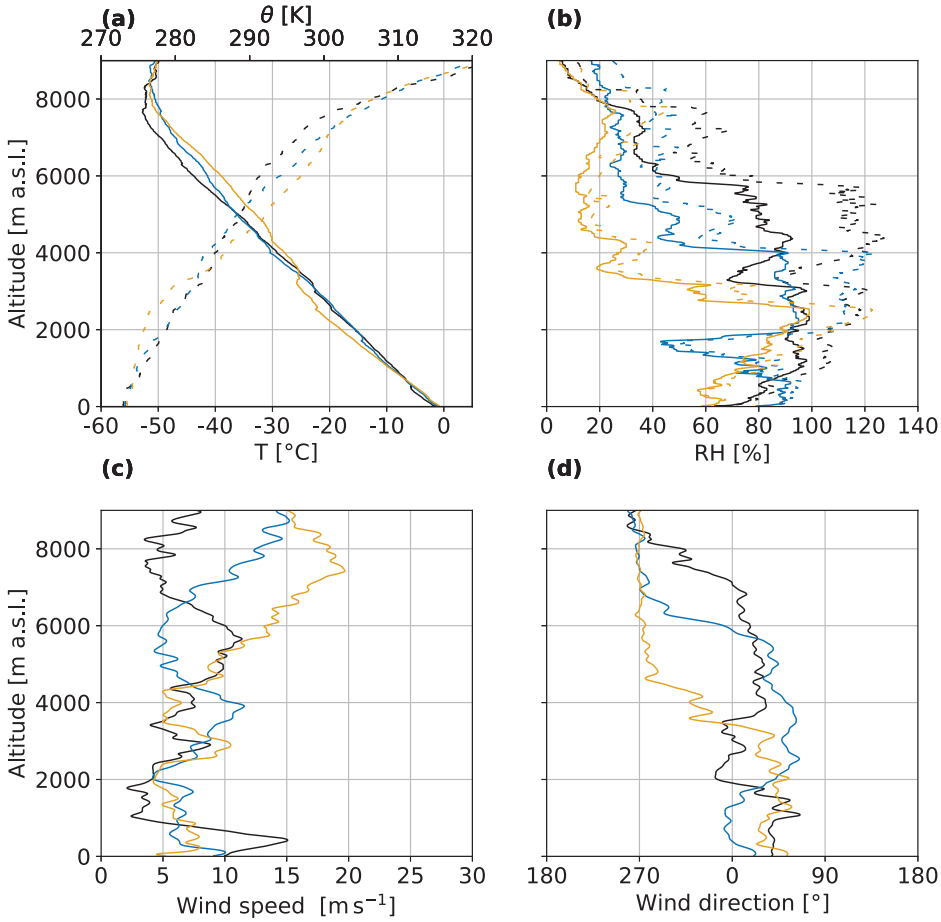

Figure 3.10 – Same as Fig. 3.7 except at 00:00 UTC (black) and 12:00 UTC (blue) on 06 January 2019, and at 00:00 UTC (yellow) on 07 January.

dominated by rimed particles at around 18:00 and 20:30 UTC. Since the lidar signal is strongly attenuated during snowfall, it does not provide any classification during the more intense precipitation periods. However, SLW must have been present throughout the event, due to the relatively high riming index and the presence of graupel in the MASC classification (Fig. 3.9d), as well as the saturated layer with respect to liquid measured by the radiosounding at 00:00 UTC on 06 January (Fig. 3.10b). The SLW layers are observed at the top of the trailing clouds, even at temperatures as low as about −30 °C (Fig. 3.9a at 14:00 UTC), consistent with *Alexander et al.* (2021), who observed such SLW layers in generating cells during three cases over Mawson (650 km to the west of Davis) and Davis stations. They found that turbulent updraughts due to the instability generated by cloud-top radiative cooling (*Vignon et al.*, 2021) were responsible for these ubiquitous SLW layers. The characteristics of the generating cells reported by *Alexander et al.* (2021) are consistent with mid-latitude studies, such as *Kumjian*

et al. (2014) who also suggested that cloud-top radiative cooling might be responsible for the updraughts observed in the generating cells. Such updraughts are present in the shower clouds of Fig. 3.9b. The cloud-top radiative cooling leads to a temperature inversion at about 2500 m below which the SLW layer is capped (00:00 UTC 07 January sounding in Fig. 3.10a, b), consistent with the observations of *Alexander et al.* (2021). This suggests that the updraughts are likely driven by cloud-top radiative cooling of the SLW layer (*Barrett et al.*, 2020; *Heymsfield et al.*, 1991; *Hogan et al.*, 2003). To see the detailed structure of one of these snow showers, Fig. 3.11 shows part of an RHI inside a shower located 26 km to the west of Davis. One can see that the core of this cell consists mainly of rimed particles, while the rest is dominated by aggregates and only about 25% of crystals are present at the top (not shown). This result can be explained by the high Z_H and low Z_{DR} values, especially in the core of the cell, where Z_H reach about 35 dBZ and lead to a classification as rimed particles (the discrimination between rimed particles and aggregates is mainly influenced by Z_H, *Besic et al.*, 2016). Unfortunately, no

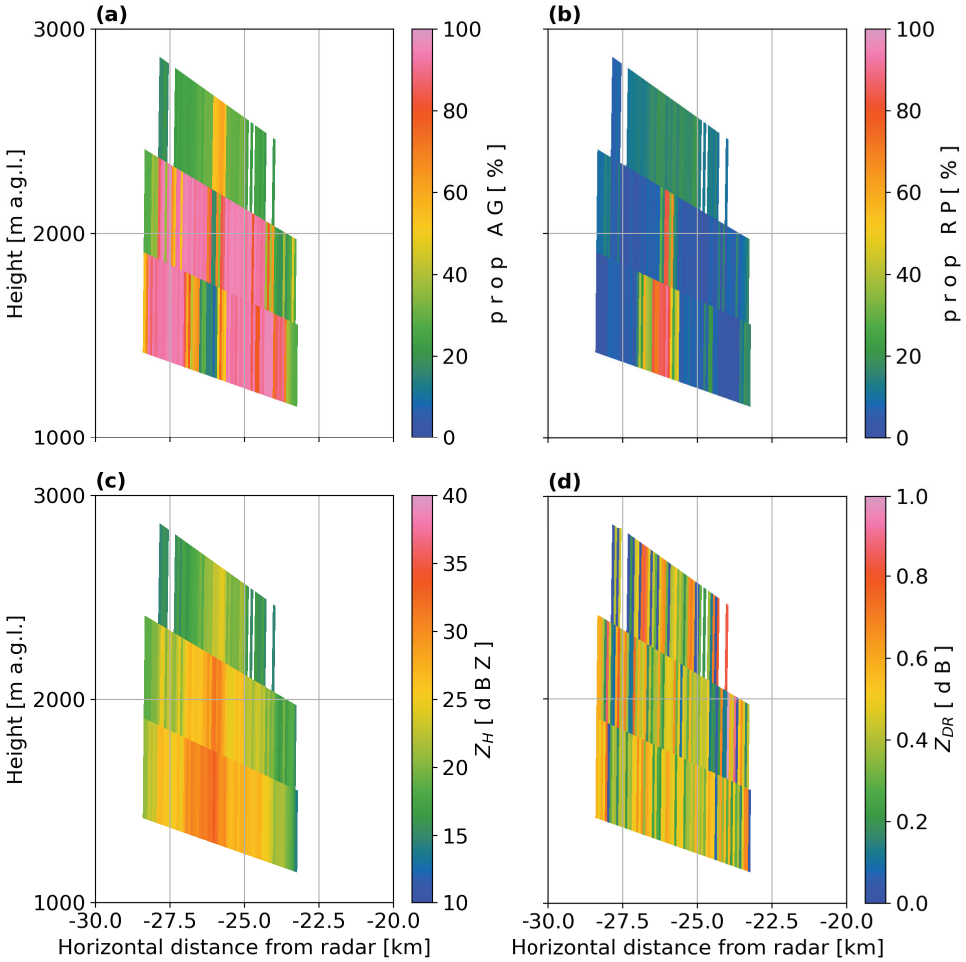

Figure 3.11 – RHI at 101° azimuth at 17:43 UTC on 06 January of **(a)** the proportion of aggregates (AG), **(b)** the proportion of rimed particles (RP), **(c)** Z_H, and **(d)** Z_{DR}.

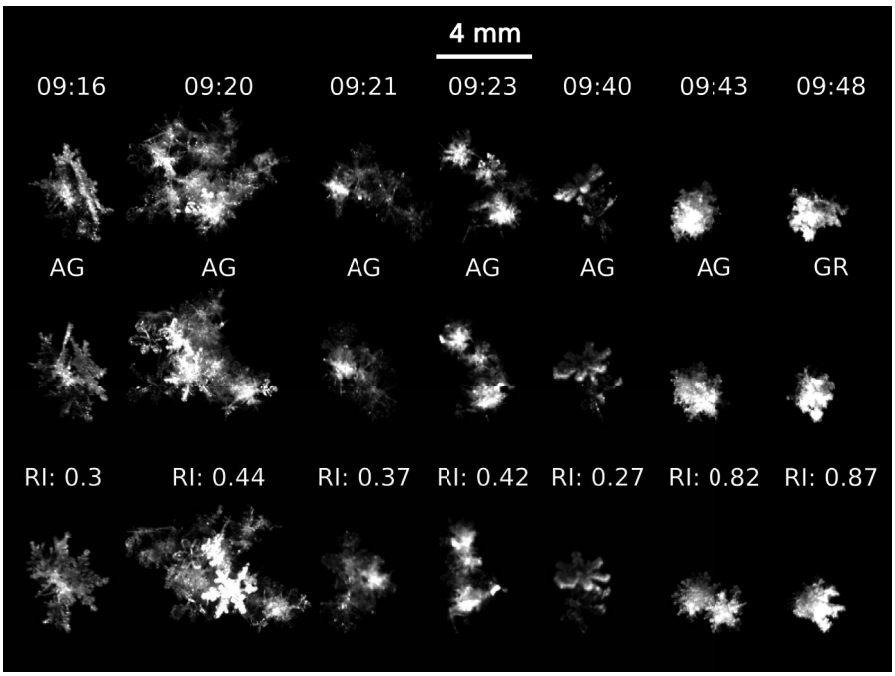

Figure 3.12 – Selection of MASC images with a quality index greater than 10.5 (very sharp images, see *Praz et al.* (2017)). The title of the first row gives the time (UTC) on 06 January, the second row the particle type (AG=aggregate, GR=graupel), and the third row the riming index (RI). The rows correspond to the three different cameras.

MASC images were collected during these showers, which could have confirmed the presence of rimed particles at the ground.

In summary, a small-scale low pressure over Prydz Bay, which was not associated with upper-level forcing, nor large-scale moisture advection, brought snowfall to Davis for almost 12 h. The main precipitating cloud was followed by snow showers containing significant riming and SLW, as suggested by RMAN and MXPol classifications. The SLW layers likely originated from turbulent updraughts due to cloud-top radiative cooling and are consistent with recent observations from *Alexander et al.* (2021).

3.6 Conclusions

In this chapter, we presented a dataset of cloud and snowfall measurements at Davis, Antarctica covering a period from mid-November 2018 to the beginning of January 2019. This summer season was characterised by relatively dry conditions with only 43% of the climatology of total precipitation over the same period. Statistics from the MASC classification shows that aggregates and graupel were the dominant hydrometeor classes. Blowing snow and precipitation mixed with blowing snow represented only 17% of the observed MASC images. We illustrated the available data with two precipitation events, which both featured SLW layers

due to updraughts likely generated by either cloud-top radiative cooling or the turbulent boundary layer, consistent with recent observations from *Alexander et al.* (2021). These SLW layers led to riming, which could be observed in the MASC and MXPol classifications. In particular, intense riming was observed in the core of convective snow-precipitating cells as large reflectivity and low differential reflectivity values.

A detailed case study of the 08 to 10 January 2019 event is presented in Chap. 5 and exemplifies how this dataset and atmospheric model simulations can be used to differentiate the role of local versus large-scale processes on snowfall microphysics. In addition to the instruments presented here, other sensors relevant for microphysical studies were measuring during the PLATO campaign. This includes in particular an MRR, which, together with BASTA and MXPol, offers one of the rare opportunities for triple-frequency radar studies in Antarctica, in addition to the AWARE dataset (*Lubin et al.*, 2020). In addition, a holographic microscope (*Chambers et al.*, 2016) provided particle images of 3 to 3000 μm, which nicely complement the MASC dataset. Future studies could hence use the full PLATO dataset to validate radar microphysical retrieval methods against two different hydrometeor imager instruments. Finally, such a ground-based in situ and remote sensing dataset opens the door to the validation of microphysical parameterisation in atmospheric models.

4 Microphysics and dynamics of snowfall associated with a warm conveyor belt over Korea

This chapter is adapted from the postprint version of the article:

- Gehring, J., A. Oertel, E. Vignon, N. Jullien, N. Besic, and A. Berne (2020b), Microphysics and dynamics of snowfall associated with a warm conveyor belt over Korea, *Atmospheric Chemistry and Physics*, *20*(12), 7373–7392, doi: 10.5194/acp-20-7373-2020

It presents a case study of an intense precipitation event over Pyeongchang, in which a warm and moist ascending airstream, called a warm conveyor belt (WCB), produced the ideal conditions for intense riming and aggregation.

4.1 Summary

On 28 February 2018, 57 mm of precipitation associated with a WCB fell within 21 h over South Korea. To investigate how the large-scale circulation influenced the microphysics of this intense precipitation event, we used radar measurements, snowflake photographs and radiosounding data from the ICE-POP 2018 campaign. The WCB was identified with trajectories computed with analysis wind fields from the Integrated Forecast System global atmospheric model. The WCB was collocated with a zone of enhanced wind speed of up to 45 m s^{-1} at 6500 m a.s.l., as measured by a radiosonde and a Doppler radar. Supercooled liquid water (SLW) with concentrations exceeding 0.2 g kg^{-1} was produced during the rapid ascent within the WCB. During the most intense precipitation period, vertical profiles of polarimetric radar variables show a peak and subsequent decrease in differential reflectivity as aggregation starts. Below the peak in differential reflectivity, the specific differential phase shift continues to increase, indicating early riming of oblate crystals and secondary ice generation. We hypothesise that the SLW produced in the WCB led to intense riming. Moreover, embedded updraughts in the WCB and turbulence at its lower boundary enhanced aggregation by increasing the

probability of collisions between particles. This suggests that both aggregation and riming occurred prominently in this WCB. This case study shows how the large-scale atmospheric flow of a WCB provides ideal conditions for rapid precipitation growth involving SLW production, riming, and aggregation. Future microphysical studies should also investigate the synoptic conditions to understand how observed processes in clouds are related to large-scale circulation.

4.2 Introduction

Precipitation is the result of a chain of meteorological processes ranging from synoptic to micro-scales. In particular for stratiform precipitation, large-scale flow drives the transport of moisture and lifting of air masses, while microphysics ultimately determines the growth and fall of hydrometeors, influencing precipitation intensity and accumulation. Therefore understanding the link between large-scale flow and microphysics is paramount to better forecasting precipitation. Extratropical cyclones are the main synoptic-scale features associated with precipitation at mid-latitudes and produce more than 80% of the total precipitation in the Northern Hemisphere storm tracks (*Hawcroft et al.*, 2012). Quasi-Lagrangian analyses of mid-latitude baroclinic storms have shown the existence of three distinctive airstreams (*Carlson*, 1980): the dry intrusion, the cold conveyor belt (*Harrold*, 1973; *Browning*, 1990; *Schultz*, 2001), and the warm conveyor belt (WCB; *Green et al.*, 1966; *Harrold*, 1973; *Browning et al.*, 1973; *Dacre et al.*, 2019). The latter can be defined as a coherent warm and moist airstream rising from the boundary layer to the upper troposphere in about 2 d (*Eckhardt et al.*, 2004; *Madonna et al.*, 2014). Climatological studies of WCBs have used a simple criterion on the ascent rate of trajectories (e.g. 600 hPa in 48 h; *Madonna et al.*, 2014).

WCBs typically rise from below 900 to about 300 hPa, and temperature along this flow typically decreases from above 0 to below −40 °C. Therefore, clouds along WCBs feature the whole spectrum from warm clouds to mixed-phase to pure-ice clouds (e.g. *Joos and Wernli*, 2012; *Madonna et al.*, 2014). WCBs are the primary precipitation-producing feature in extratropical cyclones (*Browning*, 1990; *Eckhardt et al.*, 2004) and are responsible for more than 70% of precipitation extremes in the major storm tracks (*Pfahl et al.*, 2014). However, precipitation and cloud processes also impact the dynamics of extratropical cyclones. Trajectory analyses have shown that WCBs experience a strong cross-isentropic ascent due to latent heat release (*Madonna et al.*, 2014), which leads to an increase in potential vorticity (PV) below the maximum diabatic heating level and a decrease above it (*Wernli and Davies*, 1997). This represents a direct link between microphysics and dynamics. *Joos and Wernli* (2012) studied the impact of different microphysical processes on the diabatic PV production in WCBs. They suggested that condensation of cloud liquid and depositional growth of snow and ice are the most significant diabatic heating processes in WCBs. *Joos and Forbes* (2016) showed the direct impact of specific microphysical processes on PV modification in WCBs and the subsequent downstream flow evolution.

Colle et al. (2014) studied the distribution of snow crystal habits within mid-latitude baroclinic storms over Long Island, New York. They observed moderately rimed crystals in the middle of the comma head, while heavy riming was present close to the cyclone centre. They also showed a positive correlation between vertical wind speeds, turbulence and degree of riming by means of Doppler data from a micro rain radar. Overall, this study highlights the spatial structure of microphysics occurring in winter storms and suggests a link between the dynamics of the cyclone and observed snow crystal habits.

Dual-polarisation Doppler (polarimetric) radars are useful to study precipitation microphysics as they provide information on the hydrometeors' shape, density and phase. For instance, differential reflectivity Z_{DR}, defined as the logarithmic ratio between the reflectivity factor at horizontal and vertical polarisations ($Z_H - Z_V$ in decibels), is a measure of the reflectivity-weighted axis ratio of the targets (*Kumjian*, 2013b; *Bringi and Chandrasekar*, 2001). Oblate particles (e.g. raindrops and dendrites) have positive Z_{DR} values, while prolate ones (e.g. vertically oriented ice in an electric field) exhibit negative Z_{DR} values. Z_{DR} also depends on the crystal's dielectric constant but not on the number concentration. Therefore, large aggregates tend to have small Z_{DR} values (< 0.5 dB; *Kumjian*, 2013b) primarily because they have a much lower density than solid ice but also because the collection of randomly oriented and irregular crystals leads to isotropic scattering. On the other hand, aggregates are much larger than crystals and tend to have higher Z_H values. Consequently, decreasing Z_{DR} together with increasing Z_H towards the ground is a consistent signature of the aggregation process (*Schneebeli et al.*, 2013; *Kumjian et al.*, 2014; *Grazioli et al.*, 2015b). Furthermore, the specific differential phase shift (K_{dp}; in $^\circ\,\mathrm{km}^{-1}$), which is the range derivative of the total differential phase shift on propagation (i.e. phase difference between the horizontal and vertical polarisation waves propagating forward), is related to the axis ratio, the density, the number concentration and the size of the targets. Being a lower-order moment than Z_H, it is more influenced by the number concentration such that a high number concentration of small oblate crystals can lead to an increase in K_{dp}, while Z_{DR} will barely be affected. Owing to this wealth of information, polarimetric variables have been extensively used for snowfall microphysical studies (*Bader et al.*, 1987; *Andrić et al.*, 2013; *Schneebeli et al.*, 2013; *Moisseev et al.*, 2015; *Grazioli et al.*, 2015b). The pioneering work of *Bader et al.* (1987) showed that high Z_{DR} values are associated with large dendritic crystals. More recently, *Moisseev et al.* (2015) found that enhanced values of specific differential phase (K_{dp}) are related to the onset of aggregation, producing early aggregates that can be oblate. *Grazioli et al.* (2015b) suggested that similar peaks in K_{dp} can result from secondary ice generation (leading to a high number concentration of small anisotropic crystals) or the riming of oblate ice crystals, which increases their density. These studies thoroughly analysed dual-polarisation signatures of snowfall microphysics. However, they did not consider the interactions between large-scale flow and microphysics. *Keppas et al.* (2018) studied the microphysical properties of a warm front with radar and in situ measurements in clouds. They found that a WCB formed a widespread mixed-phase cloud by producing a significant amount of liquid water, which favoured riming and secondary ice generation. However, they did not formally identify WCB

trajectories nor did they confirm that the liquid water was produced within the WCB. There is hence a need to better understand how the strong, coherent ascending motion within WCBs influences precipitation microphysics. To this end, a synergy between remote-sensing and in situ measurements, as well as trajectory analyses, is needed.

In this study, we use data from the ICE-POP 2018 campaign to study an extreme snowfall event associated with a WCB over South Korea on 28 February 2018. The location of Pyeongchang on a peninsula at mid-latitudes offers an interesting setting to study the interplay between synoptic circulation, orographic effects and microphysics. First, the surrounding Yellow Sea and East Sea provide nearby sources of moisture for precipitation, which is particularly relevant for wintertime WCBs (*Pfahl et al.*, 2014). Secondly, WCBs play a crucial role for precipitation over the Korean Peninsula: between 80% and 90% of extreme precipitation is associated with WCBs in South Korea according to a climatological study by *Pfahl et al.* (2014). The ICE-POP 2018 dataset includes, among other data, multiple-frequency radar measurements and high-resolution snowflake photographs. We also make use of the Integrated Forecast System (IFS; *ECMWF*, 2017) model from the European Centre for Medium-Range Weather Forecasts to identify WCB trajectories associated with this event.

To understand the role of the WCB during this intense precipitation event in Korea, we address the following questions:

- What was the synoptic situation leading to this intense snowfall event?
- Which microphysical processes were involved?
- How did the specific flow conditions in the WCB influence the observed microphysics?

This chapter is structured as follows. We first present additional data not introduced in Chap. 2 and used in this study (Sect. 4.3). The synoptic situation is presented in Sect. 4.4. Section 4.5 shows the evolution of the event over Pyeongchang. An analysis of the microphysics observed by radar and snowflake images during succeeding periods of interest is presented in Sect. 4.6. We then summarise the key findings of this study with a conceptual model in Sect. 4.7 before concluding in Sect. 4.8.

4.3 Dataset

4.3.1 Instruments used

In this study, we will use the MXPol, WProf and MASC data presented in Chap. 2. In addition, we will show radiosondes (3-hourly resolution) and temperature measurements from Daegwallyeong (DGW) located 2 km away from the Mayhills site (MHS, Fig. 2.1).

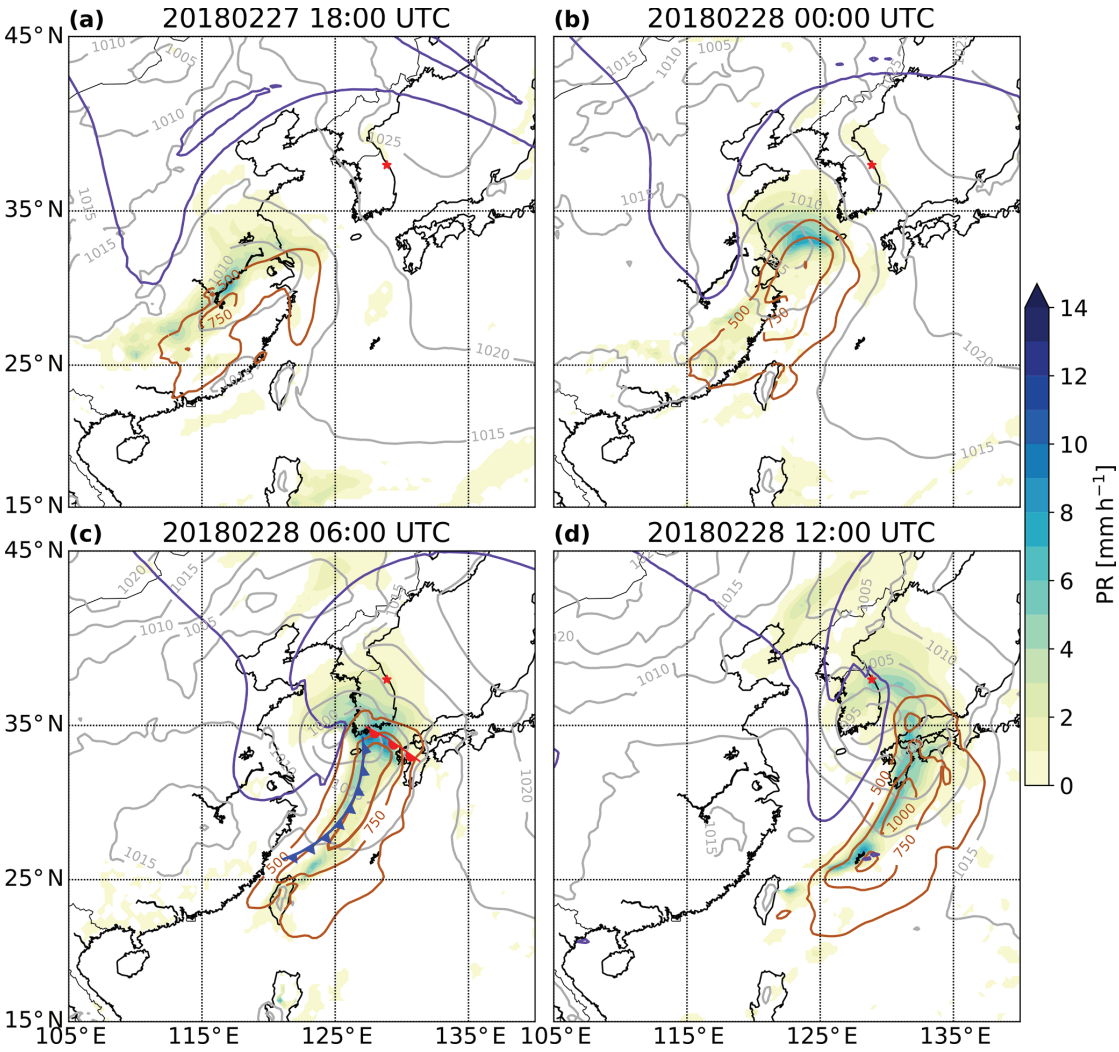

Figure 4.1 – Sea level pressure (grey contours, labels in hPa), dynamical tropopause on the 315 K isentrope (purple lines), IVT (brown contours, labels in $kg\,m^{-1}\,s^{-1}$; only values greater than $500\,kg\,m^{-1}\,s^{-1}$ are shown) and precipitation rate (PR) in $mm\,h^{-1}$ (colour-filled) at **(a)** 18:00 UTC on 27 February 2018 and **(b)** 00:00 UTC, **(c)** 06:00 UTC and **(d)** 12:00 UTC on 28 February 2018 from ERA5 data. The warm and cold fronts at 06:00 UTC were manually drawn based on an analysis of equivalent potential temperature at 850 hPa. The red star shows the location of GWU.

4.3.2 Warm conveyor belt trajectory computation

We define the large-scale WCB ascent over the Korean Peninsula from a Lagrangian perspective as a coherent ensemble of trajectories with an ascent rate of at least 600 hPa in 48 h (*Wernli and Davies*, 1997; *Madonna et al.*, 2014). The 48 h trajectories were computed with the Lagrangian analysis tool LAGRANTO (*Wernli and Davies*, 1997; *Sprenger and Wernli*, 2015) based on the 1-hourly 3D wind field of the hydrostatic model IFS (model version Cy43r3, operational from July 2017 to June 2018; *ECMWF*, 2017). The IFS is run with a spatial resolution of O1280

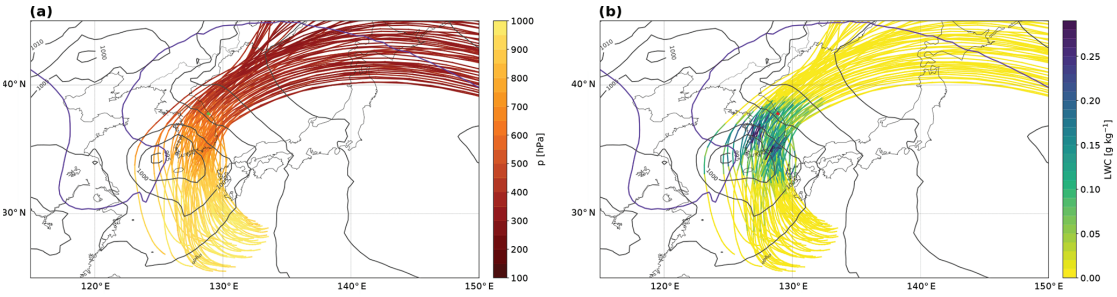

Figure 4.2 – WCB trajectories with an ascent rate of at least 600 hPa in 48 h that are located near the measurement site at 06:00 UTC on 28 February 2018. Colours indicate **(a)** the pressure level and **(b)** the LWC along the WCB air parcels. Also shown are sea level pressure (grey contours, every 5 hPa) and the dynamical tropopause at 315 K (purple). Only the WCB trajectories close to the site (green asterisk in panel **a** and red in panel **b**) are shown.

(approximately 9 km) and 137 vertical hybrid pressure–sigma levels (*ECMWF*, 2017). The IFS dataset combines operational analyses at 00:00, 06:00, 12:00 and 18:00 UTC with hourly short-term forecasts in between. The dataset was interpolated to a latitude–longitude grid with 0.5° spatial resolution for trajectory computation. To analyse the air parcel ascent in the vicinity of the measurement site, we combine 24 h backward and 24 h forward trajectories starting every hour between 00:00 UTC on 27 February and 00:00 UTC on 01 March 2018 every 50 hPa from 1000 to 200 hPa in the proximity of Pyeongchang. WCB trajectories are subsequently selected as trajectories exceeding an ascent rate of 600 hPa in 48 h. In addition to this Lagrangian representation (i.e. following the trajectories), we projected the WCB trajectories in an Eulerian reference frame above Pyeongchang. This gives for each time step and all vertical levels the position of trajectories above Pyeongchang which ascended with ascent rates of at least 600 hPa in 48 h within the period between 00:00 UTC on 27 February and 00:00 UTC on 01 March 2018. This highlights the heights at which WCB air parcels (i.e. with strong ascent at any given time) occur.

4.4 Synoptic overview and WCB

The 28 February 2018 precipitation event is the most intense of the whole ICE-POP 2018 campaign. It contributed 77% of the winter 2018 (December–February) precipitation accumulation. At 18:00 UTC on 27 February 2018 (Fig. 4.1a) a PV streamer (equatorwards excursion of stratospheric air) was located over eastern China and moved eastward towards South Korea. At 00:00 UTC on 28 February 2018 (Fig. 4.1b) a surface cyclone formed in the Yellow Sea east of the upper-level PV streamer. Around 06:00 UTC, the surface cyclone intensified as the PV streamer was approaching (Fig. 4.1c) and became fully developed with a cold front passing to the south of the Korean Peninsula and a warm front passing over Pyeongchang. The interaction between the upper-level PV streamer and the surface cyclone led to a rapid deepening of the cyclone by 25 hPa between 18:00 UTC on 27 February and 12:00 UTC on 28 February. The integrated vapour transport (IVT; *Rutz et al.*, 2014) contours show the strong moisture flux ahead of the

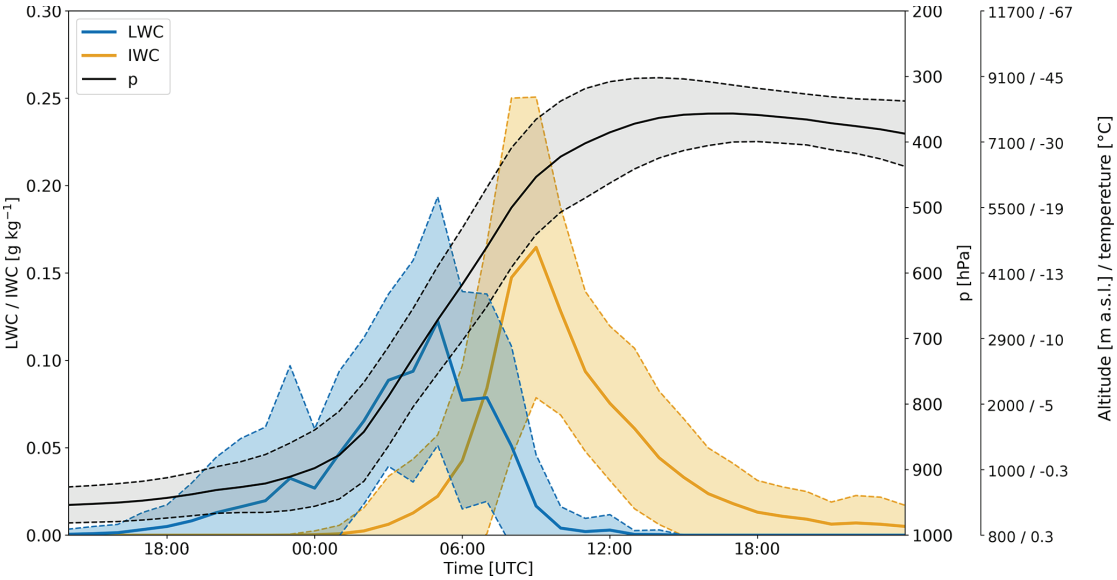

Figure 4.3 – Temporal evolution of LWC (blue line; in g kg^{-1}) and ice water content (IWC; yellow line, in g kg^{-1}) from IFS analyses along the WCB trajectories (black line and grey shading represent the pressure level of the selected trajectories in hPa) shown in Fig. 4.2. Shown are the mean (solid lines) and the standard deviation (dashed lines and shading). The altitudes and temperatures of the pressure levels (second *y* axis on the right) are taken from the radiosounding at 06:00 UTC.

cold front, with the most intense precipitation close to the cyclone centre, where the IVT gradient is the largest. At 12:00 UTC the cyclone moved further east, and the PV streamer was located over Korea, inducing an increasingly easterly flow (Fig. 4.1d). While the Yellow Sea is a known region of cyclogenesis, the cyclone frequency over Korea in winter is less than 2% (*Wernli and Schwierz*, 2006), indicating that such a synoptic situation in winter over Korea is relatively rare.

This intense precipitation event is associated with a WCB that ascended from the boundary layer to the upper troposphere and rose over the Korean Peninsula on 28 February, when the low pressure system was fully developed. Figure 4.2 shows an ensemble of trajectories that are part of the large-scale WCB airstream and that ascended near Pyeongchang at 06:00 UTC on 28 February 2018. The inflow part of the WCB (i.e. upstream of the strong ascent in Fig. 4.2a) is characterised by IVT values greater than 1000 kg m^{-1} s^{-1}, showing that the WCB transported large amounts of water vapour originating from the Yellow Sea. The trajectories rapidly ascended over South Korea, and liquid-water content (LWC) increased along the selected WCB trajectories to above 0.2 g kg^{-1} in the region of strong ascent (Fig. 4.2b). The WCB ascent in the vicinity of the measurement site was relatively fast, with ascent rates of approximately 500 hPa in 12 h (Fig. 4.3). During the relatively strong ascent from the boundary layer to the upper troposphere an extended, mostly stratiform cloud band formed, which was also responsible for the surface precipitation (Fig. 4.4a, c). The WCB transported and formed up to 0.20 g kg^{-1} of liquid water during its strong ascent in the mid-troposphere (Figs. 4.2b and 4.3). The 0 °C

isotherm was higher than 900 hPa during the event. LWC increases along the ascent of the WCB trajectories above 900 hPa (Fig. 4.3). The increase in LWC in supercooled conditions is likely a result of (i) condensation of the water droplets advected from below to above freezing and (ii) nucleation of new droplets at sub-freezing temperatures. To maintain mixed-phase conditions, the depletion of liquid water by the Wegener–Bergeron–Findeisen process has to be compensated by the production of liquid water by dynamical processes (e.g. condensation or nucleation in ascending air masses or advection of water droplets). Following this criterion, *Heymsfield* (1977) showed that for an ascending motion to maintain liquid water, the velocity of ascent has to be greater than a critical vertical velocity. We found that in this event a vertical velocity greater than 0.1 m s^{-1} would form supercooled droplets in the presence of both ice and snow particles (see Appendix B for details of the computation). The ascent rate of the WCB can be estimated from Fig. 4.3 to be 0.2 m s^{-1}. We conclude that the simulated supercooled liquid water (SLW) is a consequence of the strong large-scale ascent in the WCB.

4.5 The evolution of clouds and precipitation over Pyeongchang

In the previous section, we identified SLW associated with large-scale WCB ascents in IFS analyses. In the following, we use remote and in situ observations to corroborate the presence of SLW and to discuss its relevance for the microphysical processes taking place.

Before the onset of precipitation, a temperature inversion at 1500 m (Fig. 4.5a at 00:00 UTC) favours the formation of a low-level cloud (Fig. 4.4a). This temperature inversion is located just above a layer of potential instability with equivalent potential temperature (θ_e) gradients of about −10 K km^{-1} between 1250 and 1450 m. Other layers of potential instability are present below 3000 m (with θ_e-gradients up to −5 K km^{-1}) for all three radiosoundings at 00:00, 06:00 and 09:00 UTC. Above 3000 m, the air is saturated or close to saturation with respect to ice (Fig. 4.5b at 00:00 UTC). At 06:00 and 09:00 UTC, the air is saturated with respect to ice over almost the entire troposphere. Between 6000 and 9000 m, the relative humidity with respect to ice (RH_i) is well above saturation at 00:00, 06:00 and 09:00 UTC. This altitude range corresponds to the outflow of WCB air masses (Fig. 4.3), which often features cirrus clouds (*Madonna et al.*, 2014). These cirrus clouds in the WCB outflow are likely composed of both ice crystals formed by freezing of liquid droplets in the WCB ascent and ice crystals formed via nucleation directly from the vapour phase in upper tropospheric air masses pushed upwards by the WCB (*Wernli et al.*, 2016). This suggests that the high supersaturation with respect to ice above 6000 m is directly related to the WCB. In this view, the WCB provides favourable conditions for rapid crystal growth, leading to precipitation onset. The profile of wind speed clearly shows a strong jet of 45 m s^{-1} at 6500 m a.s.l. at 06:00 UTC (Fig. 4.5c), which coincides with the WCB air masses. The height of this jet and the lower limit of WCB air masses decrease with time, and we observe the jet just below 5000 m at 09:00 UTC.

In the layer from 4000 to 6000 m a.s.l. at 06:00 UTC an increase in wind speed with height and a rapid change in the wind direction from southerly to south-westerly result in strong vertical

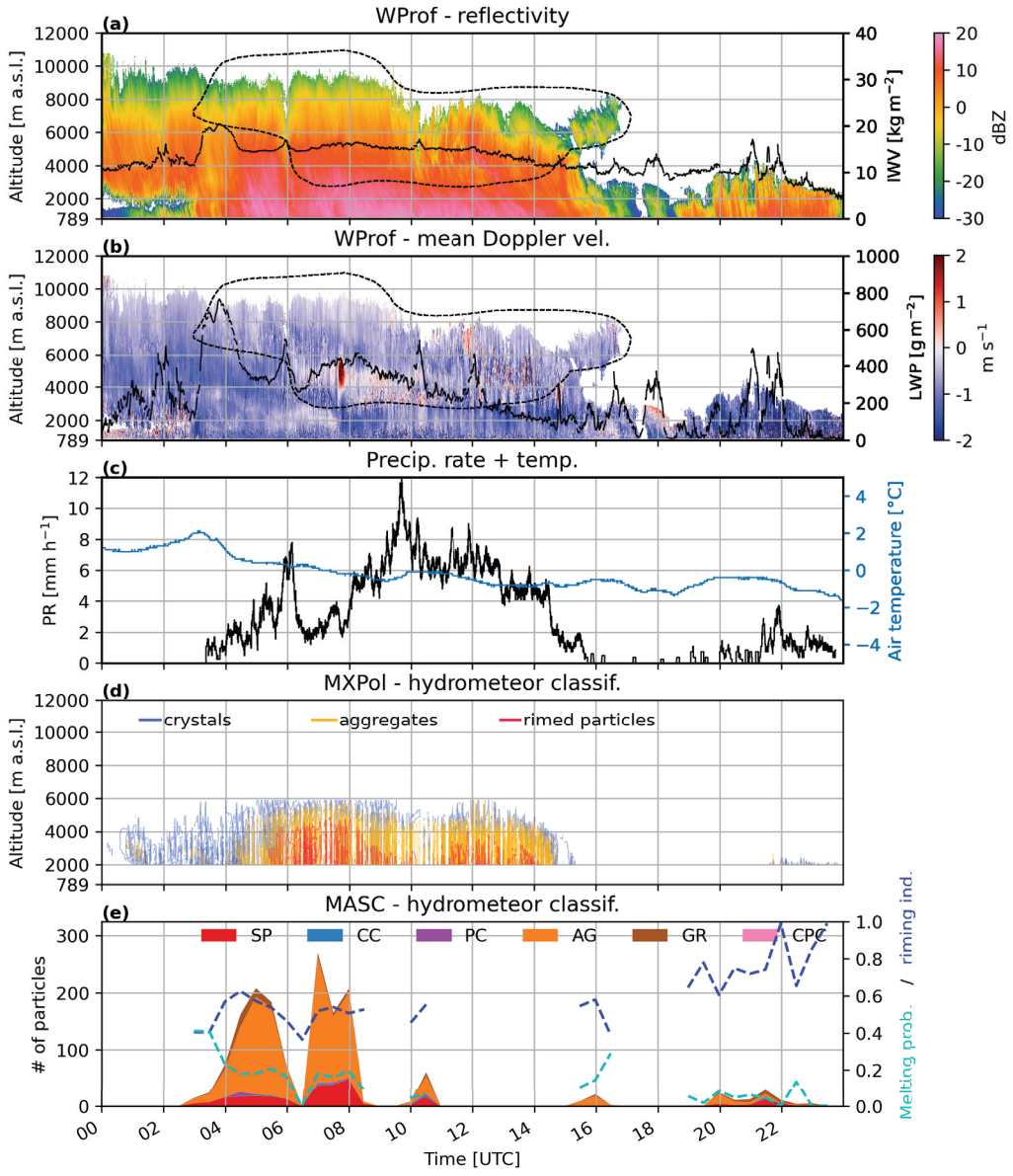

Figure 4.4 – Time series on 28 February 2018 of (a) reflectivity and IWV, (b) mean Doppler velocity (defined positive upwards) and LWP from WProf, (c) precipitation rate (PR) and air temperature at MHS, and (d) hydrometeor classification from MXPol (see Sect. 2.4.1). The isolines represent the proportion of each hydrometeor class normalised by the average number of pixels per time step (contour interval is 2%). (e) Hydrometor classification from the MASC, melting probability, and riming index (see Sects. 2.3.3 and 2.4.2). The periods 08:30–09:30 UTC and 11:00–15:00 UTC are missing data, because the cameras were covered with rime. The dashed contour on panels (a) and (b) shows the boundary of the WCB based on the projection of the trajectories in an Eulerian reference frame (see Sect. 4.3.2).

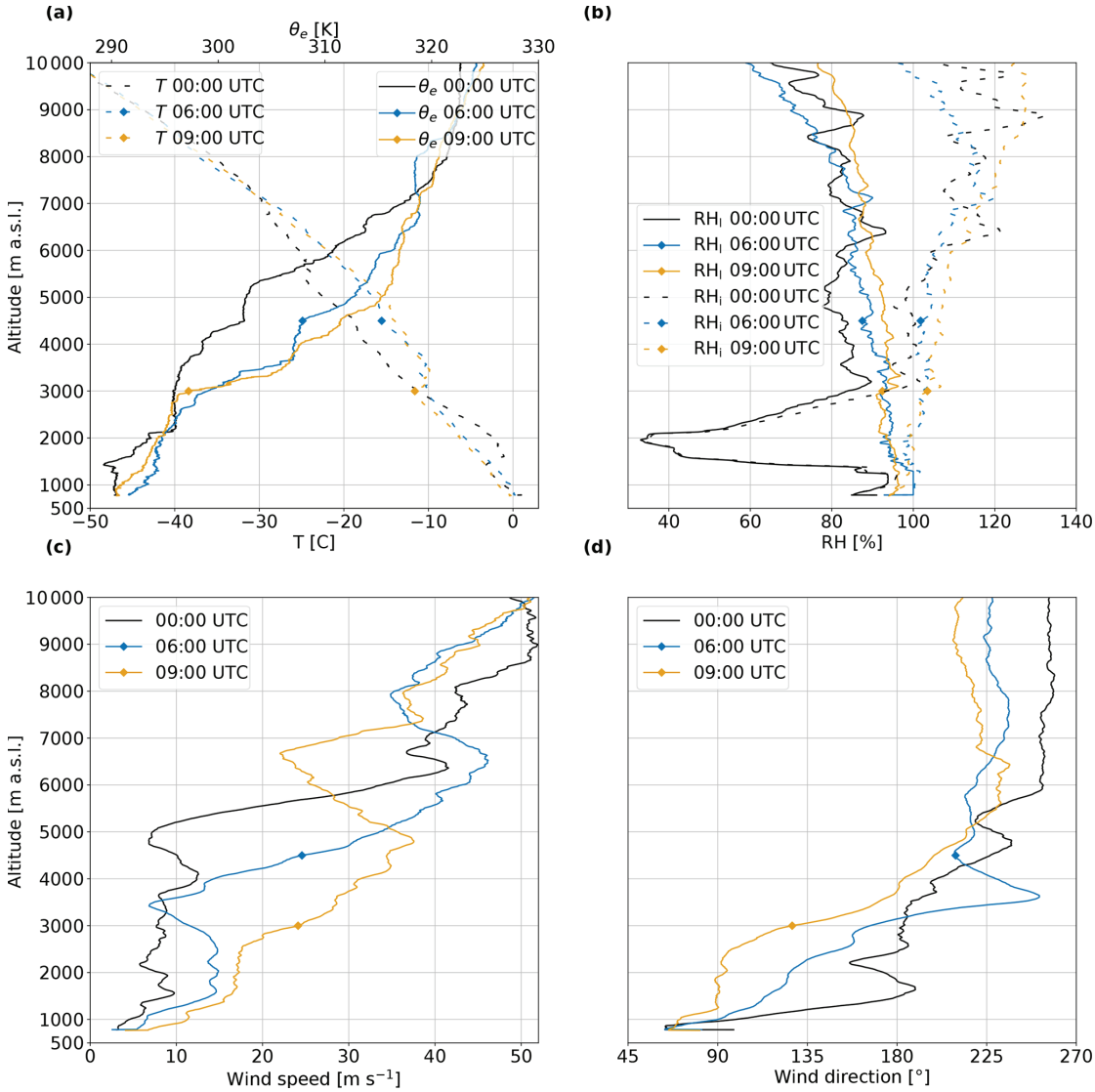

Figure 4.5 – Radiosoundings at the DGW station showing **(a)** temperature (dashed lines) and equivalent potential temperature (solid lines); **(b)** relative humidity with respect to liquid (RH_l; solid lines) and ice (RH_i; dashed lines); **(c)** wind speed; and **(d)** wind direction at 00:00 UTC (black), 06:00 UTC (blue) and 09:00 UTC (yellow) on 28 February 2018. The diamond symbols for the radiosoundings at 06:00 and 09:00 UTC show the altitude of the lower limit of the WCB (dashed contour in Fig. 4.4a, b).

wind shear. The vertical wind shear reaches values of 15 m s^{-1} km^{-1} in speed and 0.27 ° m^{-1} in direction. *Keppas et al.* (2018) identified similar values of vertical wind shear, which triggered Kelvin–Helmholtz instabilities. In Sect. 4.6.3, we illustrate the influence of this vertical wind shear within the WCB ascent region on the observed microphysics.

Figure 4.4a shows the reflectivity measured by WProf. The nimbostratus cloud approaches between 00:00 and 03:00 UTC. The cloud base is at 3100 m (Fig. 4.5b), but virgae appear down to 2000 m, where ice crystals sublimate in unsaturated air. Below the temperature inversion at 1400 m the air is close to saturation (Fig. 4.5a, b at 00:00 UTC), and a low-level cloud can be identified as a layer with reflectivity values below −5 dBZ. At 03:00 UTC surface precipitation starts and lasts until 16:00 UTC (Fig. 4.4c). A 3D gridding of the WCB trajectory positions (Fig. 4.4,a, b, dashed contour) reveals that WCB air parcels continuously ascend above the location of WProf during the entire passage of the nimbostratus cloud. At 19:00 UTC a post-frontal precipitating system sets in and lasts until 00:00 UTC on 01 March. The bimodality introduced as an example in Chap. 1 (Fig. 1.6) correlates well with the peak in LWP at 21:00 UTC (Fig. 4.4b) and is likely due to SLW in these post-frontal showers.

Within the WCB ascent regions, enhanced updraughts are present, in particular around 3000 m a.s.l. between 07:00 and 10:00 UTC (Fig. 4.4b). These overturning cells at the lower boundary of the WCB (represented by the dashed contour) are likely Kelvin–Helmholtz instabilities generated by the strong vertical wind shear observed in the radiosoundings (Fig. 4.5). Except for a moist neutral layer around 4000 m at 06:00 UTC, the profiles at 06:00 and 09:00 have stable lapse rates, which together with a strong wind shear provide favourable conditions for Kelvin–Helmholtz instabilities. A region of enhanced positive Doppler velocity can be observed from 07:30 to 08:00 UTC between 4000 and 6000 m, where the mean Doppler velocity amounts to approximately 2 m s^{-1}, indicating the presence of embedded updraughts in the WCB. Recently, case studies by *Keppas et al.* (2018), *Oertel et al.* (2019) and *Oertel et al.* (2020) identified embedded convection within the large-scale WCB. *Oertel et al.* (2019) and *Oertel et al.* (2020) showed that embedded convection leads to a local increase in precipitation intensity, while *Oertel et al.* (2020) found that it also promotes the formation of graupel particles in the model simulations. Finally, *Hogan et al.* (2002) observed that embedded convection was collocated with maxima of SLW concentration. In this chapter, we refer to these upward air motions as embedded updraughts since there is no evidence of convective instability in the radiosoundings (Fig. 4.5a). While the cause of the updraughts we observe might be different than those mentioned in *Hogan et al.* (2002), *Keppas et al.* (2018) and *Oertel et al.* (2019), the consequence for the precipitation growth processes is consistent with what we observe in this study.

Ahead of the precipitating system, the cloud contains mainly crystals (Fig. 4.4d). Intense precipitation begins around 04:30 UTC, and aggregates dominate during the whole precipitation period. Rimed particles are also present, especially between 06:00 and 08:00 UTC, when the proportion and vertical extent of rimed particles are the largest. These periods with significant rimed particles correlate well with the LWP and riming index (Fig 4.4b,e). The fact that the

MASC classification contains almost no graupel particles is because other classes can contain significant riming, as shown by the high riming index.

The maxima of LWP observed when precipitation starts just before 04:00 UTC and the peak at 06:00 UTC corresponding to the local maximum of precipitation rate (Fig. 4.4c) are probably due to the partial melting of hydrometeors since the temperature at MHS is above 0 °C. The multiple peaks after 07:00 UTC (temperature drops below freezing), which co-occur with updraughts, suggest that the updraughts favour the production of SLW in addition to the SLW produced by the large-scale ascent in the WCB. There was unfortunately no CALIPSO (satellite on-board lidar) overpass to ascertain the presence of SLW during the event. There is a local maximum in the precipitation rate just after 06:00 UTC (Fig. 4.4c), while the absolute maximum is about 12 mm h^{-1} at 09:40 UTC. Note that the surface warm front never reached Pyeongchang (only the precipitation associated with it) but moved further to the east. Hence, in contrast to the temperature in the mid-troposphere, which increased by approximately 5 to 10 °C (Fig. 4.5a) during the event, the surface temperature did not increase.

4.6 Microphysial analysis of periods of interest

In the previous section, we analysed the evolution of the dynamics and microphysics of the nimbostratus and precipitation associated with the warm front. In this section, we analyse succeeding periods that reveal the link between the temporal evolution of the WCB and the microphysics over Pyeongchang. Based on the homogeneity of the dominant microphysical processes, three different periods were selected: we first investigate the period dominated by depositional growth of crystals (Sect. 4.6.1) and subsequently analyse the effect of embedded updraughts on aggregation and riming (Sect. 4.6.2). Finally, we consider the impact of vertical wind shear and turbulence on aggregation (Sect. 4.6.3).

4.6.1 Vapour deposition: 03:00 to 04:00 UTC

The period from 03:00 to 04:00 UTC is dominated by crystals above 2000 m (Fig. 4.4d). At this time Pyeongchang is located ahead of the warm front. The vertical profiles of polarimetric variables (Fig. 4.6) show an increase in Z_H of 2 dBZ from 6000 to 2000 m, while Z_{DR} is almost constant from 6000 to 3000 m and then subsequently decreases slightly. This likely indicates the onset of aggregation at 3000 m, below which temperatures are greater than −10 °C and hence represent favourable conditions for aggregation (*Hobbs et al.*, 1974). K_{dp} values are almost zero, suggesting that the number concentration of non-spherical crystals is low. In summary, this period is characterised by the presence of crystals in limited concentration, which grew by vapour deposition and likely aggregated below 3000 m.

The selection of snowflake images (Fig. 4.7b; collected at an average temperature of 1.5 °C) mainly shows small aggregates and crystals of about 2 mm in their maximum dimension. They are partly melted (liquid water is less reflective than ice and creates the dark areas on

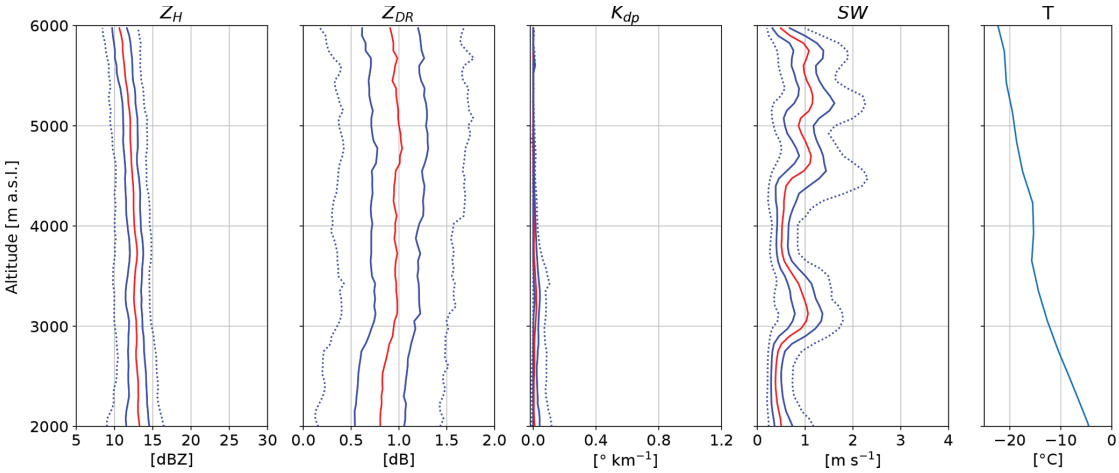

Figure 4.6 – Vertical profiles of quantiles of Z_H, Z_{DR}, K_{dp} and SW from MXPol from 03:00 to 04:00 UTC on 28 February 2018. The red line shows the median, while the solid blue lines show the 25th and 75th percentiles and the dotted blue lines the 5th and 95th percentiles. The statistics are based on 11 RHIs towards the MHS site. The data within a horizontal distance of 7 to 20 km from MXPol are selected.

the snowflake pictures), and riming is indicated by the brighter areas. The size distribution shows that most particles are below 5 mm in size, with a median of 2.2 mm. The classification shows that 64% of the observed hydrometeors are aggregates, while above 2000 m, the MXPol hydrometeor classification shows predominantly ice crystals (Fig. 4.4d). This supports our previous conclusion that below 3000 m, when the temperature increases and aggregation is more efficient, a large fraction of crystals aggregate. A total of 7% of particles were identified as graupel (Fig. 4.7b), which we could confirm by visual analysis. Again the riming could have taken place below 2000 m, which explains why no rimed particles are present from 03:00 to 04:00 UTC in the MXPol hydrometeor classification of Fig. 4.4d. Figure 4.8a shows the distribution of the riming index (0 = no riming; 1 = graupel; *Praz et al.*, 2017). The mode around 1 corresponds to the graupel particles, while half of the particles had a riming index smaller than 0.4. This shows that except for the few graupel particles, the other hydrometeor classes did not feature significant riming in comparison with other periods of the event.

4.6.2 Embedded updraughts, riming and aggregation: 06:00 to 08:00 UTC

The period from 06:00 to 08:00 UTC is characterised by embedded updraughts (Fig. 4.4b), a layer with strong vertical wind shear at 3800 m (Fig. 4.5c, d), and significant riming, as seen by MXPol (Fig. 4.4d). From 6000 to 4800 m the crystals grow by vapour deposition, leading to an increase in both Z_H and Z_{DR} (Fig. 4.9) as particles grow mainly along their longest dimension, which results in larger and more oblate crystals (*Schneebeli et al.*, 2013; *Andrić et al.*, 2013; *Grazioli et al.*, 2015b). The median of K_{dp} increases to only 0.4 °km^{-1}, suggesting that the number concentration of oblate particles is small. The temperature in this layer varies from −23 °C to −16 °C, and the air is slightly above saturation with respect to ice (Fig. 4.5a, b).

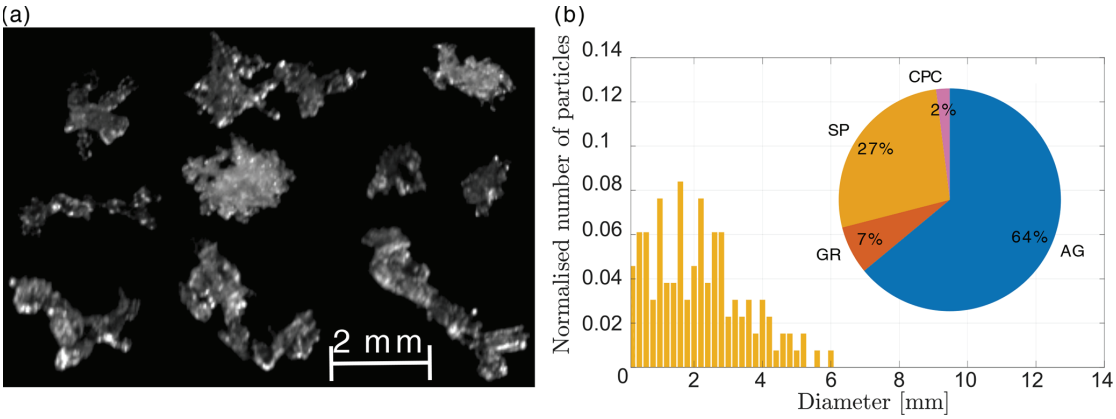

Figure 4.7 – **(a)** Selection of in-focus MASC images. **(b)** Normalised size distribution and classification of 55 particles observed from 03:00 to 04:00 UTC. SP represents small particles, CC columnar crystals, PC planar crystals, AG aggregates, GR graupel, and CPC a combination of planar and columnar crystals. The size distribution is normalised by the number of particles. The pictures of panel **(a)** were selected to be representative of the classification. The average temperature was 1.5 °C (Fig. 4.4c).

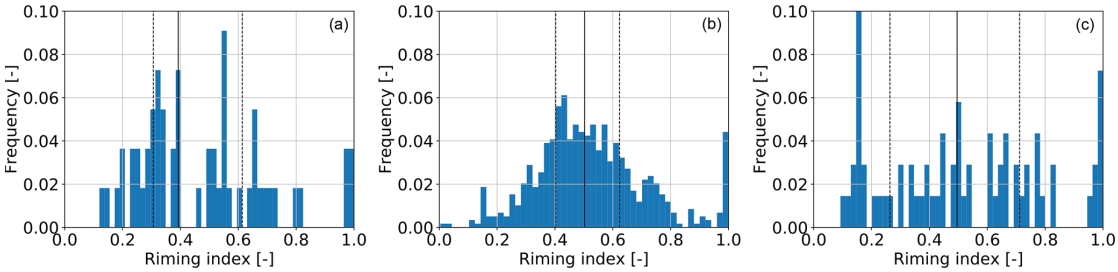

Figure 4.8 – Distribution of the riming index for all particles between **(a)** 03:00 and 04:00 UTC, **(b)** 06:00 and 08:00 UTC, and **(c)** 09:00 and 11:00 UTC. The dashed lines show the lower and upper quartiles; the solid line shows the median of the distribution.

This represents favourable conditions for depositional growth of sectored plates (*Lohmann et al.*, 2016; Fig. 8.15), while aggregation is unlikely to dominate within this temperature range according to *Hobbs et al.* (1974). However, we cannot rule out the formation of early aggregates, which at this stage would be oblate and hence contribute to the increase in Z_{DR} (*Moisseev et al.*, 2015).

At 4800 m we observe a peak and subsequent decrease in Z_{DR}, which marks the end of growth dominated by vapour deposition. We hypothesise that aggregation starts at this altitude. First, snowflakes tend to be less oblate and less dense after aggregation, which explains the decrease in Z_{DR}. Second, aggregation increases the size of snowflakes, and hence Z_H continues to increase. The observed increase in K_{dp} below the peak in Z_{DR} is a commonly observed but not fully understood feature. *Andrić et al.* (2013) proposed that secondary ice generation of small oblate crystals could explain the observed enhanced K_{dp} values. The concentration of secondary ice particles can be much larger than the number of snowflakes they originate

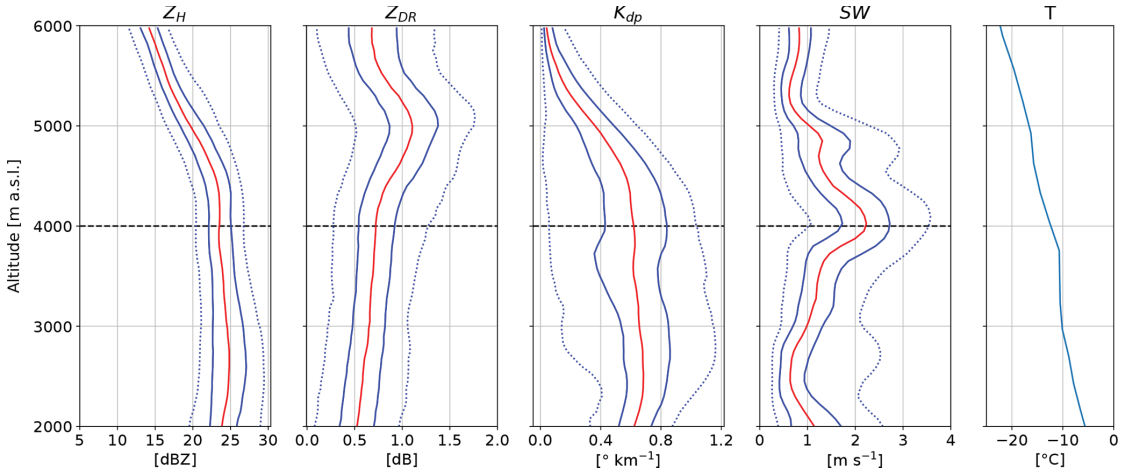

Figure 4.9 – Same as Fig. 4.6 for 06:00 to 08:00 UTC on 28 February 2018. The statistics are based on 21 RHIs towards the MHS site. The dashed black line shows the lower limit of the WCB (dashed contour in Fig. 4.4a, b).

from, which would affect K_{dp} more strongly than Z_{DR} since the former is more sensitive to concentration. *Moisseev et al.* (2015) suggested that it is the result of the onset of aggregation, producing early aggregates that are relatively oblate. Our hypothesis is that first, the generation of secondary ice by droplet shattering (*Mason and Maybank*, 1960) and by ice–ice collisions (*Vardiman*, 1978; *Takahashi et al.*, 1995; *Yano and Phillips*, 2011) contribute to the increase in K_{dp} below 5000 m a.s.l. Droplet shattering shows a maximum occurrence at −17 °C (*Leisner et al.*, 2014), which corresponds to the altitude where LWC is converted into ice water content (Fig. 4.3 around 5000 m a.s.l.). Secondary ice generation by ice–ice collision is most effective at −15 °C (*Takahashi*, 1993) and may also take place at around 5000 m a.s.l. Second, riming of already-oblate crystals will tend to increase K_{dp} because in the early stage of riming the cavities in the crystals are filled, increasing the density (and thus the dielectric response) of the hydrometeors without changing their aspect ratio. Third, rime splintering by the Hallett–Mossop process (*Hallett and Mossop*, 1974) below 2500 m a.s.l. (temperature above −8 °C) can contribute maintaining high K_{dp} values. Finally, *Korolev et al.* (2020) recently suggested that secondary ice produced by shattering of freezing droplets transported above the melting layer could be lifted to higher levels. This may enhance the concentration of secondary ice in regions of strong updraughts. Note that the higher K_{dp} values compared to the period 03:00–04:00 UTC are primarily due to the increase in precipitation intensity, but the fact that K_{dp} increases below the onset of aggregation cannot be explained by precipitation intensity only since aggregation decreases the number concentration and the oblateness of the particles. Riming will initially increase K_{dp} by first filling cavities and hence increasing the density of particles but will later lead to a decrease in K_{dp} as the rime mass will smooth the particles' shape. There has to be a mechanism that produces a high number concentration of oblate particles to explain an increase in K_{dp} in a layer dominated by aggregation and riming, and secondary ice production is a good candidate.

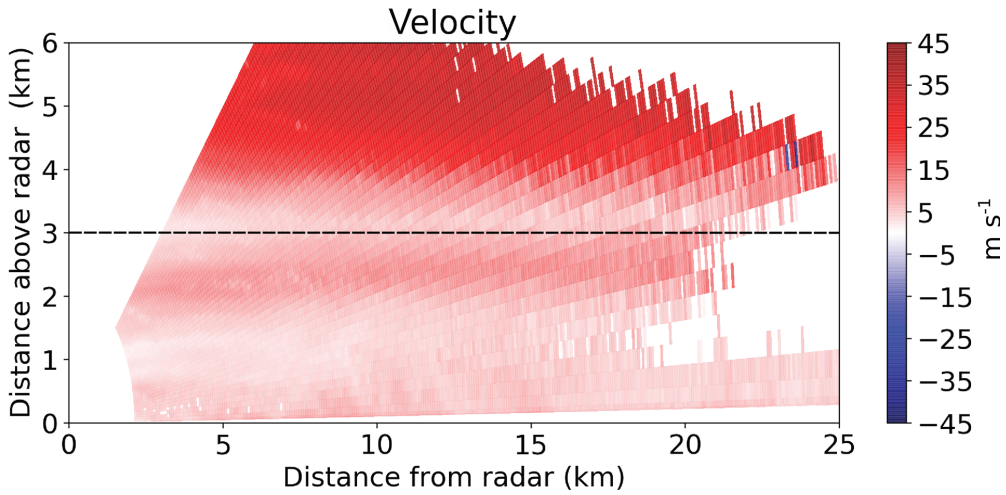

Figure 4.10 – RHI of Doppler velocity at 11° azimuth at 06:25 UTC from MXPol radar. The dashed black line shows the lower limit of the WCB (dashed contour in Fig. 4.4a, b).

At 3800 m a strong vertical wind shear in the lower part of the WCB (dashed contour in Fig. 4.4a, b at 06:00 UTC) can be observed in both the radiosoundings (Fig. 4.5c, d) and the spectral width profiles (Fig. 4.9). The jet at 6500 m at 06:00 UTC (Fig. 4.5c) can be seen as an enhancement of Doppler velocity between 4000 and 6000 m a.s.l., with a maximum of 45 m s^{-1} at 5000 m in the RHI of Fig. 4.10. This is in good agreement with the wind speed measured by the radiosonde at 06:00 UTC since the RHI is almost aligned with the wind direction. The vertical wind shear at 3800 m is visible as the Doppler velocity decreases in the lower part of the WCB and reaches a value of 0 m s^{-1} at 3000 m (combined effect of a decrease in wind speed and change in wind direction from parallel to perpendicular to the radar beam). This vertical wind shear may generate Kelvin–Helmholtz instabilities, which can trigger embedded convection (*Hogan et al.*, 2002). Moreover, orography might also play a role in lifting the easterly low-level flow, which directly impinges the Taebaek mountains from the East Sea. These sources of lifting together with the moist neutral layers below 3000 m (Fig. 4.5a) can lead to the observed strong updraughts (Fig. 4.4b), which promote aggregation by increasing the time particles are suspended in the air (*Garrett*, 2019). The effect of turbulent cells on aggregation has been discussed thoroughly in *Houze and Medina* (2005), *Medina et al.* (2005), and *Medina and Houze* (2015). *Houze and Medina* (2005) suggested that overturning cells promote both aggregation and riming. First, they can sustain the production of SLW necessary for riming. Second, turbulence increases the probability of collision between particles. Finally, aggregates are larger targets for the collection of SLW droplets, which again enhances growth by riming. While the cause of the turbulence is different here, the processes described are consistent with our measurements.

The MASC images (Fig. 4.11a) show mainly rimed aggregates of about 10 mm in their maximum dimension and two graupel particles. The average temperature of collection was 0.1 °C, and hence the particles should not be as melted as during the period 03:00–04:00 UTC. The

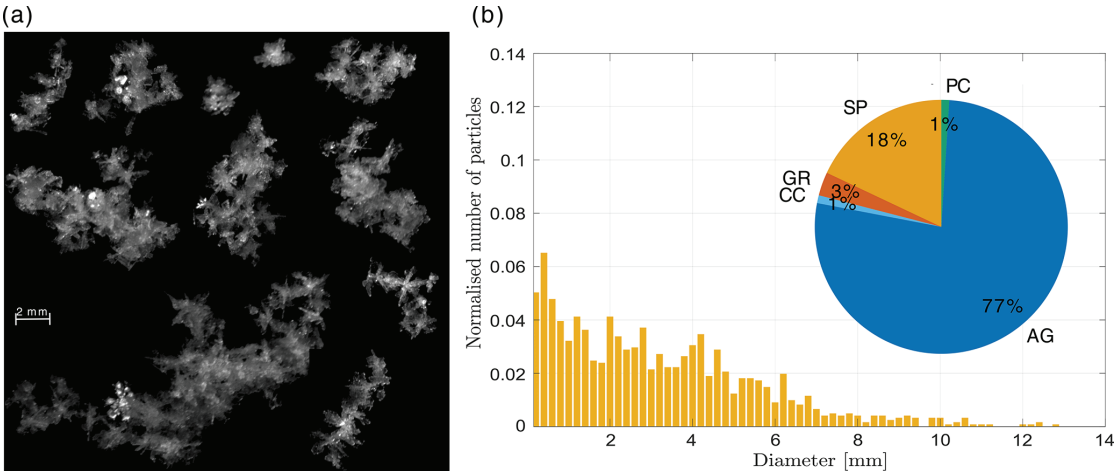

Figure 4.11 – Same as Fig. 4.7 for the period 06:00 to 08:00 UTC. The number of particles is 589. The average temperature is 0.1 °C (Fig. 4.4c).

classification shows a majority of aggregates (77%). The hydrometeor classification from *Besic et al.* (2018) classifies rimed aggregates and graupel as rimed particles, whereas the MASC-based classification from *Praz et al.* (2017) classifies only fully rimed particles as graupel, and the aggregate class also contains rimed aggregates. Therefore a direct comparison of the class aggregates between the two classification methods is difficult. The size distribution is much broader than from 03:00 to 04:00 UTC, with particles reaching 13 mm in their maximum dimension. The median amounts to 2.8 mm as there is still a significant proportion of small particles. The total number of particles is 589, while it was 55 in the previous period, showing that this period features more intense precipitation, which also makes the empirical size distribution more robust. The 75th percentile is 4.7 mm compared to 3.0 mm for the period 03:00 to 04:00 UTC, showing that the particles from 06:00 to 08:00 UTC are significantly larger. These large rimed aggregates can be attributed to the strong updraughts, which enhance the growth by aggregation and riming. Note that while the previous period (Sect. 4.6.1) featured riming below 2000 m, the precipitation rate was much smaller than from 06:00 to 08:00 UTC (Fig. 4.4c), and hence this riming did not contribute significantly to the total precipitation accumulation. The important message here is that the flow conditions in the WCB promoted rapid precipitation growth by aggregation and riming above 2000 m and are thus responsible for the large precipitation accumulation between 06:00 and 08:00 UTC. Moreover, most of the particles have higher quartiles of riming index (Fig. 4.8b) than between 03:00 and 04:00 UTC despite the lower proportion of graupel, which is due to the enhanced aggregation favouring rimed aggregates at the expense of pure graupel. We conclude that this period features the most riming both in absolute mass and in relative terms over all hydrometeor classes.

Figure 4.12 shows a range spectrogram from WProf averaged from 07:42 to 07:47 UTC and from 07:57 to 08:02 UTC. The updraught present in Fig. 4.4b can be seen as a strong shift in the mode of the spectrum from about $-0.5\,\mathrm{m\,s^{-1}}$ at 6000 m to above $2\,\mathrm{m\,s^{-1}}$ at 5000 m (Fig. 4.12a). This updraught goes along with strong turbulence, which is visible as an increase in spectral

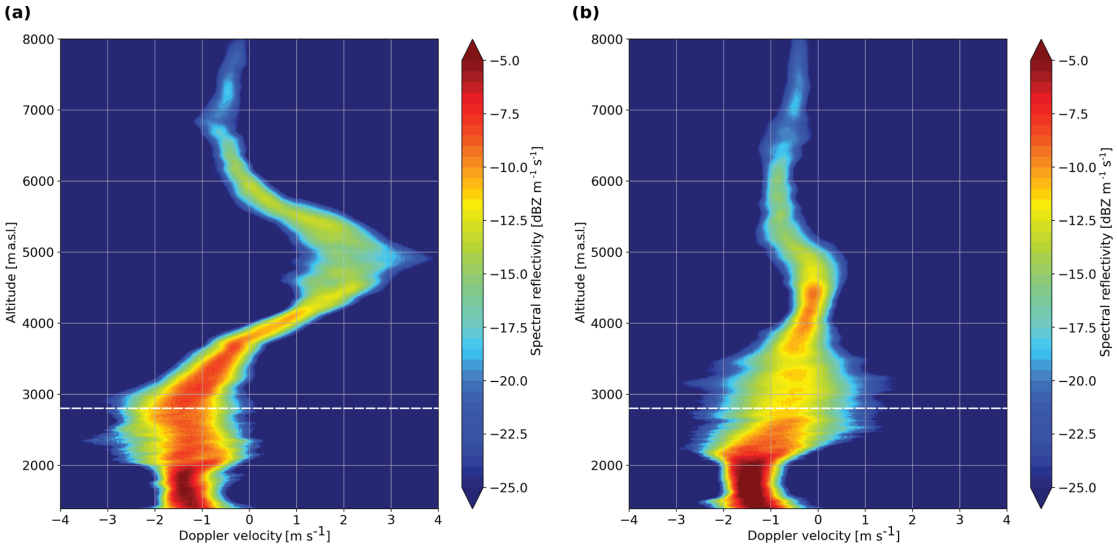

Figure 4.12 – Range spectrogram from WProf averaged **(a)** from 07:42 to 07:47 UTC and **(b)** from 07:57 to 08:02 UTC. Positive velocity values represent upward motions. The dashed white line shows the lower limit of the WCB (dashed contour in Fig. 4.4a, b).

width between 4000 and 6000 m. By 07:57 UTC (Fig. 4.12b), the increase in spectral reflectivity together with a decrease in Doppler velocity from 4800 to 4000 m suggests that large aggregates likely formed in the turbulent layer and further aggregate during their fall. This is consistent with the onset of aggregation below 5000 m observed in Fig. 4.9. The enhanced aggregation in the updraughts present from around 07:30 to 08:00 UTC leads to an increase in precipitation rate from 07:55 UTC to the maximum at 09:40 UTC (Fig. 4.4c). Particles that started falling between 4000 and 5000 m will take 85–105 min to fall to the ground, with an average effective fall speed (absolute fall speed plus updraught) of 0.8 m s^{-1}. This is consistent with the increase in precipitation intensity from 07:55 to 09:40 UTC, and the maximum could correspond to aggregates that formed in the updraught between 07:35 and 07:55 UTC. This hypothesis assumes a certain horizontal homogeneity, supported by the increase in precipitation in both rain gauge measurements at MHS (Fig. 4.4c) and GWU (not shown) that are separated by 19 km. It would imply that the embedded updraughts are responsible for the period of strongest precipitation, which also features intense riming (Fig. 4.4c), consistent with the suggestion in *Oertel et al.* (2019, 2020).

4.6.3 Shear-induced turbulence: 09:00 to 11:00 UTC

The period from 09:00 to 11:00 UTC features turbulence and intense precipitation rates (Fig. 4.4b, c). Due to a malfunction of the MASC, only pictures between 10:08 and 10:50 UTC were collected, leading to only 69 particles during this period (Fig. 4.13). There are substantially more crystals (10%) than during the other periods. Figure 4.13a shows a few small aggregates, columnar and planar crystals, and one graupel particle. The median of the size distribution is 2.7 mm, and the 75th and 95th percentiles are 3.9 mm and 6.6 mm, respectively, indicating

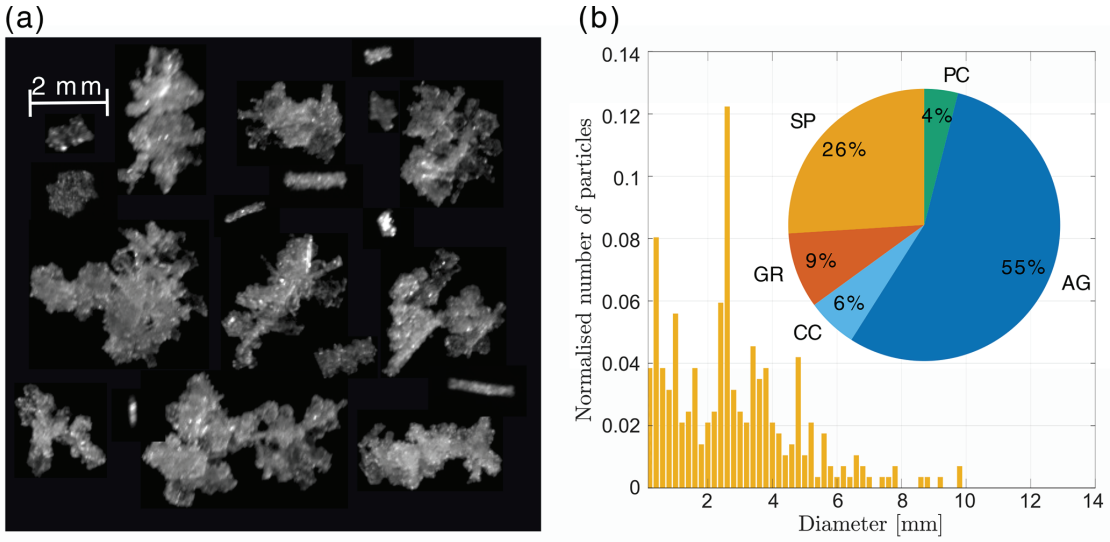

Figure 4.13 – Same as Fig. 4.7 for the period 10:00 to 11:00 UTC. The number of particles is 69. The average temperature is 0.0 °C (Fig. 4.4c).

that the particles are smaller than in the previous period. Figure 4.14 shows a less pronounced increase in Z_{DR} compared to the period between 06:00 and 08:00 UTC (Fig. 4.9), suggesting that the depositional growth rate is smaller than during the previous period. The median of Z_{DR} increases to 0.7 dB around 4200 m, where crystals and aggregates probably dominate. The median of Z_H reaches a maximum of 22 dBZ at 2000 m compared to 25 dBZ at 06:00–08:00 UTC (Fig. 4.9). This is consistent with the size distribution (06:00–08:00 UTC in Fig. 4.11) that shows more large particles than Fig. 4.13. Below 4200 m, larger aggregates start to form as temperatures exceed −15 °C and Z_{DR} decreases slightly. It is collocated with the increase in spectral width (Fig. 4.14), reflecting the vertical wind shear below the maximum wind speed (Fig. 4.5c) at 09:00 UTC. The shear layer was between 4000 and 5000 m in the period from 06:00 to 08:00 UTC, while it is now between 3000 and 4000 m. This vertical wind shear is collocated with the turbulent cells observed in Fig. 4.4b from 08:00 to 10:00 UTC around 4000 m, which suggests that they originate from Kelvin–Helmholtz instabilities. This is supported by values of the gradient Richardson number (not shown here) of 0.2 where the turbulent cells are present. The decrease in the height of the wind shear is consistent with the decrease in the height of maximum wind speed between 06:00 and 09:00 UTC (Fig. 4.5c) and explains why the altitude of aggregation enhancement by turbulence decreases with time. This was also observed by *Keppas et al.* (2018), who attributed this altitude decrease in the maximum wind speed to the passage of the warm front. On the other hand, the altitude of the onset of aggregation could increase with time as the warm front passes because the altitude of the −15 °C isotherm (relative maximum aggregation in *Hobbs et al.*, 1974) is higher at 09:00 UTC than at 06:00 UTC. Our interpretation is that the enhancement of aggregation by turbulence dominates the polarimetric signatures in our case: first, because crystals were likely growing as sectored plates and not as dendrites, the latter being more effective to aggregate at −15 °C, and second, because the intense aggregation taking place in the shear layer leads to larger aggregates than the early

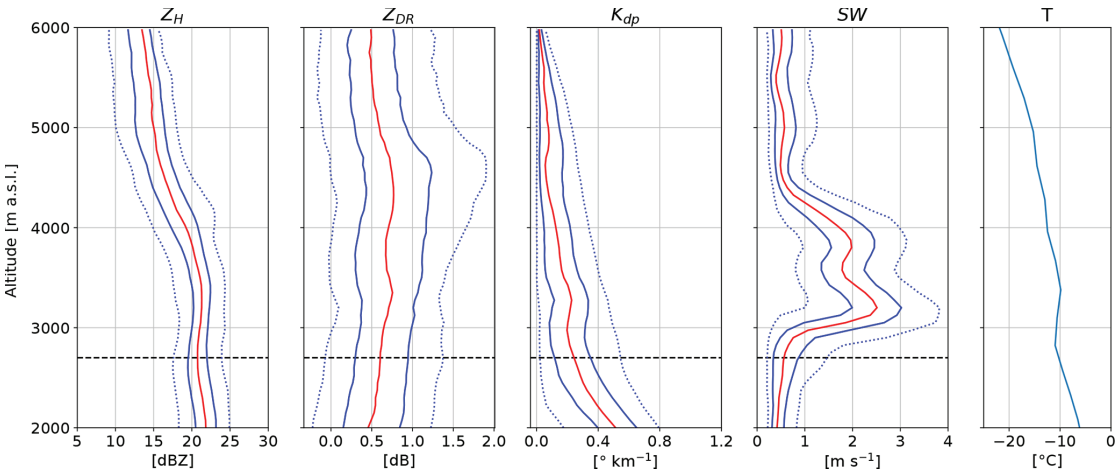

Figure 4.14 – Same as Fig. 4.6 for 09:00 to 11:00 UTC on 28 February 2018. The statistics are based on 20 RHIs towards the MHS site. The dashed black line shows the lower limit of the WCB (dashed contour in Fig. 4.4a, b).

aggregation at −15 °C, which makes the former more visible in the polarimetric profiles. The distribution of the riming index (Fig. 4.8c) is broader than for the other periods due to the higher proportions of crystal-like particles and the presence of graupel and rimed aggregates.

4.7 A conceptual model

The findings of this case study can be summarised in a conceptual model (Fig. 4.15). As the WCB rises from the boundary layer, the air saturates, and the liquid-water droplets eventually become supercooled. If the ascent rate is strong enough (which is the case for most WCBs; see Sect. 4.4), SLW can be produced and persist to the mid-troposphere. Crystals grow by vapour deposition at upper levels of the WCB ascent (see $\mathrm{RH}_i > 110\%$ in Fig. 4.5b), leading to an increase in Z_H and Z_{DR}. During their fall, they experience riming by accretion of supercooled droplets. Moreover, the vertical wind shear (large SW) at the lower boundary of the WCB creates turbulence, which enhances aggregation by increasing the probability of collision between hydrometeors. Furthermore, embedded updraughts in the WCB (as seen by positive vertical Doppler velocities) can additionally lift precipitating particles and increase their time for growth by aggregation. Finally, aggregates are larger targets for the collection of SLW, which enhances riming. This leads to large rimed aggregates and local peaks in precipitation intensity. In the layer of growth by aggregation and riming, Z_H increases, while Z_{DR} decreases. Additionally, the generation of secondary ice by droplet shattering and ice–ice collision leads to an increase in K_{dp}. In the outflow region of the WCB, crystals, which formed either by nucleation from the vapour phase or freezing of the remaining supercooled droplets, fall and may aggregate without significant riming. While this conceptual model is built upon a single case study, we postulate that the key processes, which are the production of SLW and the turbulence enhancing riming and aggregation, can take place in most wintertime mid-latitude

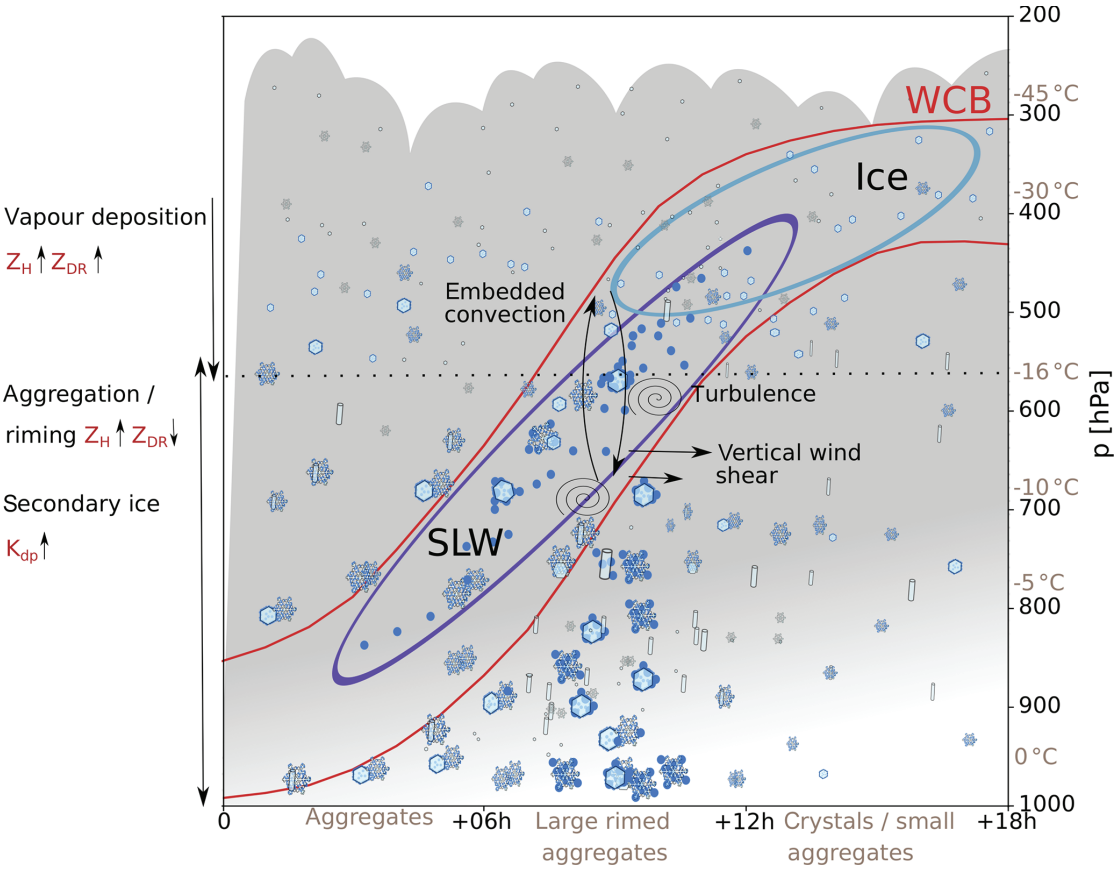

Figure 4.15 – Conceptual model in a Lagrangian reference frame (i.e. along the WCB) summarising the key findings. The temperature indications come from the radiosounding at 06:00 UTC (Fig. 4.5a). The time is indicated as hours from the start of the ascent. The ascent is representative of a strong wintertime WCB.

cyclones featuring a strong WCB.

4.8 Conclusions

This study investigates the snowfall microphysics associated with a WCB during an extreme wintertime precipitation event in South Korea. We combined Doppler dual-polarisation radar measurements, snowflake photographs and radiosonde data with IFS data and trajectories to characterise the detailed precipitation growth mechanisms associated with the large-scale WCB ascent.

The main findings can be summarised as follows:

- We identified a WCB in IFS analyses as rapidly ascending air masses (approximately 600 hPa in 12 h) in the vicinity of Pyeongchang. A strong jet and enhanced vertical wind shear within the WCB ascent region are clearly visible in radiosonde data and Doppler

velocity measurements from MXPol.

- The IFS analyses show that SLW (up to 0.2 g kg^{-1}) is produced during the rapid ascent in the WCB by condensation of water vapour. In agreement with IFS analyses, multiple peaks in LWP during the passage of the warm front corroborate the presence of SLW. The timing and presence of SLW are additionally confirmed by the presence of rimed particles observed by the MASC and a hydrometeor classification based on MXPol data.
- The vertical wind shear promotes aggregation and riming by producing SLW, updraughts and turbulence, which enhance the probability of collision between particles.
- Three periods could be identified in which the governing microphysical processes are directly influenced by the specific flow conditions in the WCB. In the first period, Pyeongchang is located below the WCB outflow (Fig. 4.4a). No strong updraughts were present, the precipitation intensity was low and we observed mainly small aggregates and crystals. In the second and third periods, Pyeongchang is located below the WCB ascent. A layer with strong vertical wind shear, whose height decreases with time, generates turbulent cells and updraughts. The precipitation intensity peaks between 7 and 10 mm h^{-1}, and large rimed aggregates are observed.

This study enables the investigation of the impact of a large-scale feature, such as a WCB, on microphysics thanks to the complementarity of atmospheric models, remote-sensing and in situ measurements. It suggests a strong coupling between processes at synoptic and micro-scales that has to be assessed when evaluating the representation of clouds and precipitation in atmospheric models. While this case study presents a detailed analysis of field measurements, additional investigations with in situ measurements in clouds – characterising the presence of SLW for instance – are needed to further constrain and evaluate the coupling between large-scale dynamical processes and microphysics in models.

5 The influence of orographic gravity waves on precipitation during an atmospheric river event at Davis, Antarctica

This chapter is adapted from the preprint version of the article:

- Gehring, J., E. Vignon, A.-C. Billault-Roux, A. Ferrone, A. Protat, S. P. Alexander, and A. Berne (2021b), The influence of orographic gravity waves on precipitation during an atmospheric river event at Davis, Antarctica, *Journal of Geophysical Research: Atmospheres, submitted*

It presents a case study of intense snowfall sublimation during an atmospheric river (AR) event at Davis, Antarctica.

5.1 Summary

Intense snowfall sublimation was observed during a precipitation event over Davis in the Vestfold Hills, East Antarctica, from 08 to 10 January 2019. Radar observations and simulations from the Weather Research and Forecasting model revealed that orographic gravity waves (OGWs), generated by a north-easterly flow impinging on the ice ridge upstream of Davis, were responsible for snowfall sublimation through a foehn effect. Despite the strong meridional moisture advection associated with an AR during this event, almost no precipitation reached the ground at Davis. We found that the direction of the synoptic flow with respect to the orography determined the intensity of OGWs over Davis, which in turn directly influenced the snowfall microphysics. We hypothesise that turbulence induced by the OGWs likely enhanced the aggregation process, as revealed by dual-polarisation and dual-frequency radar observations. This study suggests that despite the intense AR, the precipitation distribution was determined by local processes tied to the orography. The mechanisms found in this case

study could contribute to the extremely dry climate of the Vestfold Hills, one of the main Antarctic oasis.

5.2 Introduction

Snowfall in Antarctica is the main input to ice sheet mass balance (*King and Turner*, 1997), which determines the contribution of the southernmost continent to sea level rise (*Shepherd and Wingham*, 2007). On the East Antarctic coast, most of the precipitation comes either from meridional moisture advection by extratropical cyclones or is induced by orographic forcing (*King and Turner*, 1997). The surface mass balance of the East Antarctic coastal ice sheets is hence heavily influenced by the frequency and intensity of maritime moisture intrusions from lower latitudes, which often result in high precipitation accumulations (*Noone et al.*, 1999; *Nuncio and Satheesan*, 2014; *Welker et al.*, 2014). A recent study by *Turner et al.* (2019) showed that extreme precipitation events (EPEs, defined as the largest 10% of daily totals) contribute to more than 40% of the annual precipitation over much of the continent. In particular, the greatest contribution from EPEs is found on the main ice shelves, especially on the Amery Ice Shelf (less than 10 days of the highest-ranked precipitation contributing to 50% of the annual total). Davis station (69°S, 78°E) is located on the coast of the Vestfold Hills, just north-east of the Amery Ice Shelf. The Vestfold Hills are one of the few ice-free regions in Antarctica, which makes it part of the Antarctic oasis (*Pickard*, 1986). According to *Turner et al.* (2019), EPEs contribute to about 55% of the annual total precipitation in the Vestfold Hills with more than 95% of the interannual variability explained by EPEs. This shows that in the dry climate of Davis, EPEs have a significant climatological impact. In Antarctica, EPEs are often associated with narrow corridors of enhanced integrated water vapour (IWV) and integrated vapour transport, called atmospheric rivers (ARs, *Ralph et al.*, 2004; *Zhu and Newell*, 1998). Indeed, *Gorodetskaya et al.* (2014) showed that ARs were responsible for outstanding precipitation accumulations over coastal Dronning Maud land, East Antarctica. Moreover, *Wille et al.* (2021) concluded that ARs are responsible for at least 10% of accumulated snowfall over East Antarctica and a majority of EPEs. However, the fate of these intense meridional moisture advection events depends on the state of the coastal boundary layer. For instance, *Grazioli et al.* (2017b) showed that snowfall sublimation by dry katabatic winds leads to a decrease of 17% of total snowfall on the continental scale and up to 35% on the margins of East Antarctica, consistent with the more recent study of *Agosta et al.* (2019). While this low-level sublimation is very effective for light snowfall events, *Grazioli et al.* (2017b) showed that it can still lead to a decrease of about 20% for the most intense snowfall cases over Dumont d'Urville, East Antarctica. This shows that katabatic winds can substantially affect the total amount at ground level during EPEs. However, other atmospheric processes might contribute to low-level snowfall sublimation. For instance, foehn winds, which are common in the Antarctic Peninsula (*Elvidge et al.*, 2015; *Grosvenor et al.*, 2014; *Kirchgaessner et al.*, 2021) and in the McMurdo Dry Valleys (*Speirs et al.*, 2010; *Steinhoff et al.*, 2013), can lead to record-setting warming and drying of the air in the lee of a mountain (*Bozkurt et al.*, 2018). While the impact of foehn on melting

and sublimation of ice shelves has been already studied (*Cape et al.*, 2015; *Zou et al.*, 2019), its effect on snowfall sublimation in Antarctica has, to our knowledge, never been investigated. Foehn winds are associated with orographic gravity waves (OGWs) (*Damiens et al.*, 2018; *Elvidge et al.*, 2016; *Vosper et al.*, 2018), which, in East Antarctica, are generated when synoptic or katabatic winds impinge upon a mountain ridge or reach the coast (*Valkonen et al.*, 2010; *Watanabe et al.*, 2006) and they can be trapped downstream of a katabatic jump (*Vignon et al.*, 2020). *Alexander et al.* (2017) studied a gravity wave event at Davis and found that the gravity waves were generated by the interaction between a strong north-easterly synoptic flow and the orography upstream of Davis. These OGWs were responsible for temperature fluctuations that affect the formation of cirrus clouds. While OGWs in East Antarctica have been the subject of investigations in the last two decades (*Alexander and Murphy*, 2015; *Moffat-Griffin*, 2019; *Orr et al.*, 2014; *Watanabe et al.*, 2006), their impact on precipitation remains to be determined.

The goal of this study is to investigate how the synoptic evolution of an intense precipitation event (08 to 10 January 2019) and the local orography influenced the precipitation distribution and microphysics over the Vestfold Hills. We use data collected during the PLATO campaign at Davis presented in Chap. 3. We also make use of observations from a very-high frequency wind-profiling radar (hereafter VHF) and simulations from the Weather Research and Forecasting (WRF) model. We address the following questions:

1. How does the synoptic flow constrain the presence of OGWs?
2. How do OGWs impact snowfall sublimation and the spatial distribution of precipitation during this event?
3. How do OGWs influence the snowfall microphysical evolution?

This chapter is structured as follows. Section 5.3 presents additional data not introduced in Chap. 3 and used in this study. Section 5.4 presents the evolution of the synoptic conditions and the precipitation distribution of this case study. In Sect. 5.5 we analyse the dynamics and microphysics of the event during three distinct phases. The possible climatological relevance of this case study is discussed in Sect. 5.6. We finally summarise and conclude this chapter in Sect. 5.7.

5.3 Additional data used in this case study

5.3.1 WRF simulations

We carried out numerical simulations using version 4.1.1 of the WRF model with a parent domain of 27 km resolution containing three (one-way) nested domains (Fig. 5.1) with 9, 3, and 1 km resolution centred over Davis station. The boundary and initial conditions are from the ERA5 reanalysis (*Hersbach et al.*, 2020). The nudging strategy, the 96-level vertical grid and the physical package employed are the same as in the so-called 'lINP-hr' simulation of *Vignon et al.*

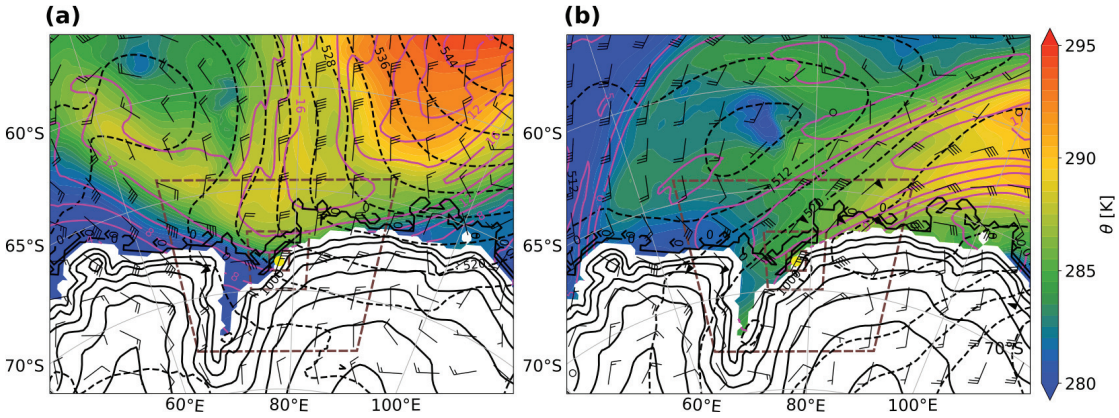

Figure 5.1 – Synoptic map from the WRF domain at 27-km resolution at **(a)** 09:00 UTC 08 January 2019, and **(b)** 00:00 UTC 10 January 2019 of potential temperature (shading in K) and wind (barbs following meteorological standard notation) at 800 hPa, geopotential height at 500 hPa (dashed contours, labels in decametre), IWV (magenta contours, labels in $\mathrm{kg\,m^{-2}}$). The brown dashed boxes show the extent of the WRF domains at 9, 3, and 1 km resolution (from the largest to the smallest domain respectively). The yellow dot shows the location of Davis on the Ingrid Christensen Coast on the eastern side of Prydz Bay. The Lars Christensen Coast is on the western side of Prydz Bay.

(2021). In particular, we used the Morrison 2-moment microphysical scheme with a new ice nucleation parameterisation adapted to the low concentrations of ice nuclei particles observed in the atmosphere off the Antarctic coasts. The topography and land-use for the simulations are from the 1-km resolution Reference Elevation Model of Antarctica dataset (*Howat et al.*, 2019) and from the AntarcticaLC2000 dataset respectively. The WRF-compatible files have been built by *Gerber and Lehning* (2020) and they show substantial improvements compared to the standard WRF forcing files used for Antarctica (which exhibited no topographical information over the Vestfold Hills).

5.3.2 Dual-frequency ratio

To compute the dual-frequency ratio (DFR) of reflectivity at X- and W-bands, vertical profiles of Z_H were extracted from MXPol's RHIs close to the location of BASTA (23° and 52° RHIs, respectively exactly over BASTA and 290 m away), at a horizontal distance between 480 and 680 m from MXPol. This time series of X-band reflectivity profiles (Z_X) can then be compared to the W-band reflectivity from BASTA (Z_W): both Z_X and Z_W profiles are binned to a common (time, height) grid with a timestep of 10 minutes and a height resolution of 50 m, which corresponds to two scan cycles of MXPol and two range gates of BASTA. The DFR is then computed as $Z_X - Z_W$, where Z_X and Z_W are in dBZ and hence the DFR is in dB. The principle of multi-frequency radar techniques was already introduced by *Atlas and Ludlam* (1961) and was used by *Eccles and Atlas* (1973) and *Carbone et al.* (1973) to detect hail. Later, *Matrosov* (1998) proposed a method based on dual-frequency radar measurements to measure snowfall rate.

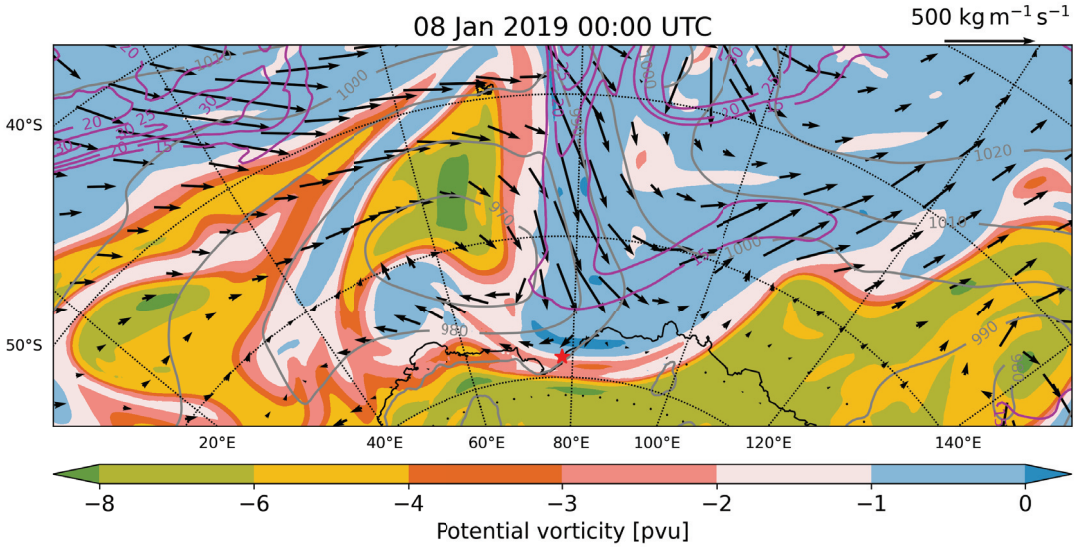

Figure 5.2 – Synoptic situation at 00:00 UTC 08 January 2019 from ERA5 data. Potential vorticity (shading in potential vorticity unit (pvu) = $\mathrm{K\,m^2\,kg^{-1}\,s^{-1}}$) at the 315 K isentrope, mean sea level pressure (grey contours, labels in hPa), integrated water vapour (magenta contours, labels in $\mathrm{kg\,m^{-2}}$), and integrated vapour transport (arrows in $\mathrm{kg\,m^{-1}\,s^{-1}}$).

In essence, the principle of dual-frequency techniques is based on the fact that hydrometeors have different backscattering properties at the two frequencies: for the lower frequency the scattering is well described by the Rayleigh approximation, while the higher frequency will be in the resonance scattering regime (sometimes referred to as the Mie regime, see Fig. 1.4) for the hydrometeors of interest. In our case, snowflakes essentially remain in the Rayleigh regime at X-band, while they transition to the Mie regime at W-band as they grow in size, which in turn leads to a plateau or a decrease in Z_W. The DFR hence reflects the median size of snowflakes and exhibits a sharp increase when processes, such as aggregation, lead to a rapid increase in snowflake size.

5.3.3 Wind-profiling radar: VHF

The Davis VHF wind-profiling radar is a 55 MHz system consisting of a 144-antenna main array with a one-way beamwidth of about 7°. Doppler radial velocities are obtained in the vertical, north, and east directions (with the off-vertical beams pointing at a 14° zenith angle), cycling every 6 min (*Alexander et al.*, 2017). The vertical range resolution is 500 m and data are acquired from about 1500 m a.g.l. to the lower stratosphere.

5.4 Synoptic evolution and precipitation distribution

At 00:00 UTC on 08 January 2019 a potential vorticity (PV) cutoff is located to the north of Davis (Fig. 5.2) and is associated with a surface cyclone. This system advects moisture polewards on its eastern flank, as can be seen by the large meridional moisture transport of around 500 $\mathrm{kg\,m^{-1}\,s^{-1}}$. This moisture advection is organised into a narrow filament of large integrated water vapour (IWV, up to 15 $\mathrm{kg\,m^{-2}}$) extending meridionally over several thousand kilometres and resembling an AR. As explained in *Gorodetskaya et al.* (2014), the thresholds used to define ARs in the mid-latitudes (e.g. *Ralph et al.*, 2004, 2006) cannot be applied to the much drier and colder Antarctic environment. For this reason, *Gorodetskaya et al.* (2014) proposed a threshold on IWV based on the zonal mean saturated IWV, which is consistent with the idea that ARs are outstanding moisture transport compared to the zonal mean (*Zhu and Newell*, 1998). Taking the thresholds for the events described in *Gorodetskaya et al.* (2014), the IWV values of Fig. 5.2 south of 50°S along the longitude of Davis would correspond to an AR. Alternatively, *Wille et al.* (2019) proposed a definition of ARs based on temporal percentiles of IWV at each location. As our study does not focus on ARs and their climatological impact on Antarctic precipitation, it is out of the scope to show that this case satisfies specific ARs definitions. Nonetheless, it is noteworthy that the narrow corridor of large IWV of Fig. 5.2 qualitatively corresponds to an AR. We will therefore refer hereafter to this feature as an AR.

The warm front of this extratropical cyclone is visible as a sharp temperature gradient to the north of Davis, while a cold air pool is located ahead of Prydz Bay (Fig. 5.1a). The thermal wind at this sharp temperature boundary leads to a barrier wind (*van den Broeke and Gallée*, 1996), which can be noticed in the wind fields of Fig. 5.1a (see also Appendix C.1). Once the cold air pool has been eroded by advection and mixing of warm air associated with the passage of the warm front, the barrier wind is not present anymore (Figs. 5.1b and C.1c, d). This together with a north-easterly flow at all heights (Fig. 5.3b and 5.4d) as the surface cyclone moves eastwards allows the atmospheric river to make landfall on the Lars Christensen Coast, discharging its moisture on the steep slopes of the ice sheet (IWV in Fig. 5.1b).

With the passage of a warm front and the presence of an AR, all the ingredients for intense precipitation over Prydz Bay are present, from a large-scale perspective. Figure 5.5 shows that there is indeed significant precipitation accumulation of up to 85 mm in 60 h. However, the spatial distribution of precipitation is very heterogeneous and shows two striking features. First, the largest accumulation is on the Lars Christensen Coast, where most of the AR makes landfall on the steep slope at the northernmost part of the coast. Second, on the Ingrid Christensen coast (i.e. where Davis is located) some wave patterns of precipitation accumulation appear with the maxima (minima) located windward (leeward) of the main ridges. Most of all, Davis is located in the broadest dry area in the lee of a ridge.

5.5 The evolution of snowfall and orographic gravity waves over Davis

In this section, we analyse the evolution of the local dynamics and snowfall microphysics over Davis to understand which processes led to the dry area over the Vestfold Hills, despite the intense large-scale moisture advection during this event. We divide the event into three distinct phases.

5.5.1 Phase I: the passage of the warm front and trapped orographic gravity waves, 02:00 to 15:00 UTC 08 January 2019

At 00:00 UTC on 08 January pre-frontal clouds are present over Davis and by 04:00 UTC a nimbostratus cloud with reflectivity values of up to 15 dBZ is extending to almost 8000 m (Fig. 5.3a). At 12:00 UTC the air is subsaturated with respect to ice below 1800 m a.s.l. (blue dashed line in Fig. 5.4b) and snowfall sublimates completely before reaching the ground. In this dry layer, turbulence can be seen as a succession of intense vertical motions in BASTA mean Doppler velocity before 14:00 UTC below 2000 m. These large vertical velocities are qualitatively well represented by WRF (green contours in Fig. 5.3b), although the magnitude is underestimated.

The passage of the warm front can be seen as a sharp increase of the −10 °C isotherm altitude at 10:00 UTC and is associated with strong turbulence, a faster decrease of pressure and an increase in wind speed. The sharp temperature gradient between the cold air pool over Prydz Bay and the warm front (Fig. 5.1a and 5.6a) causes a strong thermal wind which can be clearly seen before 10:00 UTC with backing winds with height (Fig. 5.3b), consistent with warm air advection in the Southern Hemisphere. The barrier wind resulting from this temperature gradient deflects the moist flow such that the Lars Christensen Coast is protected from intense precipitation at this early stage of the event (Fig. 5.1a, also Fig. C.1a). The thermal wind provides the ideal orientation (north-easterly) for the generation of OGWs along the Ingrid Christensen Coast, while the warm front produces large-scale lifting and likely enhanced the updraughts in the OGWs (Fig. 5.6a). The flow-topography interaction leads to a foehn effect in the lee of the ridge with clear isentropic drawdown (e.g. *Damiens et al.*, 2018), negative vertical velocity, and a relatively dry air tongue extending even downstream of Davis station (Fig. 5.6b). An hydraulic jump at the base of the ice plateau is also evident in Fig. 5.6b and manifests as a strong updraught extending up to 3500 m. Note that the Vestfold Hills correspond to the dry zone directly in the lee of the ridge, while most of the precipitation fall upstream of the ridgeline and downstream of Davis (bars in Fig. 5.6).

There is a layer with enhanced static stability between 3500 and 4000 m downstream of Davis (as indicated by the closer isentropes in Fig. 5.6b), the vertical wind shear below this layer is weak and the thermal wind is mostly present inside and above it, with the wind shifting from east-northeasterly at 3000 m to northerly at 4000 m. This layer of enhanced static stability is partly due to the hydraulic jump and subsequent flow separation, which makes the isentrope downstream of the jump and below 1800 m move apart, leading to a boundary layer

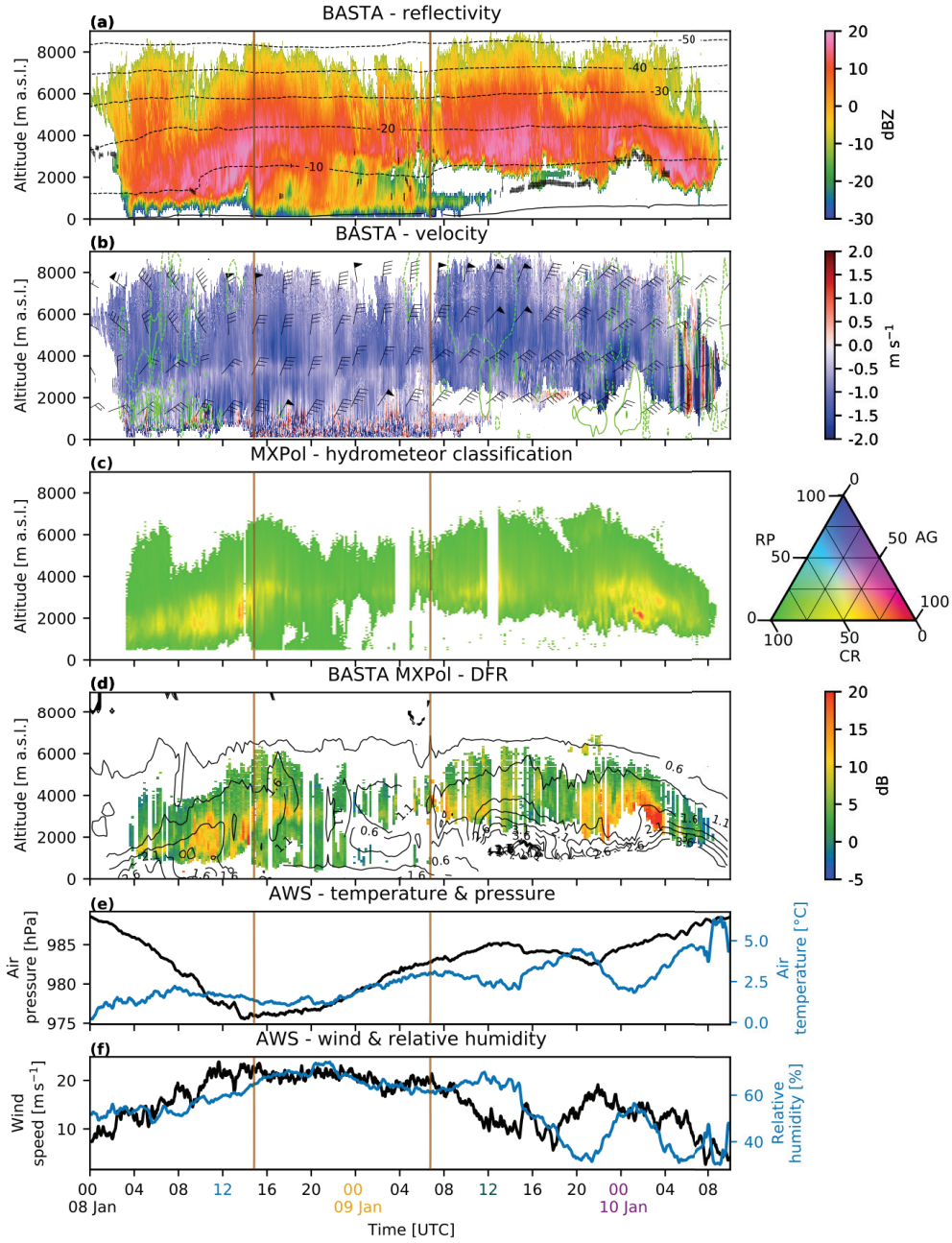

Figure 5.3 – Time series from 00:00 UTC 08 January to 10:00 UTC 10 January 2019 of **(a)** reflectivity of BASTA (shading), isotherms of WRF (black contours, labels in °C) and SLW from RMAN cloud classification data (black shading), **(b)** mean Doppler velocity from BASTA (shading, defined positive upwards), horizontal wind from VHF (barbs following meteorological standard notation), and vertical wind speed from WRF (green contours every 0.4 m s^{-1}, continuous for upwards, dashed for downwards), **(c)** hydrometeor classification based on all MXPol RHIs (shading, see Sect. 3.3), **(d)** DFR from MXPol and BASTA (shading, see Sect. 5.3.2) and D_{mean} from WRF (contours, labels in mm), **(e)** air temperature and pressure, and **(f)** wind speed and relative humidity from the AWS. The colours of the 00:00 and 12:00 UTC labels correspond to the radiosoundings shown in Fig. 5.4, the brown lines delimit the phases.

destabilisation (*Vignon et al.*, 2020). OGWs are trapped at low levels downstream of the jump (Fig. 5.6b), but extend vertically up to the layer of increased static stability (~3500 m). This corresponds to the case of waves propagating on a temperature inversion located close to the surface (i.e. ~1000 m, Fig. 5.4a) as described in *Sachsperger et al.* (2017).

From a microphysical perspective, two main zones of aggregation can be identified during the event: (i) from 08:00 to 16:00 UTC on 08 January between 1000 and 4000 m, and (ii) from 20:00 UTC 09 January to 04:00 UTC 10 January between 2000 and 4000 m. While the latter belongs to Phase III and will be further discussed in Sect. 5.5.3, we discuss their common features here. In both cases, the maxima of DFR are collocated with zones dominated by aggregates in MXPol hydrometeor classification and with maxima of mean particle mass diameter (D_{mean}) from WRF (Fig. 5.3c and d, respectively). Note that these aggregation zones are located at temperatures above −20 °C (Fig 5.3a), which represent favourable conditions for significant aggregation (*Connolly et al.*, 2012; *Hobbs et al.*, 1974; *Phillips et al.*, 2015). Although the DFR and MXPol hydrometeor classification are not totally independent (they both use Z_X), the other variables used clearly point towards aggregation (minimum of Z_W due to Mie scattering regime, visible in Fig. 5.3a, which strongly contributes to the maximum of DFR, and low Z_{DR} in Fig. 5.7b interpreted as aggregates in MXPol classification). This spatio-temporal agreement between dual-polarisation and dual-frequency variables makes our identification of aggregation robust. The simulation of D_{mean} from WRF is qualitatively consistent with the DFR in the aggregation layer (Fig. 5.3d) and shows that WRF is able to reproduce the zones of dominant aggregation.

Figure 5.7 shows a layer of enhanced Z_{DR} varying between 2000 and 4000 m during Phase I. This layer represents the end of depositional growth and the start of aggregation. Below this layer, Z_{DR} decreases drastically, while Z_H increases and reaches its maximum of 22 dBZ at 1500 m. This is due to intense aggregation taking place from 3000 to 1200 m, as can also be observed by the increase in aggregates' proportion in Fig. 5.3c and is consistent with DFR observation and D_{mean} simulation of WRF in Fig. 5.3d. Figure 5.8a shows an RHI representative of Phase I. The layers of enhanced Z_H and Z_{DR} are clearly visible at 2000 and 3000 m, respectively. The aggregation below 3000 m could be favoured by the turbulence generated by the strong vertical motions within the OGWs (Fig. 5.6b) and then advected downstream to Davis. The Doppler spectrum shown in Fig. 5.8b supports our microphysical interpretation: the depositional growth above 3000 m leads to a slight increase in the magnitude of Doppler velocity and reflectivity, while the aggregation below 3000 m causes a sharp increase in the same variables. When the aggregates enter the updraughts within the OGWs at 2200 m, the magnitude of Doppler velocity decreases and the spectral width increases due to the turbulence. This favours continuous aggregation until 1200 m, where the snowflakes sublimate. The vertical extent of the updraught as shown in this Doppler spectrum is consistent with the OGWs simulated by WRF and shown in Fig. 5.6b.

In summary, the thermal wind enhanced by the cold air pool over Prydz Bay ahead of the warm front provides the ideal flow direction below 2000 m for the generation of OGWs. A foehn

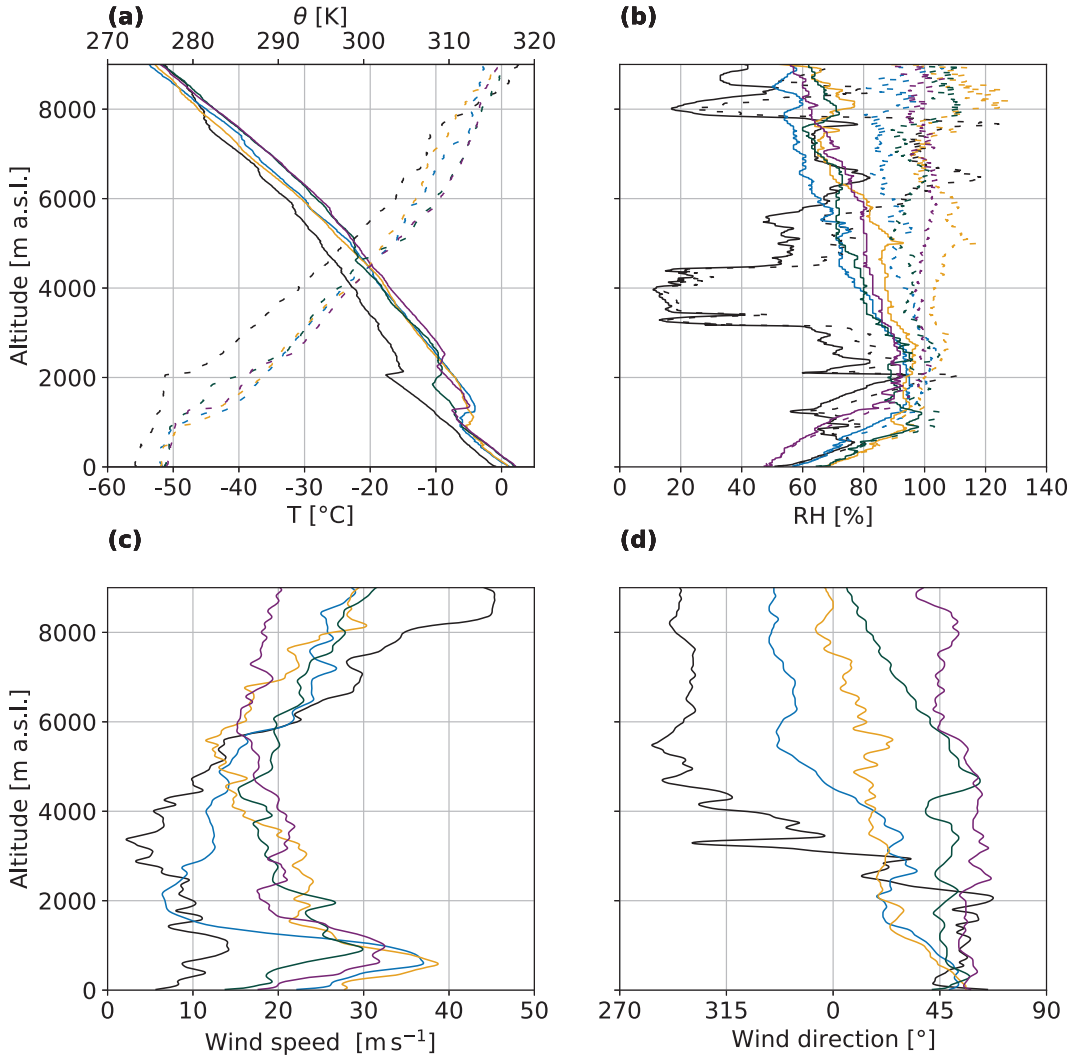

Figure 5.4 – Radiosoundings launched at Davis station on 08 January at 00:00 UTC (black) and 12:00 UTC (blue), on 09 January at 00:UTC (yellow) and 12:00 UTC (dark green), and on 10 January at 00:00 UTC (purple) of **(a)** temperature (T, solid lines) and potential temperature (θ, dashed lines), **(b)** relative humidity with respect to liquid (solid lines) and ice (dashed lines), **(c)** wind speed, and **(d)** wind direction.

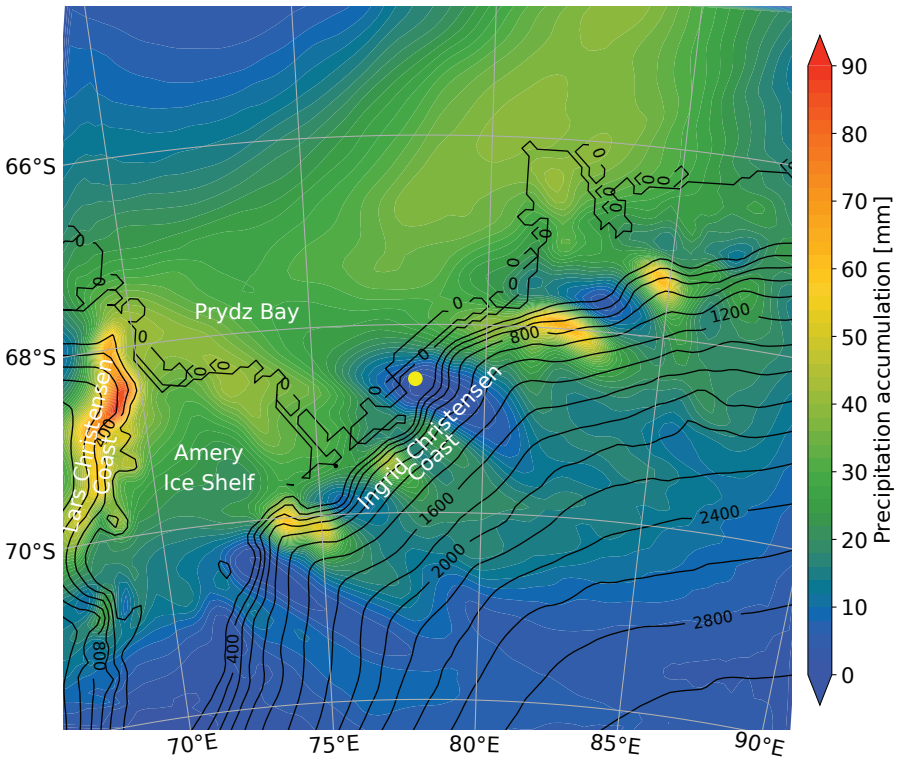

Figure 5.5 – Precipitation accumulation (shading) from the WRF 9-km resolution domain from 00:00 UTC on 08 January to 12:00 UTC on 10 January 2019 and topography (black contours, labels in m a.s.l.). The yellow dot shows the location of Davis.

effect manifesting as an isentropic drawdown in the lee of the ridge is followed by an hydraulic jump that favours the trapping of gravity waves downstream. The relatively dry foehn air that flows at low levels down to Davis station leads to total snowfall sublimation below about 1500 m above the station and explains the dry area extending over the Vestfold Hills. The OGWs also affect the snowfall microphysics by providing ideal conditions for aggregation through the generation of updraughts and turbulence.

5.5.2 Phase II: northerly flow and light precipitation at Davis, 14:00 UTC 08 January to 07:00 UTC 09 January 2019

As the warm front passes, the stable layer at around 4000 m dissipates, the thermal wind weakens, and the synoptic flow becomes north-northeasterly (Fig. 5.9a). As a consequence, winds are oriented more northerly at all heights (Fig. 5.3b at 16:00 UTC 08 January). As can be seen in Fig.5.9a, a north-northeasterly flow will not impinge perpendicularly to the ridge located to the north-east of Davis, but rather to the ridge located further south where the strongest OGWs are present. The collocation of the warm front with these intense OGWs, as during Phase I, suggests that it provides large-scale lifting enhancing the updraughts. Along with the absence of intense low-level OGWs over Davis, the foehn effect weakens (relative

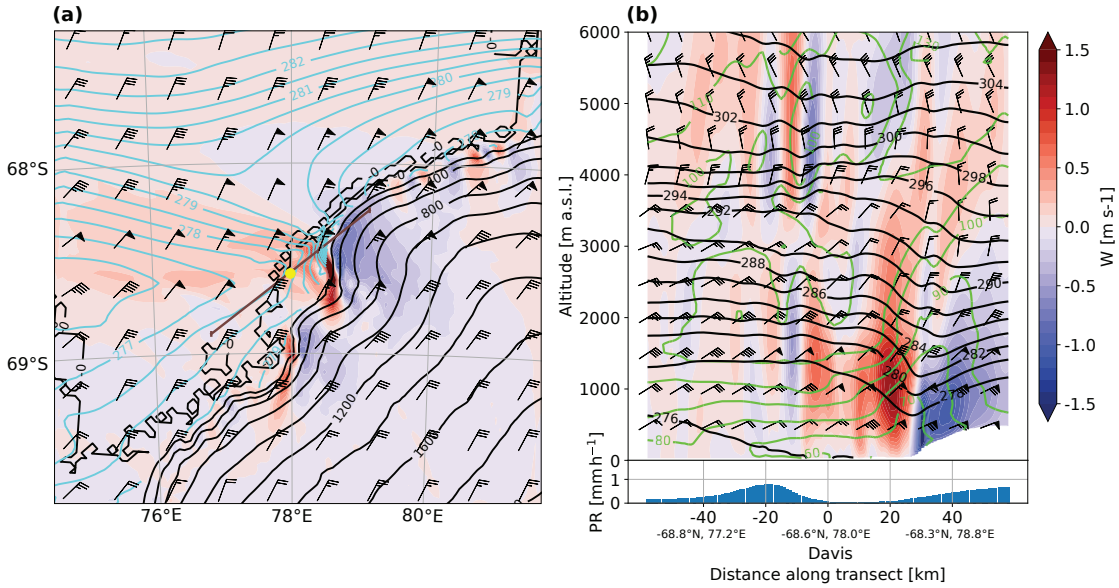

Figure 5.6 – WRF output on 08 January 2019 at 09:00 UTC. **(a)** map of the 3-km resolution domain of vertical wind velocity (shading in $m\,s^{-1}$), horizontal wind (barbs following meteorological standard notation), and potential temperature (cyan contours, masked below 100 m a.s.l.) at 850 hPa (about 1200 m a.s.l.). The black contours show the topography (labels in m a.s.l.). **(b)** cross-section of the 1-km resolution domain, corresponding to the brown line in **(a)**, of vertical wind velocity (shading in $m\,s^{-1}$), potential temperature (black contours, labels in K), RHi (green contours, labels in %) and horizontal wind (barbs following meteorological standard notation) and precipitation rate along the cross-section (blue bars in mm^{-1}).

humidity increases and air temperature decreases, Fig. 5.3e-f). The increase in relative humidity can be seen in the whole boundary layer (Fig. 5.4b). It allows light precipitation to reach Davis between 14:00 UTC 08 January and 06:00 UTC 09 January. The absence of low-level trapped OGWs during Phase II coincides with much less aggregation than during Phase I. Indeed, the layer of aggregation is less intense and confined between 3000 and 4000 m before disappearing completely after 20:00 UTC 08 January (Fig. 5.3c-d). The reflectivity values at both X- and W-bands are also weaker (Fig. 5.3a and d). Although reflectivity is significantly lower during this period, snowfall reaches the ground since sublimation is less intense. While the foehn effect is less pronounced during Phase II, it is enough to cause partial snowfall sublimation below about 2000 m (Fig. 5.3a).

The most intriguing radar signature during Phase II is the minimum of Doppler velocity observed around 3000 m, in particular between 14:00 and 20:00 UTC on 08 January (Fig. 5.3b). A careful investigation of the spectrograms from MXPol's PPIs at 90° elevation revealed that this minimum is due to an updraught varying between 0.5 and 1 $m\,s^{-1}$. Figure 5.10b shows an example of such a spectrogram, where a bimodality is present just above the updraught layer. Almost all spectrograms during the period where this minimum in Doppler velocity is observed featured both a decrease in the magnitude of the mean Doppler velocity and a bimodality. To ensure that this minimum in Doppler velocity is due to an updraught and not only to

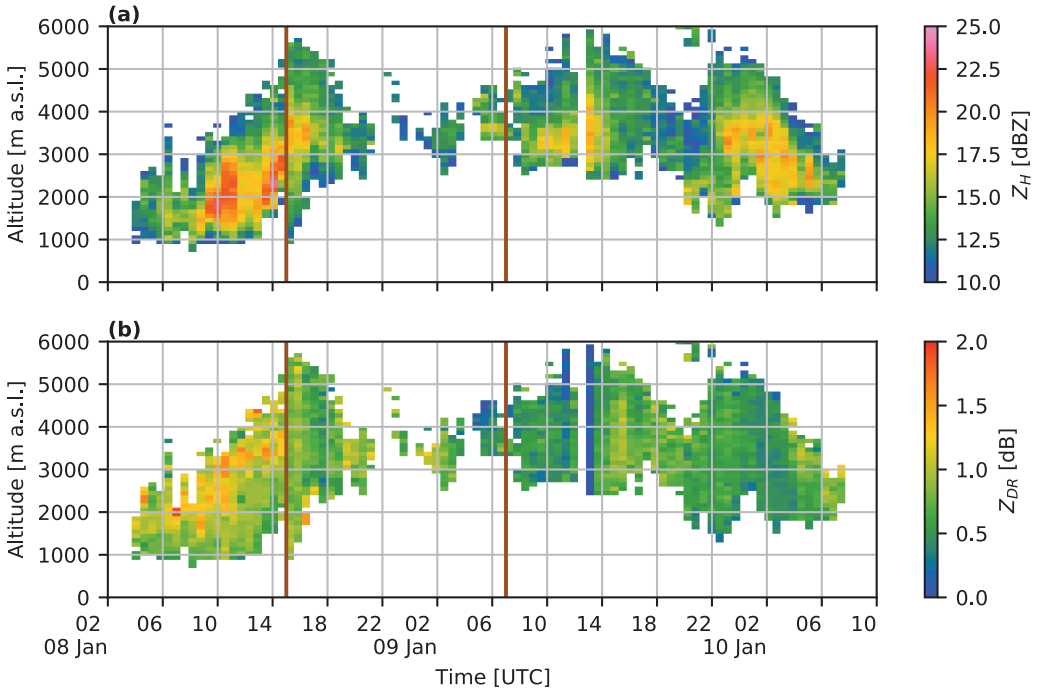

Figure 5.7 – Time series of MXPol Z_H **(a)** and Z_{DR} **(b)** from 02:00 UTC 08 January to 10:00 UTC 10 January. The profiles were extracted from the RHIs at 23° and 52° elevation from 6 to 10 km horizontal range and for elevation angles greater than 135°.

the contribution of the secondary mode in decreasing the magnitude of the mean Doppler velocity, we computed the velocity of the primary mode only (not shown), which revealed the same behaviour as the mean Doppler velocity showed in Fig. 5.3b. This updraught tends to broaden the spectrum and skew the distribution towards smaller magnitudes of Doppler velocity (Fig. 5.10b). The increase in spectral width is due to the turbulence in the updraught, similar to turbulence present in other summertime cloud systems which were observed by ship-based remote sensors near Davis and Mawson (650 km west of Davis, *Alexander et al.*, 2021). Note that it is much lighter than the turbulence observed in the boundary layer below 1000 m. The increase in skewness could be due to a size sorting effect by the updraught. The size sorting cannot however totally explain the bimodality, since it is unlikely to create such a discontinuity in the Doppler spectrum. We hypothesise that the bimodality is due to secondary ice production through collisional breakup of ice crystals (*Takahashi et al.*, 1995; *Vardiman*, 1978) at the top of the updraught. A recent study by *Sotiropoulou et al.* (2021) showed that breakup could account for the enhanced number concentration of ice crystals often measured in Antarctic clouds (*Young et al.*, 2019). They also showed that a minimum concentration as low as ~0.1 L^{-1} of primary ice crystals is sufficient. Considering the measured reflectivity during this event, the primary ice concentration is likely above this threshold. Furthermore, for secondary ice production through breakup to be efficient, snowflakes have to be partially rimed. Despite the lidar signal being almost totally attenuated, some regions of SLW (black

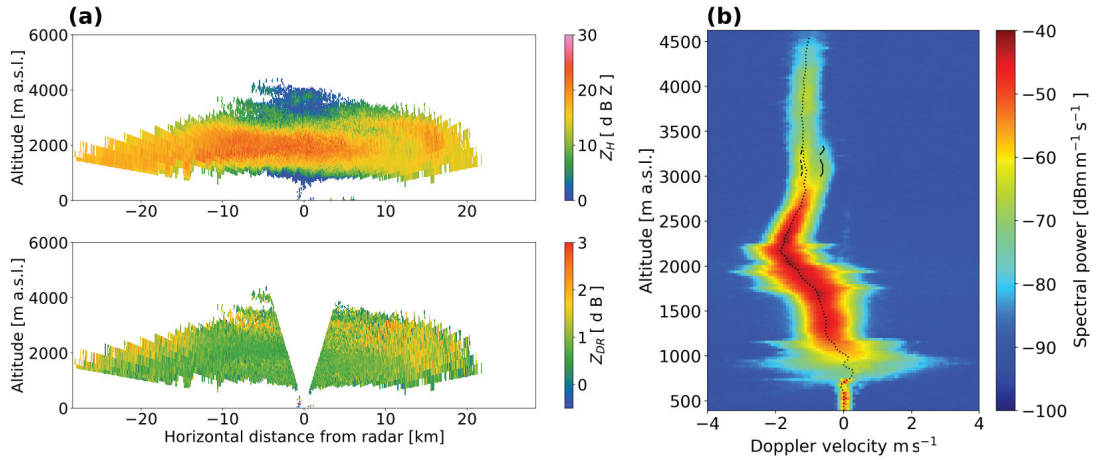

Figure 5.8 – **(a)** MXPol RHI at 52° azimuth (yellow line in Fig. 3.1) at 09:27 UTC 08 January of Z_H, and Z_{DR}. **(b)** MXPol Doppler spectrogram averaged over a PPI at 90° elevation at 09:24 UTC 08 January. The dotted line shows the mean Doppler velocity, the dashed and solid lines show, if present, the velocity of the first and second mode, respectively.

shading in Fig. 5.3a) at around 3000 m are visible during Phase II, suggesting that riming can at least partially occur. The MXPol hydrometeor classification however does not show significant occurrences of rimed particles during Phase II, likely due to its sensitivity to large rimed particles, which are not present here considering the low reflectivity values. Also, it requires a certain degree of riming for particles to be classified as rimed, which means that the crystals category can contain some rime. Moreover, photographs of snowflakes (only nine due to high wind speeds) taken by the MASC (not shown) during Phase II revealed the presence of small graupel particles, which confirm that SLW must have been present. Finally, *Takahashi et al.* (1995) showed that breakup was the most efficient at −16 °C, which corresponds to the temperature at which we observe this bimodality (Figs. 5.3a and 5.4a). Other secondary ice generation processes involving significant SLW amounts, such as rime splintering (so-called Hallett-Mossop process, *Hallett and Mossop*, 1974) and droplet shattering (*Korolev and Leisner*, 2020), are less likely to dominate here since we have no evidence for the required SLW amounts at this height. In particular, the Hallett-Mossop process operates at temperatures between −3 °C and −8 °C whereas we observe this bimodality at a temperature of −15 °C.

As to the origin of this updraught observed between about 3000 and 4000 m from 12:00 to 20:00 UTC, Fig. 5.9b shows a gravity wave train visible downstream of the ice-ridge between 3000 and 5000 m above Davis. In particular, a vertical wind speed maximum is observed above the Vestfold Hills at 3500 m, which corresponds to the altitude at which the updraught is observed in the radar data (Fig. 5.3b and 5.10b). This feature is quasi-stationary in the WRF simulations during the whole period where we observe the Doppler velocity minimum in Fig. 5.3b, suggesting that this updraught is probably due to the gravity wave train between 3000 and 5000 m shown in Fig. 5.9. *Schrom and Kumjian* (2016) observed a similar minimum in Doppler velocity near the −15 °C isotherm and hypothesised that the updraught could be

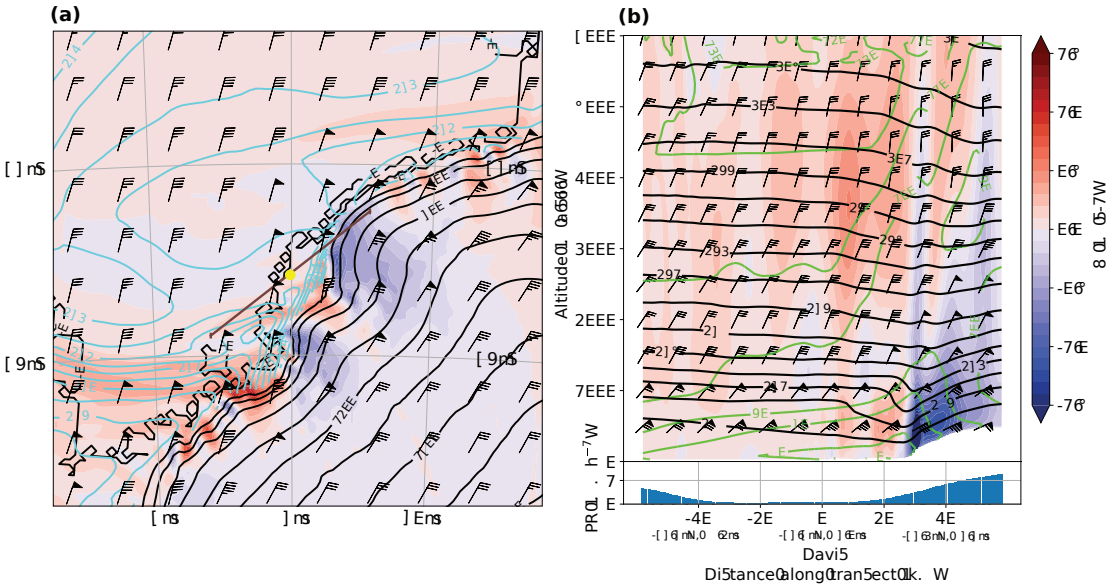

Figure 5.9 – As for Fig. 5.6 except at 18:00 UTC 08 January 2019.

induced by heating during depositional growth among other processes, which are thoroughly discussed in their study. The origin of this updraught is further discussed in Appendix C.2.

In summary, Phase II is characterised by a north-northeasterly flow at all heights, which prevents the formation of intense low-level OGWs as during Phase I and consequently the foehn effect is weaker and snowfall only partially sublimates. Nonetheless, quasi-stationary OGWs are present between 3000 and 5000 m and lead to a minimum in the magnitude of mean Doppler velocity and possibly secondary ice production.

5.5.3 Phase III: north-easterly flow and non-stationary orographic gravity waves, 07:00 UTC 09 January to 10:00 UTC 10 January 2019

Starting from 07:00 UTC on 09 January OGWs, which propagate vertically further than the low-level trapped gravity waves of Phase I, formed at the base of the ice plateau 20 km upstream from Davis (not shown). At around 14:00 UTC temperature rises, while relative humidity decreases as the foehn effect intensifies again (Fig. 5.3f). This coincides with winds below 4000 m becoming increasingly easterlies (Fig. 5.3b) due to the configuration of the upper-level low (Fig. 5.1b). This north-easterly flow impinges the ridge upstream of Davis perpendicularly and generates a band of updraughts oriented along the ridgeline (Fig. 5.11a), similar to the case study of *Alexander et al.* (2017).

After 14:00 UTC, the air temperature is anti-correlated with the relative humidity (Fig. 5.3e-f), which supports our hypothesis of a foehn wind event. Indeed, *Kirchgaessner et al.* (2021) showed that temperature and relative humidity are in antiphase during foehn events in the Antarctic Peninsula. The overall increase in temperature during the event is a combination

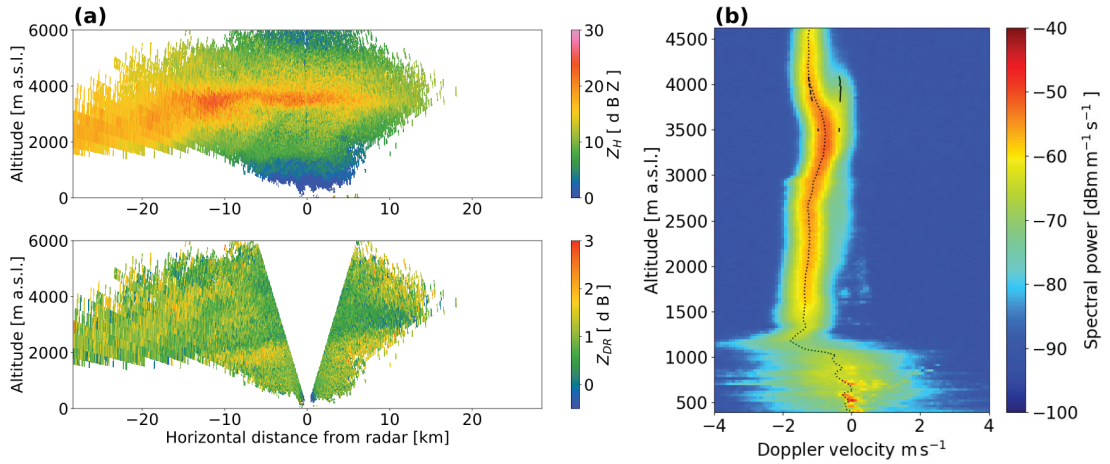

Figure 5.10 – As for Fig. 5.8 except at **(a)** 16:03 and **(b)** 16:10 UTC 08 January.

of the passage of the warm front and foehn wind. The shorter phases of temperature and relative humidity oscillations at the end of the event are due to the rapid successions of up- and downdraughts that brought the temperature up to 6 °C.

From about 20:00 UTC 09 January to 04:00 UTC 10 January a zone of intense aggregation is present (Fig. 5.3c-d). The high values of D_{mean} simulated by WRF are once again qualitatively consistent with the high values of DFR, especially between 22:00 UTC 09 January and 00:00 UTC 10 January. The zone of dominating aggregates in MXPol classification corresponds well to the high values of DFR and shows also some rimed particles (red-magenta shading in Fig. 5.3c). The lidar also detected SLW just above this mixture of aggregates and rimed particles. Note that the presence of hydrometeors further down in MXPol classification compared to BASTA is because all RHIs at an horizontal range greater than 6 km have been considered in MXPol classification, showing that the height of sublimation significantly varies spatially. Unlike during Phase I, where the zone of aggregation was topped by a layer of intense depositional growth leading to high Z_{DR} values, during Phase III the layer of aggregation is topped by smaller Z_{DR} values (Fig. 5.7) and aggregation is identified solely by the increase in Z_H and DFR.

On 10 January between 04:00 and 09:00 UTC, non-stationary OGWs trapped in the low- and mid-troposphere can be seen as a succession of intense up- and downdraughts with Doppler velocities of more than 2 m s^{-1} and a periodicity of about an hour (Fig. 5.3b). The non-stationary nature of these OGWs likely owes to the decrease in wind speed upstream of the ridge (compare Figs. 5.9a and 5.11a). WRF simulations revealed that the OGWs are propagating upstream (not shown). We hypothesise that this upstream propagation is a consequence of the gravity wave train adapting to the weaker forcing, which leads to non-stationary OGWs (*Nance and Durran*, 1997). These OGWs are qualitatively well represented by WRF (Fig. 5.3b): one can see a succession of up- and downdraughts with similar vertical extent and phase than in the Doppler velocity, although the magnitude is underestimated and the phase is

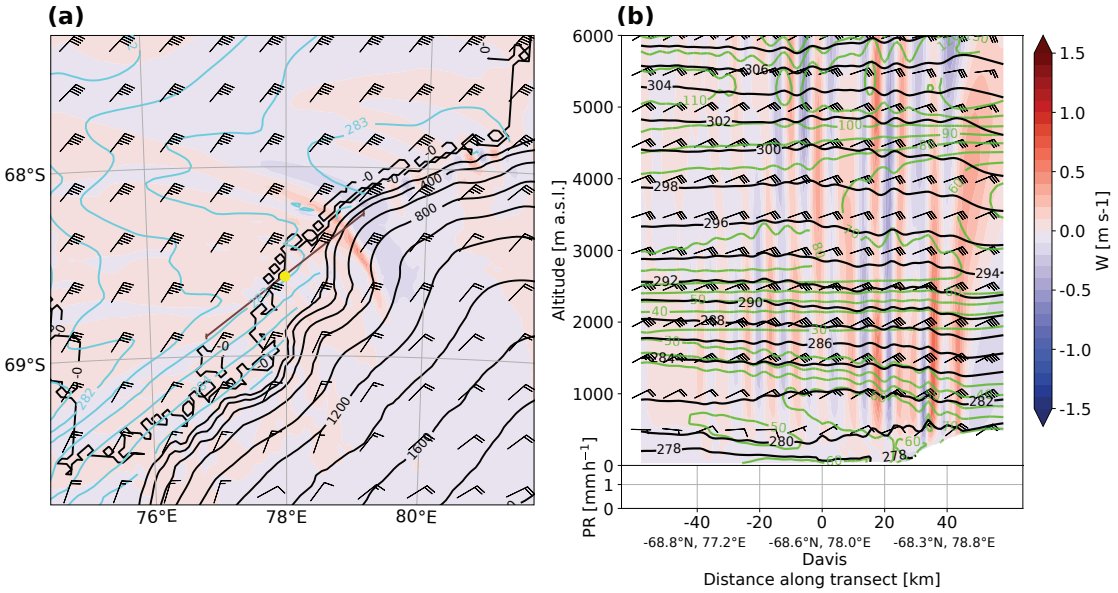

Figure 5.11 – As for Fig. 5.6 except at 07:00 UTC 10 January 2019.

shifted. These vertical motions strongly affect the vertical structure of the cloud as can be seen by the fluctuating level of maximum reflectivity (Fig. 5.3a). This can also be seen in MXPol measurements (Fig. 5.12), where the OGWs lead to an oscillation of the height of sublimation and a shift of the whole Doppler spectrum. The mean Doppler velocity at cloud top is about $-2\,\mathrm{m\,s^{-1}}$ and its magnitude increases with decreasing height as the hydrometeors likely become denser and fall faster. The rapid change from about -3 to $-4\,\mathrm{m\,s^{-1}}$ at 2000 m is probably due to an increase in the magnitude of the downdraughts. The horizontal wavelength of the OGWs is about 10 km and is consistent between MXPol measurements and WRF simulations (Figs. 5.12b and 5.11b). The OGWs are also associated with rapid fluctuations of temperature and relative humidity (Fig. 5.3f). These OGWs become visible (compared to earlier phases) in a time-series of vertical Doppler velocity above Davis because (i) they are non-stationary, (ii) they are present far enough downstream of the ice plateau, and (iii) they are sufficiently strong to lift the hydrometeors and hence lead to positive vertical Doppler velocities. Note that these strong OGWs coincide with winds shifting to easterlies for the first time during the event around 3000 m, showing again that their generation depends on the wind direction.

In summary, Phase III is characterised by a north-easterly flow generating non-stationary OGWs, which are evident in vertical Doppler velocity measurements and lead to a fluctuation of the level of sublimation.

5.5.4 Summary of the three phases

Figure 5.13 shows a conceptual model of the three phases of the event. During Phase I, Davis is located just ahead of the warm front and the low-level flow is north-easterly. The cold front

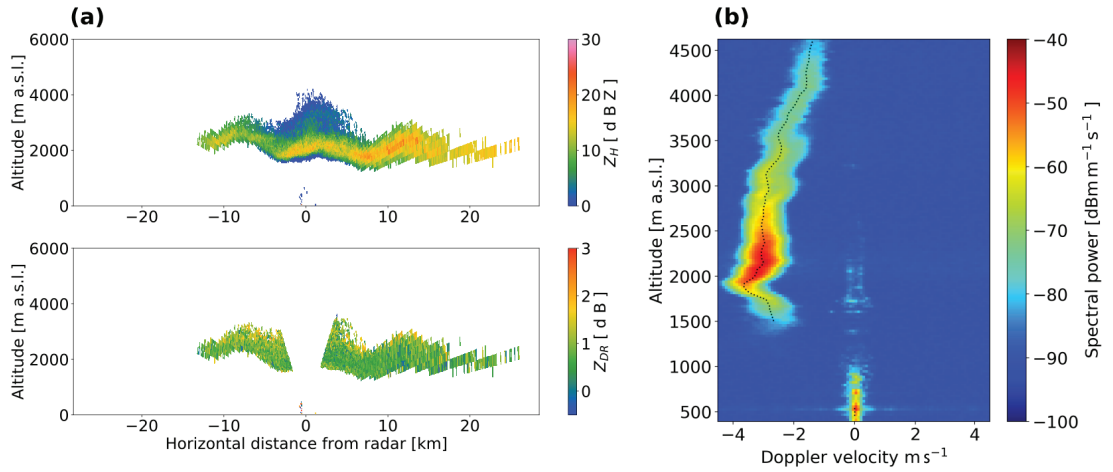

Figure 5.12 – As for Fig. 5.8 except at **(a)** 07:02 and **(b)** 07:00 UTC 10 January.

is directing the AR meridionally to the coast with precipitation maxima on the windward slopes ahead of the warm front (Fig. 5.13a, orange shading, also Fig. C.1a). Due to the sharp horizontal temperature gradient between the cold air pool over Prydz Bay and the warm sector of the cyclone, the thermal wind is directed to the east and leads to backing winds with height. This thermal wind leads to a barrier wind over Prydz Bay, which protects the Amery Ice Shelf from the large-scale flow. The north-easterly flow provides the ideal conditions for the generation of trapped OGWs, which are excited at the temperature inversion at the top of the boundary layer. The turbulence at the top of the OGWs might enhance aggregation, which is visible in the hydrometeor classification (Fig. 5.3c), the maxima of DFR (Fig. 5.3d), and the polarimetric variables (Fig. 5.7). Despite the advection of moisture by the AR and the intense aggregation, the foehn effect creates a tongue of relatively dry air that spreads over the Vestfold Hills leading to sublimation of snowfall below 1000 m a.s.l., as can be seen in the reflectivity profiles (Fig. 5.3a).

During Phase II, the surface cyclone has moved eastwards. Davis is in the warm sector, the cold air pool has been eroded (see also Fig. C.1c), which allows the moisture advected by the AR to enter Prydz Bay, leading to precipitation maxima on the windward slopes of the Ingrid Christensen Coast. Another consequence after the passage of the warm front is the weaker horizontal temperature gradient over Davis, which reduces the thermal wind, such that the flow is north-northeasterly at all heights (Fig. 5.13e). Since the flow is north-northeasterly, it does not impinge on the orography upstream of Davis, which prevents the generation of low-level OGWs above Davis. As a result, the boundary layer is moister, the sublimation is less intense and snowfall does reach the ground at Davis. The absence of low-level OGWs coincides with the lack of intense aggregation, which leads to overall smaller reflectivity values than during Phase I. A layer of moderate updraughts ($\sim 1\,\mathrm{m\,s^{-1}}$) between about 3000 m and 4000 m could be identified in Doppler velocity measurements and WRF simulations and is attributed to a gravity wave train located downstream of the ridge to the north-east of Davis. This moderate updraught is also associated with a bimodality in radar Doppler spectra, which

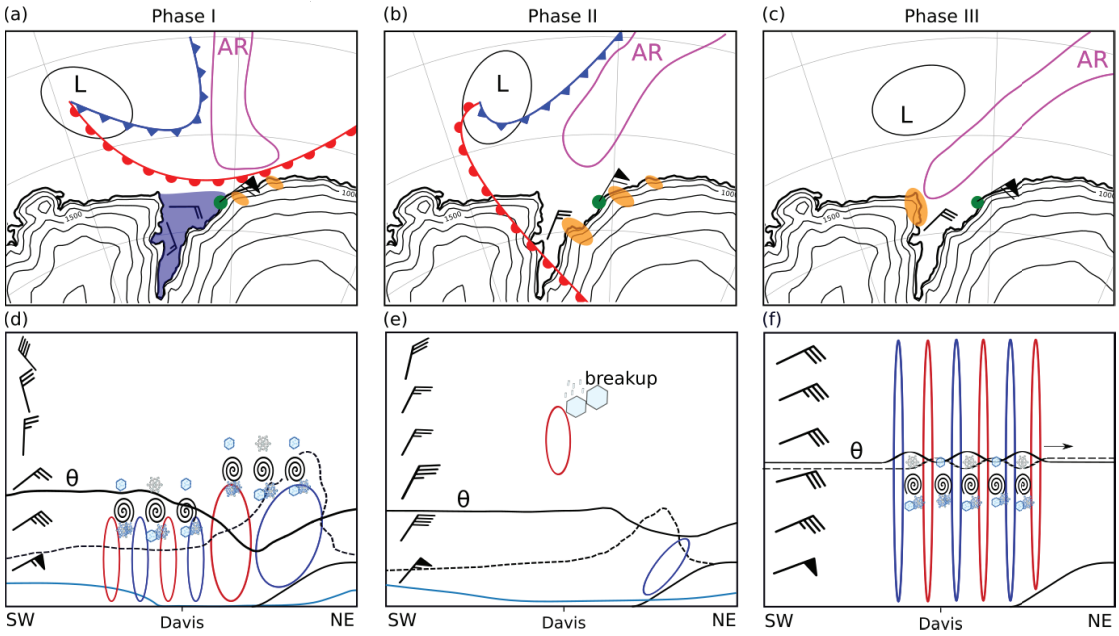

Figure 5.13 – Conceptual model of the three phases of the event. **(a)**-**(c)** maps as in Fig. 5.1. 'L' represents the low pressure system, the blue area the cold air pool. The orange shapes represent precipitation maxima, the green dot Davis. **(d)**-**(f)** cross-sections as in Fig. 5.6b. The blue and red shapes show downdraughts and updraughts respectively. The black line in the bottom panels shows an isentrope, the dashed line the height of saturation with respect to ice, and the blue line the qualitative variation of precipitation rate along the cross-section. Only the main microphysical processes are represented.

is likely due to secondary ice production by collisional breakup of ice crystals.

During Phase III, the low pressure system has split in two, the fronts have moved eastward with one of them, while the other one is directing the AR to the north of the Lars Christensen Coast (see Appendix C.3), leading to the largest precipitation accumulation over the whole event (Fig. 5.5). The flow is oriented north-easterly at all heights providing the ideal conditions for the generation of OGWs. As opposed to the OGWs during Phase I, they propagate downstream to Davis and lead to a succession of strong up- and downdraughts with a period of about 1 h visible in Doppler velocity measurements (Fig. 5.3b). The vertical gradient of relative humidity below 2000 m is the largest of the event (Fig. 5.4b) and lead to total sublimation within about 200 m of cloud base. Phase III marks the end of the event, before the PV cutoff and associated low pressure decays (not shown).

5.6 Climatological perspective

A question that arises from the results of this case study is: how representative is it in the climatology? We consider this question in this section, by discussing the possible climatological implications of our results using ERA5 reanalysis. Figure 5.5 indicates that orography played

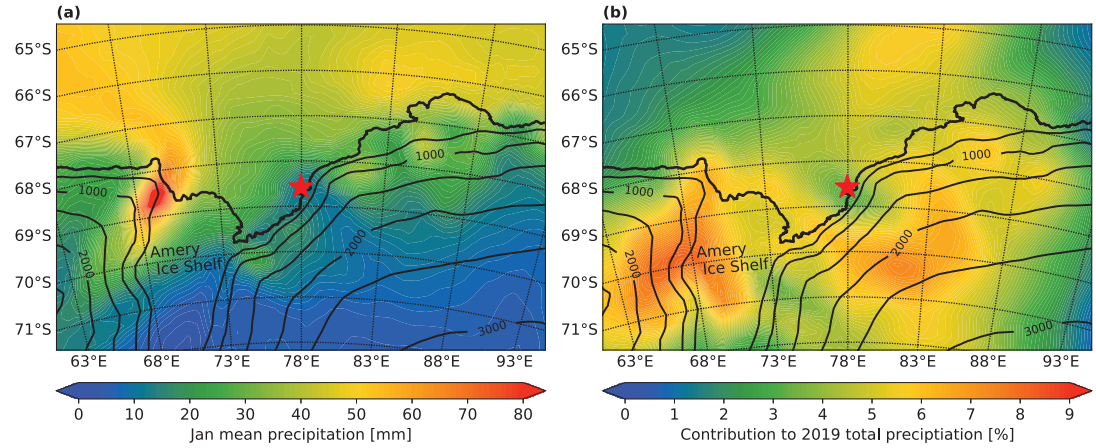

Figure 5.14 – **(a)** Precipitation climatology for January computed from 1969 to 2020. Davis is marked with the red star. **(b)** Ratio of the precipitation accumulated from 07 January 19 UTC to 10 January 19 UTC to the 2019 annual precipitation. All data are from the ERA5 reanalysis. The black contours show the ERA5 topography in m a.s.l. The thicker contour shows the coast and the ice-edge.

a major role in the distribution of precipitation during this event. This is supported by the results shown in Sect. 5.5 and we showed that the direction of the large-scale flow with respect to the orography dictates the precipitation accumulation pattern. Given that north-easterly is the most frequent flow direction during precipitation events over Davis (Fig. 4 of *Vignon et al.*, 2019), one might suspect that the precipitation accumulation shown in Fig. 5.5 could be climatologically representative. This is supported by the ERA5 climatology (Fig. 5.14a), which shows a maximum on the Lars Christensen Coast, in particular in its northernmost part, while the Ingrid Christensen Coast is much dryer, especially the region around the Vestfold Hills. This distribution is remarkably similar to the one of this event (Fig. 5.5), suggesting it is representative of the January climatology in terms of spatial distribution. The contribution of this event to the annual total precipitation of 2019 is up to 8% in the interior of the Lars Christensen Coast and around 2% in the Vestfold Hills (Fig. 5.14b). By comparing Fig. 5.14a with Fig. 5.5, we note that this event exceeds the January precipitation climatology over the northern part of the Lars Christensen Coast. This shows that this event can be qualified as extreme for the Lars Christensen Coast.

Figure 5.14 only allows us to compare the precipitation distribution of our case study with the climatology but does not make it possible to ascertain the main synoptic configurations associated with intense precipitation over Prydz Bay. Some recent studies however allow us to bring the large-scale features of our case study in a climatological perspective. *Yu et al.* (2018) studied the synoptic patterns associated with extreme precipitation at Progress station, which is located 110 km to the south-west of Davis on the Ingrid Christensen Coast. They

found that a dipole structure with a low (high) geopotential height anomaly to the north-west (north-east) of Prydz Bay together with a north-easterly advection of moisture is the dominant synoptic pattern associated with extreme precipitation at Progress station. They also mention that the ascending motions over Progress station provide favourable conditions for extreme precipitation. This synoptic description resembles the one presented in Sect. 5.4, suggesting that the synoptic conditions of our case study can be representative of extreme precipitation over Prydz Bay. Further recent studies showed that Prydz Bay is prone to intense precipitation events by enhanced meridional moisture advection. First, *Turner et al.* (2019) showed that 50% of the annual precipitation is received in less than 10 days of the heaviest precipitation over the Amery Ice Shelf. They attribute this to quasi-stationary depressions, which can occasionally transport moisture far into the Amery Ice Shelf in regions normally sheltered by the orography. The quasi-stationary nature of the PV cutoff described in Sect. 5.4 and the fact that it directs an increasingly more easterly flow (ideal for orographic enhancement on the Lars Christensen Coast) explains the relatively high contribution to the 2019 annual precipitation on the Lars Christensen coast (Fig. 5.14b). Second, *Portmann et al.* (2021) showed that Prydz Bay is located poleward of a band of high frequency of PV cutoffs around Antarctica (their Fig. 3). Furthermore, Chap. 3 of *Portmann* (2020) investigated the relevance of PV cutoffs for precipitation. They found that cutoffs involving enhanced meridional moisture transport contribute the most to extreme precipitation events. Since our case both features a PV cutoff to the north of Prydz Bay and intense meridional moisture transport, it suggests that similar synoptic configurations are common and do contribute to extreme precipitation over Prydz Bay. *Wille et al.* (2021) studied the precipitation impact of ARs in Antarctica. They showed that the frequency of ARs above Prydz Bay was about 2 days per year. They also investigated the attribution of extreme precipitation events to ARs. Their Fig. 4c shows a strong dipole over the Ingrid Christensen Coast, with the Vestfold Hills being located in a region with less than 10% of EPEs attributed to ARs, while further north-east on the coast up to 50% of EPEs are attributed to ARs. This suggests that the contribution of ARs to EPEs over Prydz Bay is highly variable, consistent with Figs. 5.5 and 5.14b. We showed that local processes can be determinant in how much an AR event contribute to the annual precipitation accumulation. Furthermore, Fig. 3b of *Wille et al.* (2021) shows large AR-related snowfall on the eastern sides of ice ridgelines, including the one to the north-east of Davis. The Vestfold Hills also appear as a minimum of total AR-related snowfall. This suggests that our case study is representative of large snowfall accumulation from ARs around East Antarctica. Finally, it also confirms our finding that local processes related to the orography, such as a foehn wind, can determine the fate of large-scale moisture advection from ARs. The study of *Grazioli et al.* (2017b) shows that the Vestfold Hills are in a region of a maximum ratio of sublimated snowfall with up to 48% of total snowfall sublimating before reaching the ground. They attribute low-level sublimation to dry katabatic winds, but they also mention that foehn winds can play an important role in the Antarctic Peninsula. Our study shows that foehn winds can lead to total snowfall sublimation also in East Antarctica and be as efficient as katabatics in doing so, at least at the scale of one event. While the foehn effect is a local process, the dynamical triggering comes more often from the large-scale flow. As stated by *Bozkurt et al.* (2018), it is hence difficult to totally disentangle

the role of local versus large-scale processes during foehn events. In the end, the interactions between the synoptic flow, the orography, and the regional-scale circulation determine the impact on precipitation.

Overall, the ERA5 climatology shown in Fig. 5.14 and the studies of *Portmann et al.* (2021), *Turner et al.* (2019), and *Wille et al.* (2021) show that we can expect the synoptic configuration of our case study to be representative of EPEs over Prydz Bay, at least in austral summer. In this view, we can hypothesise that the processes at play for snowfall sublimation over Davis shown in Sect. 5.5 might substantially contribute to the precipitation climatology of the Vestfold Hills.

5.7 Conclusions

In this study, we analysed the precipitation distribution and microphysics associated with an intense meridional moisture transport affected by OGWs over Prydz Bay, Antarctica. The complementary nature of remote-sensing instruments and WRF simulations allowed us to link local observations with the complex dynamics of this event. We divided the event into three distinct phases. Our findings can be summarised as follows:

1. The direction of the synoptic flow was the dominant factor driving the occurrence of OGWs over Davis, with an easterly to north-easterly flow favouring the development of low-level OGWs, while a north-northeasterly flow inhibited such low-level OGWs. The presence of a statically stable layer favoured the trapping of the OGWs below 2000 m during Phase I.

2. A foehn effect produced a dry airflow that spread over the Vestfold Hills and led to total snowfall sublimation during Phase I and Phase III. During Phase II, the wind backed to north-northeasterly inhibiting the formation of low-level OGWs above Davis and hence reducing the dryness of the boundary layer, which led to light snowfall reaching the ground.

3. The turbulence generated at the top of the trapped OGWs during Phase I might have led to intense aggregation, which was observable in dual-polarisation and dual-frequency radar variables. During Phase II, an updraught associated with a gravity wave train was visible in the radar Doppler velocity. Analyses of the Doppler spectrograms showed that this updraught was associated with a bimodality, which we attributed to the production of secondary ice by collisional breakup of ice particles. During Phase III, non-stationary OGWs can be clearly seen in vertical Doppler velocity measurements and lead to a fluctuation of the level of maximum reflectivity. Those OGWs are qualitatively well represented by WRF, although the magnitude is underestimated and the phase is shifted.

This study showed that despite the intense meridional moisture advection by an AR, local processes tied to the orography determined the spatial and temporal distribution of precipitation

over Prydz Bay. This stresses the importance of studying local effects when interpreting the impact of ARs in terms of surface precipitation at the regional scale. Moreover, it suggests that climate models projections and satellite measurements over regions where local processes dictate the precipitation patterns should be interpreted with care. Similarly to the study of *Grazioli et al.* (2017b), we showed that the fate of precipitation in Antarctica often comes down to complex interactions between the large-scale flow, the orography, and regional circulations, such as foehn and katabatic winds. Future studies should concentrate on the synoptic configurations during precipitation and sublimation events over Prydz Bay to determine whether the mechanisms proposed here can explain the rather peculiar precipitation climatology of Prydz Bay, and in particular of the Vestfold Hills.

6 Conclusions

6.1 Summary of the results

Precipitation results from a series of meteorological processes occurring between the large- and micro-scale. While microphysical processes determine the density, shape, and size distribution of hydrometeors, atmospheric dynamics provide boundary conditions that influence these processes. In particular for snowfall, turbulence and vertical motions have a significant impact on microphysics. The role that specific dynamical processes (e.g. WCBs and OGWs) play in snowfall microphysics needs to be further investigated.

Two international field campaigns organised in contrasting climatic regions were the perfect opportunity to get novel insights into snowfall microphysics. We first collected data in the Taebaek mountains in South Korea during the PyeongChang 2018 Olympic and Paralympic winter games (Chap. 2). We then collected measurements of clouds and precipitation (Chap. 3) at Davis station, East Antarctica. Thanks to the synergy between radar and in situ measurements collected during these two campaigns, and available atmospheric models simulations, we investigated the influence of dynamics on snowfall microphysics during two precipitation events in South Korea and Antarctica (Chaps. 4 and 5, respectively).

Overall, this thesis contributes to a better understanding of how dynamical processes occurring at different scales can influence snowfall microphysics. While specific conclusions are given at the end of Chaps. 2 to 5, we provide here the overarching conclusions of this thesis and answer the questions stated in Sect. 1.4.

Unprecedented cloud and precipitation measurements in South Korea and Antarctica

How do the datasets compare in terms of snowfall microphysics and how representative are they with respect to the regional climatology?

The ICE-POP 2018 campaign was relatively dry with 60% of the winter climatological precipitation accumulation. One single event contributed to 62% of the total winter accumulation

(December 2017–February 2018). Snowflake photographs showed that aggregates were the dominant hydrometeor type, while graupel particles represented 12% of the dataset. Radiometer measurements and hydrometeor classifications confirmed the presence of SLW during all the events we analysed.

The PLATO campaign was even drier with only 43% of the climatology of precipitation accumulation over the same period. Aggregates and graupel particles were the dominant hydrometeor classes, which shows that aggregation and riming can play a significant role in snowfall microphysics during the summer in Antarctica. We observed SLW layers during two precipitation events, which were likely generated by either cloud-top radiative cooling or by boundary layer turbulence. Hydrometeor classifications confirmed the presence of SLW.

What is the contribution of these datasets to the scientific community and what could they be used for?

The dataset collected during the ICE-POP 2018 campaign is openly available to the scientific community in a public repository (*Gehring et al.*, 2020a) and is thoroughly described in Chap. 2. It represents a unique dataset combining radar measurements at different frequencies with ground-based in situ observations in a region where such measurements were not previously available. In addition to the work presented in this thesis, the dataset was already used for other scientific publications (e.g. *Billault-Roux and Berne*, 2021; *Jeoung et al.*, 2020; *Planat et al.*, 2021). It is complementary to similar datasets in other regions and could be used to confirm microphysical studies conducted in different geographical contexts. In particular, we did not investigate the impact of the orography and this constitutes a potential for further research using this dataset.

The PLATO 2019 measurements constitute one of the rare multi-frequency radar datasets collected in Antarctica and will be publicly available in the near future. It could be used to (i) evaluate the representation of cloud and precipitation microphysics in weather and climate models and (ii) further investigate the mechanisms leading to SLW in Antarctica (e.g. *Alexander et al.*, 2021). More generally, the dataset contributes to broadening the available instrumental knowledge of cloud and precipitation processes in Antarctica.

New insights into snowfall microphysical processes in a WCB

What were the most significant dynamical processes influencing the evolution, distribution and microphysics of precipitation?

Chapter 4 provides new observational insights into snowfall microphysical processes associated with different phases of a WCB, namely the inflow, ascent, and outflow. We showed that the large-scale ascent within the WCB was strong enough to produce SLW. Embedded updraughts, identified with vertical Doppler velocity measurements, likely generated additional SLW, which enhanced riming. The WCB was associated with strong wind shear at its lower boundary, which produced turbulence and enhanced aggregation by increasing the

probability of collision between particles. The turbulence and updraughts were identified in Doppler spectrum measurements from a scanning and a vertically-pointing radar. Vertical profiles of polarimetric variables allowed us to identify riming and aggregation as a decrease in Z_{DR} and an increase in Z_H. We hypothesised that the increase in K_{dp} was likely due to secondary ice production by droplet shattering and ice-ice collision.

At which spatial scales did these processes take place and how were they influenced by geographical features?

We showed that the dominating dynamical processes affecting the microphysics occurred at the large-scale and were not significantly impacted by the Taebaek Mountains. This is not necessarily the case for WCBs crossing major mountain ranges, where the orography can significantly contribute to the large-scale ascent (e.g. *Boettcher et al.*, 2021).

Novel findings on the impact of OGWs on snowfall in Antarctica

What were the most significant dynamical processes influencing the evolution, distribution and microphysics of precipitation?

We showed that foehn winds associated with low-level OGWs can lead to total snowfall sublimation over Davis, Antarctica (Chap. 5). The direction of the synoptic flow with respect to the local orography determined the intensity of low-level OGWs, which in turn directly influenced the distribution and microphysics of snowfall. The periods with the most intense low-level OGWs were associated with total snowfall sublimation. Dual-frequency and polarimetric variables allowed to identify layers dominated by aggregation. We hypothesised that the turbulence generated at the top of the low-level OGWs were likely responsible for the enhanced aggregation. During the period with no significant low-level OGWs, an updraught was visible at about 3000 m a.s.l. in vertical Doppler velocity measurements. The Doppler spectra revealed a persistent bimodality associated with this updraught, which was likely due to secondary ice production by the collisional breakup of ice particles.

At which spatial scales did these processes take place and how were they influenced by geographical features?

This case study showed that despite intense large-scale moisture advection, the evolution and distribution of precipitation were determined by local processes tied to the orography. We proposed that foehn winds generated by north-easterly flows during precipitation events over Prydz Bay could explain the precipitation climatology of the Vestfold Hills. We discussed this hypothesis based on recent studies (*Portmann et al.*, 2021; *Turner et al.*, 2019; *Wille et al.*, 2021) and suggested directions for future studies.

The contrasting precipitation results of two intense moisture advection events

What were the common characteristics and the main differences between the two case studies?

The synoptic situation during the two case studies was surprisingly similar: they both featured a PV cutoff associated with a surface cyclone and intense moisture advection. While we focused on the large-scale ascent of the WCB during the first case study and the moisture transport of the AR in the second one, they essentially featured the same synoptic ingredients. Yet the result on precipitation was drastically different. In the first case study, the microphysics was dominated by processes tied to the large-scale flow in the WCB, while in the second one, local processes linked to the orography determined the precipitation's evolution and distribution. On the other hand, the conditions for these local processes to occur were largely controlled by the orientation of the large-scale flow, showing that it is not possible to fully disentangle the role of local versus large-scale processes in precipitation microphysics.

The synergy between atmospheric model simulations and radar measurements

The case studies of Chaps. 4 and 5 showed that the dynamical and thermodynamical fields provided by an atmospheric model, and the detailed microphysical and local dynamical processes revealed by radar measurements are complementary and provide a comprehensive picture of the complex interactions between dynamics and microphysics.

6.2 Perspectives and open questions

The two case studies in South Korea and Antarctica showed that snowfall microphysics can be dominated by either large- or local-scale processes. In particular, we identified in the first case study the role of a WCB and in the second one of OGWs on snowfall microphysics. While these case studies provided novel findings into snowfall dynamics and microphysics, their validity in other situations and their contribution to the climatology remain to be determined. Further investigations will bring the results of these case studies into perspective. Prospects for future studies and open questions are discussed in the following.

How can we improve the observations of the microphysical processes associated with WCB airflows?

Only a few studies investigated specifically the microphysics inside WCBs with measurements. The pioneering work of *Keppas et al.* (2018) motivated the case study presented in Chap. 4 and both studies show that the WCB was associated with SLW production in the large-scale ascent and the embedded updraughts, as well as with turbulence in a sheared environment, which impacted the microphysics. More recently *Binder et al.* (2020) investigated the cloud and precipitation associated with WCBs during nine Northern Hemisphere winters with ERA5 reanalysis (*Hersbach et al.*, 2020), CloudSat (*Stephens et al.*, 2002, 2009), and CALIPSO (*Winker*

et al., 2003) data. The study of *Binder et al.* (2020) is the first observations-based climatology of WCBs. They showed that embedded updraughts and SLW are ubiquitous features of the inflow and ascent phases of WCBs, suggesting that the riming observed in our case study could be a typical microphysical signature of WCBs. *Boettcher et al.* (2021) were able to match observations from aircraft, lidar, and radar to the three different phases (inflow, ascent, and outflow) of a WCB thanks to a tracer released in the WCB inflow. This allowed them to better characterise the humidity conditions in these three different phases of the WCB and to evaluate the model performances along them. It represents a crucial step towards model verification of thermodynamics and microphysics inside WCBs. We hypothesise that more observational studies of the dynamics and microphysics inside WCBs will make it possible to (i) verify whether the results of *Keppas et al.* (2018) and those presented in Chap. 4 are inherent of WCB airflows, and (ii) create a larger database of case studies serving as a test-bed for model verification. Such observations should be systematically carried with both airborne and ground-based measurements and, if possible, completed by Lagrangian matches as in *Boettcher et al.* (2021) or trajectory computations.

What is the fate of AR events in Antarctica?

The findings of Chap. 5 suggest that the precipitation accumulation resulting from an AR event can have a large spatial variability. This result is consistent with the AR climatology of *Wille et al.* (2021), which shows that the contribution of ARs to precipitation on the coast of East Antarctica is spatially heterogeneous. We suggest that precipitation during AR events on the coast of East Antarctica be further investigated to understand which mechanisms are responsible for the high spatial variability of precipitation associated with ARs. This investigation requires long-term precipitation measurements at various locations in Antarctica, as discussed in the next paragraph.

How can we conduct year-round observations in Antarctica?

Most intensive field campaigns in Antarctica are restricted to summer seasons, with only simpler measurements conducted year-round, due to harsher meteorological conditions and fewer human resources available during winter. However, most precipitation falls during this period (*King and Turner*, 1997). There is hence a need for more year-round observations of precipitation in Antarctica. This represents a technical challenge in at least three different aspects: (i) the source of power for the instruments, (ii) the communication with the instruments and data transfer, and (iii) ensuring that the instruments can operate without human interventions throughout the winter. The Atmospheric WAter Cycle over Antarctica (AWACA) project addresses these aspects and aims to conduct year-round measurements between 2023 and 2026 along different transects from the coast to the Antarctic Plateau. The data collected will represent the first year-round observations of automatic measurements with both ground-based in situ and remote sensing instruments in unmanned locations of Antarctica. We suggest that, when available, this dataset be used to study the mechanisms

responsible for snowfall sublimation and investigate if foehn winds, in addition to katabatics, also significantly contributes to sublimation. On a longer-term perspective, we propose that permanent year-round remote sensing measurements of clouds and precipitation be conducted at Antarctic stations to significantly improve our understanding of the ice sheet mass balance and cloud radiative forcing.

Climatology of foehn at Davis

The case study presented in Chap. 5 showed that foehn winds can lead to total snowfall sublimation and represents one of the rare accounts of foehn in East Antarctica. Foehn has been more extensively studied in other regions of Antarctica, such as the Peninsula (e.g. *Elvidge et al.*, 2015; *Grosvenor et al.*, 2014) and the McMurdo Dry Valleys (e.g. *Steinhoff et al.*, 2013; *Speirs et al.*, 2010). In the latter, a climatology of foehn has been recently conducted by *Speirs et al.* (2013) with automatic weather stations. They showed that the regional climate variability is driven by foehn winds. The Vestfold Hills and the McMurdo Dry Valleys are considered Antarctic oases. It is yet unknown what drives the climate of the Vestfold Hills. We propose that carrying a foehn climatology study in the Vestfold Hills will allow investigating if foehn plays an important role in the Vestfold Hills' climate.

“Difficulties are just things to overcome, after all.”

Ernest Shackleton

End of a field trip in Antarctica, 22 December 2018, Photo by J. Gehring

A Appendix of Chapter 3: elevation offset correction

As described in Sect. 3.4.4, an elevation offset likely due to a wrong encoding of the antenna position affected the measurements of the 08 to 10 January 2019 event. The elevation offset depends on the azimuth of the RHI, suggesting that the whole horizontal plane was slanted. From 03:20 UTC 08 January until 03:36 UTC 09 January, the elevation data were only affected by an offset of about 1°(Table A.2). The radar had to be turned off from 03:40 UTC to 05:00 UTC. After starting again the radar at 05:00 UTC 09 January a more significant offset of about −7° appeared. This offset was not well visible in the PPI images that we were checking during the campaign and we hence only discovered it after checking the RHIs at around 12:00 UTC. We had to stop the radar and re-position the antenna manually, in the hope that the encoder would then read the elevation correctly. We restarted again the radar at 13:05 UTC and the large offset was not present anymore, but we still had an offset that we estimated to be about 3°, depending on the RHI (Table A.2). To estimate the elevation offset for each type of RHIs and for the three different periods (before, in between, and after the periods the radar was turned off), we assume that the base of the cloud/precipitation should be approximately horizontal over a distance of 40 km. The steps we applied to compute the elevation offset are as follows:

1. Detect the lowest gates satisfying the conditions described in Table A.1.
2. Fit a line through these lowest gates: the slope of this line is the offset in elevation (Fig. A.1a).
3. If multiple cloud bases are present at different horizontal distances, fit a line through each of these sections. The offset for this RHI is defined as the average of the slopes weighted by the number of gates in each section.
4. Compute the distribution of the offsets and take the mode as the elevation offset for this set of RHIs (Fig. A.1f).
5. The offset is then subtracted to the elevation of all RHIs of this particular set and written in the metadata.

Table A.1 – Conditions to select the lowest gates of an RHI. ρ_{hv} if the copolar cross correlation coefficient, SNR_H is the signal to noise ratio at horizontal polarisation, R (H) is the horizontal (vertical) distance to the radar.

Variable	Condition
Z_H	≥ 10 dBZ
ρ_{hv}	≥ 0.8
SNR_H	≥0 dB
R	< 20 km
H	> 1000 m

Table A.2 – Values of the estimated elevation offsets (additive) for the three periods identified and the three RHIs azimuths.

	23°RHI	52 °RHI	101 °RHI
00 UTC 08 Jan–04 UTC 09 Jan	1.4	1.7	0.6
05 UTC 09 Jan–12 UTC 09 Jan	−5.9	−6.4	−9.7
13 UTC 09 Jan–10 UTC 10 Jan	3.7	3.6	0.9

Figure A.1 illustrates the method. To control that the correction is satisfying, we visually checked the two following criteria: (i) the RHI base should be approximately horizontal and (ii) the minimum of Doppler velocity should be measured at 90° elevation (if not significant vertical motions are present). This gave satisfying results to keep all RHIs of this event. Table A.2 gives the values of the elevation offsets estimated for each type of RHI and periods.

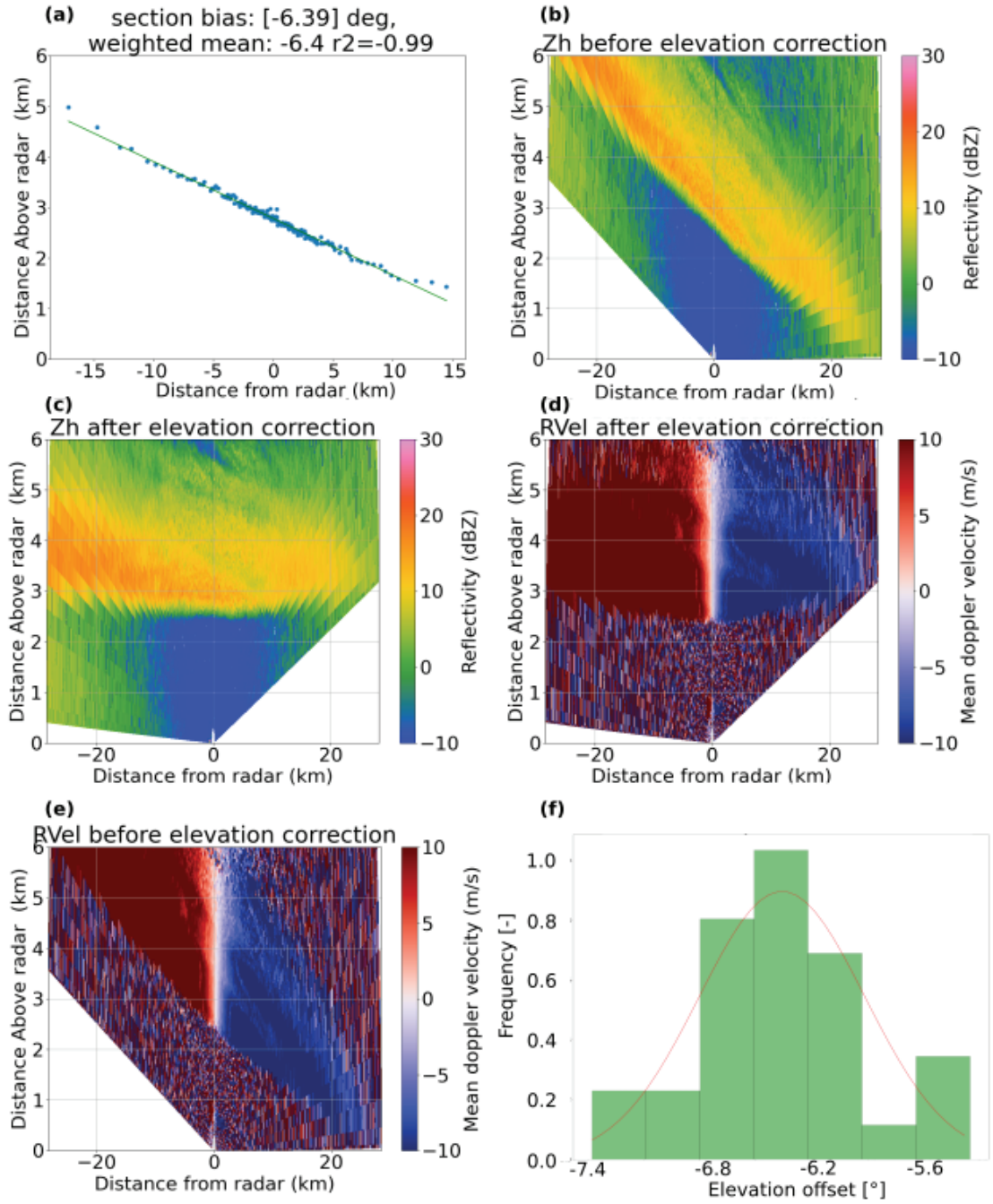

Figure A.1 – Illustration of the elevation correction on an RHI at 52°at 09:06 UTC 09 January 2019: (a) lowest gates detected satisfying the conditions of Table A.1 (blue dots), linear regression (green line), the weighted mean of the slope and the correlation coefficient $r2$ are given in the title. (b), (c) RHI of Z_H and V_D before ((d) and (e) after) the elevation correction. (f) Histrogram of the elevation offsets computed for the RHIs at 52° azimuth from 04:10 to 12:10 UTC on 09 January 2019. The red line shows a fitted probability density function. The mode is −6.4° and was used as the elevation offset for the corresponding period and RHIs.

B Appendix: of Chapter 4: estimation of the critical vertical velocity

In this appendix we show details on the estimation of the critical vertical velocity U_z^* needed to form and maintain liquid water in the presence of both ice crystals and snow. *Korolev and Mazin* (2003) showed that U_z^* can be expressed as a function of pressure, temperature, number concentration and mean size of ice crystals. We use Fig. 10 in *Korolev and Mazin* (2003), which gives the relation between U_z^* and the product of the number concentration of ice particles N_i and the characteristic size of ice particles r_i for temperatures between −35 and −5°C. Since in our case we have both ice and snow particles, we compute N_i and the number concentration of snow particles N_s separately such that the total number concentration is $N_\mathrm{tot} = N_\mathrm{i} + N_\mathrm{s}$. We also compute the characteristic size of the mixture of ice and snow particles r_tot. The expression for N_i is given by Eq. (7.40) of *ECMWF* (2016):

$$N_\mathrm{i} = 100 \exp[12.96\,(e_\mathrm{sl} - e_\mathrm{si})/e_\mathrm{si} - 0.639], \tag{B.1}$$

Table B.1 – Values of the different variables used in the computation of U_z^*. Data from IFS analysis and radiosoundings at 09:00 UTC are used. The pressure p used is 610 hPa; temperature T is −13 °C.

Variable	Value	Source
q_i	$1 \times 10^{-4}\,\mathrm{kg\,kg^{-1}}$	From IFS analysis Fig. 4.3
q_s	$6.5 \times 10^{-4}\,\mathrm{kg\,kg^{-1}}$	From IFS analysis
ρ_i	$920\,\mathrm{kg\,m^{-3}}$	Density of ice
ρ	$0.82\,\mathrm{kg\,m^{-3}}$	At $p = 610$ hPa, $T = -13$ °C and $\mathrm{RH_l} = 95$ %
e_si	198 Pa	At $p = 610$ hPa, $T = -13$ °C and $\mathrm{RH_l} = 95$ %
e_sl	224 Pa	At $p = 610$ hPa, $T = -13$ °C and $\mathrm{RH_l} = 95$ %
N_i	$2895\,\mathrm{m^{-3}}$	Eq. (B.1)
Λ	804	Eq. (B.3)
N_s	$2490\,\mathrm{m^{-3}}$	Eq. (B.2)
r_tot	309 µm	Eq. (B.7)

where e_{sl} (e_{si}) is the saturation vapour pressure with respect to liquid (ice). The expression for N_s is given by Eqs. (7.15) to (7.19) in *ECMWF* (2016). In our case it is simply expressed by

$$N_s = \Lambda^{-1} N_{0s}, \tag{B.2}$$

where $N_{0s} = n_{as} = 2 \times 10^6$ (Eq. 7.16 and Table 7.1 of *ECMWF*, 2016), and Λ is given by Eq. 7.18 of *ECMWF* (2016):

$$\Lambda = \left(\frac{n_{as} a_s \Gamma(3)}{q_s \rho} \right)^{1/(b_s+1-n_{bs})}. \tag{B.3}$$

$$\Gamma(3) = \int_0^\infty D^2 e^{-D} \, \mathrm{d}D = 2, \tag{B.4}$$

where $a_s = 0.069$, $b_s = 2$ and $n_{bs} = 0$ are given in Tables 7.1 and 7.2 of *ECMWF* (2016). The expression for r_i can be found by stating that the characteristic volume of an ice particle V_i is

$$V_i = \frac{\rho \, q_i}{\rho_i \, N_i}, \tag{B.5}$$

where ρ is the air density, ρ_i the density of ice particles and q_i the mixing ratio of ice. Assuming spherical particles, we can express r_i with

$$r_i = \left(\frac{3 \, \rho \, q_i}{4 \, \rho_i \, N_i \, \pi} \right)^{1/3}. \tag{B.6}$$

Since snow particles are spherical in IFS and considered to have the same density as ice, we have $\rho_i = \rho_s$. We define r_{tot} as

$$r_{tot} = \left(\frac{3 \, \rho \, (q_i + q_s)}{4 \, \rho_i \, N_{tot} \, \pi} \right)^{1/3}. \tag{B.7}$$

Using the values described in Table B.1, we find $N_{tot} r_{tot} = 1.7 \, \mu\mathrm{m \, cm^{-3}}$, which we can use in Fig. 10 of *Korolev and Mazin* (2003) to read U_z^* at about $-13\,^\circ\mathrm{C}$ and find $0.1 \, \mathrm{m \, s^{-1}}$.

C Appendix of Chapter 5: supplementary figures

C.1 WRF 9-km resolution domain

Figure C.1 shows meteorological fields of the WRF 9-km resolution domain. The barrier jet ahead of the cold air pool over the Amery Ice Shelf and the precipitation along the warm front are well visible in Fig C.1a, b. Once the cold air pool has been eroded, the barrier jet is not present anymore (Fig C.1c, d). The precipitation maxima are on the windward sides of the ridges of the Ingrid Christensen Coast in Fig C.1a-c, whereas at the end of the event the increasingly more easterly flow directs the moisture directly to the northernmost part of the Lars Christensen Coast (Fig C.1d)

C.2 Discussion on the origin of the updraught during Phase II

We provide here more information on the possible origins of the updraught identified as a Doppler velocity minimum at around 3000 m during Phase II in Fig. 5.3. The horizontal field of vertical wind velocity at 3000 m a.s.l. (Fig. C.2a) shows that (i) the updraughts are the strongest at the foot of the ridge to the east of Davis and (ii) OGWs are visible upstream of the ridge to the south of Davis. We hypothesise that the origin of the updraught above Davis could be either due to a lateral propagation of the updraught at the foot of the ridge to the east of Davis or an upstream propagation of the OGWs generated on the ridge to the south of Davis. The latter hypothesis is supported by the cross-section of Fig. C.2b, which suggests that these OGWs could be propagating upstream from their generation point to Davis.

C.3 Additional ERA5 synoptic maps

This section provides additional ERA5 synoptic maps to see the larger-scale evolution of the event. At 06:00 UTC 09 January (Fig. C.3), the cutoff is being reabsorbed to the stratospheric reservoir and is directing a north-easterly flow to Prydz Bay. According to *Portmann et al.* (2021), PV cutoffs around Antarctica end their life cycle preferentially by reabsorption. At 00:00

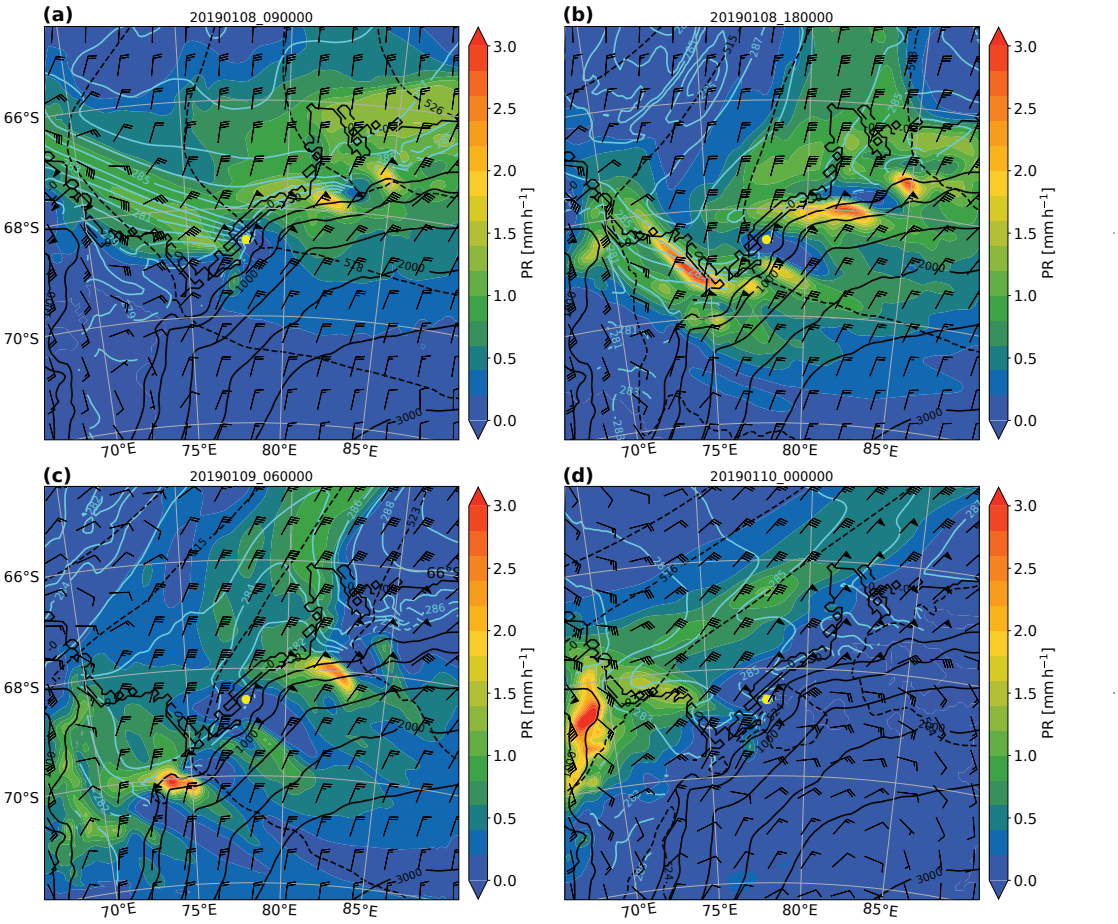

Figure C.1 – Maps of the WRF 9-km resolution domain of precipitation rate (shading in $mm\,h^{-1}$), horizontal wind at 850 hPa (barbs following meteorological standard notation), and potential temperature (cyan contours, masked below 100 m a.s.l.) at 800 hPa (about 1200 m a.s.l.). The black contours show the topography (labels in m a.s.l.). (a) at 09:00 UTC, (b) at 18:00 UTC 08 January 2019, (c) at 06:00 UTC 09 January, and (d) at 00:00 UTC 10 January.

UTC 10 January (Fig. C.4) there are two surface low pressure minima. One moved eastward with the fronts, while the other one is quasi-stationary to the north of Prydz Bay and continues to direct a north-easterly flux.

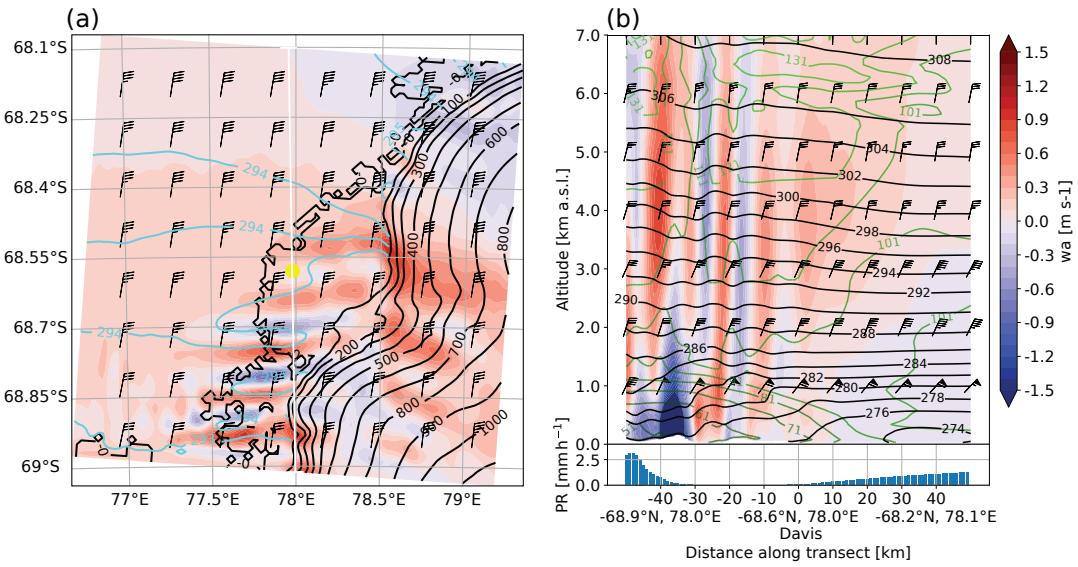

Figure C.2 – WRF 1-km resolution domain at 18:00 UTC on 08 January 2019. (a) map of vertical wind velocity (shading), horizontal wind (barbs following meteorological standard notation), and potential temperature (cyan contours) at 670 hPa (about 3000 m a.s.l.). The black contours show the topography (labels in m a.s.l.). (b) cross-section, corresponding to the white line in (a), of vertical wind velocity (shading in $m\,s^{-1}$), potential temperature (black contours, labels in K), RHi (colored contour lines in %) and horizontal wind (barbs following meteorological standard notation) and precipitation rate along the cross-section (blue bars in mm^{-1}).

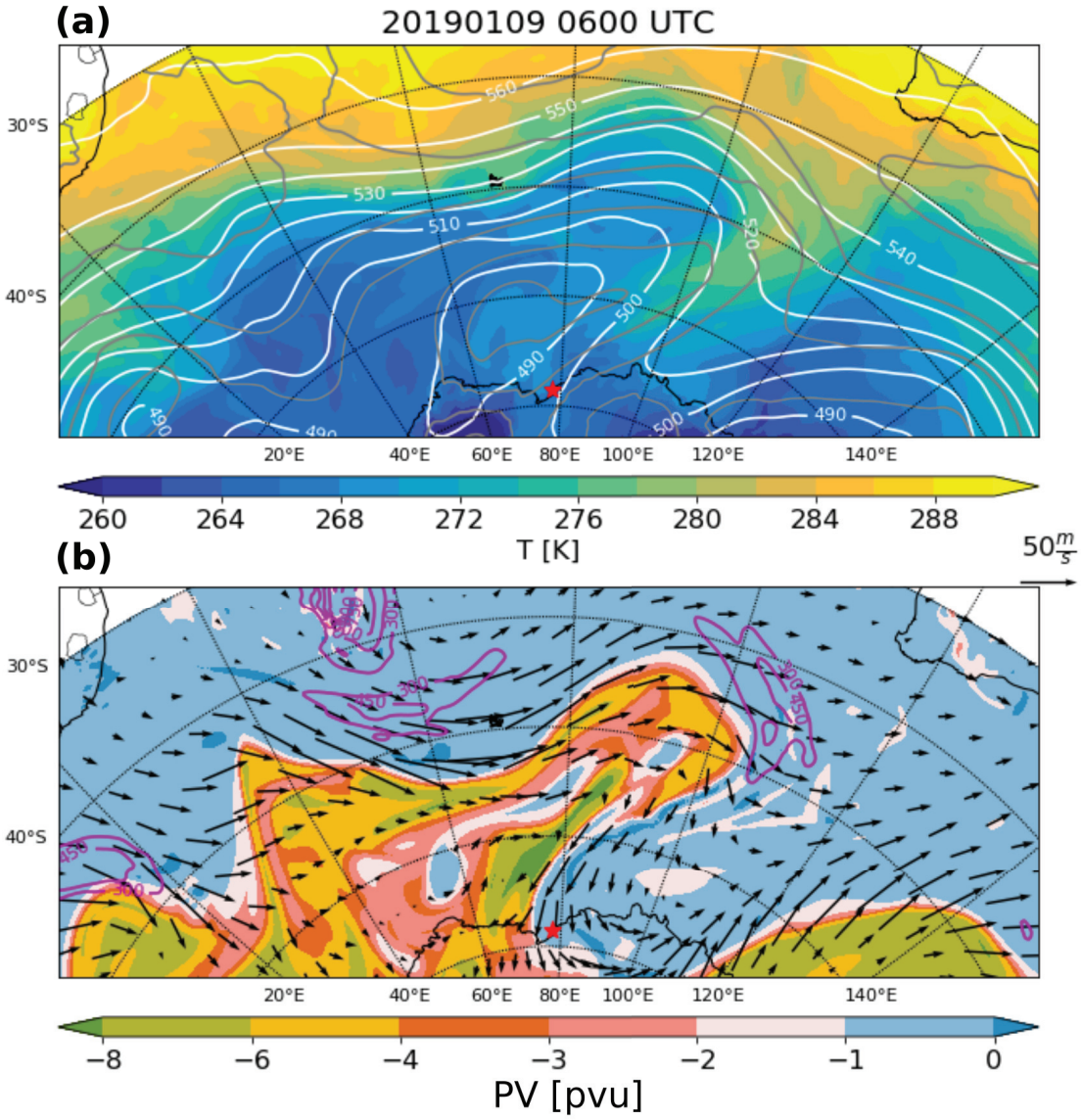

Figure C.3 – Synoptic situation at 06:00 UTC 09 January 2019 from ERA5 data. (a) Potential temperature at 850 hPa (shading), sea level pressure (grey contours), and 500 hPa geopotential height (white contours, labels in decametre). (b) Potential vorticity (shading in potential vorticity unit (pvu) = $\mathrm{K\,m^2\,kg^{-1}\,s^{-1}}$) and wind (arrows in $\mathrm{m\,s^{-1}}$ at the 315 K isentrope, and integrated vapour transport (magenta contours, labels in $\mathrm{kg\,m^{-1}\,s^{-1}}$)

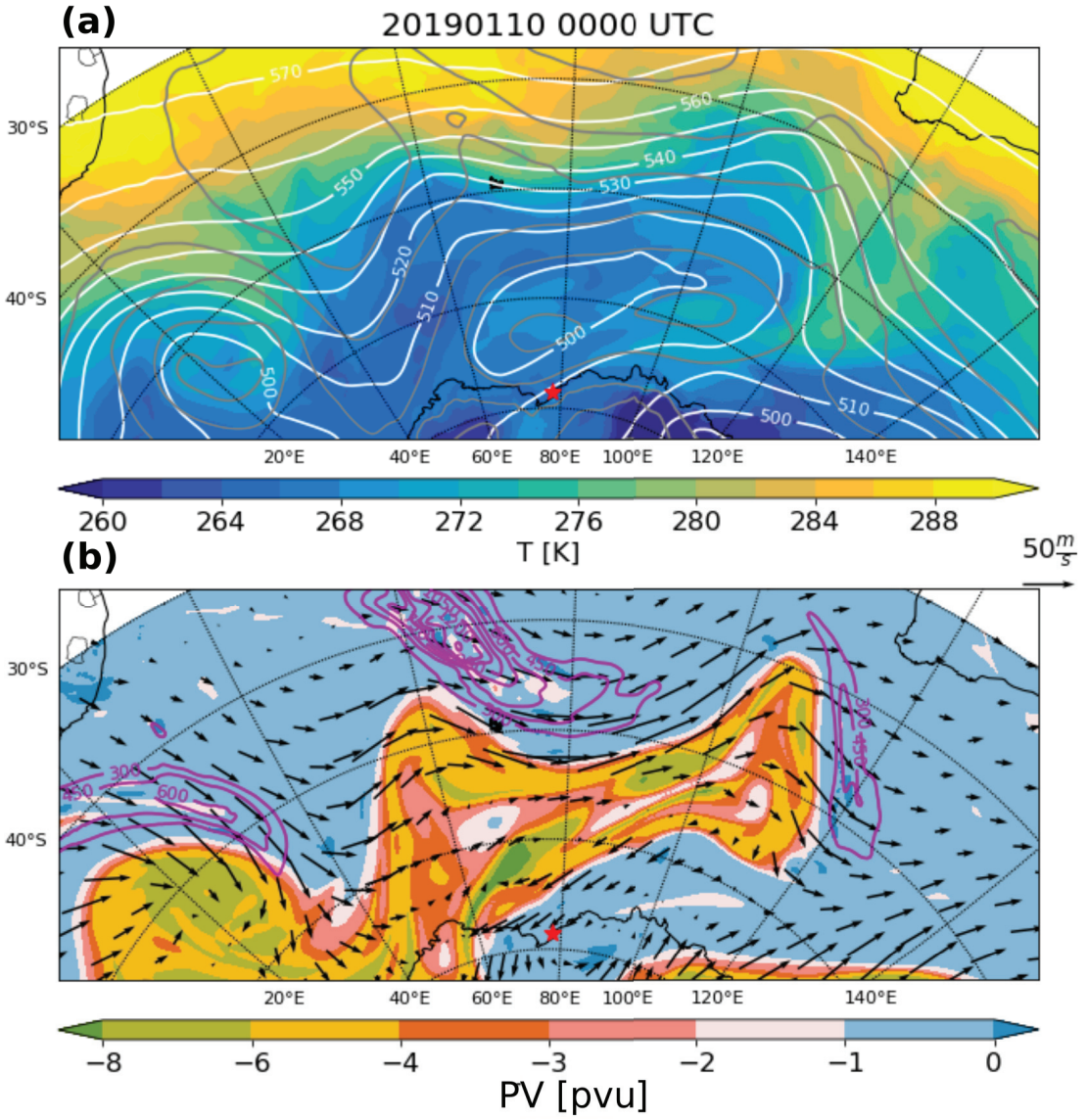

Figure C.4 – Synoptic situation at 06:00 UTC 09 January 2019 from ERA5 data. (a) Potential temperature at 850 hPa (shading), sea level pressure (grey contours), and 500 hPa geopotential height (white contours, labels in decametre). (b) Potential vorticity (shading in potential vorticity unit (pvu) = $\mathrm{K\,m^2\,kg^{-1}\,s^{-1}}$) and wind (arrows in $\mathrm{m\,s^{-1}}$ at the 315 K isentrope, and integrated vapour transport (magenta contours, labels in $\mathrm{kg\,m^{-1}\,s^{-1}}$)

Bibliography

Agosta, C., et al. (2019), Estimation of the Antarctic surface mass balance using the regional climate model MAR (1979–2015) and identification of dominant processes, *The Cryosphere*, *13*(1), 281–296, doi: 10.5194/tc-13-281-2019.

Alexander, S. P., and D. Murphy (2015), The Seasonal Cycle of Lower-Tropospheric Gravity Wave Activity at Davis, Antarctica (69°S, 78°E), *Journal of the Atmospheric Sciences*, *72*(3), 1010–1021, doi: 10.1175/JAS-D-14-0171.1.

Alexander, S. P., and A. Protat (2018), Cloud Properties Observed From the Surface and by Satellite at the Northern Edge of the Southern Ocean, *Journal of Geophysical Research: Atmospheres*, *123*(1), 443–456, doi: 10.1002/2017JD026552.

Alexander, S. P., and A. Protat (2019), Vertical Profiling of Aerosols With a Combined Raman-Elastic Backscatter Lidar in the Remote Southern Ocean Marine Boundary Layer (43–66°S, 132–150°E), *Journal of Geophysical Research: Atmospheres*, *124*(22), 12,107–12,125, doi: 10.1029/2019JD030628.

Alexander, S. P., A. Orr, S. Webster, and D. J. Murphy (2017), Observations and fine-scale model simulations of gravity waves over Davis, East Antarctica (69°S, 78°E), *Journal of Geophysical Research: Atmospheres*, *122*(14), 7355–7370, doi: 10.1002/2017JD026615.

Alexander, S. P., G. M. McFarquhar, R. Marchand, A. Protat, E. Vignon, G. G. Mace, and A. R. Klekociuk (2021), Mixed-phase clouds and precipitation in Southern Ocean cyclones and cloud systems observed poleward of 64°S by ship-based cloud radar and lidar, *Journal of Geophysical Research: Atmospheres*, *n/a*(n/a), e2020JD033,626, doi: 10.1029/2020JD033626.

Andrić, J., M. R. Kumjian, D. S. Zrnić, J. M. Straka, and V. M. Melnikov (2013), Polarimetric signatures above the melting layer in winter storms: An observational and modeling study, *Journal of Applied Meteorology and Climatology*, *52*(3), 682–700, doi: 10.1175/JAMC-D-12-028.1.

Atlas, D., and F. H. Ludlam (1961), Multi-wavelength radar reflectivity of hailstorms, *Quarterly Journal of the Royal Meteorological Society*, *87*(374), 523–534, doi: 10.1002/qj.49708737407.

Atlas, D., R. C. Srivastava, and R. S. Sekhon (1973), Doppler radar characteristics of precipitation at vertical incidence, *Reviews of Geophysics*, *11*(1), 1–35, doi: 10.1029/RG011i001p00001.

Bader, M. J., S. A. Clough, and G. P. Cox (1987), Aircraft and dual polarization radar observations of hydrometeors in light stratiform precipitation, *Quarterly Journal of the Royal Meteorological Society*, *113*(476), 491–515, doi: 10.1002/qj.49711347605.

Barrett, P. A., A. Blyth, P. R. Brown, and S. J. Abel (2020), The structure of turbulence and mixed-phase cloud microphysics in a highly supercooled altocumulus cloud, *Atmospheric Chemistry and Physics*, *20*(4), 1921–1939, doi: 10.5194/acp-20-1921-2020.

Barthazy, E., and R. Schefold (2006), Fall velocity of snowflakes of different riming degree and crystal types, *Atmospheric Research*, *82*(1), 391–398, doi: 10.1016/j.atmosres.2005.12.009.

Baumgartner, A., and E. Reichel (1975), *The World Water Balance: Mean Annual Global, Continental and Maritime Precipitation and Run-Off*, 179 pp., Elsevier Scientific Publishers.

Bentley, W. (1902), Studies among the snow crystals during the winter of 1901-2, with additional data collected during previous winters, *Annual Summary of the Monthly Weather Review*, pp. 1–33.

Berg, H. W., R. E. Stewart, and P. I. Joe (2017), The characteristics of precipitation observed over Cypress Mountain during the SNOW-V10 campaign, *Atmospheric Research*, *197*(June), 356–369, doi: 10.1016/j.atmosres.2017.06.009.

Berne, A., and W. F. Krajewski (2013), Radar for hydrology: Unfulfilled promise or unrecognized potential?, *Advances in Water Resources*, *51*, 357–366, doi: 10.1016/j.advwatres.2012.05.005.

Besic, N., J. Figueras i Ventura, J. Grazioli, M. Gabella, U. Germann, and A. Berne (2016), Hydrometeor classification through statistical clustering of polarimetric radar measurements: A semi-supervised approach, *Atmospheric Measurement Techniques*, *9*(9), 4425–4445, doi: 10.5194/amt-9-4425-2016.

Besic, N., J. Gehring, C. Praz, J. Figueras i Ventura, J. Grazioli, M. Gabella, U. Germann, and A. Berne (2018), Unraveling hydrometeor mixtures in polarimetric radar measurements, *Atmospheric Measurement Techniques*, *11*(8), 4847–4866, doi: 10.5194/amt-11-4847-2018.

Billault-Roux, A.-C., and A. Berne (2021), Integrated water vapor and liquid water path retrieval using a single-channel radiometer, *Atmospheric Measurement Techniques*, *14*(4), 2749–2769, doi: 10.5194/amt-14-2749-2021.

Binder, H., M. Boettcher, H. Joos, M. Sprenger, and H. Wernli (2020), Vertical cloud structure of warm conveyor belts – a comparison and evaluation of ERA5 reanalysis, CloudSat and CALIPSO data, *Weather and Climate Dynamics*, *1*(2), 577–595, doi: 10.5194/wcd-1-577-2020.

Boettcher, M., et al. (2021), Lagrangian matches between observations from aircraft, lidar and radar in a warm conveyor belt crossing orography, *Atmospheric Chemistry and Physics*, *21*(7), 5477–5498, doi: 10.5194/acp-21-5477-2021.

Boudala, F. S., R. Rasmussen, G. A. Isaac, and B. Scott (2014), Performance of hot plate for measuring solid precipitation in complex terrain during the 2010 Vancouver winter olympics, *Journal of Atmospheric and Oceanic Technology*, *31*(2), 437–446, doi: 10.1175/JTECH-D-12-00247.1.

Bougeault, P., P. Binder, A. Buzzi, R. Dirks, R. Houze, J. Kuettner, R. B. Smith, R. Steinacker, and H. Volkert (2001), The MAP Special Observing Period, *Bulletin of the American Meteorological Society*, *82*(3), 433–462, doi: 10.1175/1520-0477(2001)082<0433:TMSOP>2.3.CO;2.

Bozkurt, D., R. Rondanelli, J. C. Marín, and R. Garreaud (2018), Foehn Event Triggered by an Atmospheric River Underlies Record-Setting Temperature Along Continental Antarctica, *Journal of Geophysical Research: Atmospheres*, *123*(8), 3871–3892, doi: 10.1002/2017JD027796.

Brandes, E. A., K. Ikeda, G. Zhang, M. Schönhuber, and R. M. Rasmussen (2007), A statistical and physical description of hydrometeor distributions in Colorado snowstorms using a video disdrometer, *Journal of Applied Meteorology and Climatology*, *46*(5), 634–650, doi: 10.1175/JAM2489.1.

Bringi, V. N., and V. Chandrasekar (2001), *Polarimetric Doppler Weather Radar*, Cambridge University Press, doi: 10.1017/CBO9780511541094.

Browning, K. A. (1990), *Organisation of Clouds and Precipitation in Extratropical Cyclones*, 151 pp., Amer. Meteorol. Soc., Boston, MA.

Browning, K. A., M. E. Hardman, T. W. Harrold, and C. W. Pardoe (1973), The structure of rainbands within a mid-latitude depression, *Quarterly Journal of the Royal Meteorological Society*, *99*(420), 215–231, doi: 10.1002/qj.49709942002.

Cape, M. R., M. Vernet, P. Skvarca, S. Marinsek, T. Scambos, and E. Domack (2015), Foehn winds link climate-driven warming to ice shelf evolution in Antarctica, *Journal of Geophysical Research: Atmospheres*, *120*(21), 11,037–11,057, doi: 10.1002/2015JD023465.

Carbone, R. E., D. Atlas, P. Eccles, R. Fetter, and E. Mueller (1973), Dual wavelength radar hail detection, *Bulletin of the American Meteorological Society*, *54*(9), 921–925, doi: 10.1175/1520-0477(1973)054<0921:DWRHD>2.0.CO;2.

Carlson, T. N. (1980), Airflow through midlatitude cyclones and the comma cloud pattern., *Monthly Weather Review*, *108*(10), 1498–1509, doi: 10.1175/1520-0493(1980)108<1498:ATMCAT>2.0.CO;2.

Ceccaldi, M., J. Delanoë, R. J. Hogan, N. L. Pounder, A. Protat, and J. Pelon (2013), From CloudSat-CALIPSO to EarthCare: Evolution of the DARDAR cloud classification and its comparison to airborne radar-lidar observations, *Journal of Geophysical Research: Atmospheres*, *118*(14), 7962–7981, doi: 10.1002/jgrd.50579.

Chambers, T. E., M. W. Hamilton, and I. M. Reid (2016), A low-cost digital holographic imager for calibration and validation of cloud microphysics remote sensing, in *Remote Sensing of*

Clouds and the Atmosphere XXI, vol. 10001, p. 100010P, International Society for Optics and Photonics, doi: 10.1117/12.2239590.

Cole, S., R. R. Neely III., and R. A. Stillwell (2017), First Look at the Occurrence of Horizontally Oriented Ice Crystals over Summit, Greenland, *Atmospheric Chemistry and Physics Discussions*, pp. 1–45, doi: 10.5194/acp-2016-1134.

Colle, B. A., D. Stark, and S. E. Yuter (2014), Surface Microphysical Observations within East Coast Winter Storms on Long Island, New York, *Monthly Weather Review*, *142*(9), 3126–3146, doi: 10.1175/MWR-D-14-00035.1.

Connolly, P. J., C. P. R. Saunders, M. W. Gallagher, K. N. Bower, M. J. Flynn, T. W. Choularton, J. Whiteway, and R. P. Lawson (2005), Aircraft observations of the influence of electric fields on the aggregation of ice crystals, *Quarterly Journal of the Royal Meteorological Society*, *131*(608), 1695–1712, doi: 10.1256/qj.03.217.

Connolly, P. J., C. Emersic, and P. R. Field (2012), A laboratory investigation into the aggregation efficiency of small ice crystals, *Atmospheric Chemistry and Physics*, *12*(4), 2055–2076, doi: 10.5194/acp-12-2055-2012.

Dacre, H. F., O. Martínez-Alvarado, and C. O. Mbengue (2019), Linking Atmospheric Rivers and Warm Conveyor Belt Airflows, *Journal of Hydrometeorology*, *20*(6), 1183–1196, doi: 10.1175/jhm-d-18-0175.1.

Damiens, F., F. Lott, C. Millet, and R. Plougonven (2018), An adiabatic foehn mechanism, *Quarterly Journal of the Royal Meteorological Society*, *144*(714), 1369–1381, doi: 10.1002/qj.3272.

Davies, H. C., and C. Schär (1991), Orographic destabilization of a laterally sheared flow, *Tellus*, *43A*, 321–333.

Delanoë, J., and R. J. Hogan (2010), Combined CloudSat-CALIPSO-MODIS retrievals of the properties of ice clouds, *Journal of Geophysical Research: Atmospheres*, *115*(D4), doi: 10.1029/2009JD012346.

Delanoë, J., et al. (2016), BASTA: A 95-GHz FMCW Doppler Radar for Cloud and Fog Studies, *Journal of Atmospheric and Oceanic Technology*, *33*(5), 1023–1038, doi: 10.1175/JTECH-D-15-0104.1.

Doran, P. T., C. P. McKay, G. D. Clow, G. L. Dana, A. G. Fountain, T. Nylen, and W. B. Lyons (2002), Valley floor climate observations from the McMurdo dry valleys, Antarctica, 1986-2000, *Journal of Geophysical Research Atmospheres*, *107*(24), 1–12, doi: 10.1029/2001JD002045.

Doviak, R. J., and D. S. Zrnic (1993), *Doppler Radar and Weather Observations*, second ed., 274 pp., Dover Publications, Mineola, New York.

Eccles, P. J., and D. Atlas (1973), A Dual-Wavelength Radar Hail Detector, *Journal of Applied Meteorology and Climatology*, *12*(5), 847–854, doi: 10.1175/1520-0450(1973)012<0847:ADWRHD>2.0.CO;2.

Eckhardt, S., A. Stohl, H. Wernli, P. James, C. Forster, and N. Spichtinger (2004), A 15-year climatology of warm conveyor belts, *Journal of Climate*, *17*(1), 218–237, doi: 10.1175/1520-0442(2004)017<0218:AYCOWC>2.0.CO;2.

ECMWF (2016), IFS Documentation – Cy41r2, Part IV: Physical Processes, available at : https://www.ecmwf.int/sites/default/files/elibrary/2016/16648-part-iv-physical-processes.pdf (last access: 16 April 2020).

ECMWF (2017), IFS Documentation - Cy43r3: Operational implementation 11 July 2017. Dynamics and numerical procedures.

Eisen, O., et al. (2008), Ground-based measurements of spatial and temporal variability of snow accumulation in East Antarctica, *Reviews of Geophysics*, *46*(2), doi: 10.1029/2006RG000218.

Elvidge, A. D., I. A. Renfrew, J. C. King, A. Orr, T. A. Lachlan-Cope, M. Weeks, and S. L. Gray (2015), Foehn jets over the Larsen C Ice Shelf, Antarctica, *Quarterly Journal of the Royal Meteorological Society*, *141*(688), 698–713, doi: 10.1002/qj.2382.

Elvidge, A. D., I. A. Renfrew, J. C. King, A. Orr, and T. A. Lachlan-Cope (2016), Foehn warming distributions in nonlinear and linear flow regimes: A focus on the Antarctic Peninsula, *Quarterly Journal of the Royal Meteorological Society*, *142*(695), 618–631, doi: 10.1002/qj.2489.

Fabry, F. (2015), *Radar Metorology, Principles and Practice*, 256 pp., Cambridge Univ. Press, Cambridge.

Ferrone, A., and A. Berne (2021), Dynamic Differential Reflectivity Calibration Using Vertical Profiles in Rain and Snow, *Remote Sensing*, *13*(1), 8, doi: 10.3390/rs13010008.

Field, P. R., and A. J. Heymsfield (2003), Aggregation and Scaling of Ice Crystal Size Distributions, *Journal of the Atmospheric Sciences*, *60*(3), 544–560, doi: 10.1175/1520-0469(2003)060<0544:AASOIC>2.0.CO;2.

Field, P. R., and A. J. Heymsfield (2015), Importance of snow to global precipitation, *Geophysical Research Letters*, *42*(21), 9512–9520, doi: 10.1002/2015GL065497.

Fitch, K. E., C. Hang, A. Talaei, and T. J. Garrett (2021), Arctic observations and numerical simulations of surface wind effects on Multi-Angle Snowflake Camera measurements, *Atmospheric Measurement Techniques*, *14*(2), 1127–1142, doi: 10.5194/amt-14-1127-2021.

Fountain, A. G., T. H. Nylen, A. Monaghan, H. J. Basagic, and D. Bromwich (2010), Snow in the Mcmurdo Dry Valleys, aNtarctica, *International Journal of Climatology*, *30*(5), 633–642, doi: 10.1002/joc.1933.

Frank, F. C. (1982), Snow crystals, *Contemporary Physics*, *23*(1), 3–22, doi: 10.1080/00107518208231565.

Garrett, T. J. (2019), Analytical Solutions for Precipitation Size Distributions at Steady State, *Journal of the Atmospheric Sciences*, *76*(4), 1031–1037, doi: 10.1175/jas-d-18-0309.1.

Garrett, T. J., C. Fallgatter, K. Shkurko, and D. Howlett (2012), Fall speed measurement and high-resolution multi-angle photography of hydrometeors in free fall, *Atmospheric Measurement Techniques*, *5*(11), 2625–2633, doi: 10.5194/amt-5-2625-2012.

Garrett, T. J., S. E. Yuter, C. Fallgatter, K. Shkurko, S. R. Rhodes, and J. L. Endries (2015), Orientations and aspect ratios of falling snow, *Geophysical Research Letters*, *42*(11), 4617–4622, doi: 10.1002/2015GL064040.

Gehring, J., A. Ferrone, A.-C. Billault-Roux, N. Besic, and A. Berne (2020a), Radar and ground-level measurements of precipitation during the ICE-POP 2018 campaign in South-Korea, *PANGAEA*, doi: 10.1594/PANGAEA.918315.

Gehring, J., A. Oertel, E. Vignon, N. Jullien, N. Besic, and A. Berne (2020b), Microphysics and dynamics of snowfall associated with a warm conveyor belt over Korea, *Atmospheric Chemistry and Physics*, *20*(12), 7373–7392, doi: 10.5194/acp-20-7373-2020.

Gehring, J., A. Ferrone, A.-C. Billault-Roux, N. Besic, K. D. Ahn, G. Lee, and A. Berne (2021a), Radar and ground-level measurements of precipitation collected by the École Polytechnique Fédérale de Lausanne during the International Collaborative Experiments for PyeongChang 2018 Olympic and Paralympic winter games, *Earth System Science Data*, *13*(2), 417–433, doi: 10.5194/essd-13-417-2021.

Gehring, J., E. Vignon, A.-C. Billault-Roux, A. Ferrone, A. Protat, S. P. Alexander, and A. Berne (2021b), The influence of orographic gravity waves on precipitation during an atmospheric river event at Davis, Antarctica, *Journal of Geophysical Research: Atmospheres, submitted*.

Genthon, C., G. Krinner, and H. Castebrunet (2009/ed), Antarctic precipitation and climate-change predictions: Horizontal resolution and margin vs plateau issues, *Annals of Glaciology*, *50*(50), 55–60, doi: 10.3189/172756409787769681.

Genthon, C., A. Berne, J. Grazioli, C. Durán Alarcón, C. Praz, and B. Boudevillain (2018), Precipitation at Dumont d'Urville, Adélie Land, East Antarctica: The APRES3 field campaigns dataset, *Earth System Science Data*, *10*(3), 1605–1612, doi: 10.5194/essd-10-1605-2018.

Gerber, F., and M. Lehning (2020), REMA topography and AntarcticaLC2000 for WRF, *EnviDat*, doi: http://dx.doi.org/10.16904/envidat.190.

Gorgucci, E., G. Scarchilli, and V. Chandrasekar (1999), A procedure to calibrate multiparameter weather radar using properties of the rain medium, *Geosci. Remote Sens.*, *17*, 269–276.

Gorodetskaya, I. V., M. Tsukernik, K. Claes, M. F. Ralph, W. D. Neff, and N. P. M. V. Lipzig (2014), The role of atmospheric rivers in anomalous snow accumulation in East Antarctica, *Geophysical Research Letters*, *41*(17), 6199–6206, doi: 10.1002/2014GL060881.

Gorodetskaya, I. V., S. Kneifel, M. Maahn, K. Van Tricht, W. Thiery, J. H. Schween, A. Mangold, S. Crewell, and N. P. M. Van Lipzig (2015), Cloud and precipitation properties from ground-based remote-sensing instruments in East Antarctica, *The Cryosphere*, *9*(1), 285–304, doi: 10.5194/tc-9-285-2015.

Grazioli, J., D. Tuia, S. Monhart, M. Schneebeli, T. Raupach, and A. Berne (2014), Hydrometeor classification from two-dimensional video disdrometer data, *Atmospheric Measurement Techniques*, *7*(9), 2869–2882, doi: 10.5194/amt-7-2869-2014.

Grazioli, J., G. Lloyd, L. Panziera, C. R. Hoyle, P. J. Connolly, J. Henneberger, and A. Berne (2015a), Polarimetric radar and in situ observations of riming and snowfall microphysics during CLACE 2014, *Atmospheric Chemistry and Physics*, *15*(23), 13,787–13,802, doi: 10.5194/acp-15-13787-2015.

Grazioli, J., D. Tuia, and A. Berne (2015b), Hydrometeor classification from polarimetric radar measurements: A clustering approach, *Atmospheric Measurement Techniques*, *8*(1), 149–170, doi: 10.5194/amt-8-149-2015.

Grazioli, J., C. Genthon, B. Boudevillain, C. Duran-Alarcon, M. Del Guasta, J.-B. Madeleine, and A. Berne (2017a), Measurements of precipitation in Dumont d'Urville, Adélie Land, East Antarctica, *The Cryosphere*, *11*(4), 1797–1811, doi: 10.5194/tc-11-1797-2017.

Grazioli, J., J.-B. Madeleine, H. Gallée, R. M. Forbes, C. Genthon, G. Krinner, and A. Berne (2017b), Katabatic winds diminish precipitation contribution to the Antarctic ice mass balance, *Proceedings of the National Academy of Sciences*, *114*(41), 10,858–10,863, doi: 10.1073/pnas.1707633114.

Green, J. S., F. H. Ludlam, and J. F. McIlveen (1966), Isentropic relative flow analysis and the parcel theory, *Quarterly Journal of the Royal Meteorological Society*, *92*(392), 210–219, doi: 10.1002/qj.49709239204.

Grosvenor, D. P., J. C. King, T. W. Choularton, and T. Lachlan-Cope (2014), Downslope föhn winds over the Antarctic Peninsula and their effect on the Larsen ice shelves, *Atmospheric Chemistry and Physics*, *14*(18), 9481–9509, doi: 10.5194/acp-14-9481-2014.

Haiden, T., A. Kann, and G. Pistotnik (2014), Nowcasting with INCA During SNOW-V10, *Pure and Applied Geophysics*, *171*(1-2), 231–242, doi: 10.1007/s00024-012-0547-8.

Hallett, J., and S. C. Mossop (1974), Production of secondary ice particles during the riming process, *Nature*, *249*(5452), 26–28, doi: 10.1038/249026a0.

Harrold, T. (1973), Mechanisms influencing the distribution of precipitation within baroclinic disturbances, *Quarterly Journal of the Royal Meteorological Society*, *99*, 232–251.

Hawcroft, M. K., L. C. Shaffrey, K. I. Hodges, and H. F. Dacre (2012), How much Northern Hemisphere precipitation is associated with extratropical cyclones?, *Geophysical Research Letters*, *39*(24), 1–7, doi: 10.1029/2012GL053866.

Hersbach, H., et al. (2020), The ERA5 global reanalysis, *Quarterly Journal of the Royal Meteorological Society*, *146*(730), 1999–2049, doi: 10.1002/qj.3803.

Heymsfield, A. J. (1977), Precipitation Development in Stratiform Ice Clouds: A Microphysical and Dynamical Study, *Journal of the Atmospheric Sciences*, *34*(2), 367–381, doi: 10.1175/1520-0469(1977)034<0367:pdisic>2.0.co;2.

Heymsfield, A. J., L. M. Miloshevich, A. Slingo, K. Sassen, and D. O. Starr (1991), An Observational and Theoretical Study of Highly Supercooled Altocumulus, *Journal of the Atmospheric Sciences*, *48*(7), 923–945, doi: 10.1175/1520-0469(1991)048<0923:AOATSO>2.0.CO;2.

Hicks, A., and B. M. Notaroš (2019), Method for Classification of Snowflakes Based on Images by a Multi-Angle Snowflake Camera Using Convolutional Neural Networks, *Journal of Atmospheric and Oceanic Technology*, *36*(12), 2267–2282, doi: 10.1175/jtech-d-19-0055.1.

Hildebrand, P. H., and R. S. Sekhon (1974), Objective Determination of the Noise Level in Doppler Spectra, *Journal of Applied Meteorology*, *13*(7), 808–811, doi: 10.1175/1520-0450(1974)013<0808:odotnl>2.0.co;2.

Hirano, D., et al. (2020), Strong ice-ocean interaction beneath Shirase Glacier Tongue in East Antarctica, *Nature Communications*, *11*(1), 4221, doi: 10.1038/s41467-020-17527-4.

Hobbs, P. V., S. Chang, and J. D. Locatelli (1974), The dimensions and aggregation of ice crystals in natural clouds, *Journal of Geophysical Research (1896-1977)*, *79*(15), 2199–2206, doi: 10.1029/JC079i015p02199.

Hogan, R. J., P. R. Field, a. J. Illingworth, R. J. Cotton, and T. W. Choularton (2002), Properties of embedded convection in warm-frontal mixed-phase cloud from aircraft and polarimetric radar, *Quarterly Journal of the Royal Meteorological Society*, *128*(580), 451–476, doi: 10.1256/003590002321042054.

Hogan, R. J., P. N. Francis, H. Flentje, A. J. Illingworth, M. Quante, and J. Pelon (2003), Characteristics of mixed-phase clouds. I: Lidar, radar and aircraft observations from CLARE'98, *Quarterly Journal of the Royal Meteorological Society*, *129*(592), 2089–2116, doi: 10.1256/rj.01.208.

Hosler, C. L., and R. E. Hallgren (1960), The aggregation of small ice crystals, *Discussions of the Faraday Society*, *30*(0), 200–207, doi: 10.1039/DF9603000200.

Houze, R. A., and S. Medina (2005), Turbulence as a mechanism for orographic precipitation enhancement, *Journal of the Atmospheric Sciences*, *62*(10), 3599–3623, doi: 10.1175/JAS3555.1.

Houze, R. A., et al. (2017), The Olympic Mountains Experiment (OLYMPEX), *Bulletin of the American Meteorological Society*, *98*(10), 2167–2188, doi: 10.1175/bams-d-16-0182.1.

Howat, I. M., C. Porter, B. E. Smith, M.-J. Noh, and P. Morin (2019), The Reference Elevation Model of Antarctica, *The Cryosphere*, *13*(2), 665–674, doi: 10.5194/tc-13-665-2019.

Huang, G. J., V. N. Bringi, R. Cifelli, D. Hudak, and W. A. Petersen (2010), A methodology to derive radar reflectivity-liquid equivalent snow rate relations using C-band radar and a 2D video disdrometer, *Journal of Atmospheric and Oceanic Technology*, *27*(4), 637–651, doi: 10.1175/2009JTECHA1284.1.

Huang, G. J., V. N. Bringi, D. Moisseev, W. A. Petersen, L. Bliven, and D. Hudak (2015), Use of 2D-video disdrometer to derive mean density-size and Ze-SR relations: Four snow cases from the light precipitation validation experiment, *Atmospheric Research*, *153*, 34–48, doi: 10.1016/j.atmosres.2014.07.013.

Jeoung, H., G. Liu, K. Kim, G. Lee, and E.-K. Seo (2020), Microphysical properties of three types of snow clouds: Implication for satellite snowfall retrievals, *Atmospheric Chemistry and Physics*, *20*(23), 14,491–14,507, doi: 10.5194/acp-20-14491-2020.

Joe, P., et al. (2010), Weather services, science advances, and the vancouver 2010 olympic and paralympic winter games, *Bulletin of the American Meteorological Society*, *91*(1), 31–36, doi: 10.1175/2009BAMS2998.1.

Joos, H., and R. M. Forbes (2016), Impact of different IFS microphysics on a warm conveyor belt and the downstream flow evolution, *Q. J. Roy. Meteor. Soc.*, *142*(October), 2727–2739, doi: 10.1002/qj.2863.

Joos, H., and H. Wernli (2012), Influence of microphysical processes on the potential vorticity development in a warm conveyor belt: A case-study with the limited-area model COSMO, *Quarterly Journal of the Royal Meteorological Society*, *138*(663), 407–418, doi: 10.1002/qj.934.

Kalesse, H., W. Szyrmer, S. Kneifel, P. Kollias, and E. Luke (2016), Fingerprints of a riming event on cloud radar Doppler spectra: Observations and modeling, *Atmospheric Chemistry and Physics*, *16*(5), 2997–3012, doi: 10.5194/acp-16-2997-2016.

Kennicutt, M. C., et al. (2014), Six priorities for Antarctic science, *Nature*, *512*(7512), 23–25, doi: 10.1038/512023a.

Kepler, J., and C. Hardie (2014), *The Six-Cornered Snowflake*, Oxford Classic Texts in the Physical Sciences, Oxford University Press, Oxford, New York.

Keppas, S. C., J. Crosier, T. W. Choularton, and K. N. Bower (2018), Microphysical Properties and Radar Polarimetric Features within a Warm Front, *Monthly Weather Review*, *146*(7), 2003–2022, doi: 10.1175/MWR-D-18-0056.1.

Kim, Y. J., B. G. Kim, J. K. Shim, and B. C. Choi (2018), Observation and Numerical Simulation of Cold Clouds and Snow Particles in the Yeongdong Region, *Asia-Pacific Journal of Atmospheric Sciences*, *54*(3), 499–510, doi: 10.1007/s13143-018-0055-6.

King, J. C., and J. Turner (1997), *Antarctic Meteorology and Climatology*, 409 pp., Cambridge Univ. Press, New-York.

Kirchgaessner, A., J. C. King, and P. S. Anderson (2021), The Impact of Föhn Conditions Across the Antarctic Peninsula on Local Meteorology Based on AWS Measurements, *Journal of Geophysical Research: Atmospheres*, *126*(4), e2020JD033,748, doi: 10.1029/2020JD033748.

Klepp, C., et al. (2018), OceanRAIN, a new in-situ shipboard global ocean surface-reference dataset of all water cycle components, *Scientific Data*, *5*(1), 180,122, doi: 10.1038/sdata.2018.122.

Klugmann, D., K. Heinsohn, and H.-J. Kirtzel (1996), A low cost 24 GHz FM-CW doppler radar rain profiler, *Contributions To Atmospheric Physics*, *69*(1), 247–253.

KMA (2011), Climatological Normals of Korea, *Tech. rep.*, Korea Meteorological Administration, Seoul, Republic of Korea.

Kneifel, S., and D. Moisseev (2020), Long-Term Statistics of Riming in Nonconvective Clouds Derived from Ground-Based Doppler Cloud Radar Observations, *Journal of the Atmospheric Sciences*, *77*(10), 3495–3508, doi: 10.1175/JAS-D-20-0007.1.

Kobayashi, T. (1961), The growth of snow crystals at low supersaturations, *The Philosophical Magazine: A Journal of Theoretical Experimental and Applied Physics*, *6*(71), 1363–1370, doi: 10.1080/14786436108241231.

Kollias, P., E. E. Clothiaux, M. A. Miller, B. A. Albrecht, G. L. Stephens, and T. P. Ackerman (2007), Millimeter-wavelength radars: New frontier in atmospheric cloud and precipitation research, *Bulletin of the American Meteorological Society*, *88*(10), 1608–1624, doi: 10.1175/BAMS-88-10-1608.

König-Langlo, G., J. C. King, and P. Pettré (1998), Climatology of the three coastal Antarctic stations Dumont d'Urville, Neumayer, and Halley, *Journal of Geophysical Research: Atmospheres*, *103*(May 20), 10,935–10,946, doi: 10.1029/97JD00527.

Korolev, A., and T. Leisner (2020), Review of experimental studies of secondary ice production, *Atmospheric Chemistry and Physics*, *20*(20), 11,767–11,797, doi: 10.5194/acp-20-11767-2020.

Korolev, A., I. Heckman, M. Wolde, A. S. Ackerman, A. M. Fridlind, L. A. Ladino, R. P. Lawson, J. Milbrandt, and E. Williams (2020), A new look at the environmental conditions favorable to secondary ice production, *Atmospheric Chemistry and Physics*, *20*(3), 1391–1429, doi: 10.5194/acp-20-1391-2020.

Korolev, A. V., and I. P. Mazin (2003), Supersaturation of water vapor in clouds, *Journal of the Atmospheric Sciences*, *60*(24), 2957–2974, doi: 10.1175/1520-0469(2003)060<2957:SOWVIC>2.0.CO;2.

Krinner, G., O. Magand, I. Simmonds, C. Genthon, and J. L. Dufresne (2007), Simulated Antarctic precipitation and surface mass balance at the end of the twentieth and twenty-first centuries, *Climate Dynamics*, *28*(2), 215–230, doi: 10.1007/s00382-006-0177-x.

Kruger, A., and W. F. Krajewski (2002), Two-dimensional video disdrometer: A description, *Journal of Atmospheric and Oceanic Technology*, *19*(5), 602–617, doi: 10.1175/1520-0426(2002)019<0602:TDVDAD>2.0.CO;2.

Küchler, N., S. Kneifel, U. Löhnert, P. Kollias, H. Czekala, and T. Rose (2017), A W-Band Radar–Radiometer System for Accurate and Continuous Monitoring of Clouds and Precipitation, *Journal of Atmospheric and Oceanic Technology*, *34*(11), 2375–2392, doi: 10.1175/JTECH-D-17-0019.1.

Kumjian, M. (2013a), Principles and applications of dual-polarization weather radar. Part II: Warm- and cold-season applications, *Journal of Operational Meteorology*, *1*(20), 243–264, doi: 10.15191/nwajom.2013.0120.

Kumjian, M. (2013b), Principles and applications of dual-polarization weather radar. Part III: Artifacts, *Journal of Operational Meteorology*, *1*(21), 265–274, doi: 10.15191/nwajom.2013.0121.

Kumjian, M. R. (2018), Weather Radars, in *Remote Sensing of Clouds and Precipitation*, edited by C. Andronache, Springer Remote Sensing/Photogrammetry, pp. 15–63, Springer International Publishing, Cham, doi: 10.1007/978-3-319-72583-3_2.

Kumjian, M. R., S. A. Rutledge, R. M. Rasmussen, P. C. Kennedy, and M. Dixon (2014), High-resolution polarimetric radar observations of snow-generating cells, *Journal of Applied Meteorology and Climatology*, *53*(6), 1636–1658, doi: 10.1175/JAMC-D-13-0312.1.

Leisner, T., T. Pander, P. Handmann, and A. Kiselev (2014), Secondary ice processes upon heterogeneous freezing of cloud droplets, in *14th Conf. on Cloud Physics and Atmospheric Radiation*, edited by . Amer. Meteor. Soc., Boston, MA.

Lhermitte, R. (1987), A 94-GHz Doppler radar for cloud observations, *Journal of Atmospheric and Oceanic Technology*, *4*, 36–48.

Li, H., D. Moisseev, and A. von Lerber (2018), How Does Riming Affect Dual-Polarization Radar Observations and Snowflake Shape?, *Journal of Geophysical Research: Atmospheres*, *123*(11), 6070–6081, doi: 10.1029/2017JD028186.

Li, Y., and G. A. Somorjai (2007), Surface Premelting of Ice, *The Journal of Physical Chemistry C*, *111*(27), 9631–9637, doi: 10.1021/jp071102f.

Libbrecht, K. G. (2005), The physics of snow crystals, *Reports on Progress in Physics*, *68*(4), 855, doi: 10.1088/0034-4885/68/4/R03.

Listowski, C., J. Delanoë, A. Kirchgaessner, T. Lachlan-Cope, and J. King (2019), Antarctic clouds, supercooled liquid water and mixed phase, investigated with DARDAR: Geographical and seasonal variations, *Atmospheric Chemistry and Physics*, *19*(10), 6771–6808, doi: 10.5194/acp-19-6771-2019.

Lohmann, U., F. Lüönd, and F. Mahrt (2016), *An Introduction to Clouds: From the Microscale to Climate*, Cambridge University Press, Cambridge, doi: 10.1017/CBO9781139087513.

Löhnert, U., S. Kneifel, A. Battaglia, M. Hagen, L. Hirsch, and S. Crewell (2011), A Multisensor Approach Toward a Better Understanding of Snowfall Microphysics: The TOSCA Project, *Bulletin of the American Meteorological Society*, *92*(5), 613–628, doi: 10.1175/2010BAMS2909.1.

Lubin, D., et al. (2020), AWARE: The Atmospheric Radiation Measurement (ARM) West Antarctic Radiation Experiment, *Bulletin of the American Meteorological Society*, *101*(7), E1069–E1091, doi: 10.1175/BAMS-D-18-0278.1.

Luke, E. P., P. Kollias, and M. D. Shupe (2010), Detection of supercooled liquid in mixed-phase clouds using radar Doppler spectra, *Journal of Geophysical Research Atmospheres*, *115*(19), 1–14, doi: 10.1029/2009JD012884.

Maahn, M., C. Burgard, S. Crewell, I. V. Gorodetskaya, S. Kneifel, S. Lhermitte, K. Van Tricht, and N. P. van Lipzig (2014), How does the spaceborne radar blind zone affect derived surface snowfall statistics in polar regions?, *Journal of Geophysical Research*, *119*(22), 13,604–13,620, doi: 10.1002/2014JD022079.

Mace, G. G., and A. Protat (2018), Clouds over the Southern Ocean as Observed from the R/V Investigator during CAPRICORN. Part I: Cloud Occurrence and Phase Partitioning, *Journal of Applied Meteorology and Climatology*, *57*(8), 1783–1803, doi: 10.1175/JAMC-D-17-0194.1.

Madonna, E., H. Wernli, H. Joos, and O. Martius (2014), Warm conveyor belts in the ERA-Interim Dataset (1979-2010). Part I: Climatology and potential vorticity evolution, *Journal of Climate*, *27*(1), 3–26, doi: 10.1175/JCLI-D-12-00720.1.

Mason, B. J., and J. Maybank (1960), The fragmentation and electrification of freezing water drops, *Q. J. Roy. Meteor. Soc.*, *86*(368), 176–185, doi: 10.1175/1520-0469(1975)032<0974:TFAEOF>2.0.CO;2.

Matrosov, S. Y. (1998), A Dual-Wavelength Radar Method to Measure Snowfall Rate, *Journal of Applied Meteorology and Climatology*, *37*(11), 1510–1521, doi: 10.1175/1520-0450(1998)037<1510:ADWRMT>2.0.CO;2.

McFarquhar, G. M., et al. (2020), Observations of clouds, aerosols, precipitation, and surface radiation over the Southern Ocean: An overview of CAPRICORN, MARCUS, MICRE and SOCRATES, *Bulletin of the American Meteorological Society*, *-1*(aop), 1–92, doi: 10.1175/BAMS-D-20-0132.1.

Mech, M., M. Maahn, S. Kneifel, D. Ori, E. Orlandi, P. Kollias, V. Schemann, and S. Crewell (2020), PAMTRA 1.0: The Passive and Active Microwave radiative TRAnsfer tool for simulating radiometer and radar measurements of the cloudy atmosphere, *Geoscientific Model Development*, *13*(9), 4229–4251, doi: 10.5194/gmd-13-4229-2020.

Medina, S., and R. A. Houze (2015), Small-Scale Precipitation Elements in Midlatitude Cyclones Crossing the California Sierra Nevada, *Monthly Weather Review*, *143*(7), 2842–2870, doi: 10.1175/MWR-D-14-00124.1.

Medina, S., B. F. Smull, R. A. Houze, and M. Steiner (2005), Cross-Barrier Flow during Orographic Precipitation Events: Results from MAP and IMPROVE, *Journal of the Atmospheric Sciences*, *62*(10), 3580–3598, doi: 10.1175/jas3554.1.

Mitchell, D. L. (1988), Evolution of Snow-Size Spectra in Cyclonic Storms. Part I: Snow Growth by Vapor Deposition and Aggregation, *Journal of the Atmospheric Sciences*, *45*(22), 3431–3451, doi: 10.1175/1520-0469(1988)045<3431:EOSSSI>2.0.CO;2.

Mitchell, D. L., and A. J. Heymsfield (2005), Refinements in the Treatment of Ice Particle Terminal Velocities, Highlighting Aggregates, *Journal of the Atmospheric Sciences*, *62*(5), 1637–1644, doi: 10.1175/JAS3413.1.

Moffat-Griffin, T. (2019), An Introduction to Atmospheric Gravity Wave Science in the Polar Regions and First Results From ANGWIN, *Journal of Geophysical Research: Atmospheres*, *124*(3), 1198–1199, doi: 10.1029/2019JD030247.

Moisseev, D., A. von Lerber, and J. Tiira (2017), Quantifying the effect of riming on snowfall using ground-based observations, *Journal of Geophysical Research: Atmospheres*, *122*(7), 4019–4037, doi: 10.1002/2016JD026272.

Moisseev, D. N., S. Lautaportti, J. Tyynela, and S. Lim (2015), Dual-polarization radar signatures in snowstorms: Role of snowflake aggregation, *Journal of Geophysical Research: Atmospheres*, *120*(24), 12,644–12,655, doi: 10.1002/2015JD023884.

Morrison, H., et al. (2020), Confronting the Challenge of Modeling Cloud and Precipitation Microphysics, *Journal of Advances in Modeling Earth Systems*, *12*(8), e2019MS001,689, doi: 10.1029/2019MS001689.

Mosimann, L. (1995), An improved method for determining the degree of snow crystal riming by vertical Doppler radar, *Atmospheric Research*, *37*(4), 305–323, doi: 10.1016/0169-8095(94)00050-N.

Mosimann, L., M. Steiner, and W. Henrich (1993), Prediction of snow crystal shape and riming by vertical Doppler radar, *Atmospheric Research*, *29*(1-2), 85–98, doi: 10.1016/0169-8095(93)90038-P.

Myagkov, A., S. Kneifel, and T. Rose (2020), Evaluation of the reflectivity calibration of W-band radars based on observations in rain, *Atmospheric Measurement Techniques*, *13*(11), 5799–5825, doi: 10.5194/amt-13-5799-2020.

Nakaya, U. (1954), *Snow Crystals: Natural and Artificial*, 1st edition ed., Harvard University Press.

Nance, L. B., and D. R. Durran (1997), A Modeling Study of Nonstationary Trapped Mountain Lee Waves. Part I: Mean-Flow Variability, *Journal of the Atmospheric Sciences*, *54*(18), 2275–2291, doi: 10.1175/1520-0469(1997)054<2275:AMSONT>2.0.CO;2.

Nešpor, V., W. F. Krajewski, and A. Kruger (2000), Wind-induced error of raindrop size distribution measurement using a two-dimensional video disdrometer, *Journal of Atmospheric and Oceanic Technology*, *17*(11), 1483–1492, doi: 10.1175/1520-0426(2000)017<1483:WIEORS>2.0.CO;2.

Noh, Y.-J., S. D. Miller, A. K. Heidinger, G. G. Mace, A. Protat, and S. P. Alexander (2019), Satellite-Based Detection of Daytime Supercooled Liquid-Topped Mixed-Phase Clouds Over the Southern Ocean Using the Advanced Himawari Imager, *Journal of Geophysical Research: Atmospheres*, *124*(5), 2677–2701, doi: 10.1029/2018JD029524.

Noone, D., J. Turner, and R. Mulvaney (1999), Atmospheric signals and characteristics of accumulation in Dronning Maud Land, Antarctica, *Journal of Geophysical Research: Atmospheres*, *104*(D16), 19,191–19,211, doi: 10.1029/1999JD900376.

Nuncio, M., and K. Satheesan (2014), Indian Ocean Dipole and southern high latitude precipitation: Possible links, *Climate Dynamics*, *43*(7-8), 1965–1972, doi: 10.1007/s00382-013-2020-5.

Oertel, A., M. Boettcher, H. Joos, M. Sprenger, H. Konow, M. Hagen, and H. Wernli (2019), Convective activity in an extratropical cyclone and its warm conveyor belt – a case-study combining observations and a convection-permitting model simulation, *Quarterly Journal of the Royal Meteorological Society*, *145*(721), 1406–1426, doi: 10.1002/qj.3500.

Oertel, A., M. Boettcher, H. Joos, M. Sprenger, and H. Wernli (2020), Potential vorticity structure of embedded convection in a warm conveyor belt and its relevance for large-scale dynamics, *Weather and Climate Dynamics*, *1*(1), 127–153, doi: 10.5194/wcd-1-127-2020.

Orr, A., T. Phillips, S. Webster, A. Elvidge, M. Weeks, S. Hosking, and J. Turner (2014), Met Office Unified Model high-resolution simulations of a strong wind event in Antarctica, *Quarterly Journal of the Royal Meteorological Society*, *140*(684), 2287–2297, doi: 10.1002/qj.2296.

Palerme, C., J. E. Kay, C. Genthon, T. L'Ecuyer, N. B. Wood, and C. Claud (2014), How much snow falls on the Antarctic ice sheet?, *Cryosphere*, *8*(4), 1577–1587, doi: 10.5194/tc-8-1577-2014.

Panziera, L., C. N. James, and U. Germann (2015), Mesoscale organization and structure of orographic precipitation producing flash floods in the lago maggiore region, *Quarterly Journal of the Royal Meteorological Society*, *141*(686), 224–248, doi: 10.1002/qj.2351.

Petäjä, T., et al. (2016), BAECC: A Field Campaign to Elucidate the Impact of Biogenic Aerosols on Clouds and Climate, *Bulletin of the American Meteorological Society*, *97*(10), 1909–1928, doi: 10.1175/BAMS-D-14-00199.1.

Pfahl, S., E. Madonna, M. Boettcher, H. Joos, and H. Wernli (2014), Warm conveyor belts in the ERA-Interim data set (1979-2010). Part II: Moisture origin and relevance for precipitation, *Journal of Climate*, *27*, 27–40, doi: 10.1175/JCLI-D-13-00223.1.

Phillips, V. T. J., M. Formenton, A. Bansemer, I. Kudzotsa, and B. Lienert (2015), A Parameterization of Sticking Efficiency for Collisions of Snow and Graupel with Ice Crystals: Theory and Comparison with Observations, *Journal of the Atmospheric Sciences*, *72*(12), 4885–4902, doi: 10.1175/JAS-D-14-0096.1.

Pickard, J. (1986), Antarctic oases, Davis station and the Vestfold Hills., *Academic Press, Macquarie University*, pp. 1–19.

Planat, N., J. Gehring, É. Vignon, and A. Berne (2021), Identification of snowfall microphysical processes from Eulerian vertical gradients of polarimetric radar variables, *Atmospheric Measurement Techniques*, *14*(6), 4543–4564, doi: 10.5194/amt-14-4543-2021.

Portmann, R. (2020), The life cycles of potential vorticity cutoffs: Climatology, predictability, and high impact weather, Ph.D. thesis, ETH Zurich, Zurich.

Portmann, R., M. Sprenger, and H. Wernli (2021), The three-dimensional life cycles of potential vorticity cutoffs: A global and selected regional climatologies in ERA-Interim (1979–2018), *Weather and Climate Dynamics*, *2*(2), 507–534, doi: 10.5194/wcd-2-507-2021.

Praz, C., Y.-A. Roulet, and A. Berne (2017), Solid hydrometeor classification and riming degree estimation from pictures collected with a Multi-Angle Snowflake Camera, *Atmospheric Measurement Techniques*, *10*(4), 1335–1357, doi: 10.5194/amt-10-1335-2017.

Probert-Jones, J. R. (1962), The radar equation in meteorology, *Quarterly Journal of the Royal Meteorological Society*, *88*(378), 485–495, doi: 10.1002/qj.49708837810.

Protat, A., C. Klepp, V. Louf, W. A. Petersen, S. P. Alexander, A. Barros, J. Leinonen, and G. G. Mace (2019), The Latitudinal Variability of Oceanic Rainfall Properties and Its Implication for Satellite Retrievals: 1. Drop Size Distribution Properties, *Journal of Geophysical Research: Atmospheres*, *124*(23), 13,291–13,311, doi: 10.1029/2019JD031010.

Ralph, F. M., P. J. Neiman, and G. A. Wick (2004), Satellite and CALJET Aircraft Observations of Atmospheric Rivers over the Eastern North Pacific Ocean during the Winter of 1997/98, *Monthly Weather Review*, *132*(7), 1721–1745, doi: 10.1175/1520-0493(2004)132<1721:SACAOO>2.0.CO;2.

Ralph, F. M., P. J. Neiman, G. A. Wick, S. I. Gutman, M. D. Dettinger, D. R. Cayan, and A. B. White (2006), Flooding on California's Russian River: Role of atmospheric rivers, *Geophysical Research Letters*, *33*(13), doi: 10.1029/2006GL026689.

Ray, P. S., and C. Ziegler (1977), De-Aliasing First-Moment Doppler Estimates, *Journal of Applied Meteorology*, *16*(5), 563–564, doi: 10.1175/1520-0450(1977)016<0563:DAFMDE>2.0.CO;2.

Rico-Ramirez, M. A., and I. D. Cluckie (2008), Classification of Ground Clutter and Anomalous Propagation Using Dual-Polarization Weather Radar, *IEEE Transactions on Geoscience and Remote Sensing*, *46*(7), 1892–1904, doi: 10.1109/TGRS.2008.916979.

Royer, P., A. Bizard, L. Sauvage, and L. Thobois (2014), Alidation protocol and intercomparison campaigns with the R-MAN510 aerosol lidar, in *Proc. 17th Int. Symp. for the Advancement of Boundary-Layer Remote Sensing*, pp. XX–XX, Auckland, New Zealand.

Rutz, J. J., W. James Steenburgh, and F. Martin Ralph (2014), Climatological characteristics of atmospheric rivers and their inland penetration over the western united states, *Monthly Weather Review*, *142*(2), 905–921, doi: 10.1175/MWR-D-13-00168.1.

Ryzhkov, A. V., and D. S. Zrnic (2019a), Polarimetric "Fingerprints" of Different Microphysical Processes in Clouds and Precipitation, in *Radar Polarimetry for Weather Observations*, edited by A. V. Ryzhkov and D. S. Zrnic, Springer Atmospheric Sciences, pp. 207–268, Springer International Publishing, Cham, doi: 10.1007/978-3-030-05093-1_7.

Ryzhkov, A. V., and D. S. Zrnic (2019b), Microphysical and Dielectric Properties of Hydrometeors, in *Radar Polarimetry for Weather Observations*, edited by A. V. Ryzhkov and D. S. Zrnic, Springer Atmospheric Sciences, pp. 63–96, Springer International Publishing, Cham, doi: 10.1007/978-3-030-05093-1_4.

Ryzhkov, A. V., and D. S. Zrnic (2019c), Polarimetric Variables, in *Radar Polarimetry for Weather Observations*, edited by A. V. Ryzhkov and D. S. Zrnic, Springer Atmospheric Sciences, pp. 97–146, Springer International Publishing, Cham, doi: 10.1007/978-3-030-05093-1_5.

Ryzhkov, A. V., T. J. Schuur, D. W. Burgess, P. L. Heinselman, S. E. Giangrande, and D. S. Zrnic (2005), The Joint Polarization Experiment: Polarimetric Rainfall Measurements and Hydrometeor Classification, *Bulletin of the American Meteorological Society*, *86*(6), 809–824, doi: 10.1175/BAMS-86-6-809.

Sachsperger, J., S. Serafin, V. Grubišić, I. Stiperski, and A. Paci (2017), The amplitude of lee waves on the boundary-layer inversion, *Quarterly Journal of the Royal Meteorological Society*, *143*(702), 27–36, doi: 10.1002/qj.2915.

Saleeby, S. M., W. R. Cotton, D. Lowenthal, R. D. Borys, and M. A. Wetzel (2009), Influence of cloud condensation nuclei on orographic snowfall, *Journal of Applied Meteorology and Climatology*, *48*(5), 903–922, doi: 10.1175/2008JAMC1989.1.

Schaer, M., C. Praz, and A. Berne (2020), Identification of blowing snow particles in images from a Multi-Angle Snowflake Camera, *The Cryosphere*, *14*(1), 367–384, doi: 10.5194/tc-14-367-2020.

Schneebeli, M., N. Dawes, M. Lehning, and A. Berne (2013), High-resolution vertical profiles of X-band polarimetric radar observables during snowfall in the Swiss Alps, *Journal of Applied Meteorology and Climatology*, *52*(2), 378–394, doi: 10.1175/JAMC-D-12-015.1.

Schneebeli, M., J. Grazioli, and A. Berne (2014), Improved estimation of the specific differential phase shift using a compilation of kalman filter ensembles, *IEEE Transactions on Geoscience and Remote Sensing*, *52*(8), 5137–5149, doi: 10.1109/TGRS.2013.2287017.

Schönhuber, M., G. Lammer, and W. L. Randeu (2007), One decade of imaging precipitation measurement by 2D-video-distrometer, in *Advances in Geosciences*, vol. 10, pp. 85–90, Copernicus GmbH, doi: 10.5194/adgeo-10-85-2007.

Schrom, R. S., and M. R. Kumjian (2016), Connecting microphysical processes in colorado winter storms with vertical profiles of radar observations, *Journal of Applied Meteorology and Climatology*, *55*(8), 1771–1787, doi: 10.1175/JAMC-D-15-0338.1.

Schultz, D. M. (2001), Reexamining the cold conveyor belt, *Monthly Weather Review*, *129*(9), 2205–2225, doi: 10.1175/1520-0493(2001)129<2205:RTCCB>2.0.CO;2.

Schuur, T. J., A. V. Ryzhkov, D. E. Forsyth, P. Zhang, and H. D. Reeves (2014), Precipitation Observations with NSSL's X-band Polarimetric Radar during the SNOW-V10 Campaign, *Pure and Applied Geophysics*, *171*(1-2), 95–112, doi: 10.1007/s00024-012-0569-2.

Seliga, T. A., and V. N. Bringi (1976), Potential Use of Radar Differential Reflectivity Measurements at Orthogonal Polarizations for Measuring Precipitation, *Journal of Applied Meteorology (1962-1982)*, *15*(1), 69–76.

Shepherd, A., and D. Wingham (2007), Recent Sea-Level Contributions of the Antarctic and Greenland Ice Sheets, *Science*, *315*(5818), 1529–1532, doi: 10.1126/science.1136776.

Shupe, M. D., et al. (2013), High and Dry: New Observations of Tropospheric and Cloud Properties above the Greenland Ice Sheet, *Bulletin of the American Meteorological Society*, *94*(2), 169–186, doi: 10.1175/BAMS-D-11-00249.1.

Sotiropoulou, G., E. Vignon, G. Young, H. Morrison, S. J. O'Shea, T. Lachlan-Cope, A. Berne, and A. Nenes (2021), Secondary ice production in summer clouds over the Antarctic coast: An underappreciated process in atmospheric models, *Atmospheric Chemistry and Physics*, *21*(2), 755–771, doi: 10.5194/acp-21-755-2021.

Speirs, J. C., D. F. Steinhoff, H. A. McGowan, D. H. Bromwich, and A. J. Monaghan (2010), Foehn Winds in the McMurdo Dry Valleys, Antarctica: The Origin of Extreme Warming Events, *Journal of Climate*, *23*(13), 3577–3598, doi: 10.1175/2010JCLI3382.1.

Speirs, J. C., H. A. McGowan, D. F. Steinhoff, and D. H. Bromwich (2013), Regional climate variability driven by foehn winds in the McMurdo Dry Valleys, Antarctica, *International Journal of Climatology*, *33*(4), 945–958, doi: 10.1002/joc.3481.

Sprenger, M., and H. Wernli (2015), The LAGRANTO Lagrangian analysis tool - Version 2.0, *Geoscientific Model Development*, *8*(8), 2569–2586, doi: 10.5194/gmd-8-2569-2015.

Steinhoff, D. F., D. H. Bromwich, and A. Monaghan (2013), Dynamics of the Foehn Mechanism in the McMurdo Dry Valleys of Antarctica from Polar WRF, *Quarterly Journal of the Royal Meteorological Society*, *139*(675), 1615–1631, doi: 10.1002/qj.2038.

Stephens, G. L., et al. (2002), THE CLOUDSAT MISSION AND THE A-TRAIN: A New Dimension of Space-Based Observations of Clouds and Precipitation, *Bulletin of the American Meteorological Society*, *83*(12), 1771–1790, doi: 10.1175/BAMS-83-12-1771.

Stephens, G. L., et al. (2009), CloudSat mission: Performance and early science after the first year of operation, *Journal of Geophysical Research Atmospheres*, *114*(8), 1–18, doi: 10.1029/2008JD009982.

Stoelinga, M., P. V. Hobbs, and C. F. Mass (2003), Improvement of microphysical observational verification parameterization through experiment, *Bull. Amer. Meterol. Soc.*, *84*(April), 1807–1826, doi: 10.1175/BAMS-84-12-1807.

Summerson, R., and I. D. Bishop (2011), Aesthetic value in Antarctica: Beautiful or sublime?, *The Polar Journal*, *1*(2), 225–250, doi: 10.1080/2154896X.2011.626626.

Takahashi, T. (1993), High ice crystal production in winter cumuli over the Japan Sea, *Geophysical Research Letters*, *20*(6), 451–454, doi: 10.1029/93GL00613.

Takahashi, T., T. Endoh, G. Wakaham, and N. Fukuta (1991), Vapor diffusional growth of free-falling snow crystals between -3 and -23 °C, *Journal of the Meteorological Society of Japan*, *69*, 15–30.

Takahashi, T., Y. Nagao, and Y. Kushiyama (1995), Possible High Ice Particle Production during Graupel–Graupel Collisions, *Journal of the Atmospheric Sciences*, *52*(24), 4523–4527, doi: 10.1175/1520-0469(1995)052<4523:PHIPPD>2.0.CO;2.

Thériault, J. M., et al. (2012), A Case Study of Processes Impacting Precipitation Phase and Intensity during the Vancouver 2010 Winter Olympics, *Weather and Forecasting*, *27*(6), 1301–1325, doi: 10.1175/WAF-D-11-00114.1.

Turner, J., et al. (2009), Record low surface air temperature at Vostok station, Antarctica, *Journal of Geophysical Research*, *114*(D24), D24,102–D24,102, doi: 10.1029/2009JD012104.

Turner, J., et al. (2019), The Dominant Role of Extreme Precipitation Events in Antarctic Snowfall Variability, *Geophysical Research Letters*, doi: 10.1029/2018GL081517.

Valkonen, T., T. Vihma, S. Kirkwood, and M. M. Johansson (2010), Fine-scale model simulation of gravity waves generated by Basen nunatak in Antarctica, *Tellus A: Dynamic Meteorology and Oceanography*, *62*(3), 319–332, doi: 10.1111/j.1600-0870.2009.00443.x.

van den Broeke, M. R., and H. Gallée (1996), Observation and simulation of barrier winds at the western margin of the Greenland ice sheet, *Quarterly Journal of the Royal Meteorological Society*, *122*(534), 1365–1383, doi: 10.1002/qj.49712253407.

Vardiman, L. (1978), The Generation of Secondary Ice Particles in Clouds by Crystal–Crystal Collision, *Journal of the Atmospheric Sciences*, *35*(11), 2168–2180, doi: 10.1175/1520-0469(1978)035<2168:TGOSIP>2.0.CO;2.

Verlinde, J., B. D. Zak, M. D. Shupe, M. D. Ivey, and K. Stamnes (2016), The ARM North Slope of Alaska (NSA) Sites, *Meteorological Monographs*, *57*, 8.1–8.13, doi: 10.1175/AMSMONOGRAPHS-D-15-0023.1.

Vignon, E., O. Traullé, and A. Berne (2019), On the fine vertical structure of the low troposphere over the coastal margins of East Antarctica, *Atmospheric Chemistry and Physics*, *19*(7), 4659–4683, doi: 10.5194/acp-19-4659-2019.

Vignon, E., G. Picard, C. Durán Alarcón, and S. P. Alexander (2020), Gravity wave excitation during the coastal transition of an extreme katabatic flow in Antarctica, *Journal of Atmospheric Sciences*, doi: 10.1175/JAS-D-19-0264.1.

Vignon, E., S. P. Alexander, P. J. DeMott, G. Sotiropoulou, F. Gerber, T. C. J. Hill, R. Marchand, A. Nenes, and A. Berne (2021), Challenging and improving the simulation of mid-level mixed-phase clouds over the high-latitude Southern Ocean, *Journal of Geophysical Research: Atmospheres*, doi: 10.1029/2020JD033490.

von Lerber, A., D. Moisseev, L. F. Bliven, W. Petersen, A. M. Harri, and V. Chandrasekar (2017), Microphysical properties of snow and their link to Ze-S relations during BAECC 2014, *Journal of Applied Meteorology and Climatology*, *56*(6), 1561–1582, doi: 10.1175/JAMC-D-16-0379.1.

Vosper, S. B., A. N. Ross, I. A. Renfrew, P. Sheridan, A. D. Elvidge, and V. Grubišić (2018), Current Challenges in Orographic Flow Dynamics: Turbulent Exchange Due to Low-Level Gravity-Wave Processes, *Atmosphere*, *9*(9), 361, doi: 10.3390/atmos9090361.

Wang, P. K. (2013), *Physics and Dynamics of Clouds and Precipitation*, Cambridge University Press, Cambridge, doi: 10.1017/CBO9780511794285.

Watanabe, S., K. Sato, and M. Takahashi (2006), A general circulation model study of the orographic gravity waves over Antarctica excited by katabatic winds, *Journal of Geophysical Research: Atmospheres*, *111*(D18), doi: 10.1029/2005JD006851.

Wegener, A. (1911), *Thermodynamik der Atmosphäre.*, J.A. Barth, Leipzig.

Welker, C., O. Martius, P. Froidevaux, C. H. Reijmer, and H. Fischer (2014), A climatological analysis of high-precipitation events in Dronning Maud Land, Antarctica, and associated large-scale atmospheric conditions: High precipitation in Dronning Maud Land, *Journal of Geophysical Research: Atmospheres*, *119*(21), 11,932–11,954, doi: 10.1002/2014JD022259.

Wernli, H., and H. C. Davies (1997), A Lagrangian-based analysis of extratropical cyclones. I: The method and some applications, *Quarterly Journal of the Royal Meteorological Society*, *123*(538), 467–489, doi: 10.1256/smsqj.53810.

Wernli, H., and C. Schwierz (2006), Surface Cyclones in the ERA-40 Dataset (1958–2001). Part I: Novel Identification Method and Global Climatology, *Journal of the Atmospheric Sciences*, *63*(10), 2486–2507, doi: 10.1175/JAS3766.1.

Wernli, H., P. Knippertz, H. Sodemann, A. Stohl, F. Dominguez, H. Hu, and J. M. Cordeira (2016), Mid-Latitude Dynamics and Atmospheric Rivers Objective and Outline Objective, in *2016 International Atmospheric Rivers Conference*.

Wille, J. D., V. Favier, A. Dufour, I. V. Gorodetskaya, J. Turner, C. Agosta, and F. Codron (2019), West Antarctic surface melt triggered by atmospheric rivers, *Nature Geoscience*, *12*(11), 911–916, doi: 10.1038/s41561-019-0460-1.

Wille, J. D., V. Favier, I. V. Gorodetskaya, C. Agosta, C. Kittel, J. C. Beeman, N. C. Jourdain, J. T. M. Lenaerts, and F. Codron (2021), Antarctic atmospheric river climatology and precipitation impacts, *Journal of Geophysical Research: Atmospheres*, *n/a*(n/a), e2020JD033,788, doi: 10.1029/2020JD033788.

Winker, D., J. Pelon, and M. Mccormick (2003), The CALIPSO mission: Spaceborne lidar for observation of aerosols and clouds, *Proc. SPIE-Int. Soc. Opt. Eng.*, *4893*.

Wolfensberger, D., D. Scipion, and A. Berne (2016), Detection and characterization of the melting layer based on polarimetric radar scans, *Quarterly Journal of the Royal Meteorological Society*, *142*(August), 108–124, doi: 10.1002/qj.2672.

Yano, J.-I., and V. T. J. Phillips (2011), Ice–Ice Collisions: An Ice Multiplication Process in Atmospheric Clouds, *Journal of the Atmospheric Sciences*, *68*(2), 322–333, doi: 10.1175/2010JAS3607.1.

Young, G., T. Lachlan-Cope, S. J. O'Shea, C. Dearden, C. Listowski, K. N. Bower, T. W. Choularton, and M. W. Gallagher (2019), Radiative Effects of Secondary Ice Enhancement in Coastal Antarctic Clouds, *Geophysical Research Letters*, *46*(4), 2312–2321, doi: 10.1029/2018GL080551.

Yu, L., Q. Yang, T. Vihma, S. Jagovkina, J. Liu, Q. Sun, and Y. Li (2018), Features of Extreme Precipitation at Progress Station, Antarctica, *Journal of Climate*, *31*(22), 9087–9105, doi: 10.1175/JCLI-D-18-0128.1.

Zagrodnik, J. P., L. A. Mcmurdie, R. A. Houze, and S. Tanelli (2019), Vertical structure and microphysical characteristics of frontal systems passing over a three-dimensional coastal mountain range, *Journal of the Atmospheric Sciences*, *76*(6), 1521–1546, doi: 10.1175/JAS-D-18-0279.1.

Zawadzki, I., F. Fabry, and W. Szyrmer (2001), Observations of supercooled water and secondary ice generation by a vertically pointing X-band Doppler radar, *Atmospheric Research*, *59-60*, 343–359, doi: 10.1016/S0169-8095(01)00124-7.

Zhu, Y., and R. E. Newell (1998), A Proposed Algorithm for Moisture Fluxes from Atmospheric Rivers, *Monthly Weather Review*, *126*(3), 725–735, doi: 10.1175/1520-0493(1998)126<0725:APAFMF>2.0.CO;2.

Zou, X., D. H. Bromwich, J. P. Nicolas, A. Montenegro, and S.-H. Wang (2019), West Antarctic surface melt event of January 2016 facilitated by föhn warming, *Quarterly Journal of the Royal Meteorological Society*, *145*(719), 687–704, doi: 10.1002/qj.3460.

JOSUÉ GEHRING

Avenue du Moulin 22, 1110 Morges, Suisse
+41 77 430 12 10 ◇ josue.gehring@gmail.com

EDUCATION

PhD in radar meteorology 2017 – 2021
Environmental Remote Sensing Laboratory - EPFL *Lausanne, Switzerland*

Thesis title: ”Leveraging meteorological radars to investigate the influence of atmospheric dynamics on snowfall microphysics”. Supervisor: Prof. Alexis Berne.

- Field campaign at Davis, Antarctica: deploying and operating EPFL's instruments at Davis station.
- Field campaign in South Korea: operating EPFL's instruments during the 2018 Winter Olympics.

M.Sc. in Atmospheric and Climate Science 2014 – 2016
Swiss Federal institute of Technology in Zurich (ETHZ) *Zurich, Switzerland*

Master thesis: “Weather-dependent verification of precipitation forecasts”, Swiss Federal Office of Meteorology and Climatology (MeteoSwiss). Supervisors: Prof. Heini Wernli, Mr. Jacques Ambühl.

B.Sc. in Environmental Sciences and Engineering 2010 – 2014
Swiss Federal Institute of Technology in Lausanne (EPFL) *Lausanne, Switzerland*

Exchange year at the University of Natural Ressources and Life Sciences, Vienna, Austria.

WORK EXPERIENCE

Weather forecaster Since June 2020
MeteoSwiss *Geneva, Switzerland*

Teaching assistant 2017 – 2019
EPFL *Lausanne, Switzerland*

Assistant for the M.Sc. course “Spatial statistics and analysis” and for the B.Sc. courses “Physics and chemistry of the atmosphere” and “Remote sensing”.

Intern in verification of numerical weather forecasts 2015 – 2016
MeteoSwiss *Zurich, Switzerland*

Intern in research and development 2014 – 2015
meteoblue AG *Basel, Switzerland*

Intern in verification of numerical weather forecasts July - August 2013
MeteoSwiss *Zurich, Switzerland*

PUBLICATIONS

Scientific journals

- Gehring, J., E. Vignon, A.-C. Billault-Roux, A. Ferrone, A. Protat, S. P. Alexander, and A. Berne (2021a), The influence of orographic gravity waves on precipitation during an atmospheric river event at Davis, Antarctica, *Earth and Space Science Open Archive*, doi: 10.1002/essoar.10507051.1

- Gehring, J., A. Ferrone, A.-C. Billault-Roux, N. Besic, K. D. Ahn, G. Lee, and A. Berne (2021b), Radar and ground-level measurements of precipitation collected by the École Polytechnique Fédérale de Lausanne during the International Collaborative Experiments for PyeongChang 2018 Olympic and Paralympic winter games, *Earth System Science Data*, *13*(2), 417–433, doi: 10.5194/essd-13-417-2021
- Planat, N., J. Gehring, É. Vignon, and A. Berne (2021), Identification of snowfall microphysical processes from Eulerian vertical gradients of polarimetric radar variables, *Atmospheric Measurement Techniques*, *14*(6), 4543–4564, doi: 10.5194/amt-14-4543-2021
- Thurnherr, I., K. Hartmuth, L. Jansing, J. Gehring, M. Boettcher, I. Gorodetskaya, M. Werner, H. Wernli, and F. Aemisegger (2021), The role of air–sea fluxes for the water vapour isotope signals in the cold and warm sectors of extratropical cyclones over the Southern Ocean, *Weather and Climate Dynamics*, *2*(2), 331–357, doi: 10.5194/wcd-2-331-2021
- Gehring, J., A. Oertel, E. Vignon, N. Jullien, N. Besic, and A. Berne (2020a), Microphysics and dynamics of snowfall associated with a warm conveyor belt over Korea, *Atmospheric Chemistry and Physics*, *20*(12), 7373–7392, doi: 10.5194/acp-20-7373-2020
- Walter, B., H. Huwald, J. Gehring, Y. Bühler, and M. Lehning (2020), Radar measurements of blowing snow off a mountain ridge, *The Cryosphere*, *14*(6), 1779–1794, doi: 10.5194/tc-14-1779-2020
- Vignon, E., N. Besic, N. Jullien, J. Gehring, and A. Berne (2019), Microphysics of Snowfall Over Coastal East Antarctica Simulated by Polar WRF and Observed by Radar, *Journal of Geophysical Research: Atmospheres*, *124*(21), 11,452–11,476, doi: 10.1029/2019JD031028
- Besic, N., J. Gehring, C. Praz, J. Figueras i Ventura, J. Grazioli, M. Gabella, U. Germann, and A. Berne (2018), Unraveling hydrometeor mixtures in polarimetric radar measurements, *Atmospheric Measurement Techniques*, *11*(8), 4847–4866, doi: 10.5194/amt-11-4847-2018
- Weihs, P., M. Rennhofer, D. J. Baumgartner, J. Gadermaier, J. E. Wagner, J. E. Gehring, and W. Laube (2015), Potential impact of contrails on solar energy gain, *Atmospheric Measurement Techniques*, *8*(3), 1089–1096, doi: 10.5194/amt-8-1089-2015

Dataset

- Gehring, J., A. Ferrone, A.-C. Billault-Roux, N. Besic, and A. Berne (2020b), Radar and ground-level measurements of precipitation during the ICE-POP 2018 campaign in South-Korea, *PANGAEA*, doi: 10.1594/PANGAEA.918315
- Gehring, J., I. Thurnherr, and P. Graf (2020c), Vertical profiles of Doppler spectra of hydrometeors from a Micro Rain Radar recorded during the austral summer of 2016/2017 in the Southern Ocean on the Antarctic Circumnavigation Expedition (ACE)., *Zenodo*, doi: 10.5281/zenodo.3929289

Conferences

- Gehring, J., Ferrone, A., Besic, N., Vignon, E., Oertel, A., Berne, A., 2019: Microphysics and polarimetric features of snowfall associated with a warm conveyor belt during the ICE-POP 2018 campaign. *39th Int. Conf. on Radar Meteorology*, Nara, Japan, Amer. Meteor. Soc., 8B-05
- Gehring, J., Ferrone, A., Besic, N., Vignon, E., Berne, A., 2019: Snowfall microphysics and polarimetric features of a warm front during the ICE-POP 2018 campaign. *EGU General Assembly 2019*, Vienna, Austria, Geophysical Research Abstracts, Vol. 21, EGU2019-3785

Media

- Gehring, J., Ma thèse en 180 secondes, finale Suisse, 6 juin 2019, La Chaux-de-Fonds
- Gehring, J., L'invité du 5h-6h30, la Matinale 5h-6h30, RTS, 26 mars 2018, 16:47
- Gehring, J., Violentes rafales de vent à Pyeongchang, le 12h45, RTS, 14 février 2018, 01:51
- Hug, N., Il part étudier la neige des JO en Corée du Sud, La Côte, www.lacote.ch, 4 février 2018
- Müller, A-C, Il veut percer les secrets de la neige, Le Matin, www.lematin.ch, 4 février 2018

· Borloz, E., Un doctorant de l'EPFL va étudier la neige olympique à Pyeongchang, 24 heures, www.24heures.ch, 4 février 2018

INFORMATION TECHNOLOGY

Programming:	Python, R, MATLAB, Bash
Office:	LaTeX, LibreOffice, Microsoft Office

LANGUAGES

French:	Native speaker
German, English:	High proficiency, spoken and written

OTHER ACADEMIC ACTIVITIES

Reviewer Since 2020

Reviewer for *Atmospheric Chemistry and Physics* and *Weather and Climate Dynamics*.

Ce document a été imprimé au Centre d’impression EPFL,
imprimerie climatiquement neutre, certifiée myClimate.